

Sheet Molding Compound processing: Characterization and numerical representation of the flow behavior

Anna Julia Imbsweiler

Vollständiger Abdruck der von der TUM School of Engineering and Design der Technischen Universität München zur Erlangung einer
Doktorin der Ingenieurwissenschaften (Dr.-Ing.)
genehmigten Dissertation.

Vorsitz: Prof. Dr.-Ing. Wolfram Volk

Prüfende der Dissertation:

1. Prof. Dr.-Ing. Klaus Drechsler
2. Prof. Dr. Eng. Kiyoshi Uzawa

Die Dissertation wurde am 01.07.2024 bei der Technischen Universität München eingereicht und durch die TUM School of Engineering and Design am 01.11.2024 angenommen.

Technische Universität München
TUM School of Engineering and Design
Lehrstuhl für Carbon Composites
Boltzmannstraße 15
D-85748 Garching bei München
Tel.: +49 (0) 89 / 289 – 15092
Fax.: +49 (0) 89 / 289 – 15097
Email: info.lcc@ed.tum.de
Web: www.asg.ed.tum.de/en/lcc/home/

ACKNOWLEDGEMENTS

I have to thank many different people, without whom this work would not exist. First and foremost my appreciation goes to Professor Klaus Drechsler, whose supervision has been extremely valuable throughout the process. Furthermore, I would like to thank our deputy head of chair Dr.-Ing. Swen Zaremba for very helpful tips and insights into the processing of composites, helping to broaden the view on the subject.

I am also deeply grateful for the enormous support I have been given by my former group leader and then mentor Dr.-Ing. David Colin. My colleagues have also been a huge help with a lot of advice both for the process of the dissertation, as well as practical hints on how to improve the investigation. In this regard I would like to particularly thank my office mates Maximilian Steinhardt, Benno Böckl, Christian Jäger, and Leo Heidemann, who have made everyday business quite enjoyable. Further colleagues I would like to thank for their input and help for both this Thesis and my work at the chair are Reiner Rauch, Daniel Amrein, Luciano Avila Grey, Dominik Boos, Margarita Etchegaray Bello, Daniela Schreil, Vincent Backmann, Dennis Bublitz, Christian Pohl, and Thomas Witteczek. Thank you also for the coffee breaks in the kitchen or the spontaneous meet-ups in the corridors. Both have led to very fruitful topic-related discussions and soothing and fun private conversations. Amazing were also the meetings of the Ladies Lunch Club with all my female colleagues. We spent several very funny and enjoyable evenings, thank you!

Immense support was also given to me by Yasutaka Shinoura, who I had worked with on my first project. The contact with him allowed me to deepen my fascination, but also my knowledge about Japan, leading to my 3-month research stay in Kanazawa. In this regard, I want to thank Professor Kiyoshi Uzawa for welcoming me at his institute Innovative Composite Center. I also want to thank him for his role as my second supervisor for this research. Another particular thank you goes to Satoko Hoshiba and Takehiro Shirai for their continued support during my time at ICC, both on private and on work-related topics. Moreover, I want to thank the other employees of ICC, who have contributed to making this experience unforgettable: Kazuha Yamamoto, Kimuko Higashi, Yoshihiro Saito, Ryoko Toudou, Junji Tanaka.

My gratefulness for their contribution extends to my friends, who with fun, good cooking and great talks make even the most stressful moments worth while. In this regard I want to thank my best friend Sara, but also all my friends Leyla, Alex, Lars, Fanny, Paul, Florian, Johannes, Robin, Christian, and Ele.

Finally, I deeply appreciate my family, particularly my parents and my sister Teresa, for always believing in me. You have been an immense source of motivation, but also advice throughout these years, and I will be eternally grateful. Last but not least, I want to thank my partner Julius for his continued support within but also outside this research work.

ABSTRACT

With the challenging environmental goals set by the EU, Sheet Molding Compound (SMC) appears promising for lightweight applications, especially in the automotive and electronics sectors. SMC is a long-fiber-reinforced material that provides high specific strength and stiffness, low cycle times, allows a high complexity of parts, and presents a great potential to integrate recycled fibers. The performance of these parts depends on the fiber orientation and the defects stemming from the flow of the material during the compression process. Therefore, a deep understanding of the flow is crucial in order to optimize SMC parts. Since the flow behavior is highly variable and complex, very broad guidelines and safety factors exist to ensure a suitable product quality that are based on experience. The complexity of the flow also makes an appropriate numerical description of the flow challenging. To keep computation times reasonable, commercially available software tools use simplifications. Therefore, the inputs for the material card, the charge configuration and placement, the simulation and process settings and the geometry have to be chosen carefully.

Within this study a new characterization procedure to determine the parameters for the rheology is developed. It includes the variability of the material, but is also easily applicable in an industrial context. Furthermore, a new flow test bench was developed, allowing a characterization of out-of-plane flow. It was adopted for a study of the influence of charge configurations on the compression pressure and the flow of the SMC. The study revealed that a separation between sheets or overall in the charge in direction of the flow significantly reduces the compression pressure. Therefore, it is advantageous to cut the sheet in proximity to ribs that are perpendicular to the sheets in order to favor a complete filling and avoid typical defects, such as weld lines or resin rich areas on the tip of the rib. Additionally, it could be concluded that the fiber orientation in the charge is very important, especially for small charges, since an orientation in flow direction keeps the pressure lower than if the fibers are perpendicular to the flow direction.

The new material cards determined with the new characterization procedure and with the results for the charge variations were validated by producing and simulating different geometries. The flow length showed good agreement in reality and in simulation, with the numerical flow being in the range predicted by the simulations. It could be concluded that it is advantageous to determine different material cards to cover the range of the variability. The variation in the flow length however, was smaller for the simple plate than for the plate with a rib.

With this research a significant step towards a better understanding of the flow of SMC has been made, allowing a more comprehensive inclusion in SMC process simulation and therefore, a more realistic numerical depiction of the flow. Furthermore, a better understanding of the flow of SMC allows a broader use of the material, including SMCs made with recycled carbon fibers.

KURZFASSUNG

Angesichts der anspruchsvollen Umweltziele der EU erscheint Sheet Molding Compound (SMC) vielversprechend für Leichtbauanwendungen, insbesondere in den Bereichen Automobil und Elektronik. SMC ist ein langfaserverstärktes Material, das eine hohe spezifische Festigkeit und Steifigkeit, kurze Zykluszeiten, eine hohe Komplexität der Teile und ein großes Potenzial zur Integration von recycelten Fasern bietet. Die Leistung dieser Teile hängt von der Faserorientierung und den durch den Fluss des Materials während des Kompressionsprozesses verursachten Defekten ab. Daher ist ein tiefes Verständnis des Flusses entscheidend, um SMC-Teile zu optimieren. Da das Fließverhalten sehr variabel und komplex ist, existieren sehr grobe Richtlinien und Sicherheitsfaktoren, die auf Erfahrung basieren, um eine geeignete Produktqualität zu gewährleisten. Die Komplexität des Flusses macht auch eine angemessene numerische Beschreibung des Flusses herausfordernd. Für akzeptabel kleine Berechnungszeiten verwenden kommerziell verfügbare Softwaretools Vereinfachungen. Daher müssen die Eingaben für die Materialkarte, die Ladekonfiguration und Platzierung, die Simulations- und Prozesseinstellungen sowie die Geometrie sorgfältig ausgewählt werden.

In dieser Studie wurde ein neues Charakterisierungsverfahren zur Bestimmung der Parameter für die Rheologie entwickelt. Es berücksichtigt die Variabilität des Materials, ist aber auch leicht in einem industriellen Kontext anwendbar. Darüber hinaus wurde ein neuer Flussprüfstand entwickelt, der eine Charakterisierung des out-of-plane Flusses ermöglicht. Er wurde für eine Untersuchung des Einflusses der Charge auf den Kompressionsdruck und den Fluss des SMC angepasst. Die Studie ergab, dass eine Trennung zwischen den Schichten oder insgesamt in der Charge in Fließrichtung den Kompressionsdruck erheblich reduziert. Daher ist es vorteilhaft, das Sheet in der Nähe von Rippen zu schneiden, die senkrecht zu den Sheets stehen, um eine vollständige Füllung zu begünstigen und typische Defekte wie Schweißnähte oder harzreiche Bereiche an der Spitze der Rippe zu vermeiden. Zusätzlich konnte festgestellt werden, dass die Faserorientierung in der Charge sehr wichtig ist, insbesondere bei kleinen Mengen, da eine Orientierung in Fließrichtung den Druck niedriger hält als wenn die Fasern senkrecht zur Fließrichtung ausgerichtet sind.

Die Materialkarten, die mit dem neuen Charakterisierungsverfahren und den Ergebnissen für die Chargenvariationen bestimmt wurden, wurden durch die Herstellung und Simulation verschiedener Geometrien validiert. Die Fließlänge zeigte in der Realität und in der Simulation eine gute Übereinstimmung, wobei der numerische Fluss im Bereich der durch die Simulationen vorhergesagten Werte lag. Es konnte nachgewiesen werden, dass es vorteilhaft ist, verschiedene Materialkarten zu bestimmen, um die Bandbreite der Variabilität abzudecken. Die Variation der Fließlänge war jedoch bei der einfachen Platte kleiner als bei der Platte mit einer Rippe.

Mit dieser Forschung wurde ein bedeutender Schritt zu einem besseren Verständnis des Flusses von SMC gegangen, was eine umfassendere Einbeziehung in die SMC-Prozesssimulation und damit eine realistischere numerische Darstellung des Flusses ermöglicht. Darüber hinaus ermöglicht ein besseres Verständnis des Flusses von SMC eine breitere Nutzung des Materials, einschließlich SMCs aus recycelten Carbonfasern.

Contents

Nomenclature	xiii
List of abbreviations	xvii
List of figures.....	xix
List of tables	xxix
1 Introduction	1
1.1 Motivation.....	2
1.2 Objectives and research questions	4
1.3 Reference material	4
1.4 Outline.....	5
2 State of the art	9
2.1 SMC production process.....	9
2.1.1 SMC Production	9
2.1.2 SMC Process.....	10
2.2 Numerical description of the flow	16
2.2.1 SMC simulation tools	17
2.2.2 3DTimon.....	22
2.3 Rheological characterization.....	25
2.3.1 Characterization procedure for process simulation	25
2.3.2 SMC flow characterization.....	29
3 Standardization of the characterization procedure	39
3.1 Parameters for the curing kinetics.....	40
3.1.1 Measurement and analysis approach	41
3.1.2 Results and discussion	42
3.1.3 Conclusion, further investigations, next steps	48
3.2 Parameters for the rheological model	51
3.2.1 Procedure to obtain the viscosity parameters	51
3.2.2 Results and discussion	54
3.2.3 Conclusion, further investigations, next steps	63
3.3 Calibration of the material card	66

3.3.1	In-plane flow calibration.....	66
3.3.2	Out of plane calibration	77
3.3.3	The new calibration procedure.....	97
3.4	The new procedure for flow characterization	98
3.5	Discussion	99
4	A new bar flow test bench for SMC flow characterization	101
4.1	Methods.....	103
4.2	Development process	103
4.3	The test bench.....	105
4.3.1	Functioning principle	107
4.3.2	First version of the test bench	108
4.3.3	Functional tests	110
4.4	Discussion	111
5	Investigation of charge variations influencing the flow behavior with numerical representation	113
5.1	Test parameters	114
5.1.1	Specimen configurations.....	114
5.1.2	Process Conditions.....	116
5.2	Results and discussion.....	117
5.2.1	Comparison of basic configurations	119
5.2.2	Variations of the single amount charges	122
5.2.3	Evaluation of the double amount charges	126
5.3	Numerical representation	130
5.3.1	Simulation settings.....	130
5.3.2	Calibration to the experimental variability	133
5.4	Guidelines.....	137
5.5	Summary of the numerical approach and discussion	140
6	Validation of the developed approach for SMC filling simulation... 143	
6.1	Approach	143
6.1.1	SMC part production.....	144
6.1.2	Simulation settings.....	146

6.2	Comparison of empirical and numerical results	148
6.2.1	Empirical results	149
6.2.2	Numerical results	152
6.2.3	Comparison.....	156
6.3	Influence of the process and simulation settings	157
6.4	Discussion and conclusion	164
7	Conclusion and Outlook.....	167
7.1	Summary and conclusion	167
7.2	Future research.....	170
	References	173
A	Appendix.....	187
a	DSC measurements and analysis	187
b	Sensitivity analysis results	192
c	Data sheets	198
d	Handbook for the rheological characterization.....	199
B	Publications.....	213
C	Supervised student theses.....	215

Nomenclature

Symbol	Unit	Description
Greek letters		
α	%	Curing degree
α_{gel}	%	Gelation point
$\dot{\gamma}$	1/s	Shear rate
η	Pa.s	Viscosity
η_0	Pa.s	Viscosity at t=0
η_1	Pa.s	Viscosity at t=1
λ	mm	Local value of z at which the shear stresses are zero
μ	Pa.s	Viscosity in squeeze flow tests
ρ	g/cm ³	Density
τ	-	Material specific constant in the viscosity model
τ_{ii}	Pa	Deviatoric stress
Latin letters		
a	-	Material specific constant in the viscosity model
A_1	-	Material specific constant to describe the Arrhenius temperature dependency
A_2	-	Material specific constant to describe the Arrhenius temperature dependency
A_{comp}	mm ²	Area of force application for compression piston in bar flow setup
A_{sens}	mm ²	Area of force application for pressure sensor
b	-	Material specific constant in the viscosity model

Symbol	Unit	Description
c_p	J/K.kg	Specific heat
D	-	Material specific constant in the viscosity model
E	-	Material specific constant in the viscosity model
E_1	-	Material specific constant to describe the Arrhenius temperature dependency
E_2	-	Material specific constant to describe the Arrhenius temperature dependency
F	N	Compression force during squeeze flow tests
F_{comp}	N	Compression force in bar flow tests
F_{sens}	N	Force applied on pressure sensor
g_i	N	Body force acting on the continuum
h	mm	Gap height
\dot{h}	mm/s	Closing speed
k	W/m.K	Thermal conductivity
ll	-	Lower limit of a parameter of the curing kinetics or of the viscosity
m	-	Kinetic exponent in the Kamal equation
n	-	Kinetic exponent in the Kamal equation
p	MPa	Pressure
p_{new}	-	New parameter in the calibration
p_{old}	-	Old parameter in the calibration
p_{sens}	MPa	Pressure applied on pressure sensor
\dot{q}	J/s	Heat flow during curing
$\dot{Q}_{viscous\ heating}$	J/s	Heat flow from viscous dissipation

Symbol	Unit	Description
\dot{Q}	J/s	Heat flow from an arbitrary heat source
Q_0	J	Total amount of generated heat in the exothermic curing reaction
r_0	mm	Initial charge radius in squeeze flow tests
$r(t)$	mm	Time dependent charge radius in squeeze flow tests
S	W/m.K	Viscosity-dependent flow conductance of the thin parts
t	s	Time
T	°C	Temperature
T_0	°C	Temperature at the beginning of the curing reaction
T_{tot}	°C	Temperature at the end of the curing reaction
u_i	m/s	Fluid velocity vector in direction i
ul	-	Upper limit of a parameter of the curing kinetics or of the viscosity
v_0	mm/s	Initial compression speed during squeeze flow tests
$v(t)$	mm/s	Time dependent compression speed during squeeze flow tests
\varnothing_{comp}	mm	Diameter of cylinder in bar flow test
\varnothing_{sens}	mm	Diameter of pressure sensor

List of abbreviations

Abbreviation	Description
CAE	Computer-aided engineering
CFRP	Carbon fiber reinforced plastics
CO ₂	Carbon dioxide
CPU	Central processing unit
CSMC	Carbon fiber sheet molding compound
DBS	Direct bundle simulation
DFS	Direct fiber simulation
DSC	Differential scanning calorimetry
EU	European Union
FVC	Fiber volume content
GSMC	Glass fiber sheet molding compound
Ip	In-plane
LCC	Chair (Lehrstuhl) of Carbon Composites
NDT	Non-destructive testing
Oop	Out-of-plane
SMC	Sheet molding compound
UTM	Universal testing machine

List of figures

Fig. 1-1	Views of the reference material: a) uncured SMC sheet; b) Profactor picture of cured plate; c) more complex SMC part with rib; d) and e) detail pictures of a bent and straight fiber bundle respectively; f) detail of bundle edge, with more random overall orientation of fiber bundles.	4
Fig. 1-2	Outline of this research work.	7
Fig. 2-1	Schematic representation of the sheet production for the SMC process [30].	10
Fig. 2-2	SMC molding process steps.	10
Fig. 2-3	Exemplary parts for SMC application: a) Forged Composites from Lamborghini [53], b) spare wheel pan of Mercedes AMG E-Class made with SMC from ASTAR SA [54], c) rear door of Toyota Prius PHV made with SMC from Mitsubishi Rayon [31], d) car rim made by Blackwave GmbH [55].	12
Fig. 2-4	Thickness variability for a 75 cm wide (y-direction) and 285 cm long (x-direction) SMC sheet, whereas x refers to the sheet production direction (data from [S20]).	13
Fig. 2-5	Typical flow-induced defects that significantly lower the mechanical properties of an SMC part: a) weld line represented in simulation and on a microscopy picture [62]; b) microscopy image showing voids and pure resin regions [S15].	14
Fig. 2-6	Results for tensile, compressive and shear moduli in 0°, 45° and 90° directions towards the flow of the material during the compression with scatter for plates with two charge configurations: half (H) and fourth (F) area coverage (adapted from [S19])	15
Fig. 2-7	Comparison of the orientation tensor A_{xx} for the same process settings in the SMC module in 3DTimon 10 R6.0 and Moldflow 2019 (adapted from [S18])	19
Fig. 2-8	Experimental results compared to the results for 3DTimon, Moldex3D and Moldflow for the compression height and force over time for a flat plaque (top) and a w-profile (bottom) (adapted from [89]).....	20
Fig. 2-9	Functioning principle of the direct fiber simulation (DFS) implemented in 3DTimon [88, 93, 94].	21

Fig. 2-10	Inputs and outputs for industrially available CAE software package 3DTimon, with the simulation itself represented as a black box, as it is not accessible and only the overall algorithms are known	22
Fig. 2-11	Typical procedure to set up a material card for SMC filling simulation	26
Fig. 2-12	DSC measurements: a) Schematics of the test [100]; b) exemplary result for a curve resulting for the heating rate 10 °C/min for the material adopted in this study CARBKID PGK5250 [44].	26
Fig. 2-13	Generated heat and resulting reaction rate for a curve at the heating rate of 10 °C/min for the SMC material adopted in this research CARBKID PGK5250 [44].	28
Fig. 2-14	Functioning principle of squeeze flow tests and typical specimen	28
Fig. 2-15	Overview of flow characterization principles for approaches derived from squeeze flow testing (adapted from [42, 106])	30
Fig. 2-16	Squeeze flow test variation of constant volume compared to constant cross section, exemplarily shown with the flow test setups of Dumont et al. [65] (left) and Lee et al. [69] (right).	31
Fig. 2-17	Squeeze flow testing variations: a) Setup for a UTM for an open mold and linear flow from Oelgarth [122]; b) Closed mold setup with pressure sensors arranged along the flow channel [67]; c) Charge configurations tested in an open mold with linear flow by Abrams et al. [120] and Boylan et al. [121].	32
Fig. 2-18	Out-of-plane flow testing setups: a) Stepped plate with incline [128]; b) plate with honeycomb geometry protruding from the surface [40]	33
Fig. 2-19	SMC charge during the compression: a) Formation of lubricating layers at the surfaces in contact with the heated mold and detail representation of the flow front (adapted from [46, 120]); b) Temperature, viscosity and flow velocity resulting from the temperature distribution [69].	34
Fig. 2-20	Side view of the SMC charge during the compression: a) experimental setup for the recordings (adapted from [61]); b) Flow front for closing speeds of 1 mm/s and 5 mm/s, with a reverse fountain for the first and a constant flow front progress for the second velocity (adapted from [134]); c) Flow front progression recorded in [61] for the compression speeds 2 mm/s and 15 mm/s, again showing the reverse fountain for the lower closing speed.	35

Fig. 2-21	Deformation of a charge with 5 black and white layers in thickness and in radial direction in comparison for 1.75 mm/s and 10 mm/s [70].....	36
Fig. 2-22	Resulting specimens after the compression of a circular SMC charge with 7 layers with different colors with (left) and without vacuum (right) seen from the top at 144 °C and 2.5 mm/s compression speed [115].....	37
Fig. 3-1	Results for all tests performed at 30 °C/min.....	42
Fig. 3-2	Process to obtain the reaction rate by determining a baseline for the reaction heat peak (top), then referencing the generated heat to a flat baseline at level 0 (bottom left), and finally calculating the reaction rate (bottom right).....	44
Fig. 3-3	Influence of the baseline on the resulting reaction rate: three plausible baselines for the curve at 10 K/min (left), and the resulting reaction rates compared to the averages of the reaction rates for 20 K/min and 40 K/min.....	45
Fig. 3-4	Reaction rates for all five samples tested with 40 K/min heating rate and the resulting average.....	46
Fig. 3-5	All averages of the reaction rates for all tested heating rates.....	46
Fig. 3-6	Exemplary fitting result for the chosen heating rates 10 K/min, 30 K/min, and 50 K/min (image taken of the fitting tool provided by the software solution 3DTimon).....	47
Fig. 3-7	Schematic representation of the developed procedure summarizing the three main steps of the measurements, the data analysis and the fitting, with the related guidelines.....	48
Fig. 3-8	Comparison between the range covered by all five tests performed at the heating rate 50 K/min in 2020 and 2023.....	49
Fig. 3-9	Comparison between the reaction rates for the data from 2020 and newly obtained data from 2023 for the heating rate of 50 K/min.....	50
Fig. 3-10	Squeeze flow tests: a) setup in a universal testing machine for 250 kN equipped with parallel plates, thermal chamber and video extensometer; b) 3-layered SMC specimen with thermocouples and steel plate used at top and bottom.	52
Fig. 3-11	Squeeze flow results displayed as force over displacement for the low temperature results of room temperature, 55 °C and 85 °C.....	54

Fig. 3-12	Exemplary specimen for a test at 85 °C on the left compared to the size of a charge before the test on the right: the specimen is partially cured and shows long and uneven flow paths	55
Fig. 3-13	Squeeze flow results displayed as force over displacement for the high temperature results of 120 °C and 130 °C.....	56
Fig. 3-14	Specimens that resulted from the squeeze flow tests performed at 120 °C on the top and 130 °C on the bottom for each compression speed.....	57
Fig. 3-15	Exemplary selection of the relevant section for the fitting for high temperature fitting (top) and low temperature fitting (bottom).....	60
Fig. 3-16	Relevant range for the fitting of the viscosity parameters for all tested curves with low temperature results (top) and high temperature results (bottom).....	61
Fig. 3-17	Schematic representation of the recommended procedure for the determination of the viscosity parameters for SMC, displaying a dependence of the viscosity from the temperature, the degree of curing and the shear rate.....	62
Fig. 3-18	Comparison of the results obtained from the first squeeze flow tests from 2020 and the new tests from 2023: comparison of the results obtained for 10 mm/min compression speed at 55 °C (top) and 120 °C (bottom).....	64
Fig. 3-19	Comparison of the results for the test series of 2023 for 10 mm/min and 60 mm/min compression speed for both 55 °C and 120 °C tests.	65
Fig. 3-20	Simulation of squeeze flow tests, with circular charge of 100 mm in diameter and 8.4 mm thickness in the center of a circular mold.....	66
Fig. 3-21	Simulation result for the force over displacement compared to experimental result after fitting the squeeze flow results for the low and high temperature viscosity models for the test performed at 130 °C and 10 mm/min.	68
Fig. 3-22	Sensitivity analysis result with upper and lower limit compared to the numerical reference for the parameters m (top) and A_2 (bottom).	69
Fig. 3-23	Calibration steps performed on the squeeze flow simulations starting with the parameters from the fitting of the curing kinetics and the viscosity parameters.	72
Fig. 3-24	Procedure for the calibration of the rheological parameters with squeeze flow tests for the in-plane flow.	73

Fig. 3-25	Influence of the temperature on the suitability of a specific parameter value, exemplarily setting parameter α to 21 compared to 0.4.....	74
Fig. 3-26	Influence of simulation settings on the outcome of the simulation: a) comparison of the two adopted versions for this research being 3DTimon R4.0 from 2020 and 3DTimon R8.1.1 from 2023; b) comparison of different mesh sizes in x-, y-, and z-directions.	75
Fig. 3-27	Schematics of the test: a) the bar flow test setup developed in Chapter 4; b) disc pile specimens adopted for the flow characterization with displacement control.....	78
Fig. 3-28	Simulation of the bar flow test with the initial charge and the flow of the material in the bar during the compression.	80
Fig. 3-29	Juxtaposition of the compression force in the simulation with the material card resulting from the in-plane calibration with compression force in the experimental result, including its range from the performed tests.	81
Fig. 3-30	Specimens resulting in the bar flow experiment and the simulation.	82
Fig. 3-31	Exemplary result for the sensitivity analysis for displacement control for the parameters m of the curing kinetics and τ of the viscosity model.....	82
Fig. 3-32	Calibration of the curing kinetics and viscosity model in the bar flow simulation starting with the result from the in-plane result showing the ten applied calibration steps in direct comparison with the experimental average and the covered range of the experimental curves.	84
Fig. 3-33	Bar flow test setup in CAD [131] with highlight of crucial features.	86
Fig. 3-34	Material placement, cavity and flow pattern: a) overall measurements of the cylindrical opening and charge placement, b) exemplary result after the compression, with material that has flown into the bar.	87
Fig. 3-35	Spiral charge of SMC: a) front and top view, with top view being an actual specimen, b) measurements of each rectangle rolled up to a spiral.....	87
Fig. 3-36	Process simulation model of the bar flow test, with the initial cylindrical charge at the tip of the flow channel on the left and the full model with the material flowing into the channel on the right.....	89
Fig. 3-37	Results of the piston position over time for all five performed tests and the respective average for 132 °C (top) and 128 °C (bottom).....	89

Fig. 3-38	Simulation result compared to experimental result considering the material card obtained after the in-plane fitting.	90
Fig. 3-39	Sensitivity analysis result with upper and lower limit compared to the numerical reference for the parameters m (left) and τ (right).	91
Fig. 3-40	Calibration steps performed on the bar flow simulations for force control, starting with the parameters from the calibration of the in-plane flow of the curing kinetics and the viscosity parameters.	92
Fig. 3-41	Influence of simulation settings on the outcome of the displacement signal: a) comparison of the set closing speed and the closing speed of 1 mm/s; b) comparison of different mesh sizes in x-, y-, and z-direction.	94
Fig. 3-42	Procedure for the calibration of the out-of-plane flow, applied for both the displacement control and the force control results.	95
Fig. 3-43	Application of the calibration steps from the displacement control to the force control and comparison of the results for the two different procedures: a) result for all ten calibration steps; b) direct comparison of the resulting piston position for both procedures.	96
Fig. 3-44	Schematics of the calibration procedure with in-plane procedure as first step, followed by the out-of-plane calibration, where it can be chosen between displacement control and force control.	98
Fig. 3-45	Schematic overview of the modified characterization procedure for the establishment of a suitable material card for SMC.	99
Fig. 4-1	Control cycle between objectives, activities and results, and detail of results, adapted from [143–147].	103
Fig. 4-2	Setup of the test bench and identification of the main components.	105
Fig. 4-3	Barflow test setup with detail of handles and metal plates and placement inside RUCKS thermoforming press covered with an aluminum box for improved thermal management.	106
Fig. 4-4	Inside of the lower mold with a pressure sensor at the beginning of the flow channel and eight temperature sensors aligned along the low channel.	107
Fig. 4-5	Functioning principle: a) measurements of the cavity and the initial charge, with exemplary charge from the test series, b) load application surface and flow direction with exemplary specimen from the test series.	107
Fig. 4-6	Configuration in the first version, related problems and their respective solutions for the new version. All options have been	

	implemented, except for the last one, which shall be done before any future testing.	109
Fig. 4-7	Result of the pressure and temperature recording during the functional tests for the final version and the first version.	110
Fig. 5-1	The charge configurations considered in this study: a) configuration of a disc pile charge, b) configuration of a spiral charge, consisting of a rolled up rectangle, c) prepared disc pile charge, d) prepared spiral charge	115
Fig. 5-2	Press profile showing the upper tool displacement position and speed, and the maximum force set for the compression step.....	116
Fig. 5-3	Results for all performed tests and the averages calculated for each sequence	118
Fig. 5-4	Exemplary interruptions during the compression reflected in the recorded pressure signal	119
Fig. 5-5	Comparison between the single amount non-oriented disc pile charge and the spiral charge	119
Fig. 5-6	All specimens of the basis (single amount disc pile, non-oriented, within pot life) and the single amount spiral charges: a) detail of the tips for disc charges after the test (right) compared to a disc of uncured SMC before the test (covered with carrier foil); b) all specimens in comparison; c) direct comparison of exemplary specimen for each test series	120
Fig. 5-7	Spiral charge showing the recurring separation between inner and outer layers of fibers within the sheet	121
Fig. 5-8	Results for disc pile charges compared to reference (in blue): a) oriented (red) vs. non-oriented reference (blue), b) old material newly tested (light green) vs. old material tested one year earlier (dark green) vs. reference with new material (blue)	123
Fig. 5-9	Two disc pile charges with 28 discs with different heights due to varying sheet thickness	125
Fig. 5-10	Comparison of the averages and the covered range of the data for the results of the first and second trial of the spiral charges	125
Fig. 5-11	Comparison of the averages of the results for double amount charges with single amounts	127
Fig. 5-12	Specimens resulting for the double amounts: a) all specimens for the double amount disc and spiral charges, b) comparison between a	

	double amount spiral charge (top) and a double amount disc charge (bottom).....	129
Fig. 5-13	Charge configurations used in flow simulation for the disc pile charge and for the two versions of the spiral charge.	132
Fig. 5-14	Comparison of the simulation results for different charge settings replicating the disc pile charge and the spiral charge.....	132
Fig. 5-15	Process of calibration of the material card to the upper and lower limits of the experimental range.	133
Fig. 5-16	Calibration of the material card for the spiral charge showing the experimental average and the variation in the force signal in comparison to the result with the material card from the out-of-plane calibration and the results for the calibration steps.	135
Fig. 5-17	Assessment of the variability for the simulation with disc pile charges and spiral charges, displaying the result for the five tests, the average and the covered range.	136
Fig. 5-18	Charge variations simulated in the evaluation of the variability of the simulation: a) weights of each charge; b) top view of the simulated spiral charges.	137
Fig. 6-1	SMC parts produced within this study, with charge configuration and main flow direction: a) geometry of simple plate; b) geometry of plate with rib; c) charge configuration with 1/3 coverage for the simple plate; d) charge configuration with 1/3 coverage for the plate with rib.	144
Fig. 6-2	Plate production: a) Wickert WKP 3000 S press at Toray AMCEU used for the plate production; b) lower mold made of SMC for the plate geometry with rib.....	145
Fig. 6-3	Plate production: a) typical charge with five entire layers and a sixth partial layer placed between the third and fourth layer; b) exemplary incompletely filled plate; c) exemplary incompletely filled plate with rib; d) detail of incompletely filled rib.	146
Fig. 6-4	Simulations of the filling time of the plate and the plate with rib at the beginning and end of the compression, as well as at two intermediate steps; a detail of the partially filled rib is also displayed on the bottom right.	148
Fig. 6-5	Flow front results for all produced plates in direct comparison for: a) the simple plate; b) the plate with rib; c) the rib.	149

Fig. 6-6	Details of the flow front: a) protruding edge with visible sheet angle; b) Surface deformation along the flow front and pure resin and release agent front; c) layered structure of the flow front; d) closed flow front with bent layer slowing down the flow; e) detail of fibers oriented in flow direction on the surface of the plate; f) detail of chaotic fiber orientation for one strand within mostly fibers oriented in flow direction.	151
Fig. 6-7	Result of the filling time simulation for both the simple plate and the plate with rib for the three defined material cards of the basis, the higher and lower limits identified for the standard stacked SMC charge.	153
Fig. 6-8	Detail of the filling of each rib for the basis simulation settings and the limits with a representation of all results overlapped.....	154
Fig. 6-9	Comparison of the stroke data for the three variations with the basis, the limit high and low for both configurations of the simple plate (p) and the plate with rib (r).....	155
Fig. 6-10	Direct comparison between the results for the produced plates and the simulations with the “basis” material card: a) results for the simple plate; b) results for the plate with rib; c) detail of the rib.....	156
Fig. 6-11	Charge variation during the production: a) charge as tested, with a significant variation in the thickness; b) translation into simulation for both geometries with the representation of full layers compared to the more complex charge with full layers and an additional piece placed on top.	159
Fig. 6-12	Flow of SMC in the plate and the plate with rib for the charge variation with full layers and an additional smaller piece on top.	160
Fig. 6-13	Results for the simulations with the charge variation with a juxtaposition of the filling result and the summary of the final thickness of the geometries, and the maximum flow length and rib filling.	161
Fig. 6-14	Results for the filling time, the temperature distribution and the pressure distribution at the end of the compression for the mesh variations performed for the simple plates.....	162
Fig. 6-15	Results for the filling time, the temperature distribution and the pressure distribution at the end of the compression for the mesh variations performed for the plates with rib.....	163

Fig. A- 1	All tests at 20 K/min.....	187
Fig. A- 2	All tests at 30 K/min.....	187
Fig. A- 3	All tests at 40 K/min.....	188
Fig. A- 4	All tests at 50 K/min.....	188
Fig. A- 5	All tests at 60 K/min.....	189
Fig. A- 6	All reaction rates and resulting average at 20 K/min	189
Fig. A- 7	All reaction rates and resulting average at 30 K/min	190
Fig. A- 8	All reaction rates and resulting average at 50 K/min	190
Fig. A- 9	All reaction rates and resulting average at 60 K/min	191
Fig. A- 10	Sensitivity analysis of the curing parameters for squeeze flow tests	192
Fig. A- 11	Sensitivity analysis of the viscosity parameters for squeeze flow tests ...	193
Fig. A- 12	Sensitivity analysis of the curing parameters for bar flow tests with force control	194
Fig. A- 13	Sensitivity analysis of the viscosity parameters for bar flow tests with force control	195
Fig. A- 14	Sensitivity analysis of the curing parameters for bar flow tests with displacement control.....	196
Fig. A- 15	Sensitivity analysis of the viscosity parameters for bar flow tests with displacement control.....	197

List of tables

Tab. 2-1	Juxtaposition of material models and processing settings for SMC process simulation software solutions Moldex3D, 3DTimon and Moldflow (based on [89])	18
Tab. 3-1	Measured DSC test sequences	41
Tab. 3-2	Summary of the generated heat for all tested curves, and calculation of the average for each heating rate	43
Tab. 3-3	Test parameters for the squeeze flow tests, including temperature, the amount of performed repetitions, and the closing speeds	52
Tab. 3-4	Test sequence applied for the squeeze flow tests consisting of eight steps, including the involved action, as well as the set stop criterions	53
Tab. 3-5	Key values for the performed squeeze flow tests, including the temperature of each test, the maximum force and the compression start, which corresponds to the first contact with the SMC of the upper compression plate (force reaches 1 kN). The notation is as follows: “Temperature [-;°C]_closing speed [mm/min]”.	58
Tab. 3-6	Simulation settings with the reference value in reality, with focus on the compression settings, the charge and the simulation setting.....	67
Tab. 3-7	Result for the sensitivity analysis performed for the squeeze flow tests at 130 °C, showing the effect the upper and lower limit adopted have on the resulting force signal.	70
Tab. 3-8	Summary of the calibration steps performed on the squeeze flow simulations for the rheological parameters showing the changed parameters, the old and new values, the lower limit (ll) for the calculation, the reference material card for the new adaptation, as well as the result.....	71
Tab. 3-9	Rheological parameters resulting from the in-plane calibration to be used as a basis for the subsequent steps in direct comparison with the original parameters from the fitting result.	73
Tab. 3-10	Process settings and material data utilized for this evaluation, as well as the corresponding chosen simulation settings for the process settings and the material. Purely simulative settings are also summarized.	79
Tab. 3-11	Result of the sensitivity analysis for displacement control related to the force signal and the curing behavior.	83

Tab. 3-12	Summary of the calibration steps performed on the bar flow simulations for displacement control for the rheological parameters showing the changed parameters, the old and new values, the lower limit (II) for the calculation, the reference material card for the new adaptation, as well as an evaluation of the result.	84
Tab. 3-13	New set of parameters for the curing kinetics and viscosity model after the out-of-plan calibration in comparison to the parameters from the in-plane calibration. The changed parameters are highlighted by being bold.	85
Tab. 3-14	Process parameters applied for the bar flow tests, as well as process simulation settings within 3DTimon depicting the tests.	88
Tab. 3-15	Sensitivity analysis of the curing kinetics and viscosity parameters, summarizing the influence on the curing and the compression speed.	91
Tab. 3-16	Summary of the calibration steps performed on the bar flow simulations for force control for the rheological parameters showing the changed parameters, the old and new values, the lower limit (II) for the calculation, the reference material card for the new adaptation, as well as an evaluation of the result.	93
Tab. 3-17	Parameters for the curing kinetics and the viscosity model resulting from the calibration of the bar flow with force control.	93
Tab. 3-18	Parameters used in the two material cards, with the parameters that were changed in the calibration and therefore, differ in bold.	97
Tab. 4-1	Evaluation of flow test setups adopted in literature for the investigation of the flow behavior of SMC, with regard to the type of flow to be obtained, the application site of the setup, the complexity of the geometry, and the accuracy of the pressure data.....	102
Tab. 4-2	Morphological box for the flow test bench, with the chosen configuration marked with blue (1 st version) and green (2 nd version) dots. The main configurations are connected with a blue (1 st version) and a green (2 nd version) line.	104
Tab. 5-1	Performed charge variations.....	115
Tab. 5-2	Key results for the basis disc charge (single amount, quasi-isotropic, new material), and the single amount spiral charge	121
Tab. 5-3	Key results for the basis, the oriented charge, the tests with the old material, and for the old material in tests performed one year prior	124
Tab. 5-4	Key parameters resulting for the single amount spiral charge in the first and second (and final) trial	126

Tab. 5-5	Key results for the single and double amount disc pile charges, and for the single and double amount spiral charges.....	128
Tab. 5-6	General simulation settings for the charge variations.....	131
Tab. 5-7	Characteristics of the disc pile charge and the spiral charge in comparison, and related replica in simulation. Experimental values refer to the average values obtained during the tests.	131
Tab. 5-8	Calibration steps performed for the lower and upper limit of the experimental range and final viscosity parameters for the three material cards (changes in bold).	134
Tab. 5-9	Calibration steps performed for the spiral charge and resulting viscosity parameters. The changes induced by the calibration are highlighted in bold.	135
Tab. 5-10	Summary of the influence of each charge configuration on the peak pressure comparing the left to the right	138
Tab. 6-1	Settings for the compression, the charge and the simulation in comparison to the values in the real production of the plates and the plates with rib.....	147
Tab. 6-2	Results for the flow length of each plate listed as maximum and minimum overall, maximum and minimum referred to the furthest flow front with complete through thickness filling and the average calculated from the five taken data points (max, min, 2 cm from left and right edge, and middle), as well as the flow length in each rib.	150
Tab. 6-3	Results for the thickness of each produced plate based on six measurements taken at 2 cm from the edges on each side of the plate and in the middle, as well as at 20 cm from the flow start with a micrometer gauge.....	152
Tab. 6-4	Results for the compression time, the final thickness, and the maximum and minimum flow length in simulation for all three configurations run for each geometry, as well as longest and shortest flow length of the material inside the rib.	154
Tab. 6-5	Comparison of the flow length for the same moments for the basis simulation and the simulations with the limit high and low.	155
Tab. 6-6	Overview of the identified variations found in reality and their translation into simulation settings, and the different mesh sizes compared to each other.	158

Tab. 6-7 Resulting geometry thickness, longest flow length, maximum rib filling height and simulated volumes for the performed mesh variations.164

1 Introduction

It is well known that our planet Earth is undergoing drastic environmental changes due to excessive human exploitation and pollution. Therefore, a multitude of initiatives and agreements have been set over the past decades on national and international level to counteract it. Most recently, during the 28th Conference of Parties (COP28) 159 countries set the goal that global emissions shall be reduced by 43 % by 2030 compared to current levels [1]. This goal perfectly aligns with the goal set within the European Green Deal of Europe reducing its emission by 55 % by 2030 and becoming the first climate-neutral continent by 2050 [2].

One of the main culprits for the high total emissions is the transportation sector. With ever increasing demand for at home deliveries and an overall increase in sold goods in the current capitalistic world, the transportation sector is rapidly expanding. Unfortunately, this high demand in transportation comes at a high cost, being responsible for 25 % of the European Union (EU)'s total greenhouse gas emissions [3]. In order to address this problem, the EU has set very challenging goals for itself in the realm of the reduction of emissions in transportation over the past years. An example is the European Green Deal, stating that by 2030 the emissions from cars shall be reduced by 55 % and those from vans by 50 %. By 2035 new cars should even have no emissions at all [2]. Furthermore, the EU is working on a proposal for new goals in the reduction of emissions for heavy duty and city busses [4]. By 2050 it strives to reduce all CO₂ emissions due to transport by 90 % [5]. This fits perfectly with the goals set for the aerospace sector for example in the Paris Agreement, in which 195 countries signed for a significant reduction of the pollution due to the aerospace industry [6].

A reduction in emissions in the transportation sector can be achieved by making transportation more efficient in their fuel consumption and substituting combustion engines with alternative energy sources. Lightweight is a crucial piece of the puzzle in both options, as a reduced weight entails reduced necessity of kinetic energy to move the vehicle [7, 8]. 10 % weight reduction leads to up to 7 % reduction in fuel consumption [9] and increases the range for an electric car, as less energy and therefore, less electricity is needed to travel the same distance [10]. For this goal of lightweight parts, carbon fiber reinforced plastics (CFRPs) are an optimal solution, given their high mechanical properties [11–13]. The highest mechanical properties can be obtained when applying endless fibers. However, geometrically complex parts cannot be made with only continuous fibers, due to the required continuity of the filaments, limiting their application for the automotive sector to relatively simple parts. Furthermore, most CFRP processes need

high cycle times in order to ensure accurate placement of the fibers and textiles, homogenous distribution of the resin and the achievement of the intended thickness. These cycle times may be acceptable in the aerospace industry with a high degree of manual labor, but they are not suitable for the automotive industry with cycle times of only a few minutes. Moreover, many processes with endless fibers cause a significant amount of waste [14]. In the aerospace industry alone the estimated scrap rate is 30 % [15]. When looking at a total production of CFRP in 2018 of 128.5 kt [16] and a conservative estimate of 10 % scrap production across all industries [17], that results in 12.8 kt of CFRP scrap worldwide each year.

1.1 Motivation

A highly promising material to tackle the above mentioned challenges of high part complexity [18], short cycle times [19], and low amounts of scrap, are sheet molding compounds (SMC). They are an ideal solution for lightweight parts in high volume production. SMC with carbon fibers is particularly suitable for the automotive industry, offering high specific strength and stiffness, short cycle times of only a few minutes and little to no scrap [20]. Due to the use of long fibers of typically 25 mm in bundles, the overall mechanical performance is higher than for short fibers. Therefore, SMC is the perfect trade-off between high mechanical performance of laminates with endless fibers and the high volume potential of short fiber reinforced parts [21, 22]. This advantage is also attested in the application of SMC (with glass fibers) for exterior body panels in high volume production already in the 1980s [23]. Nowadays, SMC is already established in the automotive industry for non-structural parts, such as body panels and covers, but there is an ever increasing interest in bringing high performance SMC parts to the market [24]. To this purpose, high performance carbon fiber SMC (CSMC) is developed, with high fiber weight content of 40 - 52 %, as well as tow sizes of 3k – 12k [25]. Furthermore, as SMC consists of long fibers, the fiber scrap from other processes can be used, giving it a huge potential in reducing the emissions during production, by reducing the amount of raw materials being produced overall [26–28].

The part manufacturing of SMC consists in the sheet being cut into a simple geometry, placed into the lower mold and then being compressed under a specific temperature, pressure and closing speed [20, 29, 30]. Due to the elevated temperature, the viscosity is significantly reduced and with the application of the pressure, the material flows into every open space in the cavity. This allows the production of highly complex 3D geometries, such as trunk lids [31] within only a few minutes and without any scrap. [30]

However, the flow patterns induced during the compression of the material are very complex, due to the complexity of the SMC material, with fibers in bundles, high void content at the beginning of the compression, variations in thickness, density and fiber volume content as well as chaotic fiber orientation in the plane [32–35]. The flow is responsible for the most important characteristics, like the fiber orientation and many

process induced defects that reduce the mechanical performance [36]. Especially high in-mold flow has been proven to decrease mechanical performance due to tow deformation and the inclusion of voids [37, 38]. This high complexity of the flow of SMC, has led to a money and time consuming approach of trial-and-error when designing parts and developing SMC processes. High safety factors are applied, especially when using SMC from recycled fibers in order to ensure sufficient quality and repeatability. For example for the development of SMC products, very general, simple and unofficial guidelines exist, such as the adoption of wall thicknesses of at least 2.5 mm.

Furthermore, the complexity and variability of the material make numerical modeling highly challenging, as in order to consider all aspects, the simulation would be too detailed and the computation time would be too high. In order to reduce run times, several researchers have developed numerical approaches focusing on one aspect or the other, such as the bundle configuration of the fibers or the voids present in the SMC. [39] The same applies for commercially available tools for the simulation of the SMC compression process. The goal is to find a strategy around the micro and meso scale, by collecting experimental parameters and defining mathematical models describing the macroscopic flow behavior. [40–43]

However, the simulative approaches still need to be further improved, especially for high performance parts, leading to the SMC part manufacturing industry not applying the solutions yet. Also the flow behavior needs to be better understood, in order to allow the safety factor to be reduced and the guidelines to be more specific. This leads to a lower wall thickness, which leads to saved material and weight.

Therefore, in order to reduce the time consuming and costly trial-and-error approach, two main aspects shall be improved:

1. the flow testing for an overall better understanding of the flow behavior, and
2. the accuracy of the flow prediction in process simulation.

For the first point, numerous existent flow measurement possibilities do not take into account the complexity of SMC parts by not testing the out-of-plane flow. However, this is crucial, if highly complex parts shall be produced with the material. For the process simulation, a standardization of the characterization procedure is not existent, not allowing a comparison of the results. Furthermore, the material characteristics are summarized in the material card with only one set of parameters for each material. However, as mentioned at the beginning of this section, SMC material is highly variable and, thus, a depiction with only one set of parameters does not take into account the range of possible outcomes. Moreover, given the high complexity of the material, finding balance between the level of detail and the computation time, as well as the description of the charge at the beginning of the process is difficult.

1.2 Objectives and research questions

The overall goal of this research endeavor is reducing the time and money spent in developing new parts and determining the best process conditions when adopting a new SMC material based on the flow behavior. To this scope, the complex flow of SMC has to be understood and characterized. Furthermore, commercially available process simulation tools to predict the flow behavior shall be enhanced.

Four detailed objectives can be identified:

1. Develop a characterization process to obtain the parameters for the material card describing the flow behavior to be possibly applied as a standard. The process shall include the variability of the material and the possibility to be applied to different mathematical descriptions of the flow.
2. Develop a flow characterization method including out-of-plane flow and the investigation of differences among charge configurations.
3. Quantify industrially recurring charge variations, to understand the material behavior better and quantify the limitations of the simulation.
4. Determine guidelines based on the findings in each step for faster and cheaper part development and process definition in the future.

1.3 Reference material

The material CARBKID PGK5250-R63 is used in this research [44] (appendix c). Fig. 1-1 shows the raw material, a finished part and details of cured SMC plates with no flow.

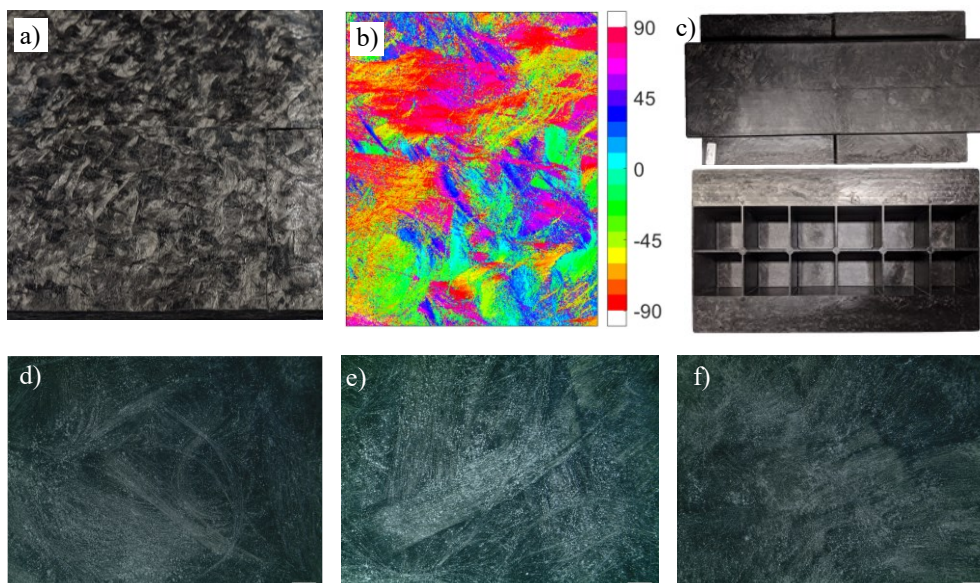


Fig. 1-1 Views of the reference material: a) uncured SMC sheet; b) Profactor picture of cured plate; c) more complex SMC part with rib; d) and e) detail pictures of a bent and straight fiber bundle respectively; f) detail of bundle edge, with more random overall orientation of fiber bundles.

The material has 25 mm long fiber bundles, with a fiber content of 52 wt% and an aerial weight of 2.5 ± 0.2 kg/m². As can be seen in Fig. 1-1a, the material has chaotic fiber orientation in the plane, in the same fashion as any other typical SMC material. The picture in Fig. 1-1b was taken with a Profactor sensor on the surface of a plate made of SMC. It is also visible in the Profactor picture as well as in Fig. 1-1d, e and f that the fibers are randomly oriented. Bundles can sometimes be easily visible in the surface, varying from a very simple configuration of a straight strand (Fig. 1-1e) to a very complex configuration with the bundle being spread and the ends being bent and pointing in completely different directions (Fig. 1-1d). Furthermore, the bundles spread to sometimes up to 1.5 cm in Fig. 1-1 f. Moreover, the thickness of the raw material can vary. The same applies for the density, which is given as 1.38 ± 0.05 g/cm³ in the data sheet.

The resin system of this material is vinyl ester, which is not as reactive as epoxy resins. However, the additives and other components of the resin system are not known. The forming temperature is given at 150 °C, which fits perfectly with the glass transition temperature, being slightly higher at 170 °C. The curing time at the given processing temperature of 150 °C is only 35 ± 5 s. This makes the material very suitable for the short cycle times of the automotive industry. The specific mechanical properties are also very good, with the tensile strength being ≥ 240 MPa and the tensile modulus ≥ 30000 MPa. For the bending characteristics the strength is ≥ 330 MPa, and the modulus ≥ 27000 MPa. Moreover, the shrinkage is negative due to the quantity of fibers, and is only -0.05 ± 0.05 %.

Although the material was the same throughout the duration of the research, different batches were used for both testing and part production.

1.4 Outline

To answer the research questions and reach the objectives mentioned in Section 1.2, this research work was split into seven chapters, as shown in Fig. 1-2.

In **Chapter 2** an extensive assessment of the state of art of SMC is given. Starting with the sheet production and the SMC compression process, it sets the basis to understand the variability of the material related to the flow behavior. A summary of SMC simulation endeavors follows, stating how this challenging material is handled in numerical representations. The main focus lies again on the flow behavior. The third main content discusses the state of technology of the characterization of the flow. It is subdivided into two subjects, the first talking about the procedure applied to obtain the parameters of the material card that describe the rheological behavior of the material, which includes the curing kinetics and the viscosity. The second section summarizes the existent flow characterization setups and summarizes tests that have been performed for a better understanding of the complex material behavior during the compression.

Chapter 3 addresses the first main research question about establishing and standardizing an industrially applicable characterization procedure to include the variability of the material. The existent general procedures for the determination of material parameters for the curing kinetics and the viscosity are further detailed in order to comply with specific criteria defined at the beginning of the chapter. The first step is the characterization of the curing kinetics. To this purpose, DSC measurements are performed for different heating rates and evaluated, in order to establish a precise procedure for future endeavors. Afterwards, the viscosity parameters are determined for the low and high temperature. To this purpose, squeeze flow tests are performed and following the same theoretical approach as for the DSC measurements, a suitable procedure in line with the defined criteria is set. Once all parameters are set, they need to be calibrated. This step is split into an in-plane flow and an out-of-plane flow calibration, being performed with squeeze flow simulations and bar flow simulations respectively. For the barflow tests and simulation, the calibration is further varied for displacement controlled and force controlled compression. A sensitivity analysis is performed for each configuration, to serve as a facilitation for future calibrations.

In **Chapter 4** a new flow test bench is developed that allows the characterization of the out-of-plane flow. The test setup is developed to be applied in a context as close to the normal SMC process as possible. Therefore, it is applicable inside a press, with the same pressure, temperature and speed ranges as for typical SMC part manufacturing. The flow test bench also allows further understanding of the flow of SMC inside ribs as well as in small openings, allowing a multitude of helpful conclusions for optimized processing and charge configuration.

In **Chapter 5** the test setup developed in Chapter 4 is adopted for an evaluation of several charge variations and their impact on the compression pressure, as well as the limitations in simulation in the representation of charges. Two basic charge variations are determined and further varied to a total of six test series. Several guidelines can be derived from the test sequence for improved charge configuration for different geometrical features, but also for improved processing, by adapting the charge to either reduce the compression pressure or to obtain a highly repeatable pressure signal. Furthermore, the charges are replicated in simulation, pointing out the limitations and setting guidelines for the interpretation of the results.

In **Chapter 6** the knowledge acquired about the material from the charge testing, as well as about the established material card with the newly developed procedure is validated. For the final validation, plates are produced with and without ribs. The production of the plates is numerically replicated with the material cards and the guidelines derived in each previous chapter. The flow length of this simulation is compared to the plates produced with the SMC process in an industrial environment.

Chapter 7 “Summary and Outlook” summarizes the content of this work and discusses the findings in detail. Based on the discussion, several further investigation possibilities

for the flow but also SMC as a whole are given, presenting an outlook on this fascinating material.

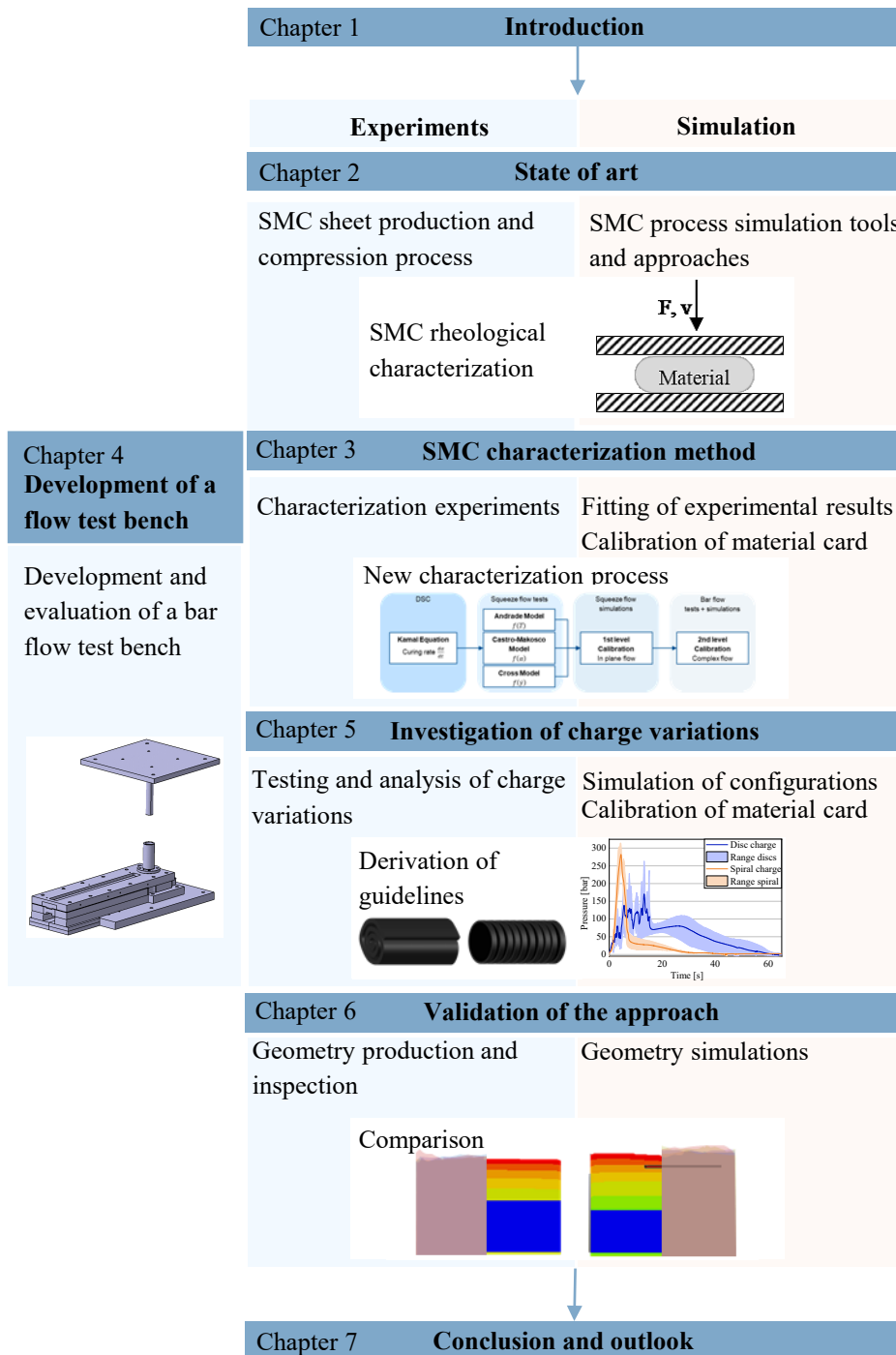


Fig. 1-2 Outline of this research work.

2 State of the art

In order to understand the challenges related to working with SMC, it is necessary to know the material and its processing. Therefore, the following sections outline the most relevant aspects for the research questions being investigated within this work. Section 2.1 addresses the production process of the sheets, and their compression process to obtain SMC products. Section 2.2 presents currently available process simulation possibilities, and their limitations. Those include the challenges related to a numerical representation of the flow of a material as complex and variable as SMC. It is therefore, imperative to understand the flow of the material as thoroughly as possible with rheological testing. The state of the art in rheological testing for SMC is presented in Section 2.3.

2.1 SMC production process

Broadly defined as long-fiber-reinforced material, SMC consists of a thermosetting matrix, and 25 mm long fibers. With glass fibers as the reinforcement, the material has been in use since the 1960s, bearing a long history of utilization. The adoption of carbon fibers started in the early 1990s, due to the higher stiffness given by the fiber type together with excellent specific mechanical properties [45]. The resin is usually a vinyl ester, epoxy or poly ester basis, with fillers and additives to optimize the material depending on the requirements. The resin cures within a very short amount of time, between 30 s and 3 min, allowing very short cycle times of only a few minutes, which is crucial to the automotive industry. Therefore, the material has been widely employed especially for large covers with a non-structural and semi-structural role. SMC is used to refer to both, the material and the compression process. However, within this work it will be referred to as the material. In order to produce parts made of SMC, two main processes can be identified:

- the sheet production, to create the prepreg, and
- the compression process, representing the actual molding of a part.

2.1.1 SMC Production

The production process for the sheets is schematically shown in Fig. 2-1.

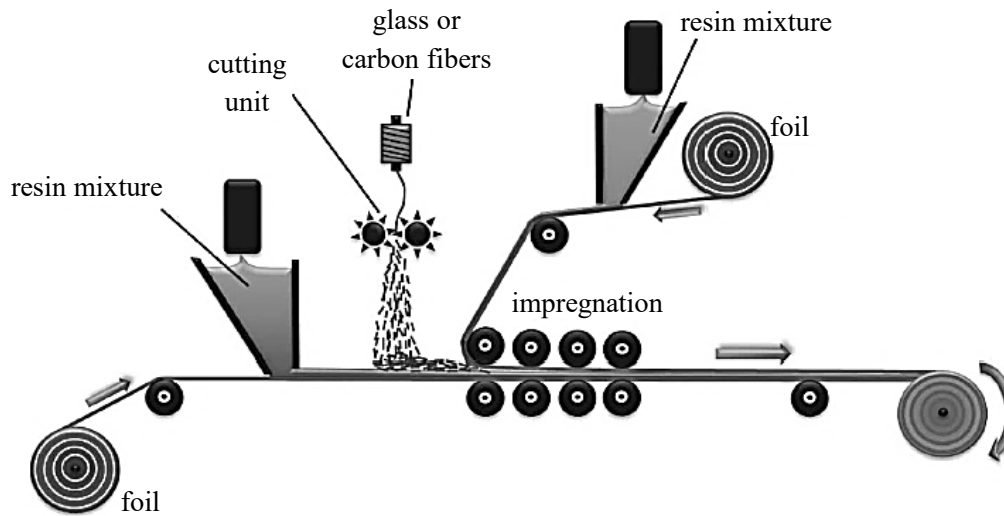


Fig. 2-1 Schematic representation of the sheet production for the SMC process [30].

A typically 1.5-2 m wide carrier foil is coated with the resin mixture. Endless glass or carbon fibers are chopped to the desired length and sprinkled onto the resin film. With this random orientation pattern the characteristics in the plain of the sheet are assumed to be isotropic. On top of the fibers, another carrier foil coated with resin is placed. This layer is then compressed in a sequence of rollers that facilitate a complete impregnation and an even thickness that typically varies from 1-3 mm. The sheet is then rolled up or, for glass fibers, folded, left to age at room temperature for several days [46], transported to the part producer and then stored at very low temperatures around -20 to -25 °C. The resin paste contains a multitude of additional components with the resin and hardener, such as fillers to increase the viscosity significantly, giving the sheet the necessary stability for easy handling. Also several additives exist, to optimize a part for its supposed function [47].

2.1.2 SMC Process

In order to produce parts with the SMC material, a compression process is necessary, which has been described in a multitude of comprehensive composite literature [20, 29, 30, 48–52]. The process is typically subdivided into four steps, as shown in Fig. 2-2.

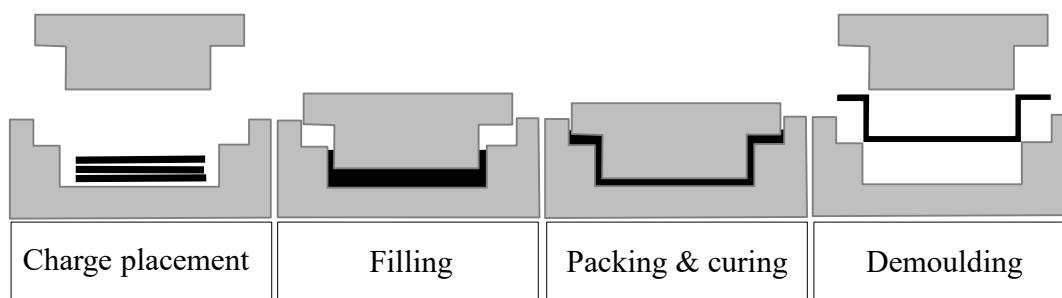


Fig. 2-2 SMC molding process steps.

In the first step, the defrozen SMC sheet previously cut into a suitable shape, is stacked until the required weight is reached, and placed inside the mold. The press is closed at pressures around 100-150 bar. The mold typically has temperatures ranging from 130 °C to 160 °C [30]. The compression is typically displacement controlled with a closing speed between 1-3 mm/s.

Once the press has reached the final thickness, it remains closed for 3-10 min, allowing the material to cure before reopening the tool and ejecting or demolding the part. Within the tool, a vacuum can be applied in order to decrease the void content in the final part. Due to the high pressure and with suitable settings for the closing speed and temperatures of the upper and lower mold, the void content of the sheets can be greatly reduced during the process even without vacuum.

Evidently, SMC has a very short cycle time, making it a composite process that is well suitable for the automotive industry. The process is overall not cost intensive as the pressure and temperature are relatively low, and applied for a brief amount of time. Due to the material's high flowability, very complex shapes and large parts can be produced with only one compression step, integrating functions and avoiding subsequent bonding steps. The flow also allows for the sheets to be cut into simple shapes, as during the compression the whole cavity will be filled. This reduces the amount of scrap almost to 0 %. Furthermore, as the fibers are long and not endless, the handling of the raw material is much more convenient and the material is overall cheaper. A decrease in the strength and stiffness compared to endless fibers follows, but the material still meets the requirements of many applications with intermediate to low performance requirements, being significantly better than the values for non-reinforced plastics. Last but not least, one of the main advantages for vehicle producers having to meet environmental and recycling goals, is that the waste from other processes using endless fibers can be used to create SMC, as well as recycled fibers.

These advantages have led SMC to be widely adopted in the automotive industry for non-structural and semi-structural parts, and more recently even structural parts. Fig. 2-3 shows typical applications for SMC.

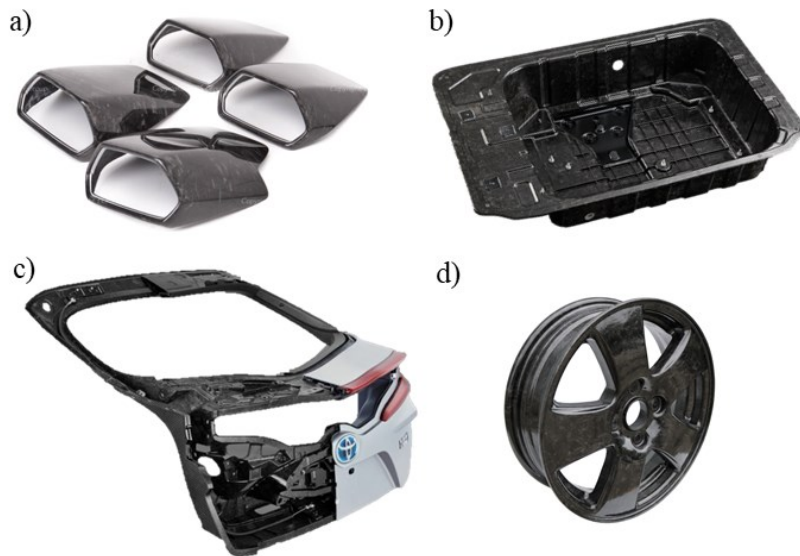


Fig. 2-3 Exemplary parts for SMC application: a) Forged Composites from Lamborghini [53], b) spare wheel pan of Mercedes AMG E-Class made with SMC from ASTAR SA [54], c) rear door of Toyota Prius PHV made with SMC from Mitsubishi Rayon [31], d) car rim made by Blackwave GmbH [55].

Fig. 2-3a shows an example of Forged Composites®, trade marked by Lamborghini, mainly used to produce visible cover parts for inside the cars [53]. Fig. 2-3b, c and d show more complex parts, including a spare wheel pan for Mercedes AMG E-Class made with Carbkid [54], the same material used in this research, a trunk lid for Toyota [31], and a wheel rim for cars produced by Blackwave GmbH [55].

SMC is also used in hybrid solutions, as with its flowability it can potentially bond well to other layers. Therefore, in recent studies the integration of endless fibers as UD reinforcement or as woven fabric has been under investigation. The aim is combining the high mechanical characteristics of endless fibers and the possibility of creating complex shapes given by SMC. There are very different approaches being tested currently, among which the use of stitched structures, made with tailored fiber placement (TFP) or UD reinforcements consisting of prepreg material that are subsequently covered with SMC and bonded in the compression step of the SMC [56]. A similar example is the ongoing research project Deepflow funded by the Ministry of Economic Affairs and Climate Action (grant number KK5135814). The goal is to produce a hydrofoil fin with long carbon fibers and a UD reinforcement.

Despite having many benefits, SMC shows some very challenging characteristics, first and foremost the high variability of the sheets. Due to the sheet production process consisting of a random sprinkling process for the fibers, several characteristics of a sheet, such as the density, fiber orientation, fiber content and sheet thickness, vary significantly. Exemplary measurements of the thickness taken for CARBKID [44], the material used for this work, can be seen in Fig. 2-4.

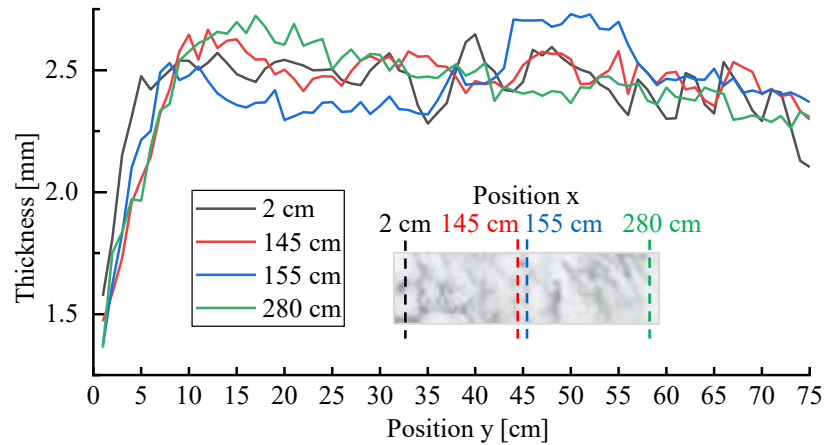


Fig. 2-4 Thickness variability for a 75 cm wide (y-direction) and 285 cm long (x-direction) SMC sheet, whereas x refers to the sheet production direction (data from [S20]).

As can be seen in Fig. 2-4, the variation of the thickness of an SMC sheet is significant over a small width of 75 cm, with the value varying between 2.25 cm and 2.75 cm between 10 and 65 cm in y-direction. The thickness was measured with a micrometer gauge with three decimal points resolution. Consequently to the above mentioned values being highly variable in SMC, the mechanical characteristics have a high variability, which was investigated by a multitude of researchers for the tensile stiffness and strength as well as related strain patterns [37, 57–60]. The variability of tensile values has also been tested at the LCC [S20]. The internal values of the tensile modulus for plates made with the same material CARBKID [44] ranged from 21.6 GPa to 33.5 GPa [S20]¹. For the values found in literature, the values range from 25 GPa to 41 GPa [37, 57–60]. However, these values were obtained for tests performed with different resin systems and fiber volume contents. Additionally, the tensile characteristics seem to be better in the direction of the sheet production, suggesting that the assumed isotropy in the plane of the SMC does not actually apply, confirming the results obtained by Nony-Davadie et al. [35]. The movement of the foil in production direction seems to have an influence on the orientation of the fibers, favoring a slight prevalence for the movement direction of the transport band.

Another great challenge related to the processing of SMC is the flow inside the mold during the compression. As previously mentioned, the material has many components that interact with each other, favoring or limiting the flowability. Additionally, the flow front is not uniform, as the fibers directly in contact with the upper and lower mold protrude faster than the remaining material [61]. Given the amount of influencing elements, the current approach to developing SMC parts is based on decades of experience and general guidelines with a very high safety factor to include even the worst scenario

¹ Four plates were tested with 100 % coverage, two of them with one sheet and two with two sheets, all oriented the same way relatively to the sheet production direction. The tests were performed for specimens cut in 0 and 90° towards the sheet production direction.

in the wide range of possibilities. To determine the process settings of pressure, tool temperature and press closing speed a trial-and-error approach is still state of the art. This approach is very time and resource consuming.

Nevertheless, determining the right settings is crucial, because many defects occurring in SMC parts are caused during the process. Especially the defects caused by the flow of the material during the compression have a major impact on the mechanical properties of the final part. A typical flow-induced defect are weld lines and voids, as shown in Fig. 2-5.

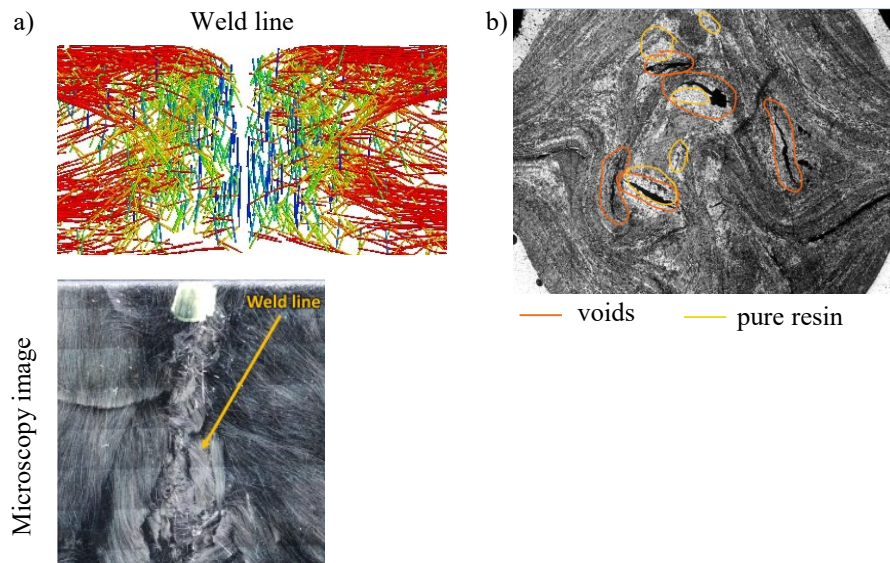


Fig. 2-5 Typical flow-induced defects that significantly lower the mechanical properties of an SMC part: a) weld line represented in simulation and on a microscopy picture [62]; b) microscopy image showing voids and pure resin regions [S15].

As can be seen in the Fig. 2-5a, in case of a weld line the fibers align along the edges on both sides, creating a weak spot as there is no link of fibers between one side and the other [62]. Also voids can be created due to the flow of the material, as shown in Fig. 2-5b. The specimen shows a cross section of a rib intersection, where the material had to cover a relative long flow distance of about 4 cm [S15]. Depending on the geometry of a part, the flow can become turbulent, causing the fibers to entangle. This can either prevent the material from flowing further, causing unfilled areas, or only the resin can pass through, causing weak spots without reinforcement. The flow of the material also causes the fibers to change orientation. SMC parts are assumed to be isotropic, but this is far from reality, as the fibers align with the flow direction to a certain degree [63], inducing anisotropies. Research has shown that up to a certain level of reorientation of the fibers, the effect is comparable to endless fibers, increasing the mechanical characteristics in flow direction. However, if the degree of flow increases, the so called bundling effect happens, where the connection between the bundles is very low. This favors delamination and reduces the mechanical properties to the properties of the pure resin [58, 64].

The influence of the degree of flow can be seen in the comparison in Fig. 2-6, showing the tensile, compressive and shear strength for specimens taken from plates with two different flow lengths [S19].

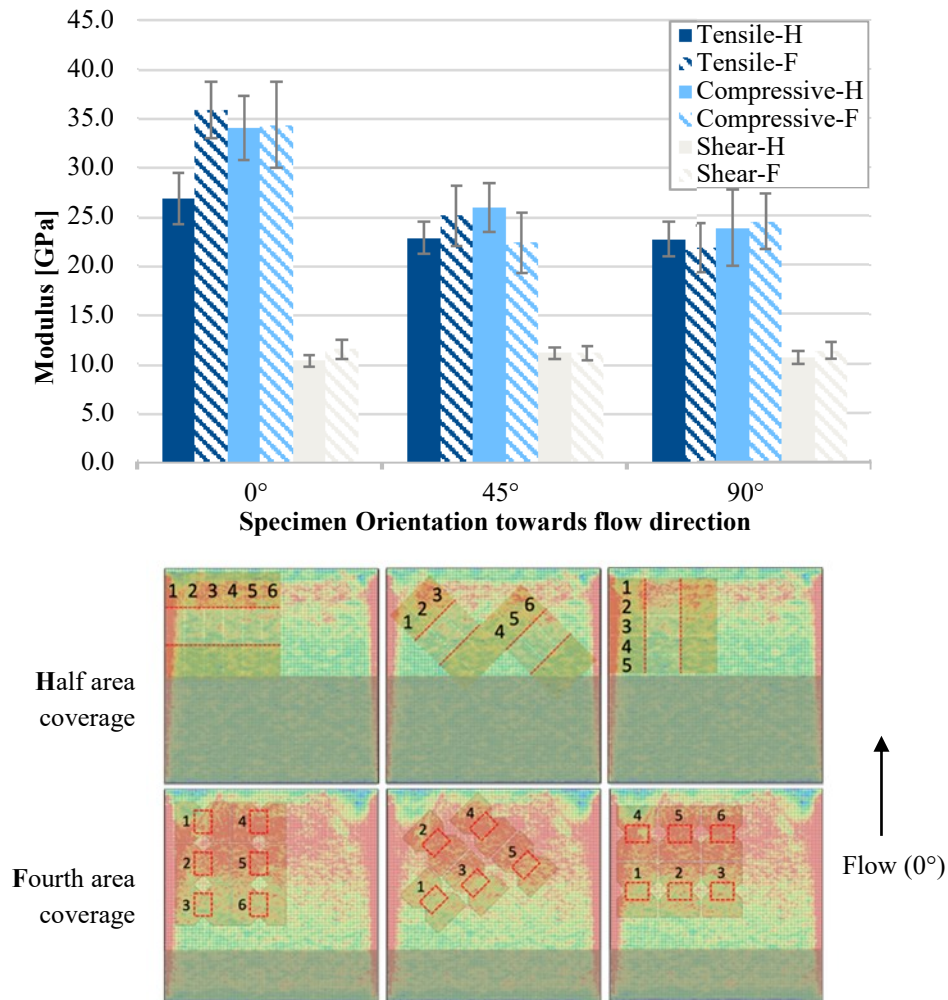


Fig. 2-6 Results for tensile, compressive and shear moduli in 0°, 45° and 90° directions towards the flow of the material during the compression with scatter for plates with two charge configurations: half (H) and fourth (F) area coverage (adapted from [S19])

As can be seen in Fig. 2-6, the specimens were taken from the area not covered by the charge at the beginning of the compression. The specimen placement is exemplarily shown for the tensile tests with the half area plates (H), and for the shear test specimens for the fourth area plates (F) overlapped with the simulation results obtained for the fiber orientation degree in flow direction (red is the highest degree of orientation in x-direction, while blue is the lowest). A trend can be identified that the moduli in 0° direction are the highest, 45° is much lower, and 90° is the lowest, suggesting a similar behavior to endless fibers. However, it cannot be stated that a longer path, leading to a higher

degree of orientation, also leads to higher performance. This is partially true, but as explained above, high flow paths can also lead to bundle separation, ultimately losing the advantageous performance of the fibers.

The results found in literature lead to the same general conclusions of the flow inducing anisotropy in the flow plane [37, 57, 58]. As the flow influences both the final fiber orientation and the formation of many defects, it is crucial to understand the flow of SMC in order to be able to predict it, and find the best suitable process conditions to obtain parts with good mechanical properties. Due to the complexity of the material, currently the adopted approach is the time- and cost-intensive trial-and-error. However, several numerical descriptions of the flow of SMC have developed.

2.2 Numerical description of the flow

The development of a numerical description for SMC is highly challenging due to the complexity of its material. Over the past decades several mathematical descriptions of the flow have been developed in an academic context, focusing on a specific characteristic influencing the flow, such as the bundle configuration of the fibers, fiber knots, fillers, voids, etc. [36, 65–74]. However, these approaches can only focus on one aspect at a time and can only be applied for small geometries in order not to require excessive computation times. Therefore, the usual approach applied for SMC simulation is on macroscale. The functional dependence of the material and the subsequent mathematical descriptions are determined by performing experiments [75].

The identified functional dependence of the viscosity of a thermosetting compound can generally be defined as [76–80]:

$$\eta = f(T, \dot{\gamma}, \alpha) \quad (1)$$

where T is the temperature, $\dot{\gamma}$ the shear rate and α the degree of curing.

In some cases research suggests including the fibers [63]. However, their influence is difficult to quantify, and it is already captured when determining the other values, if the fibers are included in the tests.

One of the possible rheological descriptions to take into account all the above mentioned dependencies for SMC is based on the Andrade, the Castro-Macosko and the Cross models [80]:

- Temperature-dependent Andrade model

$$\eta_0 = a * e^{-b/T} * T \quad (2)$$

- Curing reaction rate-dependent Castro-Macosko model [81, 82]

$$\eta_1 = \eta_0 * \left(\frac{\alpha_{gel}}{\alpha_{gel} - \alpha} \right)^{D+E\alpha} \quad (3)$$

- shear rate-dependent Cross model

$$\eta = \frac{\eta_1}{1 + \left(\frac{\eta_1 \dot{\gamma}}{\tau^*}\right)^{1-n}} \quad (4)$$

where η is the viscosity, T is the temperature, α is the degree of curing, α_{gel} is the gelation point of the material, a, b, τ^*, n, D and E are material specific constants.

As can be seen from equation 3, the rheology of SMC is closely linked to the curing kinetics. Several formulas have been established to describe the curing behavior of SMC mathematically, some taking into account the type and amount of filler or additive, diluents [83] or promoters [84, 85]. However, same as for the rheological description, the higher the level of detail, the higher the computation time. Therefore, Kamal [76, 77, 86] defined a simpler equation for epoxy and polyester resins only including the temperature dependence:

$$\frac{d\alpha}{dt} = (A_1 e^{-E_1/T} + A_2 e^{-E_2/T} \alpha^m) * (1 - \alpha)^n \quad (5)$$

T is the temperature, α is the degree of curing, A_1, A_2, E_1, E_2 are material specific constants to describe the Arrhenius temperature dependency, m and n are kinetic exponents. This equation shows a reasonable accuracy of the analytical data compared to the experimental data [76–78, 86, 87].

This formula is considered as an industrial standard for the reaction kinetics and is applied in different commercially available software solutions, like 3DTimon COMPOSITEPRESS™, and Cadpress by The Madison Group [29, 88], Moldflow from Autodesk, Inc., and Moldex 3D by CoreTech System Co., Ltd..

2.2.1 SMC simulation tools

A direct juxtaposition for the material models and the process settings for Moldex3D, 3DTimon and Moldflow can be seen in Tab. 2-1, adapted from [89].

Tab. 2-1 Juxtaposition of material models and processing settings for SMC process simulation software solutions Moldex3D, 3DTimon and Moldflow (based on [89])

	Moldex3D	3DTimon (Euler/Morphing)	Moldflow	
Material model	Newtonian fluid (constant)			
	Castro Macosko			
	Power-law Castro Macosko	Cross Castro Macosko	Cross Castro Macosko	
	Castro Macosko			
	Cross Castro Macosko Herschel-Bukley			
Cure kinetics	Kamal equation	Kamal equation	Kamal equation	
Uncured/cured density	Constant	Constant	Constant	
Specific heat/ thermal conductivity	Constant		Constant	
	Linear function	Constant	Tabulated (lin. interp.)	
	Tabulated (lin. interp.)			
Pre-heating	Yes	No	Yes	
Initial conversion rate	Yes	Yes	Yes	
Different mould half temperatures	No	No	No	
Processing settings	Closure control	Speed	Speed	Speed
	Closure control data types	Stepwise Polylines	Stepwise	Stepwise
	Closure control input method	Manual input	CSV import Manual input	Manual input
	Max. force	Yes	Yes	Yes
	Max. speed	Yes	No	Yes
	Switch-over criteria	Force		Force
		Percentage fill Time	Max. force only	Percentage fill Time
Holding force	Any value	Max. force only	Any value	

As can be seen from Tab. 2-1 table, all software solutions have similar material model and processing settings options. All three have been originally developed for injection molding with optional short fiber reinforcement.

The adaptation for the compression process, and for long fibers followed subsequently. The qualitative result of the simulation tools is overall very similar, as can be seen in Fig. 2-7, showing the comparison of the results for the fiber orientation tensor A_{xx} between 3DTimon 10 R6.0 and Moldflow 2019.

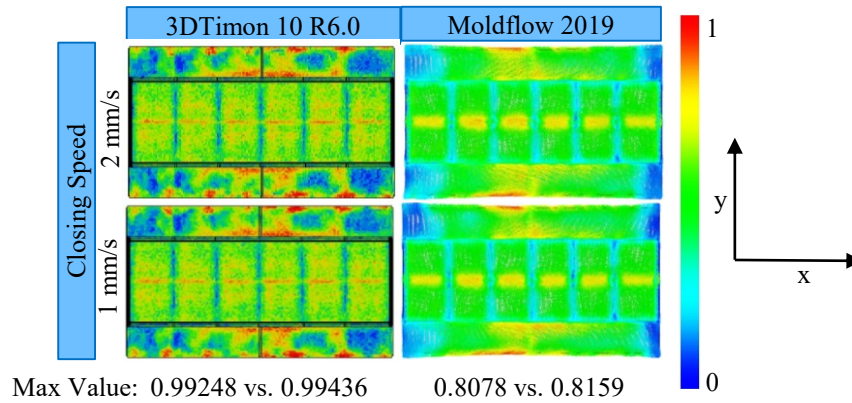


Fig. 2-7 Comparison of the orientation tensor A_{xx} for the same process settings in the SMC module in 3DTimon 10 R6.0 and Moldflow 2019 (adapted from [S18])

It is evident, that the qualitative result for the fiber orientation tensor A_{xx} is qualitatively very similar between the software solutions. However, the degree of orientation is higher in 3DTimon, reaching 0.99, compared to 0.80-0.81 for Moldflow.

Unfortunately, the inclusion of long fibers, arranged in flexible bundles flowing together is very complicated. The prediction of the force signal within all software solution has been heavily criticized over the past few years by different researchers [89–91]. For example Qian et al. [89] compared the signal results for the same part and process settings to one another Fig. 2-8. It is visible that all solutions cannot predict the compression force accurately for the flat plaque. However, for the w-profile, the force signal for the Euler and Morphing method in 3DTimon seems to predict the force more accurately than the other solutions. The force signal for the simple plate is also predicted the closest by 3DTimon, however, it is much higher in the simulation than in the experiment. This is probably due to utilizing the same material card, typically calibrated to a complex part. This issue will be further addressed in the next section.

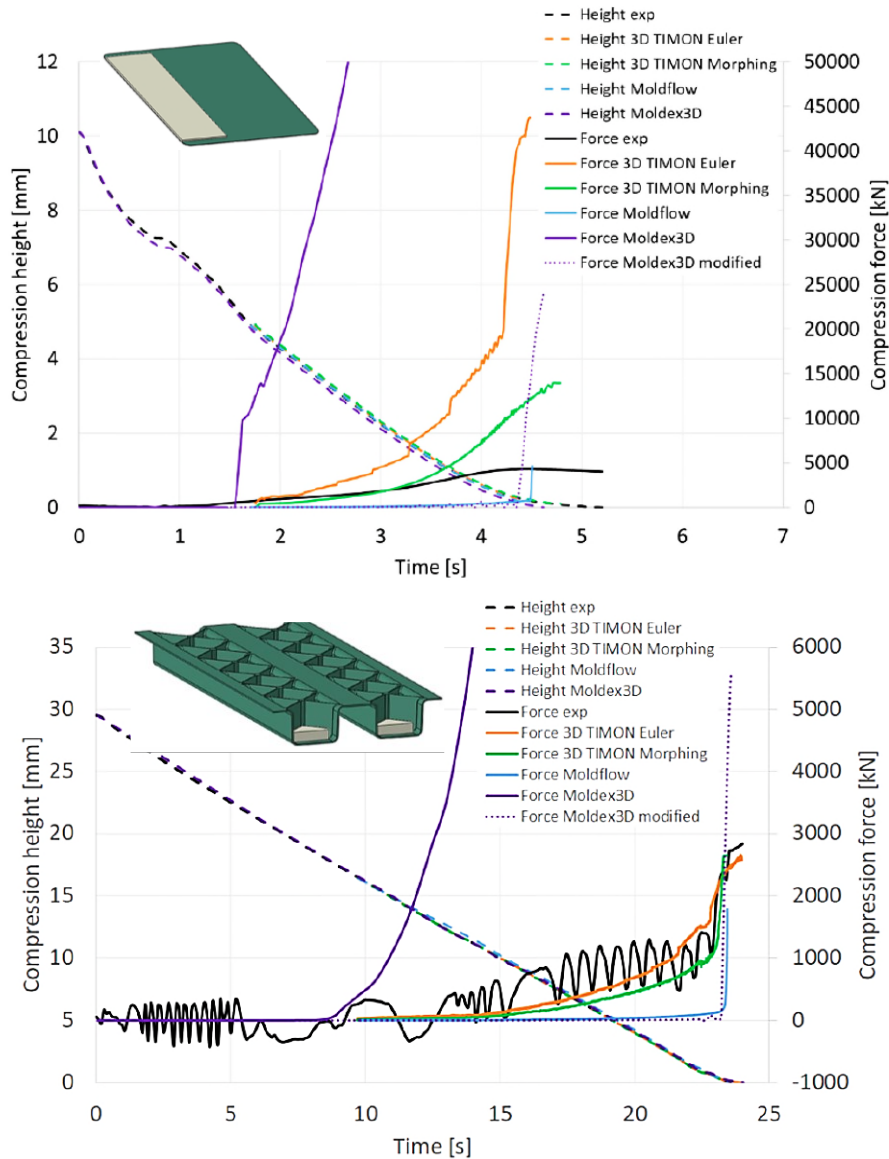


Fig. 2-8 Experimental results compared to the results for 3DTimon, Moldex3D and Moldflow for the compression height and force over time for a flat plaque (top) and a w-profile (bottom) (adapted from [89])

Equally important to the force prediction is the prediction of the filling of a part and the final fiber orientation. Especially with long flow paths fiber reorientation and concentration can occur, leading to resin rich areas and great variations in fiber volume content (FVC) and therefore, density [63]. At the same time, the fibers are not only influenced by the flow, they also act on it.

Rothenhäusler et al. [90] compared the same software tools as in the previous study, and included the Direct Bundle Simulation (DBS) approach made up of several custom sub-routines in Simulia ABAQUS [38]. The comparison was done for the force, the velocity, and the closing gap profiles, as well as the prediction of the final fiber orientation and FVC for a plate geometry with hexagonal ribs on top. The authors conclude, that the industrially available solutions on macroscale can help in a design phase, giving a broad

idea of the final fiber orientation, but are not suitable for an accurate prediction of the FVC. Especially for confined regions several interactions would have to be taken into account: fiber-fiber, fiber-matrix, fiber-mold. The authors point out, that in 3DTimon the force prediction is much higher than in the real part, because the formation of a lubricating layer at the contact surface with the mold is neglected in the numerical representation. Neglecting the lubricating layers leads to high shear stress. The mesoscale solution for Abaqus on the other hand, can predict the FVC and the final orientation much more accurately at the cost of more computation time. In Moldex3D and Moldflow the fibers are included only in a post-processing. In the DBS in Abaqus, the bundles are modelled under the assumption that the bundles tend to remain intact. This solution is being developed by SIMUTENCE GmbH [92]. The approach for the inclusion of the fibers in 3DTimon is Direct Fiber Simulation (DFS). A schematic representation of the fiber model used in the DFS can be seen in Fig. 2-9.

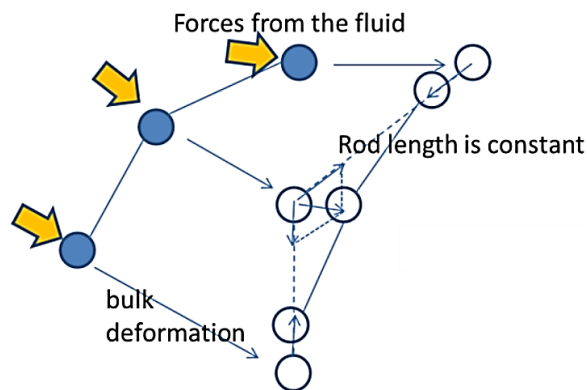


Fig. 2-9 Functioning principle of the direct fiber simulation (DFS) implemented in 3DTimon [88, 93, 94].

The fibers consist of rods connected by nodes that have different degrees of freedom. Any movement, rotation and bending of the fibers is calculated based on the forces acting on the nodes by the fluid. Based on this schematic, the interaction between fibers is not calculated. The amount of subdivisions of a fiber can be set in the simulation inputs, but the higher the number, the longer the simulation will take. The result is a representation of the final orientation of the fibers as a result of the flow, which can be used as an input for structural simulations predicting the mechanical properties. However, only a representative portion of the realistic total amount of fibers is represented. Furthermore, only a one-way causality is applied from the flow to the fibers: the motion of each fiber is based on the flow velocity field [91, 95]. Despite this simplification of the one-way coupling and the absent fiber-fiber interaction, the prediction of the fiber behavior is well predicted for long fibers [91, 96].

The simulation software adopted throughout this research activity is the industrially available tool 3DTimon. Overall characteristics of the software have been presented above in direct comparison to other software tools. However, a more detailed description of the adopted process simulation tool is given within the next subsection.

2.2.2 3DTimon

3DTimon is a CAE system, originally developed in 1996 for injection molding by Toray Engineering D Solutions Co., Ltd. [88].

Overview

The overall schematics of inputs and outputs of the simulation is given in Fig. 2-10.

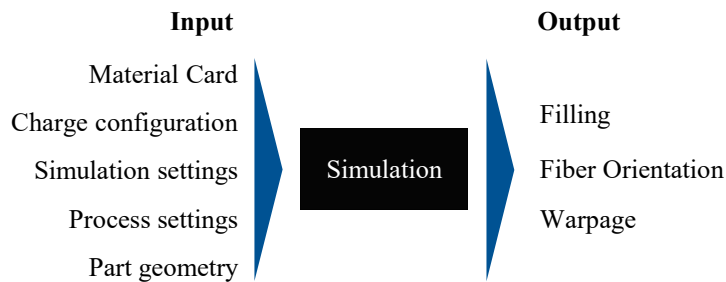


Fig. 2-10 Inputs and outputs for industrially available CAE software package 3DTimon, with the simulation itself represented as a black box, as it is not accessible and only the overall algorithms are known

As can be seen in Fig. 2-10, the software is a black box, as only the overall algorithms are known and changes to it are not possible. However, the inputs can be changed and will influence the outcome. Those inputs are:

- The material card: one set of parameters has to be chosen for each material to be simulated. These parameters include a multitude of physical characteristics, among which the parameters of the curing kinetics and the viscosity model (eq. 2-5);
- The charge configuration: the charge geometry, but also the fiber orientation in the charge can be defined with a constant value for each direction;
- The simulation settings: the mesh, the clamping force, the processing settings, etc. all have to be defined in the simulation and a realistic copy of the empirical process has to be established. The closer the simulation is to reality, the better the forecast to be obtained with the numerical solution;
- The part geometry.

The analysis capabilities of the software are subdivided into four stages of flow, pack, warp and fiber, which summarize the outputs of the simulation. In the filling step, the material flows in dependence of the temperature and the pressure and fills the cavity, potentially showing unfilled areas and weld lines. The next step is “Pack”, where the compaction of the material happens. During this step, the mold is completely filled and the press holds a constant compression pressure until the material is fully cured. In a next step, the fiber orientation during the filling until the end of the process is calculated, based on the results of the filling process. To this purpose, the software depicts the fibers with the DFS, as shown in Fig. 2-9. The last step is “Warp”, which depicts the warpage

of the geometry due to the fiber orientation and the compaction of the part during the process.

Algorithms

As previously stated, 3DTimon is a black box when it comes to the algorithms used in the simulation. However, the overall models and assumptions adopted are known. A few aspects have been mentioned in Section 2.2 when comparing the different available numerical solutions, but a more detailed summary is due.

The assumptions are [97]

- No subdivision of the resin in lubricating layer and plug flow
- the fiber orientation has a one-way causality with the flow [91, 95]
- no fiber-fiber interaction
- incompressible fluid
- no inertia or gravity
- no in-plane flow velocity in z-direction
- heat conductivity only in thickness direction.

For the simulation of the flow, 3DTimon adopts the traditional equations of fluid dynamics: the continuity equation, the momentum equation and the energy equation. [97]

The continuity equation is given as

$$\frac{\partial \rho}{\partial t} + \frac{\partial}{\partial x}(\rho u_x) + \frac{\partial}{\partial y}(\rho u_y) + \frac{\partial}{\partial z}(\rho u_z) = 0 \quad (6)$$

where ρ is density, t is time, and u_i is the fluid velocity vector in direction x , y , and z . Given the assumptions of incompressibility, steady state, the neglect of inertia and gravity, for a non-Newtonian melt the equation can be simplified to

$$\frac{\partial u_x}{\partial x} + \frac{\partial u_y}{\partial y} + \frac{\partial u_z}{\partial z} = 0. \quad (7)$$

The momentum equation in x -direction, also called Cauchy momentum equation, if expressed in deviatoric terms, states:

$$\begin{aligned} \rho \left(\frac{\partial u_x}{\partial t} + u_x \frac{\partial u_x}{\partial x} + u_y \frac{\partial u_x}{\partial y} + u_z \frac{\partial u_x}{\partial z} \right) \\ = - \frac{\partial p}{\partial x} + \left(\frac{\partial \tau_{xx}}{\partial x} + \frac{\partial \tau_{yx}}{\partial y} + \frac{\partial \tau_{zx}}{\partial z} \right) + \rho g_x, \end{aligned} \quad (8)$$

where p is pressure, g_i is the body force acting on the continuum, and τ is deviatoric stress.

The third equation governing the flow is the energy equation, which for constant properties can be expressed as

$$\rho c_p \frac{DT}{Dt} = k \left(\frac{\partial^2 T}{\partial x^2} + \frac{\partial^2 T}{\partial y^2} + \frac{\partial^2 T}{\partial z^2} \right) + \dot{Q}_{viscous\ heating} + \dot{Q}, \quad (9)$$

where c_p is specific heat, T is temperature, k is thermal conductivity, $\dot{Q}_{viscous\ heating}$ is viscous dissipation and \dot{Q} is an arbitrary heat source.

In order to reduce the complexity of the simulation, and therefore, reduce CPU time, 3DTimon avoids the Navier-Stokes equations for 3D flow of non-Newtonian polymers and instead uses a Hele-Shaw approximation for a 2.5D flow simulation. This approach is called Light 3D. [88]

With a further assumption of neglecting the in-plane velocity gradient in z-direction, due to the small thickness of SMC parts the Hele-Shaw model is

$$\frac{\partial}{\partial x} \left(S \frac{\partial p}{\partial x} \right) + \frac{\partial}{\partial y} \left(S \frac{\partial p}{\partial y} \right) - \dot{h} = 0, \quad (10)$$

where h is the gap height between the mold halves, \dot{h} is the closing speed, and S is the viscosity-dependent flow conductance of the thin parts. S is expressed as

$$S = \int_0^h \frac{(z-\lambda)^2}{\eta} dz, \quad (11)$$

where λ is the local value of z at which the shear stresses are zero.

The energy equation can also be further simplified based on the assumptions of the dominance of the heat conduction in thickness direction [96]:

$$\begin{aligned} \rho c_p \left(\frac{\partial T}{\partial t} + u_x \frac{\partial T}{\partial x} + u_y \frac{\partial T}{\partial y} + u_z \frac{\partial T}{\partial z} \right) \\ = k \frac{\partial^2 T}{\partial z^2} + \eta \left(\frac{\partial u_y}{\partial z} \right)^2 + \eta \left(\frac{\partial u_x}{\partial z} \right)^2 + Q_0 \frac{d\alpha}{dt}, \end{aligned} \quad (12)$$

where ρ is the density, c_p the specific heat, T is the temperature, u_i is the fluid velocity vector in direction x , y , and z , respectively, k is thermal conductivity, \dot{Q} heat generation due to the exothermic reaction in the thermoset curing process, Q_0 stands for the total amount of generated heat in the exothermic curing reaction, and $\frac{d\alpha}{dt}$ is the curing reaction rate.

The dependency of the viscosity from the temperature, the curing rate and the shear rate is described respectively by the previously introduced models of Andrade [98], Castro-Macosko [81, 82], and Cross [99] (eq. 2-4). The curing reaction rate has been presented in eq. 5 and is described by the Kamal equation [76, 86].

Simulation inputs

As mentioned, the algorithms of the simulation tool cannot be changed or adapted. However, all the mentioned inputs can be freely chosen. The more accurate these inputs are, the better the simulation result is. However, in some cases a trade-off is necessary, between accuracy and CPU time. An excellent example is the definition of the mesh among the simulation settings. 3DTimon offers the choice between two different meshing methods

- Euler method
- Morphing method.

The Euler method uses a multi-layer voxel mesh to discretize the part by several elements over the thickness, whereas the morphing method utilizes a one-layer tetra mesh to represent the final part geometry (mold-closed shape). The Euler method is advantageous in the representation of the 3D charge with a discretization possibility in thickness direction. The more subdivisions there are in thickness direction, the higher the prediction accuracy is for the flow of the material, as well as the resulting movement of the fibers. However, the two main drawbacks are the very high number of elements, which increases the CPU time significantly, and the limitations in contouring due to the cubic shaped elements, which leads to terraced steps in the geometry. When using the Euler method, the final part is meshed with one layer of tetra elements. These are then stretched into the initial stage before the compression. During the compression the elements deform back to the original unstretched size. This mesh element shape of tetraeders allows the meshing of complex geometries without stepping and with a decisively smaller number of elements. This leads to a decreased CPU time, but slightly decreases the accuracy of the prediction. [96]

Another aspect mentioned as input for the simulation is the material card. The software allows the use of one parameter set for each simulation, which includes as parameters related to the rheological behavior of the material, as well as any relevant information about the fibers and their movement, and the warpage. These parameters are obtained by characterizing the material to be simulated. The procedure to characterize the rheological behavior of SMC is presented in the following section.

2.3 Rheological characterization

Rheology is the study of flow and deformation of materials under applied forces. The viscosity is the most common material parameter and describes the resistance to an applied stress. In order to run simulation for a specific material, all unknown parameters for the viscosity and the entire mathematical description have to be identified and summarized in a material card. The characterization process for process simulation is presented in Subsection 2.3.1. In order to identify the suitable parameters, experiments determining the required parameters are necessary. In particular, suitable flow testing methods are necessary. In Subsection 2.3.2 existent flow testing setups for SMC are presented, as well as the identified influences on the flow.

2.3.1 Characterization procedure for process simulation

For SMC there is no standard procedure to do this, but there is a generally accepted approach, depicted in Fig. 2-11.

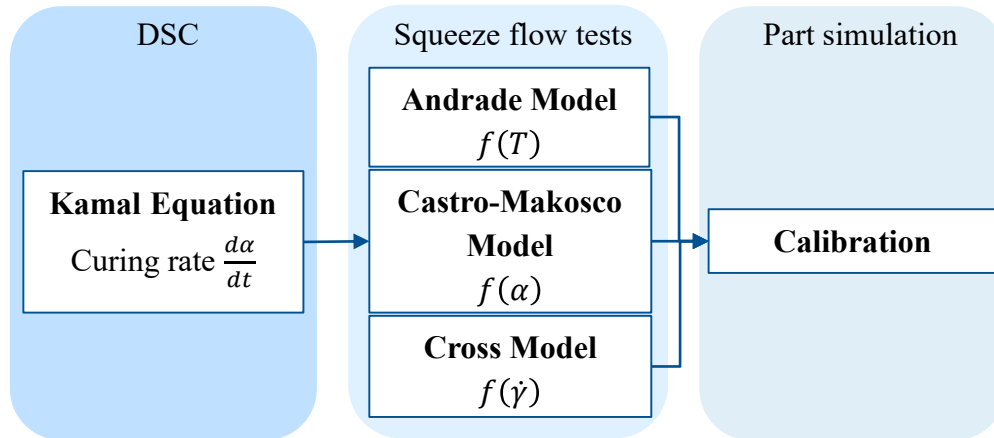


Fig. 2-11 Typical procedure to set up a material card for SMC filling simulation

The first step is performing Differential Scanning Calorimetry (DSC) measurements in order to obtain the curing kinetics of the material. For these tests three different heating rates should be chosen and for each, one test is typically performed. The schematics of the test are shown in Fig. 2-12.

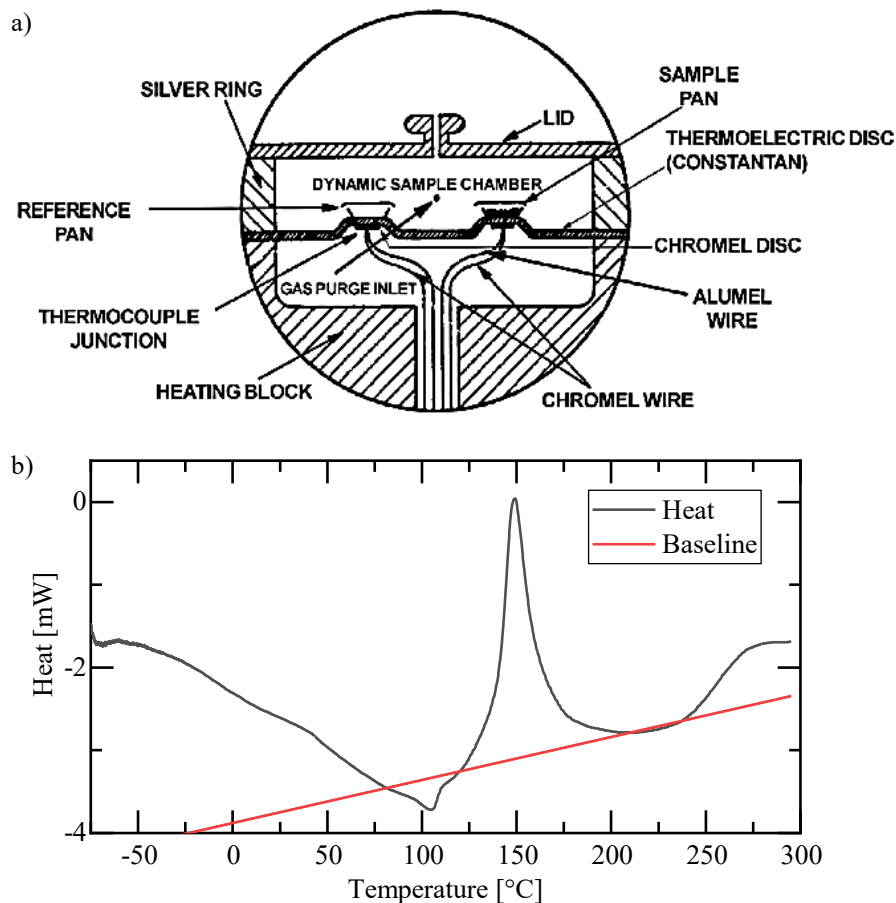


Fig. 2-12 DSC measurements: a) Schematics of the test [100]; b) exemplary result for a curve resulting for the heating rate 10 °C/min for the material adopted in this study CAR-BKID PGK5250 [44].

In Fig. 2-12a the general principle of a DSC measurement is shown, with the circular specimen placed inside a crucible next to an empty reference crucible. The resin to be tested should weight between 5 and 7 mg. The material is heated with a constant heating rate until it is fully cured, and then cooled down. As explained in Section 2.1, a myriad of additives and fillers exist for SMC materials. Typically, the exact chemical composition of industrially available SMC is a trade secret of the manufacturer of the sheet. Therefore, a test with a low heating rate is necessary, in order to understand the composition better in terms of exothermal and endothermal reactions and their overlaps, as well as the ignition or thermal decomposition temperature. The temperature range has to be wide enough to allow the machinery to reach a constant increase in temperature before the curing reaction starts. Furthermore, the sequence has to be set to reach a temperature that guarantees that the curing has completed. It should allow the testing cell to return to a constant heating rate after the curing has happened.

To determine the Kamal coefficients, the curing rate is necessary, which is calculated from the reaction heat. The reaction heat is the integral of the curing peak of the phase change of interest.

The heat generated or subtracted during the process is displayed as heat flow, as shown in Fig. 2-12b. Each reaction displays a peak. Once the peak related to the phase change of interest is identified, a baseline has to be set. The lower delimitation of the integral is set with a baseline. If the curve is completely or approximately flat in the temperature regions before and after the reaction the baseline is horizontal or linear and links the starting and the ending point of the reaction. If more than one reaction occurs at the same temperature and the heat of each reaction has to be determined separately, a sigmoidal baseline has to be chosen [101–103]. In most cases, when the material has only one component able to cure, the baseline is flat or linear, making it easy to identify. However, if the material contains more than one component, the identification of a baseline is dependent on the experience of the analyzer. [101–103]

The heat flow during the reaction can be determined as the surface underneath the peak according to the following equation [104]

$$\dot{q} = Q(T)\Delta T \quad (13)$$

Where $Q(T)$ is the generated momentary heat; ΔT is the temperature difference between T_0 and T . For the fitting the reaction rate is necessary, which represents the progression of the curing. The reaction rate is the degree of progression of the reaction and is calculated with

$$\alpha = \frac{Q(T)[T_0; T]}{Q(T)[T_0; T_{tot}]} \quad (14)$$

The graphic representation of this calculation is shown in Fig. 2-13.

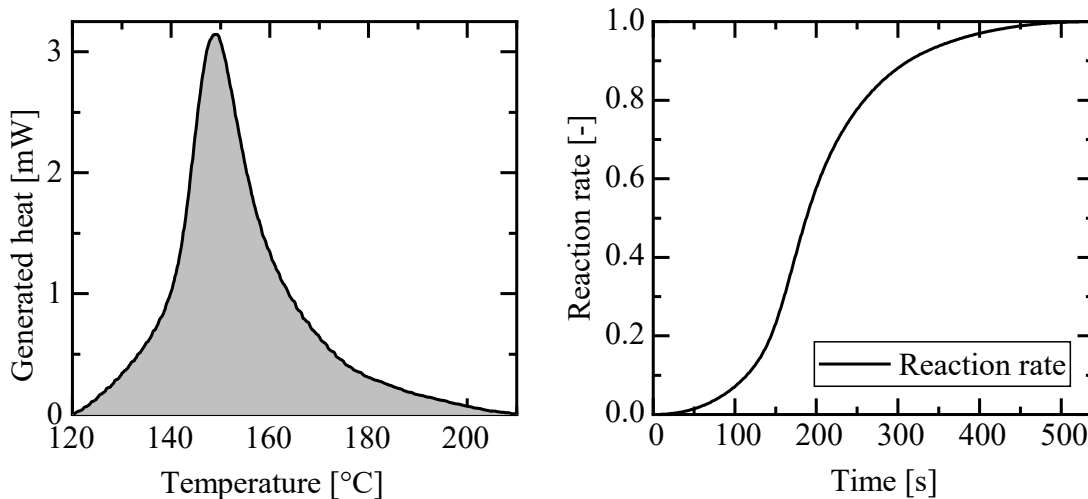


Fig. 2-13 Generated heat and resulting reaction rate for a curve at the heating rate of 10 °C/min for the SMC material adopted in this research CARBKID PGK5250 [44].

The results of the reaction rate shall be fitted to the mathematical description of the curing behavior in order to obtain the material specific parameters.

To obtain the viscosity parameters, a flow test has to be performed. Unfortunately, standard rheometers and viscometers cannot be used as the long fibers cause considerable friction and therefore, heat up the material, leading to its curing [105]. The unofficial standard for SMC is a squeeze flow test (Fig. 2-14) [20, 73, 106–112] (Variations and comparisons of flow tests are presented in Subsection 2.3.2.1).

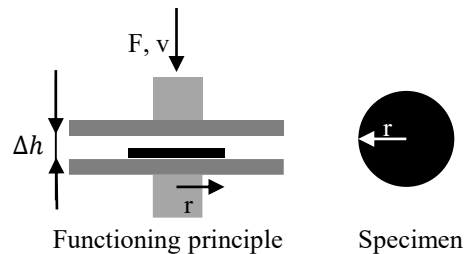


Fig. 2-14 Functioning principle of squeeze flow tests and typical specimen

The test setup consists of two parallel plates at a distance Δh with several SMC discs in between with radius r . The material compression happens at constant speed v , by applying a force F and at different constant temperatures, usually one test per setting. The temperatures range from room temperature to normal process temperature and can be applied with a thermal chamber or by directly heating the compression plates with cartridges.

The viscosity of the material, and the shear rate are calculated from the force signal with the following equations

- viscosity [107]:

$$\mu = \frac{2[h(t)]^3 F(t)}{3\pi v_0 R^4} \quad (15)$$

- Stefan equation [113]:

$$\dot{\gamma} = \frac{3 * v(t)r(t)}{2 * h^2} \quad (16)$$

μ being the viscosity, $\dot{\gamma}$ the shear rate, $h(t)$, $r(t)$, $F(t)$, and $v(t)$ being the time dependent height and radius of the specimen, as well as the force and closing speed, v_0 the initial closing speed, R the initial radius. The data is fitted to the viscosity model to obtain the material specific parameters. For a final calibration, a part is produced that is similar to the geometry that is in development. A simulation is also set up for this geometry and the parameters are adapted manually in order to improve the simulation outcome. This step is necessary, because the flow of the material is one of the most important but also most complex aspects to determine, both for the numerical representation of the flow and for a better understanding of the material flow in general. In order to improve the outcome of the flow testing and therefore, maybe avoid the calibration step, several flow testing setups have been adopted and a few charge variations have been investigated over the past decades.

2.3.2 SMC flow characterization

In order to work with SMC, it is crucial to understand the flow of the material. In the following sections, both the existing test methods (Subsection 2.3.2.1) and the performed charge variations (Subsection 2.3.2.2) are presented.

2.3.2.1 Test methods

Over the past decades, many adaptations and variations of experimental setups to characterize the flow of SMC have been developed. In an overall perspective, these can be subdivided based on varying characteristics, such as whether they are applied in a testing machine or in a press, the type of heating system, the complexity of the setup, the type of flow tested, etc. As mentioned in the previous Subsection 2.3.1 and schematically shown in Fig. 2-14, the traditional setup is squeeze flow tests. However, the standard geometry of the two compression plates has been varied. A good overview was published by Duhic et al. [106] and Schommer et al. [42], as shown in an adapted form in Fig. 2-15.

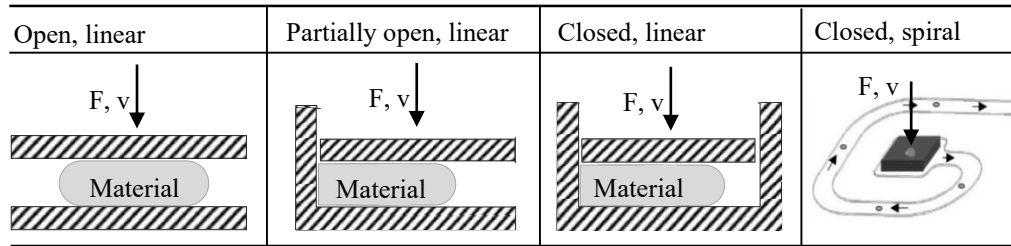


Fig. 2-15 Overview of flow characterization principles for approaches derived from squeeze flow testing (adapted from [42, 106])

The first option (first column) depicts an open mold with linear flow, which represents the schematics of a typical squeeze flow test setup. The typical charge shape is a circle. The adoption of this setup for the flow characterization of SMC was introduced by Lee et al. in 1981 [69] as the standard setup for a UTM. However, it has also been adapted to be used inside a press in 1977 [114]. For both variations, the setup has been adopted by a multitude of researchers ever since [20, 42, 61, 66, 70, 106–112, 115–119]. Exceptions using a rectangular shape for the tests with open mold do exist [36, 42], but typically the rectangular shape is applied for the partially open or closed molds. In the second configuration, the flow is still linear, but the flow has a delimitation on one side, making the cavity a partially open mold. Abrams et al. [120] and Boylan et al. [121] adopted this kind of setup for their research into numerical modeling of SMC flow (see Fig. 2-17c) as well as Lin et al. [119], Oelgarth [122], and Ritter [123]. The third and most complex configuration for linear flow is the closed mold, as applied i.e. by Hohberg et al. [67] (see Fig. 2-17b), Kau et al. [124], and Specker [125]. A fourth option is spiral flow, which has to be done in a closed mold in order to force the flow into a specific direction. This approach was introduced by Rabinovich et al. [126].

For the test setups, several variations exist, differentiating between considered aspects. The first variation to be addressed, is that the open linear squeeze flow tests can be applied with a constant cross section (also known as constant area) or a constant volume [127]. An example for each configuration is shown in Fig. 2-16.

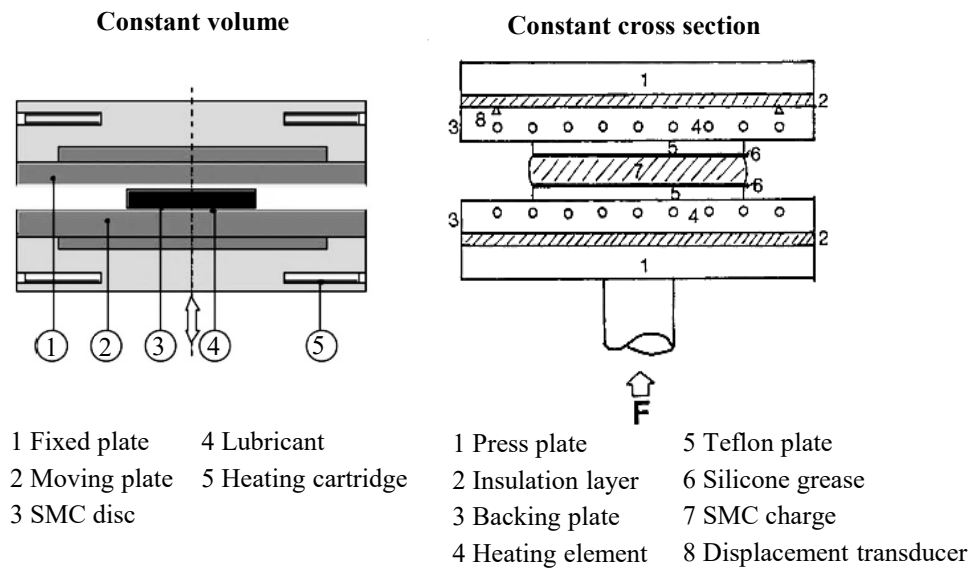


Fig. 2-16 Squeeze flow test variation of constant volume compared to constant cross section, exemplarily shown with the flow test setups of Dumont et al. [65] (left) and Lee et al. [69] (right).

As can be seen in Fig. 2-16, Dumont et al. [65] performed tests with a constant volume of the material. This means that the cross section of the compression plates was bigger than the cross section of the charge. The material flows on the surface towards the edges with a certain shear viscosity. Lee et al [69] performed tests with constant cross section, with the compression plates having the same diameter as the SMC specimens. The material is squeezed out on the sides, allowing a closer investigation of the edge effect. Both setups have their advantages and disadvantages and the choice between one and the other should be made carefully. Constant cross section avoids edge effects, reducing influences on the stress response due to the compression to a minimum. Constant volume will show the influence of anisotropy and the overall homogeneity of the semi-finished SMC product [42].

Many more variations exist regarding the setup, more specifically the pressure application, the signal tracking, and the heat generation. Fig. 2-17 displays some exemplary variations of the above mentioned squeeze flow alternatives. The test can be performed in a UTM, as for the setup shown in Fig. 2-17a developed by Oelgarth [122] or in a manufacturing press. The UTM has integrated data tracking for the displacement and the force, and very precise closing speeds. The heat can be generated with a thermal chamber engulfing the setup or with heating cartridges inside the compression plates. When the flow test setup is placed in a manufacturing press, typical production settings for SMC can be obtained, with the heat generation happening over the press. However, pressure and displacement tracking is more complex or not integrated in industrial SMC presses and the accuracy of the data is not very high. To counteract, when flow testing is performed in SMC presses, additional pressure and displacement tracking is integrated, by using i.e. a transducer [69]. In some cases the compression plates are also

equipped with pressure sensors, to obtain a more precise pressure distribution reflecting the stresses due to the compression. Hohberg et al. [67] developed such a setup in order to characterize SMC material for their numerical model. The schematics are exemplarily shown in Fig. 2-17b.

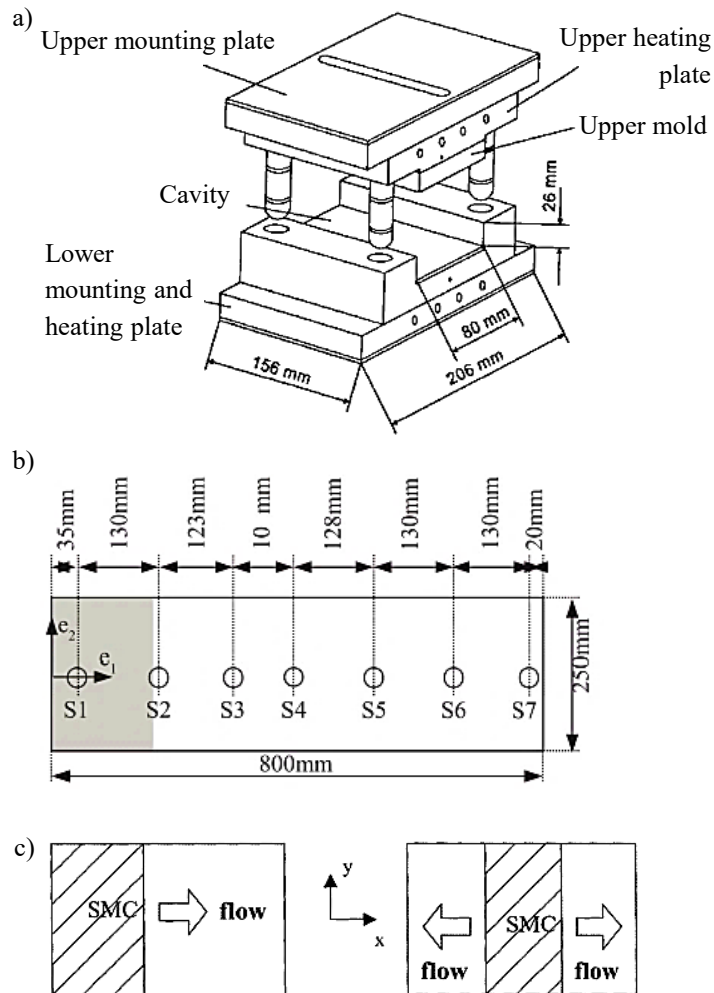


Fig. 2-17 Squeeze flow testing variations: a) Setup for a UTM for an open mold and linear flow from Oelgarth [122]; b) Closed mold setup with pressure sensors arranged along the flow channel [67]; c) Charge configurations tested in an open mold with linear flow by Abrams et al. [120] and Boylan et al. [121].

A further variation to be performed when testing the flow of SMC is the charge placement and geometry, as was performed in [120, 121] (see Fig. 2-17c). With the charge variation, the flow length was varied, in order to understand its influence on the final part filling better. An additional variation is the flow tracking with a camera system from the side in order to observe the progression of the flow front. This has been done by several researchers [61, 65, 115, 117]. The results are presented in the following subsection about the investigated flow behavior of SMC.

Apart from the in-plane flow testing methods, also more complex geometries have been adopted for SMC flow testing, in order to observe out-of-plane flow behavior. Two examples can be seen in Fig. 2-18.

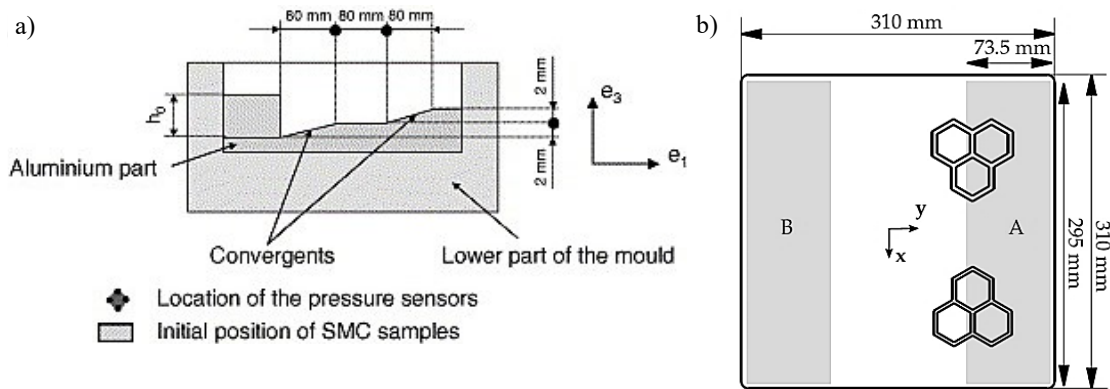


Fig. 2-18 Out-of-plane flow testing setups: a) Stepped plate with incline [128]; b) plate with honeycomb geometry protruding from the surface [40]

The simplest adaptation from in-plane flow can be seen in Fig. 2-18a from Dumont et al. [128] displaying a modified plate geometry with some thickness changes connected by inclined surfaces. In Fig. 2-18b another plate adaptation can be seen, showing a more complex geometry with out-of-plane flow, with honeycomb structures protruding from the surface that were filled during the compression. The thickness at the top is 2 mm, with an incline of 2° and a height of 3.5 mm [40].

Further variations of out-of-plane flow testing have been introduced by Jeong et al. [129] and also adopted in the research of Kim et al. [130], consisting of a T-shape mold. The rectangular charge was placed on top of the rib opening, which was 6.35 mm wide at the tip and 9.8 mm deep.

The last variation for SMC flow testing is an independent test stand [131], presented in detail in Subsection 3.3.2.2. The mold consists of a bar equipped with temperature sensors along the flow channel. The mold offers the possibility to select among three different thicknesses for the channel, ranging from 1.5 to 3.5 mm. This configuration is geometrically close to ribs, a typical feature in SMC parts. The pressure of 9 bar is applied constantly through a pneumatic actuator that moves a piston inside a cylinder of 30 mm in diameter. The displacement of the piston is tracked with a linear potentiometer. The temperature is generated with heating cartridges inside the lower mold.

The test setups were developed to investigate the flow behavior of SMC material, in order to numerically replicate it and derive guidelines for manufacturing. The following subsection presents the knowledge acquired about the flow of SMC material with these flow tests.

2.3.2.2 Behavior of SMC during compression

With the previously introduced flow testing setups for SMC, the material behavior in general and more specifically, the flow behavior, has been investigated for several decades. In this subsection, the main influences on the flow behavior of SMC are summarized. It is to be noted that results for both carbon fiber SMC (CSMC) and glass fiber SMC (GSMC) are presented. Especially coloring of charge layers can only be performed for GSMC.

During the compression process SMC is assumed to be incompressible. However, it has been proven that the sheets have a high void content [132, 133]. Therefore, at the beginning of the compression, the material is only compressed, with a change in thickness, but no flow. Only once the voids are significantly diminished, the flow begins and the material can be assumed as incompressible. [66]

Moreover, due to the heated molds in contact with the outermost layers of SMC, the charge can be subdivided into two regions with different flow behavior, as shown in Fig. 2-19.

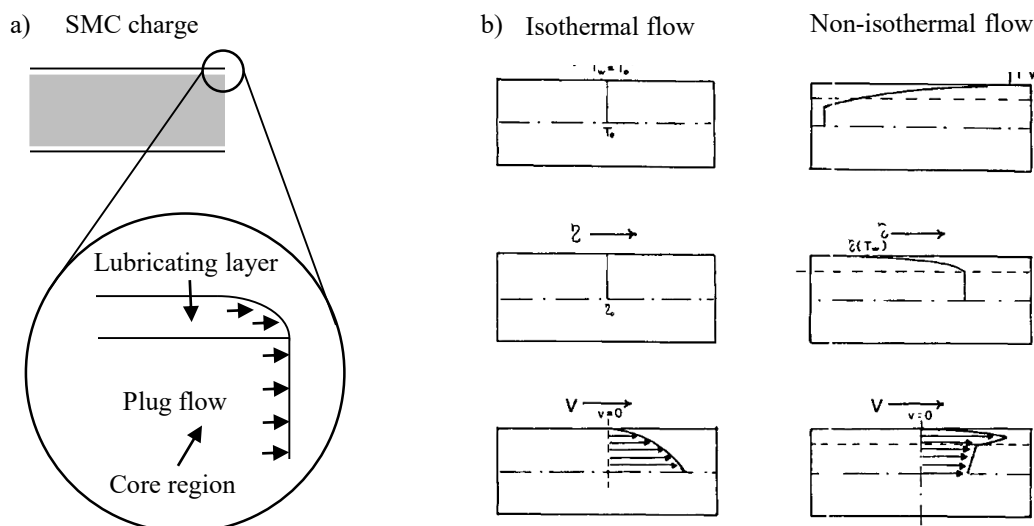


Fig. 2-19 SMC charge during the compression: a) Formation of lubricating layers at the surfaces in contact with the heated mold and detail representation of the flow front (adapted from [46, 120]); b) Temperature, viscosity and flow velocity resulting from the temperature distribution [69].

The two regions to be identified in the SMC charge during the compression are the lubricating layers and the core region. The latter is characterized by plug flow, with the material still at room temperature. On the outermost surface of the SMC charge the material is in contact with the heated mold and therefore, increases in temperature. The increase in temperature causes a decrease in the viscosity, which decreases the friction between the mold surface and the charge. Therefore, the material in the center can spread homogeneously perpendicular to the compression direction, while the lubricating layers

favors the slippage of the material against the mold surface, almost annihilating the resistance. [69, 110, 120, 125]

Apart from the temperature, the fiber length also influences the flow. The shorter the fibers, the lower the compression pressure can be and the higher the probability is for a part to be completely filled [69]. However, a decrease in fiber length also induces a decrease in mechanical performance, as the two aspects of length of the fibers and mechanical performance are directly proportional.

The behavior of the slippage of the charge on the mold surface can also be seen in recordings of the development of the charge shape from the side for closing speeds in the area of 1 or 2 mm/s, as is visible in Fig. 2-20.

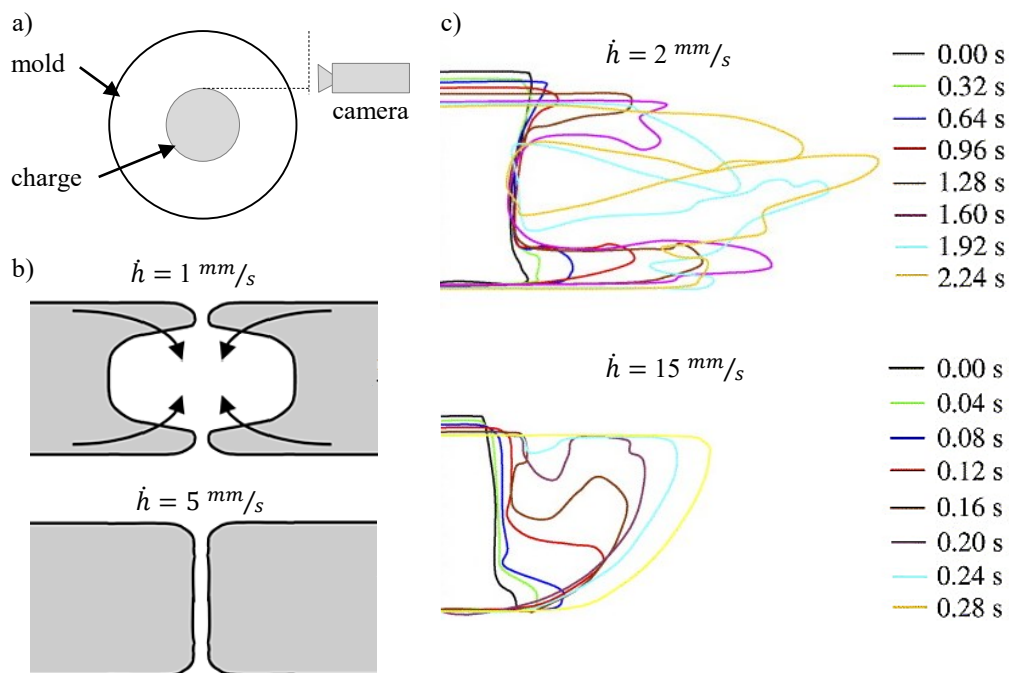


Fig. 2-20 Side view of the SMC charge during the compression: a) experimental setup for the recordings (adapted from [61]); b) Flow front for closing speeds of 1 mm/s and 5 mm/s, with a reverse fountain for the first and a constant flow front progress for the second velocity (adapted from [134]); c) Flow front progression recorded in [61] for the compression speeds 2 mm/s and 15 mm/s, again showing the reverse fountain for the lower closing speed.

The flow front progressions were recorded following the schematics displayed in Fig. 2-20a, with a camera mounted to the side of the circular charge, observing the flow front progression. It is visible in Fig. 2-20b and c that the typical compression speeds of SMC around 1 mm/s [134] or 2 mm/s [61] lead to a so-called reverse fountain flow, with the lubricating layers protruding, as they move faster. This is due to the temperature distribution and therefore, the viscosity difference between the different thickness positions of the charge. When the compression speed increases however, this behavior cannot be

observed anymore, as the material does not have time to develop a significant temperature gradient over the charge thickness. With lower viscosity in contact with the mold, the material is kept in position on the outer surface due to high friction. Therefore, the flow front progresses at a constant speed over the thickness, as can be seen for the closing speed of 5 mm/s in Fig. 2-20b. If the compression speed is increased further to 15 mm/s the material does not move on the tool side that is moving during the compression.

The same test setup was also adopted by several other authors investigating the deformation of single charge layers in thickness direction and in radial direction. In order to identify the different layers, they were differently colored. Exemplary work can be seen in Fig. 2-21 [70].

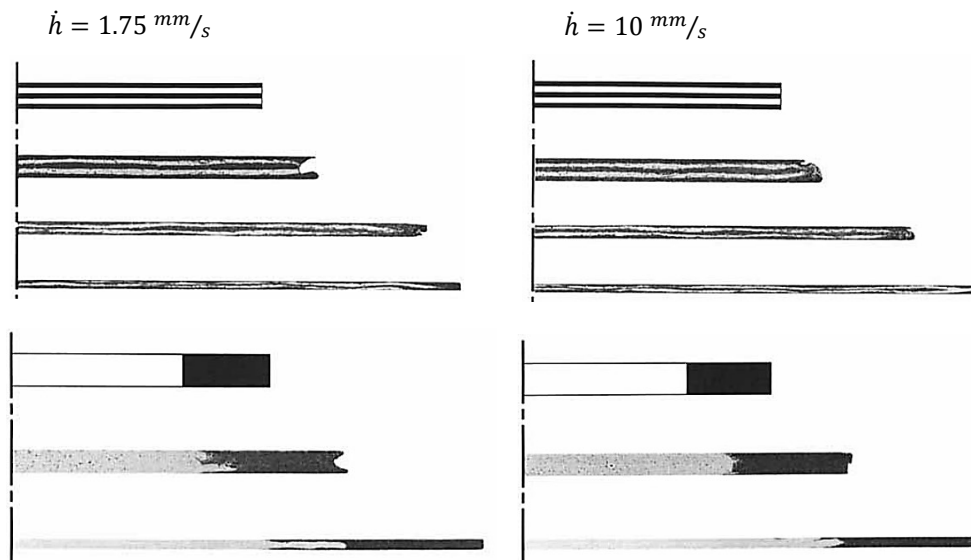


Fig. 2-21 Deformation of a charge with 5 black and white layers in thickness and in radial direction in comparison for 1.75 mm/s and 10 mm/s [70]

The reverse fountain is also evident in both layering options for the closing speed of 1.75 mm/s in Fig. 2-21. This material behavior is also not present for the higher closing speed of 10 mm/s, where the flow front resembles more the behavior seen before for 15 mm/s. For this higher compression speed, there seems to be less slip between the charge and the mold surface and more slip between the layers. For the radial layering shown on the bottom of Fig. 2-21, the flow front is quite different. The material seems to try and resist movement, and therefore, some of the black colored charge covers the white colored charge in the overlapping area at the end of the compression. This mixing of the two radial layers seems to decrease significantly with an increase in the compression speed. [70]

The authors performed this evaluation also for other layer amounts, starting with three layers, up to six layers. For the layering in thickness direction, the flow behavior does not seem to be influenced by the charge thickness for the low closing speed, whereas for

the high closing speed the slip between layers is most evident in the charge with six layers and diminishes with diminishing amount of layers. At three layers, the effect nearly disappears. For the radial layering there seems to be no noticeable difference in the flow front due to the charge thickness. [70]

Another aspect to be investigated is the influence of the application of vacuum during the compression of SMC. To this purpose, Olsson et al. [115] also investigated a GSMC charge with differently colored layers, as shown in Fig. 2-22.

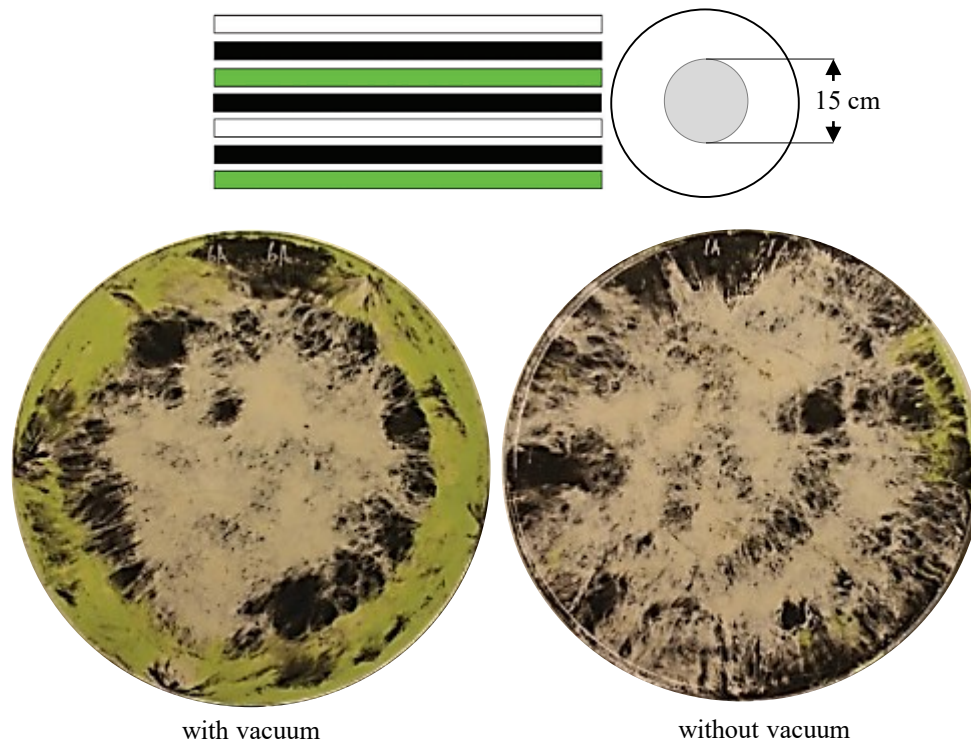


Fig. 2-22 Resulting specimens after the compression of a circular SMC charge with 7 layers with different colors with (left) and without vacuum (right) seen from the top at 144 °C and 2.5 mm/s compression speed [115].

The difference between performing the process with vacuum and without can also be seen in Fig. 2-22 below the charge schematics, with the resulting specimens shown from above. The results are from the processing done at 144 °C and 2.5 mm/s. With the application of vacuum, a high amount of the green colored SMC from the bottom layer came to the top, while the intermediate green layer was completely enclosed. For the application without vacuum this phenomenon happened less. The authors especially point out that with vacuum, with lower compression speed and lower temperature, the mixing of the layers is reduced and therefore, a more uniform flow of the SMC can be achieved. [115]

Further investigations were also performed by interrupting the compression at different steps and comparing the deformation of the surface layers. In both the round and the square shaped charge the deformation of the top layer is minimal. [65, 117]

Investigations of charge variations have also been performed by several researchers for a multitude of reasons, among which the understanding of the flow behavior, but also the validation of numerical results. In the simplest configuration the charge configuration was varied for a plate geometry, by changing the charge coverage, and the positioning. Varying the charge coverage leads to varying flow length, which has mostly been investigated in relation to the resulting mechanical properties. This has been addressed in depth in Section 2.1. The charge positioning, however, has been performed on both simple [120, 130] and complex geometries [36, 67]. The first configuration was aimed at understanding the influence of the flow on the orientation of the fibers and the induced variation in fiber contents. The fiber displacement and content distribution are also of concern in the more complex parts. However, Castro and Griffith [36] placed different charge shapes at different positions in a mold of a corvette hood and compared the molding forces and filling patterns obtained in simulation and reality.

3 Standardization of the characterization procedure

Section 2.3 describes the typical procedure for the determination of the parameters for the viscosity model and the curing kinetics to create a material card for process simulation. This approach aims at obtaining one set of parameters for the material card, and is usually based on one test per sequence. This does not take into account the high variability of SMC, resulting from the sheet production process (Section 2.1). Furthermore, the approach is not standardized, only broad recommendations can be obtained from simulation software developers, but there is no basis for a comparability between the results. Additionally, as described in Section 2.3, for the calibration the data from the production of a real part is compared to the simulation result, and the parameters are adapted, until the results are as similar as possible. In order to use the simulation in the part or process development, the part used for the calibration has similar features, like ribs or wall thickness, as the part to be developed or pressed. Therefore, it is necessary to already have an existing part and process that are similar to the new ones for the calibration, making the process inconvenient. Additionally, the complexity of the flow increases significantly between squeeze flow, showing only in-plane flow, and a part, also having multiaxial out-of-plane flow.

Given the issues of the state of the art highlighted above, this chapter addresses each of them and proposes a viable solution. The goals can be summarized as follows:

1. adapting the procedure for the determination of the parameters for the viscosity model and the curing kinetics, to be compliant with predefined requirements (next paragraph)
2. understanding and limiting human factors in the data evaluation during the procedure
3. understanding the influence of the determined parameters on the simulation outcome
4. deriving guidelines for future testing.

The requirements set for the developed procedure are

- including the variability of the raw SMC
- being independent from a part, with no link to specific geometrical features for the calibration
- being simple and quick

- being easily applicable in an industrial context, meaning state of the art equipment that is easy to acquire or typically already present in processing companies or SMC producers should be preferred
- being flexible towards the mathematical description of the rheological model and curing kinetics.

In this Thesis, the procedure is developed based on the rheological model and the curing kinetics described in Section 2.2, consisting of the Castro-Macosko and the Cross-Andrade models for the viscosity, and the Kamal equation for the curing kinetics. As shown in Tab. 2-1, those mathematical descriptions are common to all commercially available software solutions currently on the market for process simulation of long fiber reinforced materials. Therefore, the consideration of this particular description allows for a simple direct application of the results of this Thesis. Nevertheless, the approach is equally applicable to other mathematical descriptions.

In order to reach the predefined goals, each one of the steps of the characterization procedure is investigated separately: Section 3.1 focuses on the curing kinetics, Section 3.2 on the in-plane flow testing and Section 3.3 on the calibration. In Section 3.4 the newly developed procedure for the flow characterization is presented and guidelines are set, and in Section 3.5 follows a discussion.

3.1 Parameters for the curing kinetics

The content of this section has been previously published in similar form in [K1].

The first set of parameters necessary for the material card are those for the Kamal equation describing the curing kinetics, as shown in Section 2.2. The most common technique to determine the material specific parameters of the Kamal equation is Differential Scanning Calorimetry (DSC) (Section 2.3) [29, 79, 87, 135, 136]. A total of six parameters is needed: the kinetic exponents m , and n , as well as the material specific constants A_1 , A_2 , E_1 , and E_2 . The aim of the Kamal parameters is to describe the curing kinetics of the material for the statistically most relevant configurations. However, related challenges of the material, as presented in Section 2.1, such as the variability have to be included. Specifically related to DSC measurements the following challenges are identified:

- For the measurement, 5-7 mg of resin are necessary for each specimen (see Section 2.3). However, the material is typically made available to SMC part producers as an uncured sheet with the fibers already impregnated with the resin system. In order to know the amount of resin within one specimen, the density of the interested circular area of 4 mm in diameter has to be known. To determine the density the uncured specimen would have to be submerged in water (Archimedes principle), or cured and then the resin can be burnt out or removed via etching. Unfortunately, none of those possibilities allows an accurate determination of the density without destroying the specimen.

- The weight of the resin also has to be known in order to determine a precise heat flow. However, as mentioned above, this is not possible.
- The resin of SMC has volatile components that can be styrene [47] or bisphenol A (BPA) [137], depending on the resin system. These components continually exit the material, reducing its weight, specifically the weight of the resin.
- SMC consists of already mixed resin. Therefore, the curing of the material continually proceeds until the end of pot life. Depending on the storage temperature during all steps of the sheet production process, the transport and storage after mixing resin and hardener (Subsection 2.1), the shelf life can pass faster or slower. An SMC part producer does not know how much the curing has proceeded in the moment they adopt the material. However, the measurement can only record the reaction from the moment the material is tested.

All the above mentioned aspects create uncertainties within the measurements. The aim of this chapter is to present a procedure for the determination of the Kamal parameters that manages all these uncertainties.

3.1.1 Measurement and analysis approach

The measurements were performed with a DSC Q200 machinery from TA Instruments. Tab. 3-1 shows the six tested heating rates from 10 °C/min to 60 °C/min, their respective temperature sequences, and the repetitions for each setting.

Tab. 3-1 Measured DSC test sequences

Temperature sequence [°C]	Heating rate [°C/min]	Repetitions
-80 → 300 → -80 → 300 °C → RT	10	1
80 → 350°C → 80 → 350°C → RT	20	3
	30	5
	40	5
0 → 350°C → 0 → 350°C → RT	50	5
	60	5

RT= room temperature

In order to identify the starting and end temperature to be considered, the approach presented in Section 2.3 was applied, and a first test with a heating rate of 10 °C/min for the range from -80 °C to 380 °C was chosen. The curing has been identified in the range between 110 °C and 210 °C. For all following tests, the temperature range was chosen accordingly, to optimize runtime based on guidelines presented in Section 2.3. In order to capture and quantify the variability of the material, especially in relation to the resin weight, five repetitions were performed for all tests at 30 °C/min or higher heating rate. Only three repetitions were performed for the tests at 20 °C/min, since the heating rate is far from the usual application of SMC and therefore, the input was deemed as less relevant.

The material used in the tests is the same as for the entire evaluation within this thesis CARBKID PGK5250-R63 from Astar S.A. [44]. The tested specimens are circles of SMC with a diameter of 4 mm. The weight of the specimens varied from 10.84 mg to 15.21 mg, which correspond to 5.07 mg and 7.13 mg respectively in order to have the necessary 5-7 mg of resin, considering the indicated 52 wt% fiber content of the tested SMC [44]. The specimens were cut and weighted two days before the test was performed and during that time a weight decrease of the specimen of up to 1.16 mg could be recorded. It can be assumed, that the lost weight is given by evaporated resin components, meaning that the weight loss can be solely attributed to the resin. This changes the density and the weight ratios of the compound. However, the above indicated resin weights are calculated with the weight contents given by the data sheet of the SMC.

Baselines were set, and the reaction rates were calculated before performing the fitting with the ReactiveMoldFitting® tool provided with the simulation software 3DTimon from Toray Engineering Co., Ltd (presented in Section 2.3).

3.1.2 Results and discussion

The result for all five repetitions performed with the reaction rate of 30 °C/min are shown in Fig. 3-1.

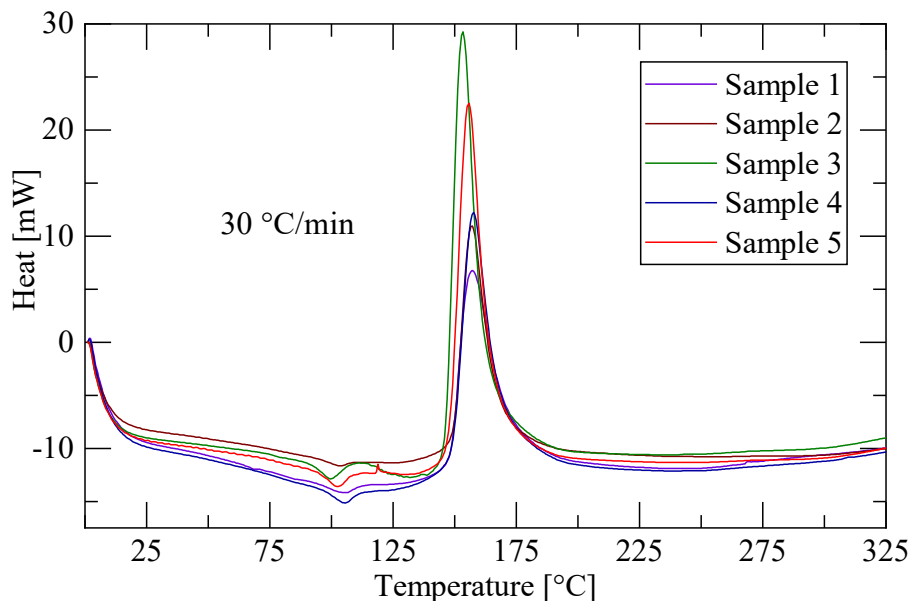


Fig. 3-1 Results for all tests performed at 30 °C/min

Even though the testing sequences are the same, each test data differs from the others. This is due to the challenges of SMC when performing DSC measurements that have been addressed in the introduction to this evaluation. A crucial element is the heat generated during the measurement, a value related to the weight of the pure resin of the specimen. However, the pure resin weight is calculated with the density given on the data sheet. But the density will change due to the volatile components and due to the inhomogeneity of the density itself over the sheet. Therefore, all five curves differ in

their basal heat level. Moreover, the curing reaction has very different curves. Sample 3 shows a very fast reaction that happens a few degrees earlier than the other tests and has a significantly higher peak. Sample 1 on the other hand, has the lowest peak. If all specimens have the same degree of curing, the area under the peak should be exactly the same. However, in this case it seems like sample 1 has already progressed more than the other specimens. Given the typical storage times for SMC as described in the introduction, it can happen that a specimen is processed, when the pot life is almost over. Therefore, this case also needs to be covered in the simulation and therefore, be represented in the material card. All other curves are shown in the appendix a and display a similar variability in the height of the base heat and of the peak for the curing reaction.

The heat generated during each of the tests is summarized in Tab. 3-2.

Tab. 3-2 Summary of the generated heat for all tested curves, and calculation of the average for each heating rate

Sample	Heating rate [K/min]	Generated heat [mW]	Sample	Heating rate [K/min]	Generated heat [mW]
10	10	414.61	50_1	50	1054.14
ave		414.61	50_2	50	1036.14
20_1	20	950.80	50_3	50	979.30
20_2	20	464.13	50_4	50	907.22
20_3	20	729.49	50_5	50	988.97
ave		714.81	ave		993.16
30_1	30	795.59	60_1	60	646.66
30_2	30	654.84	60_2	60	1007.98
30_3	30	1095.46	60_3	60	870.69
30_4	30	897.51	60_4	60	907.53
30_5	30	912.05	60_5	60	959.10
ave		871.09	ave		878.39
40_1	40	799.92			
40_2	40	617.65			
40_3	40	804.34			
40_4	40	873.08			
40_5	40	964.71			
ave		811.94			

As can be seen, the generated heat is in a similar range considering the average for all heating rates except for 10 K/min. This can be due to the specimen being already partially cured before the test. Furthermore, this test was one of the last to be done. During one of the previous tests, a bit of the material was burnt, so the calibration had to be repeated. The test sequence of 10 K/min was performed in between the five calibration runs. Therefore, the calibration was not ideal. For all other heating rates there is at least one curve with a much lower result for the generated heat, such as test 2 for 30 °C/min with 654.84 mW, test 2 for 40 °C/min with 617.65 mW, test 1 for 60 °C/min with 646.66 mW and test 2 for 20 °C/min with 464.13 mW. 50 °C/min on the other hand,

displays rather constant and high results, all above 900 mW. Nevertheless, for the determination of the curing kinetics, the reaction rate is necessary. This value is independent from the quantitative aspects of the generated heat. It is solely dependent on the qualitative development. To obtain the reaction progression, a baseline has to be defined for each test curve. It is visible in Fig. 3-1 that the curve is not flat, displaying a linear development between 105 °C and the end of the heating ramp at 350 °C. Therefore, the appropriate baseline for the material is linear. This can also be seen in the generated heat curve shown in Fig. 3-2 for 10 K/min, where the process for this evaluation is shown.

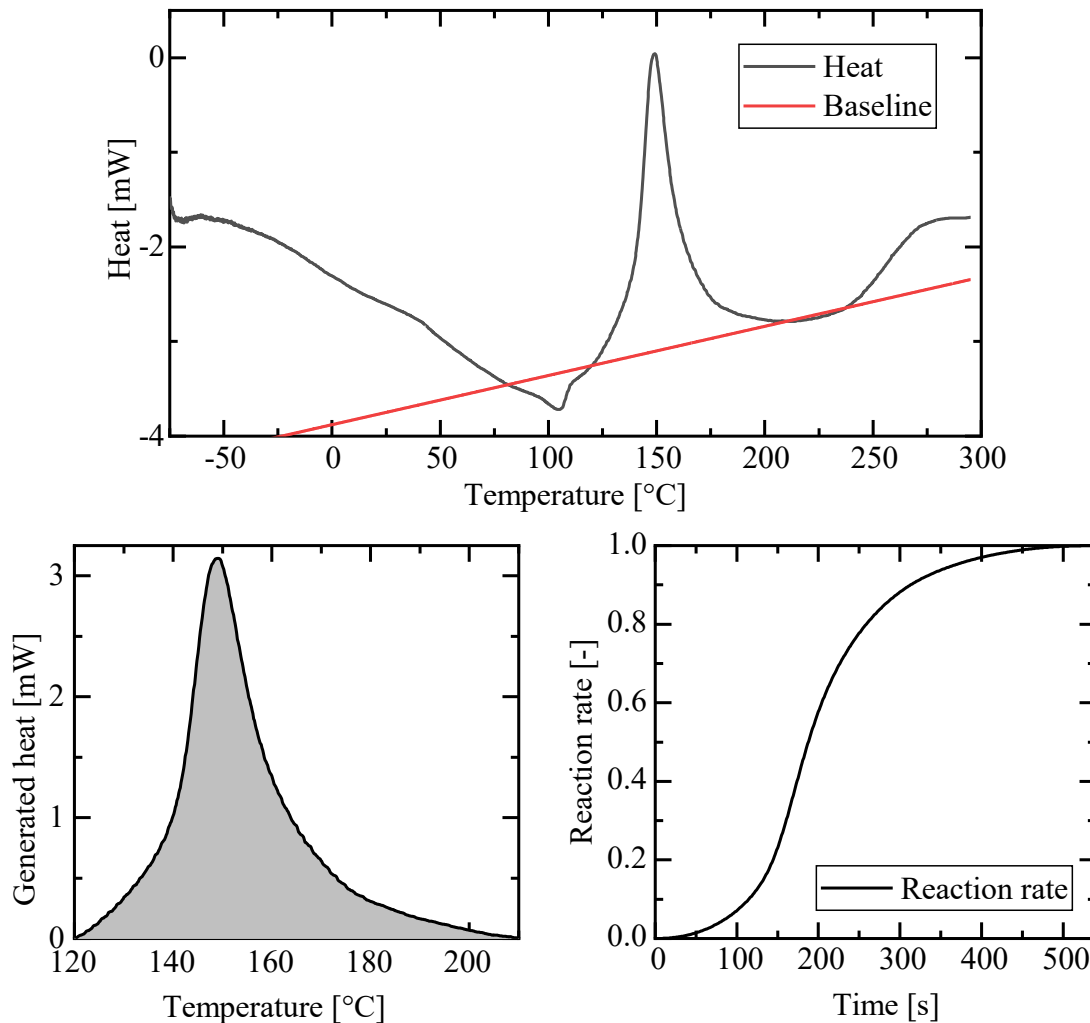


Fig. 3-2 Process to obtain the reaction rate by determining a baseline for the reaction heat peak (top), then referencing the generated heat to a flat baseline at level 0 (bottom left), and finally calculating the reaction rate (bottom right)

In this case it is visible that the development of the heat after the peak is not linear after 225 °C. Nevertheless, this applies to all other tested curves and can therefore, be used for the evaluation. As the determination of the baseline is dependent on human experience, a first evaluation was performed, to understand the impact of different start and end points of the reaction. To this purpose, three different baselines were defined for

three exemplary heat flow curves for the heating rates 10 °C/min, 20 °C/min and 40 °C/min. The comparison of the resulting heating rates can be seen in Fig. 3-3.

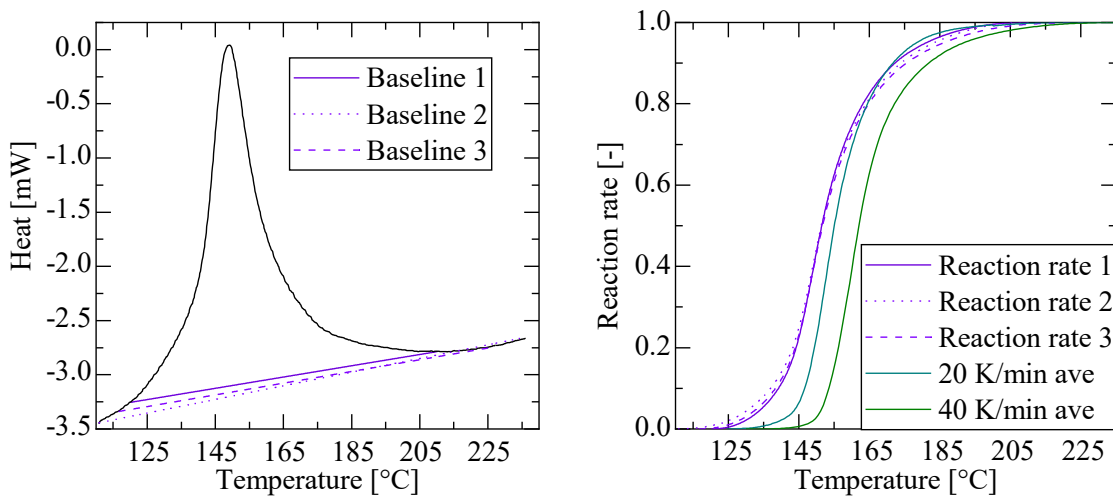


Fig. 3-3 Influence of the baseline on the resulting reaction rate: three plausible baselines for the curve at 10 K/min (left), and the resulting reaction rates compared to the averages of the reaction rates for 20 K/min and 40 K/min

The diagram on the left shows the curing curve resulting for 10 °C/min with three possible baselines. The diagram on the right shows the three corresponding resulting reaction rates for 10 °C/min heating rate. In order to understand the magnitude of the variation, it is shown in comparison with the averages for 20 °C/min and 40 °C min. It is evident that despite the baselines having different starting points, orientation, and end points, in comparison with other reaction rates for higher heating rates, the difference is not so evident anymore. Therefore, in order to include the variability of the material into the evaluation, a baseline was set for each test result, determining its reaction rate. Only afterwards, the average of all reaction rates for one heating rate was calculated, reducing the influence of the user on every single baseline and considering the statistically most relevant reaction rate for the fitting. The average reaction rate for 40 °C/min is shown in Fig. 3-4.

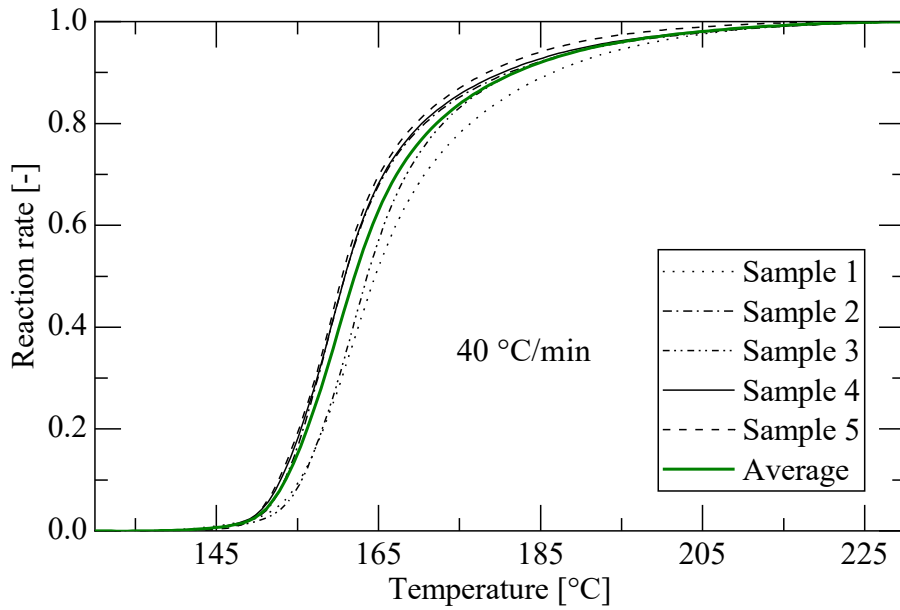


Fig. 3-4 Reaction rates for all five samples tested with 40 K/min heating rate and the resulting average.

As can be seen, all reaction rates are very similar. All other averages and the related sample curves can be found in the appendix a. The summary of the calculated averages for the reaction rates for all heating rates can be seen in Fig. 3-5.

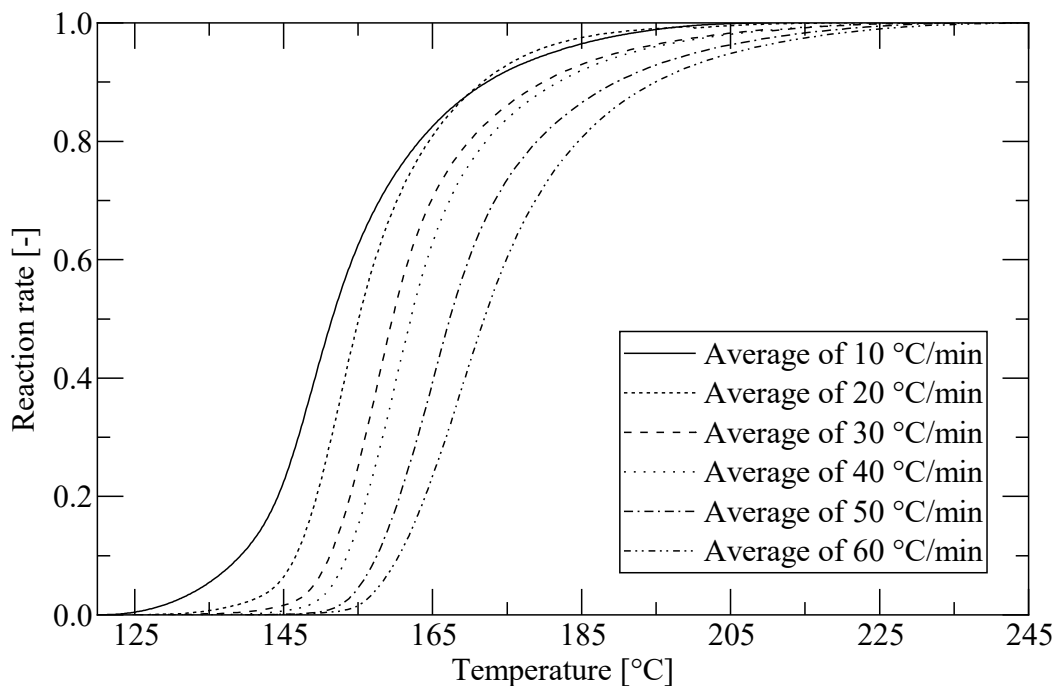


Fig. 3-5 All averages of the reaction rates for all tested heating rates.

The heating rates up to 50 °C/min show a realistic curve, with a steep start of the reaction between 0 and 10 % reaction rate. The progression of the reaction from 10 % until 70 % happens equally for all curves, showing parallel progression for the heating rates between 20 °C/min and 50 °C/min. Moreover, all curves with heating rates equal and

above 20 °C/min exhibit a slower end of the reaction starting at 70 % until completion over a temperature range of about 50 °C. However, the curve for 60 °C/min shows a beginning of the reaction until 10 % that is slower than the others. As the represented curve is the result of the averages of all five tests performed at 60 °C/min this development appears to repeat itself in each measurement. This development of the curve is due to the design of the DSC equipment, not suitable for higher heating rates. Machinery with higher heating rates would allow this kind of evaluation, but would not perform measurements at low heating rates, which are also relevant. Therefore, a tradeoff is necessary, as the adopted DSC machinery is designed for heating rates of about 20 °C/min, which is much lower than the heating rate of more than 1200 °C/min occurring with the SMC material during the compression step of the manufacturing process. Furthermore, the curves representing the tests at 10 °C/min and 20 °C/min intersect at about 90 % curing. The reason for this intersection is that the reaction at 10 °C/min is slower at the beginning, while at 20 °C/min the reaction slows down later than all others. These differences can be due to the choice of the baseline. The influence of the baselines are bigger for 10 °C/min and 20 °C/min. This might be due to the reduced amount of repetitions. The adopted fitting tool allows the fitting of up to three different curing rates. Therefore, from the six tested heating rates the most appropriate combination of three has to be selected. It is recommendable to cover a heating rate range as wide as possible, to determine Kamal parameters that are accurate for all heating rates. Based on all these considerations, the most recommendable testing sequences are those at 10 °C/min, 30 °C/min and 50 °C/min.

The result of the fitting tool in 3DTimon for the average curves for the heating rates of 10 K/min, 30 K/min and 50 K/min is exemplarily displayed in Fig. 3-6

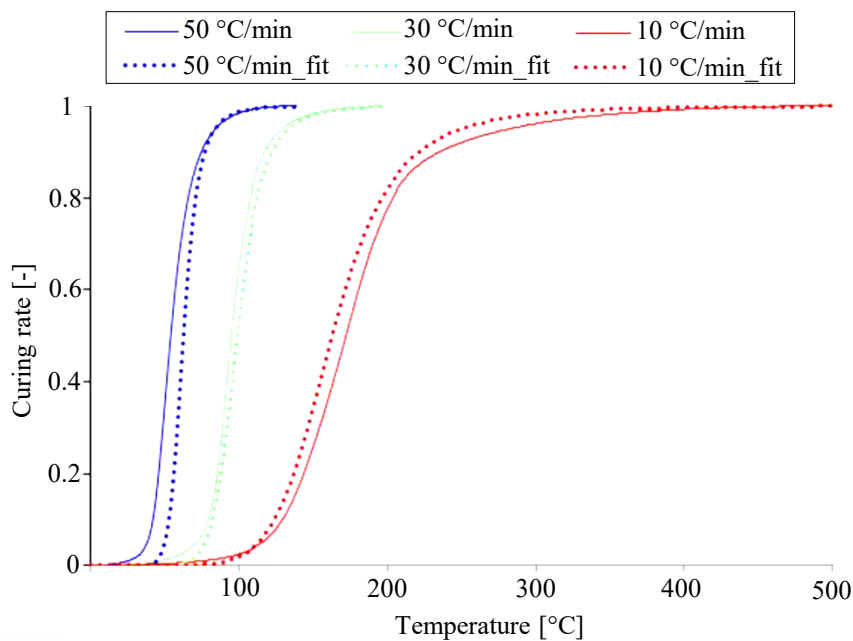


Fig. 3-6 Exemplary fitting result for the chosen heating rates 10 K/min, 30 K/min, and 50 K/min (image taken of the fitting tool provided by the software solution 3DTimon)

As can be seen, a difference between the fitted curve and the tested curve is visible. As the goal is to fit the intermediate value as best as possible. This will lead to the fitting result of the higher heating rate to happen later than in the real test, whereas for the lower temperature it will be the contrary, with the fitting showing an earlier reaction than the test. Unfortunately, the fitting tool is provided as a black box, which does not allow to see the fitting strategy or the number of iterations considered. However, if only one fitting is performed, it is usually necessary to make a few adaptations manually by changing the values directly in the tool. The identified procedure consists of 3 steps, as shown in Fig. 3-7.

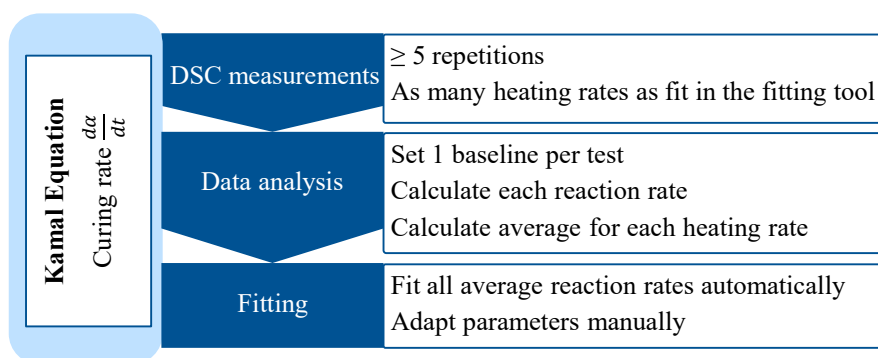


Fig. 3-7 Schematic representation of the developed procedure summarizing the three main steps of the measurements, the data analysis and the fitting, with the related guidelines

The first step consists of the DSC experiments, which should include five tests per heating rate, and as many different heating rates the fitting tool can fit at the same time. In this study, those were three. Furthermore, the chosen heating rates should cover a range of heating rates as wide as possible within the capabilities of the available machinery. Therefore, within this study the heating rates of 10 °C/min, 30 °C/min and 50 °C/min were chosen. For each resulting heat flow curve a baseline has to be set and the reaction heat has to be calculated accordingly. In order to consider the variability of the material, an average reaction rate shall be calculated for each heating rate with the five performed tests. A fitting shall be performed, with all average reaction rates together. To improve the fitting, the parameters can be adapted manually.

3.1.3 Conclusion, further investigations, next steps

Within this study on the determination of the Kamal parameters for the curing kinetics of SMC, a suitable procedure could be identified, as shown in Fig. 3-7. This procedure complies with the overall goals set for the entire procedure, as it takes into account the variability of the material, human factors, industrial applicability, geometrical and mathematical independency.

Within a new study performed in the student thesis [S11], the same SMC material CAR-BKID PGK5250-R63 has been tested following the developed procedure. The goal of the study was finding out how well the developed procedure can be applied to a new batch of the same material and what differences there are in the measurements. The same

equipment and fitting tool were used, and a new batch of the same material. The experimental setup was the same as recommended, performing five repetitions for the heating rates of 10 K/min, 30 K/min, and 50 K/min. A direct comparison between the covered range between the previous tests from 2020 and the ones performed in 2023 for the heating rate 50 K/min can be seen in Fig. 3-8.

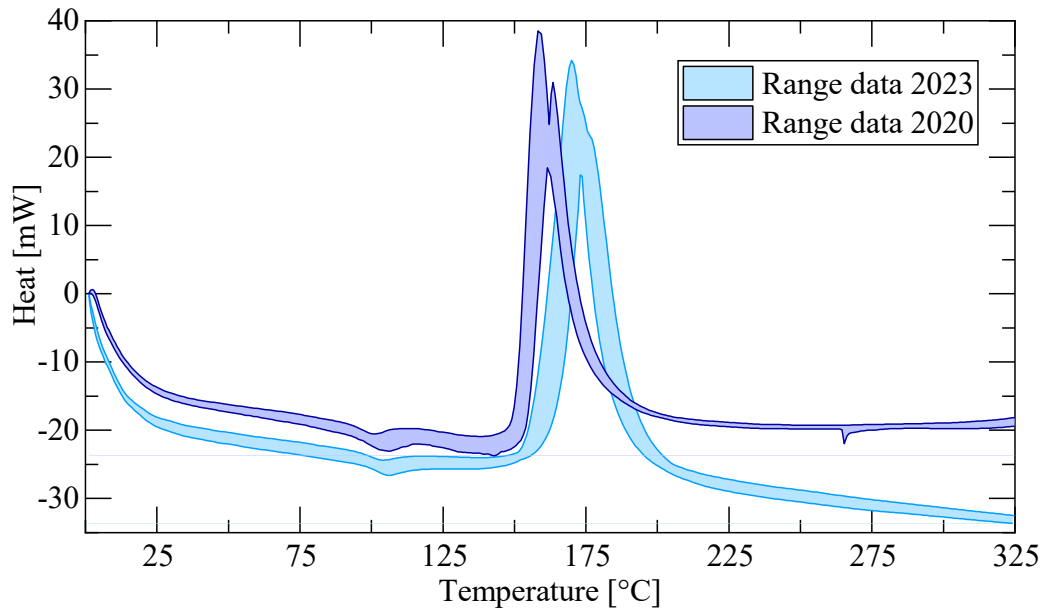


Fig. 3-8 Comparison between the range covered by all five tests performed at the heating rate 50 K/min in 2020 and 2023

All repetitions performed during the same test series seem to be very similar as the ranges are rather narrow. Both tests series display a relaxation enthalpy around 100 °C, and a linear development with almost the same incline preceding and following the relaxation enthalpy. However, the heat data measured in 2020 is overall higher than the heat recorded in 2023. Furthermore, the curing reaction happens around 150 °C for the data from 2020 and around 160 °C for the new data from 2023. The qualitative development of the peaks appears to be very similar, both in shape and height difference towards the baseline. Since the relevant data is the generated heat overall, it is irrelevant what the starting heat and the peak heat are in order to obtain the reaction rate. Only the difference between these two values is relevant. However, the peak is narrow for the old data and also returns to the baseline at a higher heat level. Therefore, the total heat released during the tests in 2020 is lower than that for the new tests. This does have an influence on the reaction rate. This difference also means that the pot life of the specimens from 2020 was probably already more progressed before the measurement than for the ones from 2023. This difference in the recorded heat signals lead to different average reaction rates, as can be seen in Fig. 3-9.

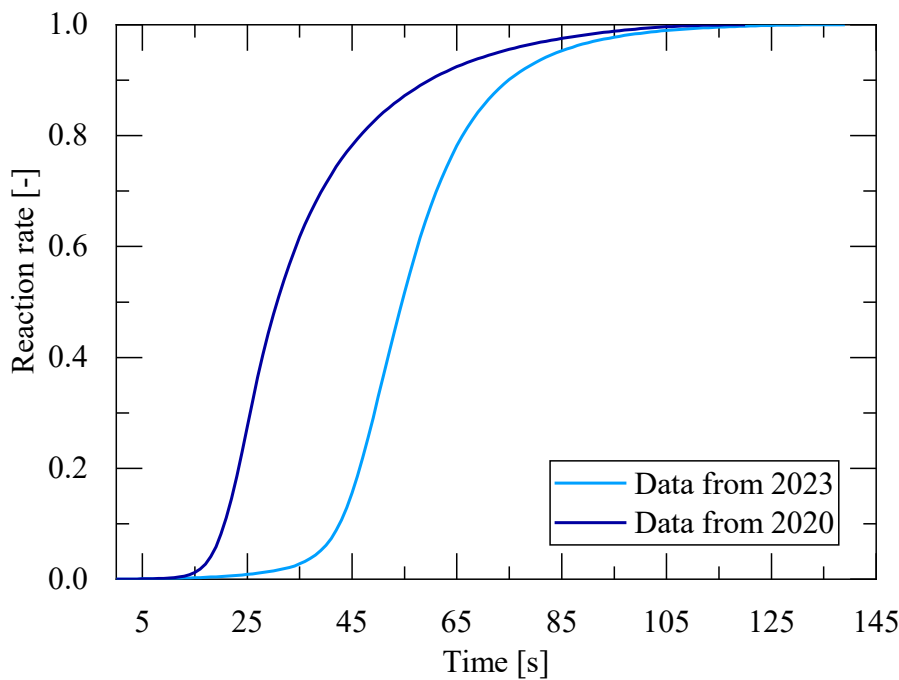


Fig. 3-9 Comparison between the reaction rates for the data from 2020 and newly obtained data from 2023 for the heating rate of 50 K/min

Evidently, the reaction rates for the same heating rate of 50 K/min looks quite different, with the fastest increase in the reaction rate starting around 15 s for the data from 2020 and around 40 s for the data from 2023. This delayed reaction rate is a direct consequence of the reaction happening later for the data from 2023, as shown in Fig. 3-8. The delay can be seen as well in the end of the curve, where the one from 2020 stops after 120 s, whereas the one from 2023 stops after 140 s. The incline of the linear ascent during the peak of the reaction is very similar in the range between 10 % and 70 % reaction rate, but is quite different before and after those values. Based on these results it is evident, that the batch can have a significant influence on the reaction rate. This could be related to different factors:

- Changes in the equipment over the years, due to a multitude of different materials being tested
- Different progression in the pot life of the tested material
- Chemical differences in two batches.

It is likely, that all the above aspects had an influence, although the second reason is probably most relevant, as mentioned in the considerations about Fig. 3-8. An additional evaluation was performed within this student thesis [S11] comparing the reaction rates and performing the fitting for the averages, but also limit cases. The results showed that the difference in the fitting result is smaller than the error between the fitting and the input data itself. This finding confirms the validity of the determination of only one set of Kamal parameters, as written in the process suggested. Despite answering a few open questions from the tests performed in 2020 with the next test series carried out in 2023,

several aspects still need to be better understood and optimized. The first aspect to be further varied is the material, as different batches, different materials or different pot life progressions could be tested together. Furthermore, tests with other comparable equipment could be interesting, as well as measurements with a hyper DSC, which can apply heating rates closer to the heating rates in the process. However, this machinery is not very common in industrial context. Moreover, different fitting approaches as well as a fitting with more than three fitting curves could be interesting. In order to perform this fitting, a new fitting tool should be developed, possibly including an automatic analysis of the curves starting from the import of the data from the DSC and following the suggested procedure. This could increase the efficiency of the process significantly.

3.2 Parameters for the rheological model

The content of this subsection has been previously published in similar form [K2].

The second set of parameters to be determined, are the parameters for the rheological model, presented in Section 2.2. To this purpose, squeeze flow tests are state of the art (Section 2.3), and were therefore, performed. Within this study, a suitable procedure for the performance of the tests and the analysis has been identified.

3.2.1 Procedure to obtain the viscosity parameters

Squeeze flow tests are the typical test method for the characterization of the rheological behavior of SMC, as described in Section 2.3. Many different setups are presented, with varying sensor arrangements. However, for the necessary experimental data for the fitting tool in 3DTimon, all the setups would be suitable, as the needed data are the force and the displacement, and consequently the deformation over time. The setup of the squeeze flow test bench, the specimen configuration, and the test matrix are shown in Fig. 3-10.

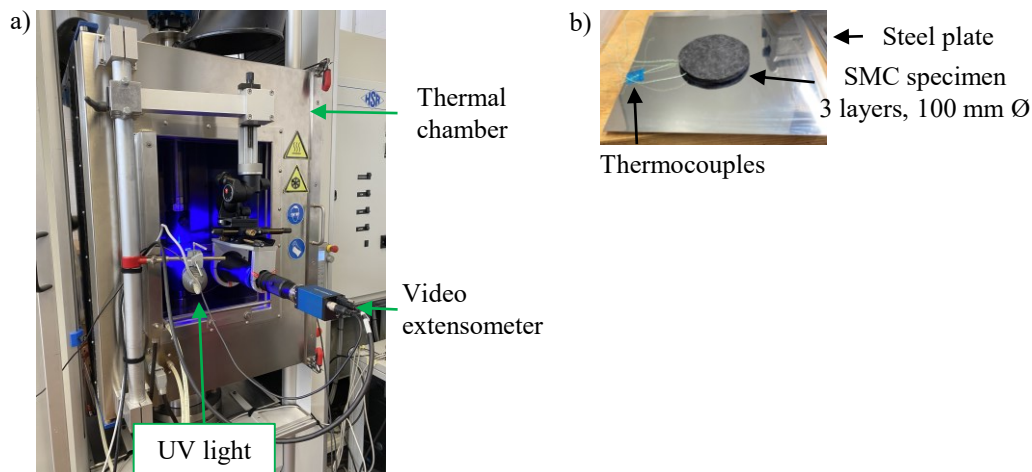


Fig. 3-10 Squeeze flow tests: a) setup in a universal testing machine for 250 kN equipped with parallel plates, thermal chamber and video extensometer; b) 3-layered SMC specimen with thermocouples and steel plate used at top and bottom.

The test setup consisted in two parallel plates fixed in a UTM from Hegewald & Peschke Inspect 250 for compression forces up to 250 kN. A video extensometer tracked the displacement of the plates, and controlled the constant closing speed. To test the specimens at specific temperatures a thermal chamber was used. The temperature was controlled with a temperature sensor in contact with the lower plate inside the chamber. The specimens, shown in Fig. 3-10b, consisted in three circular layers of SMC material with 100 mm in diameter. Furthermore, thermocouples were inserted between the layers, to record the curing reaction. For better handling of specimens between tests, and additional protection of the test setup from the resin, additional steel plates on top and bottom of the specimens were used. These plates were heated inside the thermal chamber and taken out for the specimen placement only right before the tests. The test matrix is shown in Tab. 3-3.

Tab. 3-3 Test parameters for the squeeze flow tests, including temperature, the amount of performed repetitions, and the closing speeds

	Temp. [°C]	Repetition	Closing speed [mm/min]		Temp. [°C]	Repetition	Closing speed [mm/min]
Low temperature	25±3	3	1	High temperature	120±3	1	1
			3				3
			10				10
	55±3	3	1		130±3	1	1
			3				3
			10				10
	85±3	3	1				
			3		3		
			10		10		

A tolerance of 3 °C was applied to the start temperatures. However, during the test, the temperature had to be kept constant. For the closing speed three different options were

considered, starting with 1 mm/min, 3 mm/min, and 10 mm/min. 10 mm/min was considered the maximum allowed closing speed for the adopted machine. For the low temperature tests, three repetitions were performed, since the flow behavior of the material is very variable. Unfortunately, for the high temperature tests, only one repetition was performed for each setting, because the impact on the machine from the expected high forces due to the material curing during the compression was deemed too high by the laboratory staff. In order to avoid suspected potential subsequent imprecision of the machine, only one test was performed. The exact test sequence is shown in Tab. 3-4. The closing speed of 10 mm/min is used for the example. For the other closing speeds, they have to be applied in step 5 instead of the 10 mm/min.

Tab. 3-4 Test sequence applied for the squeeze flow tests consisting of eight steps, including the involved action, as well as the set stop criterions

Step	Action	Stop criterion
1	Move $v = 50$ mm/min to $x = -10$ mm	$F = 2$ kN
2	Move $v = 2$ mm/min to 40 N, limit = 0 mm	$S \geq -6$ mm
3	Hold position 30 s	-
4	Tare $F = 0$ N	-
5	Move $v = 10$ mm/min to $x = 0.2$ mm	$F = 250$ kN
6	Hold force 30 s	-
7	Hold position 30 s	-
8	Move $v = 50$ mm/min to $x = -25$ mm	-

As can be seen in Tab. 3-4, at first the closing is quite fast from -25 mm to -10 mm, then slowing down to only 2 mm/min until the force rises to 40 N, signaling a first contact with the material. After the first contact, a waiting time of $t = 30$ s is applied, as it is standard in current SMC manufacturing, in order to give the material a bit of time to start heating up from room temperature. Especially for epoxy resins this waiting time is usually higher than 30 s to have the curing reaction cover a longer period of time and therefore, be less explosive. This improves surface and overall quality of SMC parts. The data necessary for the fitting tool provided with the simulation tool 3DTimon is subdivided into high and low temperature viscosity. The separation depends on whether the curing happens during the compression. For the fitting of the low temperature range, the data has to be represented as viscosity over shear rate, whereas for the high temperature range, the viscosity over time is necessary. For the calculation of the data, the equations (6) for the viscosity, and (7) for the shear rate presented in Section 2.3 were applied. Therefore, the necessary experimental data includes the displacement, the force, the plate distance, and therefore the height of the specimen over time, and the specimen radius. In the fitting tool only five curves for the low temperature and three curves for the high temperature can be input. The temperature and the closing speed have to be entered in the tool. Only a maximum of 208 entries are possible for each curve, and a relevant section has to be chosen.

3.2.2 Results and discussion

The data recorded by the machine is the force over the displacement. For better readability of the data, the negative displacement values from the UTM are transformed into positive values. To this purpose, the position $x = -10$ mm of the machine, where the compression started, was changed to $x = 0$ mm. In Fig. 3-11 the results are shown for the low temperature tests.

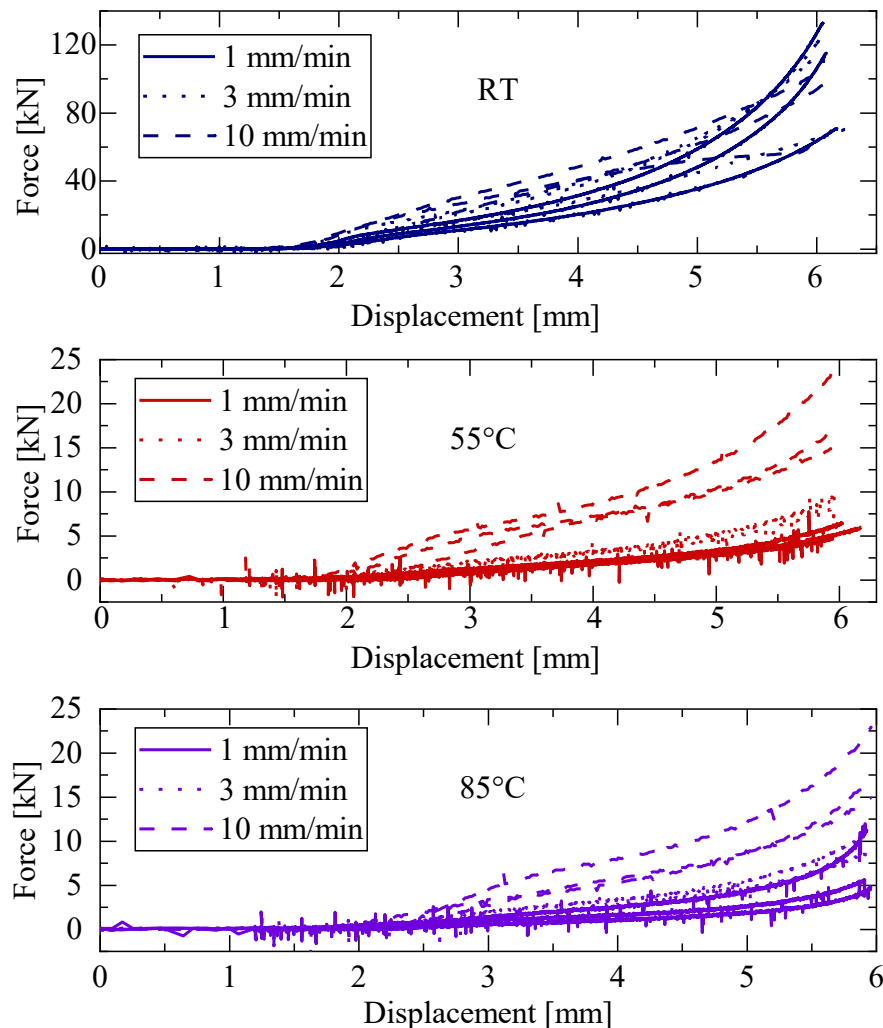


Fig. 3-11 Squeeze flow results displayed as force over displacement for the low temperature results of room temperature, 55 °C and 85 °C

As can be seen in Fig. 3-11 the curves have the same qualitative development, with an increase in the force at the first contact with the material. Despite the constant closing speed, a slight drop in the compression force can be observed, followed by an increase that is steeper than before the drop. This behavior is more pronounced the higher the closing speed is. This is due to the viscoelastic material behavior, which leads to the material resisting deformation more at the first contact, but then relaxes a little bit, before bracing itself. However, despite the qualitative comparability, the force is five times higher for RT compared to the other tests. This is due to the viscosity decreasing due to

the temperature in the tests at 55 °C and 85 °C. Furthermore, in all tests at RT the difference between the curves for the lower closing speeds of 1 mm/min and 3 mm/min and the higher one at 10 mm/min is not as pronounced. However, until the displacement of 5 mm the curves for 10 mm/min have the higher force signals, 1 mm/min the lowest and 3 mm/min is in the middle. Unfortunately, it could not be explained, why this tendency is inverted after 5 mm compression, leading to the force for 1 mm/min being the highest. However, the initial subdivision reflects the results in the tests for the other temperatures. This behavior is due to the material resisting the deformation. The faster it shall be deformed, the higher the resistance is. In general the curves for the same settings are very similar, but some differences can be observed nonetheless. For example among the curves for RT and 10 mm/min closing speed, and 85 °C and 10 mm/min closing speed, one curve each has a different shape than the others, which can be due to many reasons relying in the high variability of the raw material, like fiber content, but also the curing progression before the testing. Especially the variability in the thickness can be seen, as the force increase starts at different displacements. Moreover, the compression was stopped manually in many cases at a thickness of 2 mm of the SMC, which leads to varying curve lengths. The exact values are summarized below in direct comparison to the high temperature tests in Tab. 3-5.

The specimens for the low temperature viscosity did not or not fully cure during the test. Therefore, the material flows to the sides until the compression stops. An exemplary partially cured specimen obtained in a test at 85 °C is shown in Fig. 3-12 compared to the initial charge.

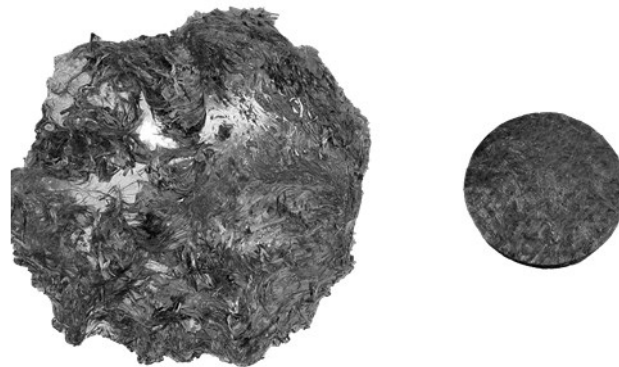


Fig. 3-12 Exemplary specimen for a test at 85 °C on the left compared to the size of a charge before the test on the right: the specimen is partially cured and shows long and uneven flow paths

The specimen has tripled its size during the test, with the material flowing until the edge of the compression plates. The material is partially cured, which can be seen by some areas of the surface reflecting the light. However, most of the specimens remained uncured, as the temperature and the exposure time combination was not sufficient for it to cure. Furthermore, the material configuration looks very inhomogeneous in the tested specimen compared to the specimen before the compression, which confirms the complex flow state. Interestingly, the reflecting areas have a smooth surface, which was in

contact with the compression plates, while the material around them is thinner, suggesting that due to the viscosity, the material flew a bit further once the compression had terminated. In some specimens a little bit of resin and fiber separation happened, with pure resin spots appearing next to the specimen on the steel plates, which confirms the reduction in viscosity of the overall compound and of the resin with increasing temperature.

For the high temperature curves, the results for the force over the displacement can be seen in Fig. 3-13.

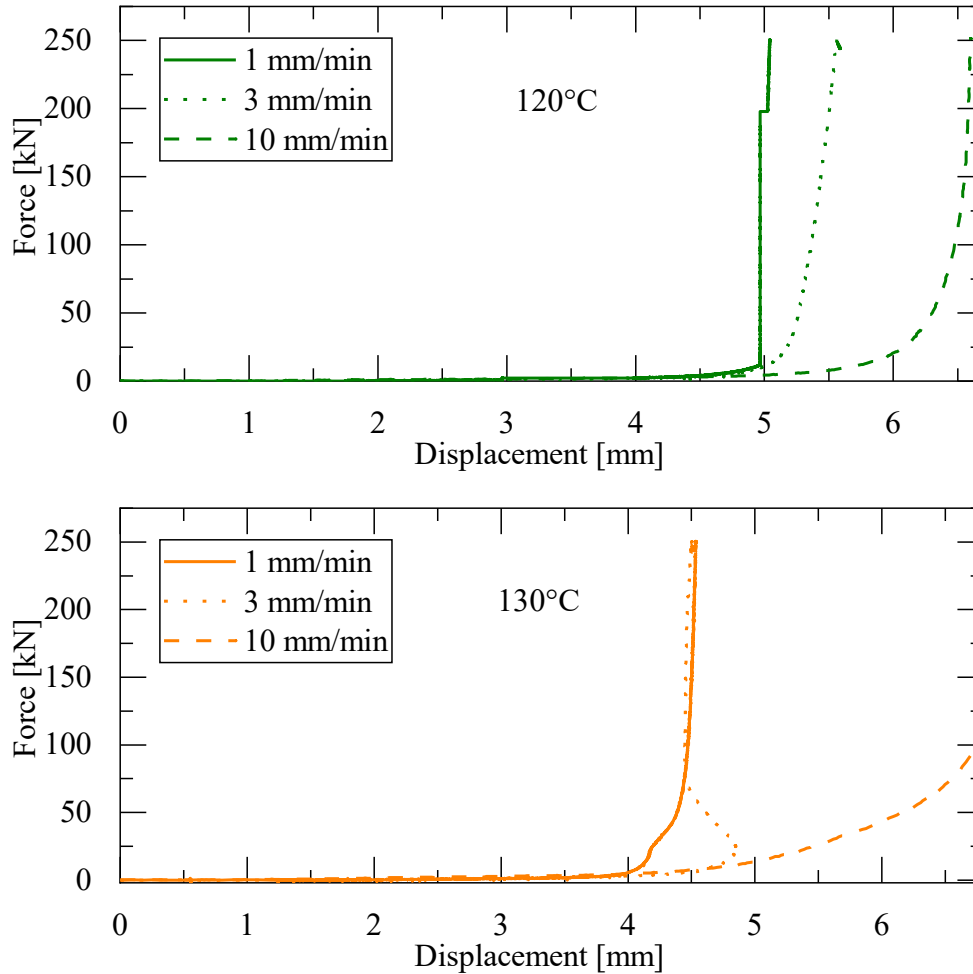


Fig. 3-13 Squeeze flow results displayed as force over displacement for the high temperature results of 120 °C and 130 °C

As can be seen in Fig. 3-13 for almost all tests the stop criterion of the maximum force of 250 kN was reached. The steep force increase is due to the material being already cured. For 120 °C this happens around 5 mm displacement for 1 mm/min and 3 mm/min, and only slightly later around 6.5 mm for the highest closing speed of 10 mm/min. In the last case, the curing happened at the end of the compression. For 130 °C the curing happens a bit earlier around 4.5 mm displacement. This complies with the resin curing faster at a higher temperature. The third curve, tested with 10 mm/min closing speed, on

the other hand, only shows the start of the curing, as at 6.75 mm the signal has already reached 100 kN. These curves follow the same qualitative behavior of the previous curves before the curing, with the force increasing after the contact with the material, but then dropping slightly, before increasing again, due to the viscoelastic material properties. The 3 mm/min curve at 130 °C displays an unusual development, with the displacement apparently being reversed. This behavior is unusual, but it could be due to a slight movement of the compression plate on the side of the video extensometer, leading to the measurement stripes to be closer together for a very brief amount of time, before the plate set back to the usual parallel position. This did not happen during any of the other tests, but in subsequent tests with the parallel plates this behavior could also be observed. For future tests, an additional measurement of the parallelism of the plates should be added. Unfortunately, only one repetition per setting was possible due to concerns about the impact of the tests on the machinery. Therefore, the scatter of the results for the high temperature tests could not be determined.

The high temperature tests aim at testing the material during the curing, in order to assess the viscosity with a varying curing degree. Therefore, all specimens obtained from the high temperature tests were fully cured and deformed only very little, as can be seen in Fig. 3-14.

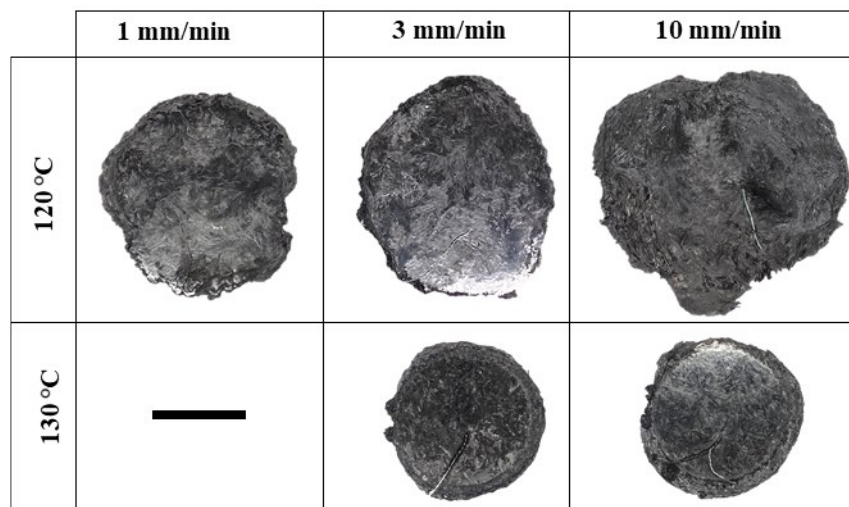


Fig. 3-14 Specimens that resulted from the squeeze flow tests performed at 120 °C on the top and 130 °C on the bottom for each compression speed¹

In the specimens for 130 °C on the bottom of Fig. 3-14, the circle of the initial SMC charge is still visible. Therefore, the overall deformation is minimal. As displayed in the diagrams, the material was still compressed about 3 mm, but this mainly caused a change in thickness, as the uncured SMC sheets contain a high amount of voids [138–140]. The

¹ One specimen is missing, because it broke during its removal from the steel plate. This is due to the release agent in the SMC not coming to the surface evenly, which sometimes made it difficult to separate the specimen from the underlying surface.

void content can span from 1.5 % to 5.5 % for a fiber content of 29 wt% to 23 % for 50 wt% fiber content [139]. The material in this study contains 52 wt% fibers, being at the upper end of the spectrum. For 120 °C the deformation is definitely higher, especially for the specimen tested at 10 mm/min. As seen in the diagram, that test did only cure once the compression was completed. For all specimens the surface is more even than for the previous tests at low temperatures, which means the specimens have a rather constant thickness distribution. This is due to the material being cured once the compression was completed and therefore, not being able to flow to the sides after the compression, as had happened before.

The key values from the tests, such as maximum force, the start temperature of each test and start of compression related to the displacement are summarized in Tab. 3-5.

Tab. 3-5 Key values for the performed squeeze flow tests, including the temperature of each test, the maximum force and the compression start, which corresponds to the first contact with the SMC of the upper compression plate (force reaches 1 kN). The notation is as follows: “Temperature [-;°C]_closing speed [mm/min]”.

		Temp. [°C]	Max force [kN]	Comp. start [mm]			Temp. [°C]	Max force [kN]	Comp. start [mm]	
Low temperature	RT_1	23	115.12	1.74	High temperature	120_1	120	250.55	2.95	
		23	132.83	1.65		120_3	120	250.55	2.55	
		23	70.73	1.71		120_10	120	251.45	1.92	
	RT_3	23	123.82	1.71		130_1	130	250.46	2.84	
		23	114.96	1.61		130_3	130	250.43	2.38	
		23	71.88	2.01		130_10	130	94.33	1.58	
	RT_10	23	105.47	1.57						
		23	66.40	1.44						
		23	99.68	1.89						
	55_1	57	7.78	2.62						
		58	6.03	2.95						
		58	5.61	3.12						
		55_3	58	8.25	2.48					
			55	9.69	2.25					
			58	9.69	2.39					
	55_10	58	14.91	2.44						
		58	16.72	2.10						
		58	23.57	1.96						
	85_1	85	5.64	2.62						
		85	4.85	3.62						
		85	12.01	2.70						
85_3	87	11.06	2.43							
	85	8.60	3.00							
	85	10.93	2.43							
85_10	85	16.72	2.12							
	87	22.97	2.39							
	87	14.91	2.54							

As can be seen in Tab. 3-5, the temperature tolerance for the tests could be satisfied well, with a maximum deviation of +3 °C for 55 °C and +2 °C for 85 °C, but with most tests having the exact desired temperature. The measurement was performed by the thermal chamber with a thermal detector placed underneath the lower compression plate. In order for the setup to have the desired temperature, an overshooting was necessary before opening the thermal chamber to place the specimen inside. This is where the variation in the temperature comes from. For the low temperatures, as also mentioned in the diagrams, the force signal for RT is the highest for all three closing speeds, reaching a peak at 132.83 kN. The compression start is also similar, with a minimum of 1.57 mm and a maximum of 2.01 mm, which corresponds to a difference of 0.44 mm in the overall thickness of each specimen. However, this looks quite different for the other two low temperature settings. For 55 °C and 85 °C, the compression start seems to happen later the higher the compression speed is. This is due to the compression start being set as the first time the force signal reaches 1 kN. The faster the compression is, the higher the delay in the signal will be. However, the differences are in the range of fractions of seconds. The overall difference between the minimum and maximum displacement for the compression start for 55 °C and 85 °C is 1.16 mm and 1.50 mm respectively. This variation is also due to the variation in thickness of the single sheets that has been addressed in Section 2.1. The force signal also behaves in a similar manner for 55 °C and 85 °C being lower for 1 mm/min, intermediate for 3 mm/min and the higher for 10 mm/min, but never exceeding 25 kN. For the high temperature, five curves out of six reached the stop criterion of maximum force 250 kN. Only the last test at 130 °C could be completed before the maximum force was reached. This is due to the fast closing speed, allowing enough time for the material to flow during the compression. This behavior should also be seen for 120 °C and 10 mm/min closing speed, but as previously seen in Fig. 3-13 the compression continued a few seconds longer than for the other tests. If it would have been interrupted at the same position as the test at 130 °C, the maximum force would also not have been reached. The variation of the compression start is in the same digits as for the low temperature tests, being 1.03 mm for 120 °C and 1.26 mm for 130 °C. Considering all charges, the maximum difference between all values is 2.18 mm, which is quite considerable, as the overall average thickness of the charge was only 7.71 mm. However, as previously mentioned, the difference for each temperature is smaller, and the response of the signal linked to the compression speed also seems to have an influence on the starting point, leading the tests with higher compression speed to display an overall lower thickness and vice versa.

3.2.2.1 Data preparation for the fitting

All curves were analyzed with the equations (6) and (7) presented in Section 2.3 to comply with the inputs necessary for the fitting tool. Once analyzed, the relevant section of the curve is selected, as shown in Fig. 3-15.

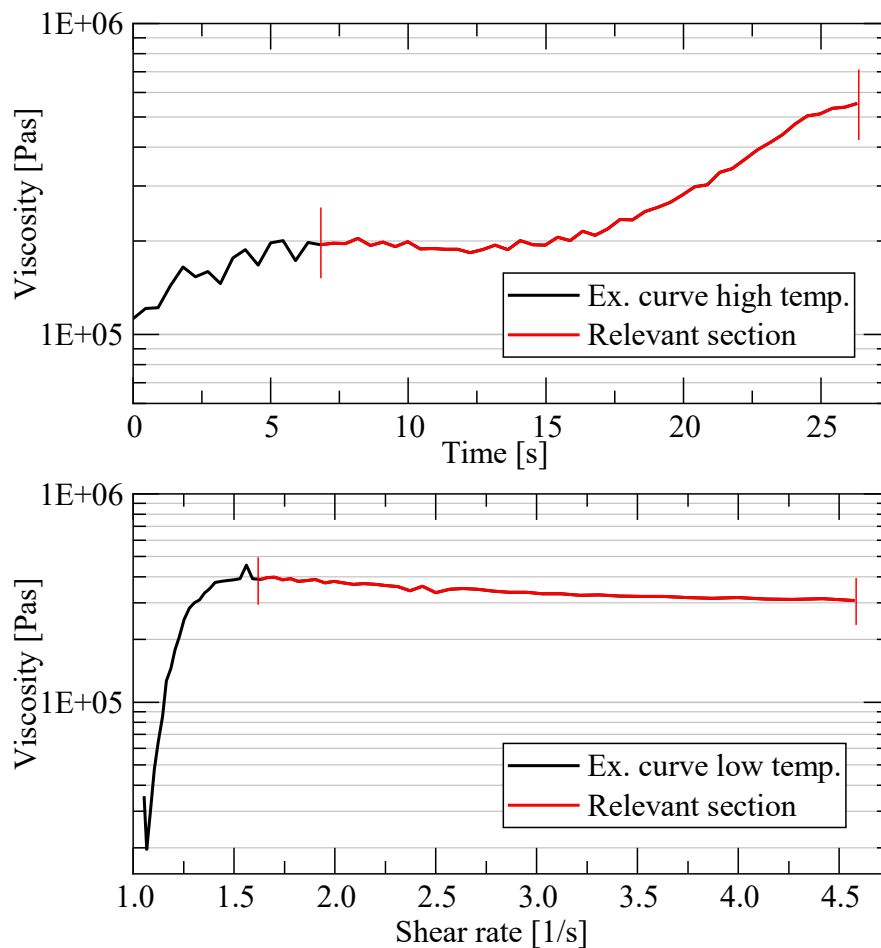


Fig. 3-15 Exemplary selection of the relevant section for the fitting for high temperature fitting (top) and low temperature fitting (bottom)

It can be observed that after the more or less steep increase at the beginning of the compression, the viscosity shows a linear descent. For the high temperature, once the curing reaction happens, the viscosity starts increasing again, due the dependency between reaction rate and temperature. For the low temperature viscosity, the relevant part of the curve is the linear decrease of the viscosity before the curing. For the closing speed 1 mm/min, the results are excluded from further considerations, as the force signal is much noisier than the others, and the relevant sections do not display any reduction of the viscosity in neither the low nor the high temperature tests. This is due to the low speed setting, which is far from real SMC compression conditions of around 1-3 mm/s. Therefore, the tests at 1 mm/min were not considered further for the fitting.

The results of the analysis only showing the relevant data sections can be seen in Fig. 3-16.

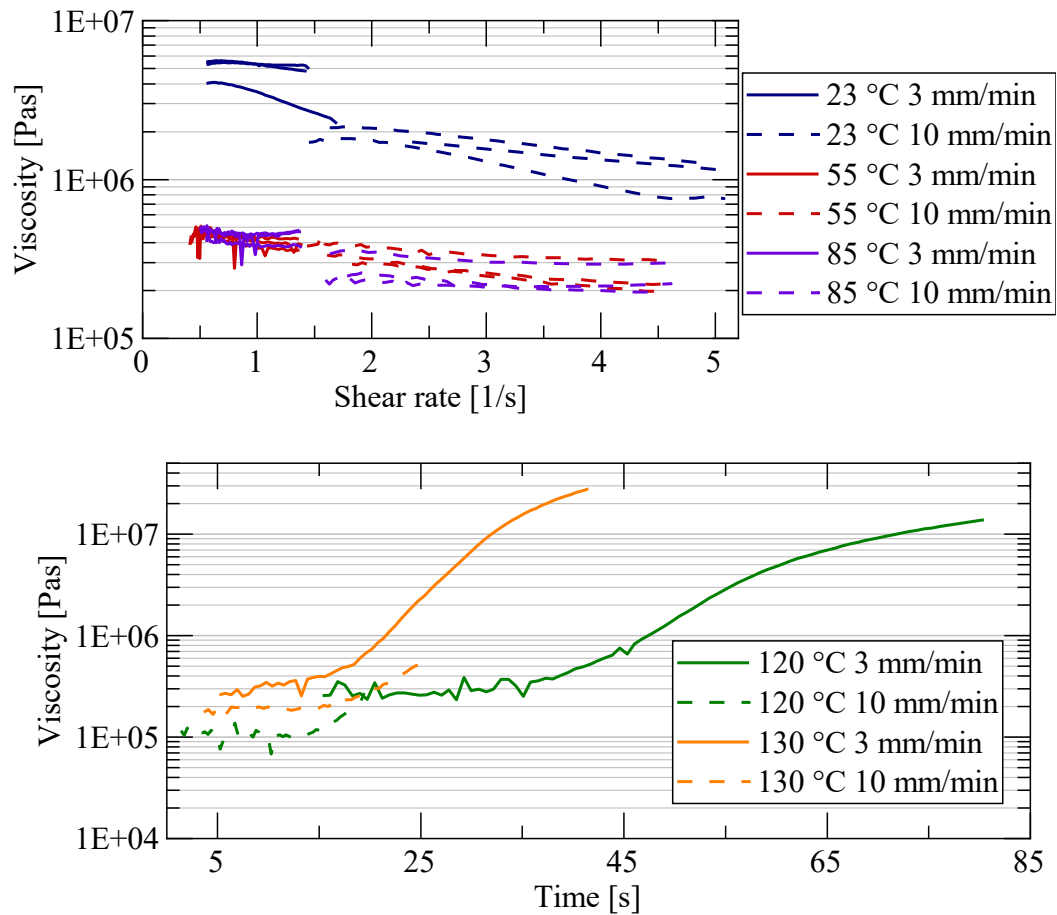


Fig. 3-16 Relevant range for the fitting of the viscosity parameters for all tested curves with low temperature results (top) and high temperature results (bottom)

As can be seen in Fig. 3-16, the relevant curve sections resulting for the low temperature and 3 mm/min cover a small section of the shear rate, whereas for 10 mm/min, the curve is longer, but includes very few data points, sometimes only 12 or 15. The overall viscosity values seem to coincide for 3 mm/min for 55 °C and 85 °C, and the results for 10 mm/min are only slightly higher for 55 °C compared to 85 °C. For the high temperature results at 3 mm/min closing speed, the decrease in viscosity before the steep increase due to the curing is depicted in 27 data points for both 120 °C and 130 °C, as the curing progressed very fast. For 10 mm/min the curves have a relevant section that is considerably longer for the low temperature, and will therefore, lead to better fitting results. Nevertheless, higher closing speeds of 60 mm/min or higher, would have been very interesting, as it would correspond to the lower limit for typical SMC processing of 1 mm/s. However, this was not included in the capabilities of the adopted UTM at the time.

3.2.2.2 Data fitting

Given the temperature tolerance of 3 °C, it was decided not to calculate and consider averages for the curves with multiple results. Furthermore, in the fitting software, the

exact testing temperature has to be entered, which makes it possible to consider all tested curves. For both the low temperature fitting and for the high temperature fitting up to five curves can be considered. The fitting was performed by entering the intermediate curves for each temperature and closing speed. However, the result of the fitting is not displayed in the tool for the low temperature viscosity, which does not allow a further manual adjustment. Furthermore, the tool only allows to enter 208 data points. Therefore, if the data exceeds this value, it has to be reduced accordingly. A further adjustment of the parameters will be performed with the subsequent calibration steps presented in Section 3.3.

3.2.2.3 Identified procedure for the viscosity parameters

Based on the findings from this study, a promising method for the determination of the rheological parameters could be identified, as summarized in Fig. 3-17.

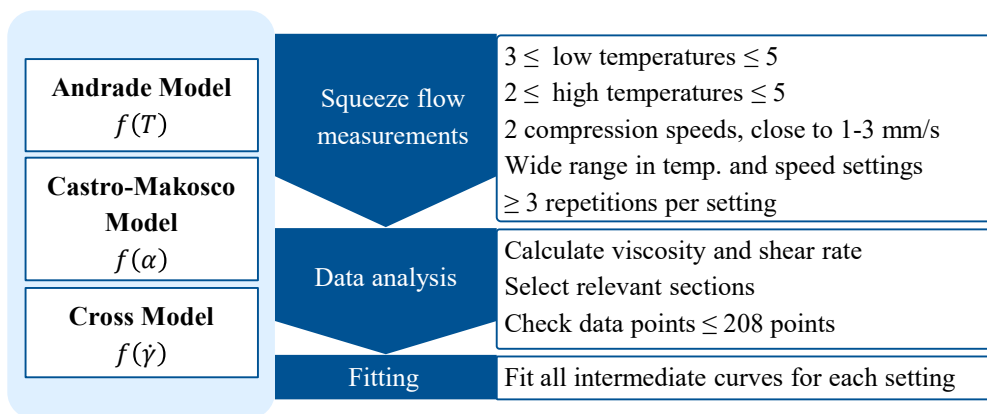


Fig. 3-17 Schematic representation of the recommended procedure for the determination of the viscosity parameters for SMC, displaying a dependence of the viscosity from the temperature, the degree of curing and the shear rate.

In the first step, two closing speeds shall be chosen. These should be as close to the real process as possible, so for a UTM one of the choices should be the highest allowed closing speed. The second one can be chosen, but the bigger the difference to the first choice, the bigger the difference between the resulting curves and the more the influence of the closing speed can be determined. Therefore, the suggestion is to select a closing speed equivalent to or lower than half of the first one. This means that for a closing speed of 10 mm/min, the second one should be equal to or lower than 5 mm/min. Three temperatures should be chosen for the temperature region before the curing happens. The same principle applies as for the closing speed, that the covered range should be as big as possible. Therefore, the lowest temperature shall be room temperature, which SMC has when it is placed inside the mold at the beginning of the process. The highest temperature for the low temperature region shall be about 40 °C below the indicated processing temperature for the material. The third temperature shall be the intermediate value between the highest and the lowest. For the high temperature tests, the chosen temperatures should not be too high, in order to prevent curing before the compression

started. Therefore, one of the temperatures should be the lower indicated processing temperature. The other temperature can be chosen between at least 10 °C lower than the lower limit, and the upper limit. However, the relevant part of the curve becomes smaller the higher the temperature is, as the material cures faster. In order to capture the variability of the material, at least three repetitions for each setting shall be performed.

After the selection of the parameters follows the analysis, as presented above, by calculating the viscosity and the shear rate, prepare the diagrams, choose the intermediate curves, chose the relevant section, and perform the fitting.

Given the high variability of the material, it could be beneficial to increase the repetitions to five. This would also account for variations in the specimen preparation, environmental differences, like the room temperature. It could also be beneficial to know the exact weight of the specimens, in order to draw conclusions about the influence of the weight on the force signal. Furthermore, in SMC processing the material is typically heated by the mold, which is heated by the press. Using heated plates for the tests could be beneficial to be closer to the actual SMC process. However, the influence on the results of the different heating methods is not known.

3.2.3 Conclusion, further investigations, next steps

Within this subsection, a method was developed to determine the parameters for the viscosity model adopted in SMC process simulation. The procedure complies with the requirements set for the overall procedure, as it is flexibly applicable to any other viscosity model with the same functional dependency of the viscosity that is applied in this model. Furthermore, the test setup is very simple, and consists of parts typically present at the site of SMC part manufacturers. The inclusion of the viscosity has only been partially applied, as the influence of the limiting curves was determined, but only a total of three curves was tested. However, according to the presented fitting results, the variability from this test sequence was negligible. It is not clear, whether this applies to specific conditions of the test or of the material and shall be further investigated. In order to ensure a wider coverage of the possible range of the relevant characteristics, it could be advisable to include five tests in the tested sequences. Especially for the high temperatures the repetitions should be more than in this study. Furthermore, the procedure is independent from a specific geometry, and easily applicable within a short time span.

In a subsequent testing sequence in [S7], the tests have been repeated considering the same temperatures, the same setup, but the closing speeds of 10 mm/min and 60 mm/min, as in 2023 the adopted UTM could be run with that closing speed. The latter corresponds to the industrially applied closing speed of 1 mm/s. A comparison of the new results and the previous data is shown in Fig. 3-18. As can be seen in both diagrams, the start of the compression happens at a very comparable time in both test series. The qualitative development of the curves at low temperature also follow the qualitative development described for the results of 2020, with an increase in force, followed by a

steady reduction, followed by a more significant increase in force, giving the curve a very undulated appearance. However, the force signal is higher in the tests performed in 2023. This is certainly influenced by the difference in material batches and also the moment within the pot life the material has been tested.

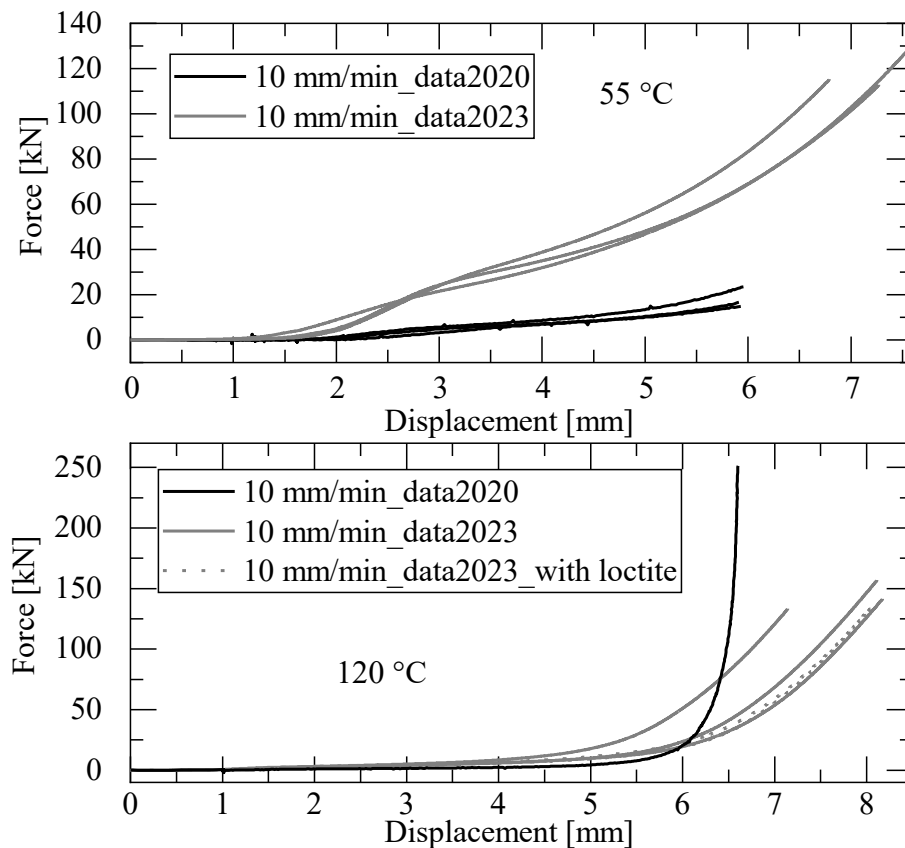


Fig. 3-18 Comparison of the results obtained from the first squeeze flow tests from 2020 and the new tests from 2023: comparison of the results obtained for 10 mm/min compression speed at 55 °C (top) and 120 °C (bottom).

For the tests at 55 °C, the difference is very high already at 3 mm displacement, which could be due to the material possibly being in contact with the heat for a longer period of time. The preparation of the test took a few seconds longer during this test series, before even starting the test sequence. This certainly influences the curing of the material, which leads to an increase in viscosity and therefore, a higher force signal as a result. For the tests at 120 °C on the other hand, although at first the force increases faster, the difference is less significant. Moreover, in the test series from 2020 the specimen was fully cured during the compression, leading to the increase of the force signal to the maximum value of 250 kN and not changing the displacement value any further. In the more recent test series from 2023 it seems like none of the specimens already fully cured during the compression, as the force signal is still rising once the compression is interrupted. Based on the two comparisons, it seems like the specimens for 50 °C were further along in their pot life compared to the previously tested ones, whereas for 120 °C it is the contrary. This is probably due to the test sequence, as in the series from 2023 the

tests were performed with a few days in between. However, most specimens were outside the freezer during the whole test series, leading to a significant difference in the progression in the pot life. Certainly the storage temperature is very significant for SMC material and shall be investigated more closely in the future. On a marginal note, the use of Loctite Frekote 770-NC on the steel plates as additional release agent to the internal release agent of the SMC, does not seem to have an influence on the outcome of the test. Meanwhile, it facilitates the cleaning significantly.

A direct comparison between the results at 10 mm/min and 60 mm/min for both temperatures of 55 °C and 120 °C is shown in Fig. 3-19.

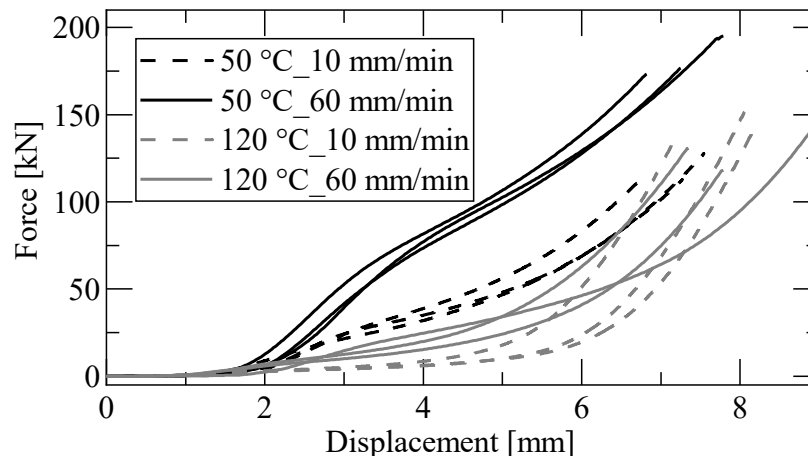


Fig. 3-19 Comparison of the results for the test series of 2023 for 10 mm/min and 60 mm/min compression speed for both 55 °C and 120 °C tests.

As seen for the test series from 2020, also for the tests of 2023, for both temperatures the higher compression speed leads to a higher force signal. However, the lower temperature reaches a higher force, as the viscosity is lower. For 120 °C the material is close to curing or within the curing process, which first decreases the viscosity, optimizing the flow of the material, which is the goal in SMC processing. None of the curves shows complete curing during the compression. Overall, for this test series of 2023 and this comparison, it can be concluded, that Loctite does not change the results, the qualitative development of the force over displacement curves does not change, the pot life moment of the SMC is very important, meaning storage is important, and for higher vicinity to typical SMC processes, 60 mm/min should be a standard compression speed for squeeze flow tests, as the goal of the simulation is to depict it as well as possible.

Based on the findings presented in this section about squeeze flow testing, closer consideration of the influence of the weight of the specimens would be interesting, as well as the difference between different heat sources such as the thermal chamber, and heating cartridges inside the plates. Furthermore, investigations could be performed about the influence on the flow of release agents or different mold temperatures. The latter could be performed by heating the metal plates to different temperatures before putting them into the thermal chamber. This would allow for a direct comparison of the impact

of the surface temperature. In order to assess the applicability of the presented method to other materials, it would be necessary to test the approach. As presented in Section 2.2 however, the flow behavior of a resin type is broadly very similar and, typically not influenced significantly by potential additives and filler.

3.3 Calibration of the material card

Once the parameters are fitted with the squeeze flow test data, all necessary data to describe the flow can be written in a material card, and simulations can be run. However, it is state of the art to calibrate those parameters by producing a part (Section 2.3), simulating the process and afterwards adapting the parameters until the simulation result is as desired. The issue is, that the more complex a part is, the lower is the probability that the material will behave the same way with another geometry. Furthermore, this process does not comply with the requirements set for the procedure at the beginning of this chapter of simplicity, flexibility, and geometrical independence. To this goal, the calibration has to be performed without using a tool for an SMC part. In order to identify a suitable calibration process, the investigation was performed in two consecutive steps: in-plane flow for simulations of parts with predominantly in-plane flow, and out-of-plane flow for more complex parts. To improve the simulation outcome by perfecting the material parameters, sensitivity analyses are performed.

3.3.1 In-plane flow calibration

The content of this subsection has been published in similar form [141].

This chapter describes the procedure for the in-plane flow calibration, consisting in simulating the squeeze flow process, comparing the result to the experimental data, and consequently, adapting the parameters. The resulting material card is more suitable to accurately represent the materials behavior for in-plane flow, and can therefore, be used for geometries where in-plane flow is predominant.

3.3.1.1 Simulation settings

The squeeze flow tests described in Subsection 3.2.1 were implemented into the simulation software 3DTimon, as can be seen in Fig. 3-20.

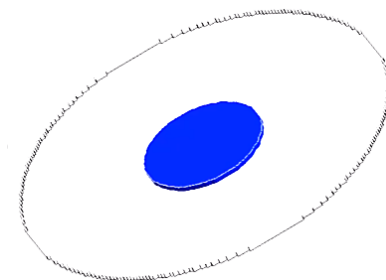


Fig. 3-20 Simulation of squeeze flow tests, with circular charge of 100 mm in diameter and 8.4 mm thickness in the center of a circular mold.

The charge consists of a circular shape of \varnothing 100 mm within a circular mold. This adaptation allowed to save computation time, as less elements were involved, but still the necessary cavity surface was present. The size of the cavity was based on the deformations from the actual test, where the specimens did not reach the edges of the compression plates for the high temperature tests. The chosen tests to be replicated numerically were 130 °C, with 10 mm/min closing speed. The highest tested temperature and closing speed were chosen, as they represent the closest values to a typical SMC compression process. All simulation settings regarding the compression settings, the charge and the simulation settings are summarized in Tab. 3-6.

Tab. 3-6 Simulation settings with the reference value in reality, with focus on the compression settings, the charge and the simulation setting.

	Unit	Simulation	Reality
Compression settings			
Temp upper mold	°C	130	130
Temp lower mold	°C	130	130
Compression speed	mm/s	1.667	1.667
Clamping force	ton	25	25
Waiting time	s	40	~40
Charge			
Material		CARBKID	CARBKID
Volume	mm ³	65100.5	65971.5
Thickness	mm	8.4	~8.4
Fiber orientation		2D random	2D random
Temperature	°C	25	~25
Simulation settings			
Mesh	x-y-z	2-2-0.2	-
Steps		Flow	-
Mesh method		Euler	-

The compression process is split into two steps, as before the compression starts, several seconds pass in which the material has time to heat up. Therefore, the first step is a waiting time of 40 s, with no displacement and no clamping force. In the second step, the compression happens. The closing speed is the same as in the real tests of 0.1667 mm/s or 10 mm/min with the clamping force of 25 tons, corresponding to 250 kN, the maximum compression force set for the UTM. The mold temperatures for the upper and lower half is set to 130 °C. This corresponds to the temperature measured in the thermal chamber during the test, from the beginning to the end. The charge material is CARBKID PGK5250, the same as throughout this research. The adopted material card comes from the fitting of the Kamal parameters and the viscosity parameters in the previous chapters. The charge height was set to 8.4 mm, resulting from considering the charge as three layers of SMC with the average value for the sheet thickness identified during variability investigations within [S20]. The resulting volume for these measurements is 65971.5 mm³. In the simulation the selected charge is a bit smaller, as the size

of the mesh in x- and y-directions does not allow a more precise selection. The temperature of the charge at the beginning of the test is room temperature, which was set as 25 °C in the simulation, the value it approximately corresponded to in reality. The fiber orientation is the same as for typical SMC being 2D random. The Euler method was adopted for the simulations and the mesh was set to 2, 2, and 0.2 mm in x-, y-, and z-direction respectively. From the four available simulation steps to be performed in 3DTimon, only the first one of “Flow” was considered in this evaluation. In order to improve the result, the parameters of the curing kinetics and the rheological model shall be calibrated. To identify the parameters to be adapted for a higher accuracy of the simulation result a sensitivity analysis was conducted by separately changing each viscosity and Kamal parameter to its upper and lower limit. The simulation result at 130°C and 10 mm/min closing speed was selected as reference. The values considered for the analysis are summarized in the following subsection.

3.3.1.2 Sensitivity analysis and calibration for squeeze flow

The curves resulting for the chosen settings with the parameters obtained from the fitting of the intermediate values performed in Subsection 3.2.2 can be seen in Fig. 3-21.

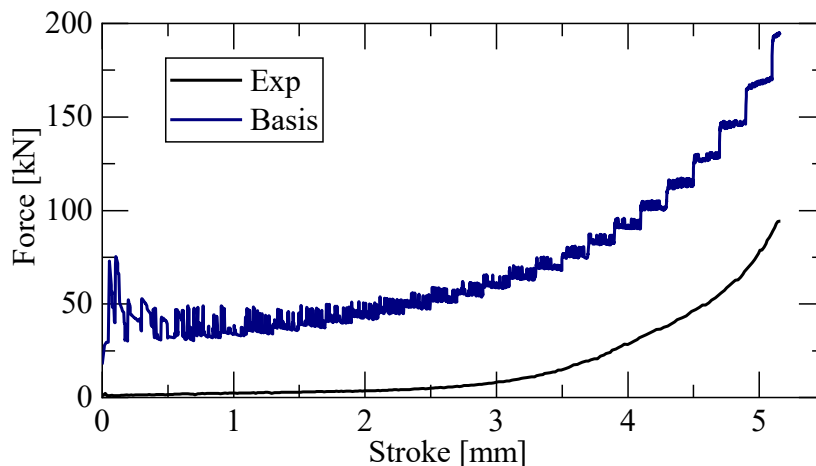


Fig. 3-21 Simulation result for the force over displacement compared to experimental result after fitting the squeeze flow results for the low and high temperature viscosity models for the test performed at 130 °C and 10 mm/min.

The numerical result shows some deviation from the experimental result throughout the progression of the displacement, with the force signal always exceeding the empirical data. The initial force seen in the simulation does not start at 0 kN due to the clamping force. The signal also shows an oscillatory response, which could not be fully explained. Nevertheless, the force increases linearly to approximately 2.5 mm for both signals, but the incline is steeper for the simulation. Once the curing of the material starts, the force increases more significantly in both simulation and reality. However, once again the simulation signal increases faster. Moreover, the numerical force signal shows a stepped result, which is due to the Euler method and the element subdivision in z-direction. However, it was tested that a further reduction of the element size in z-direction does

not reduce the stepping considerably, while noticeably increasing the computation time. Nonetheless, the qualitative development of the curve for 130°C is very similar for both experiment and simulation.

The sensitivity analysis is performed by setting each parameter separately to its upper and lower limits as stated within the fitting tool provided with 3DTimon (the limits are summarized in Tab. 3-7). Fig. 3-22 shows the influence of the curing kinetic parameters m and A_2 on the force development compared to the numerical result (all other results are shown in the appendix b).

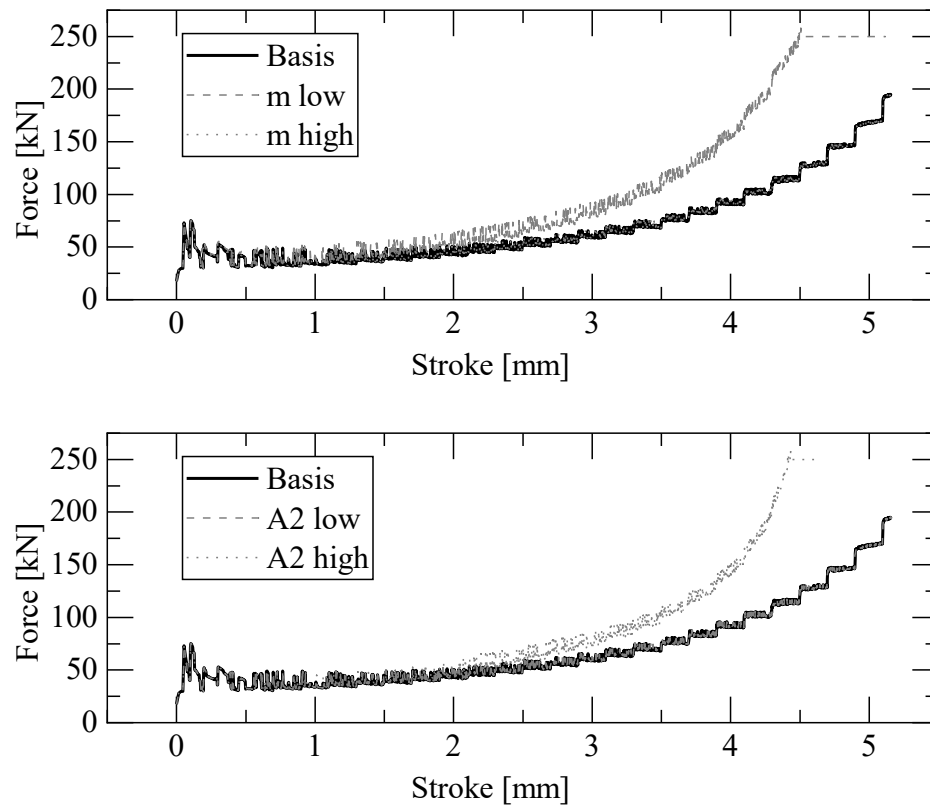


Fig. 3-22 Sensitivity analysis result with upper and lower limit compared to the numerical reference for the parameters m (top) and A_2 (bottom).

Based on this example, in order to increase the resulting compression force m has to be decreased, whereas A_2 has to be increased. For a decrease in the force. The procedure was applied to all parameters of the curing kinetics and rheological model. The results of the sensitivity analysis are summarized in Tab. 3-7, stating the influence each parameter change has on the force signal. The upper and lower limits of each parameter are taken from the fitting tool provided by 3DTimon. As can be seen in Tab. 3-7, the variation if most parameters did not or only slightly change the result. The parameters with the biggest influence are the kinetic exponent m , and the material constant E_2 for the Kamal parameters, and n , τ , a , and b for the rheological models, where the force changes significantly, sometimes getting to its maximum, and sometimes decreasing to 0.

Tab. 3-7 Result for the sensitivity analysis performed for the squeeze flow tests at 130 °C, showing the effect the upper and lower limit adopted have on the resulting force signal.

	Parameter	Limit Low	Force	Limit high	Force	
Curing kinetics	m	1.00E+02	↑↑	2.00E+03	↓	↑↑ increase
	n	1.00E+02	=	2.00E+03	=	↓ minimal decrease
	A1	1.00E-02	=	1.00E+13	=	= equal
	A2	3.00E+09	=	1.00E+11	↑↑	↓↓ decrease
	E1	1.00E-02	SS	1.00E+13	=	SS short shot
	E2	6.00E+06	↑↑	9.00E+06	↓	e error
Viscosity	n	1.00E+00	↓↓	9.99E+02	↑↑	
	τ	1.00E-07	↓↓	1.00E+13	↑↑	
	a	1.00E-07	↓↓	1.00E+13	↑↑	
	b	1.00E+00	↓↓	1.00E+13	e	
	D	1,20E-04	=	1,20E+04	=	
	E	1,00E-04	=	1,00E+04	=	

Based on these findings, the simulation result was calibrated by identifying the parameters with most promising changes based on the sensitivity analysis being a , $n_{viscosity}$, b and τ . For the overall calibration approach, in a first step all afore mentioned suitable parameters shall be changed and the simulation shall be repeated with the new parameter. The result of the force over displacement shall be compared between the old and new parameter and the experimental result. Two aspects are of interest in the comparison, being one the linear development of the force signal during the first half of the compression, and then the exponential increase in the second half. In a quantitative comparison of the result, the issue is that each simulation displays a significant increase in the compression force at the beginning of the compression, which is proportional to the clamping force, but also to the varied viscosity parameters. It seems to be linked to the software itself and cannot be removed at the current development stage. Therefore, the aim of the calibration is a good prediction of the qualitative development of the force, so that by subtracting the initial force increase from the maximum compression force, the same value will result for the force. Once all parameters have been tested, the two most promising ones based on qualitative development of the curve in the force-over-displacement diagram shall be adapted further. For the further adaptation, it shall be decided, if the new result requires an increase or a decrease in the predicted force. In order to keep the process suitable for industrial application, it shall be short. Therefore, a total of ten calibration steps shall be performed and the most suitable result shall be adopted for the material card. For the calculation of the parameters a suitable procedure had to be identified. Since the range of each parameter covers several orders of magnitude, a simple rule of proportion for linear development cannot be applied, because the change of the parameter would be too big. Therefore, a new approach has been developed, aiming at finding a new value for each parameter that is in the same order of

magnitude or in an adjacent one. The calculation of the new parameters was performed following eq. 14:

$$p_{new} = \frac{p_{old} - ll}{2} \pm p_{old} \quad (14)$$

where p_{new} and p_{old} represent the new and the old values of the parameter, and ll is the lower limit of the parameter in question. For a decrease, the new parameter results from the subtraction of the two factors, whereas for an increase the factors are summed. If the change due to a specific parameter change is too big, but the parameter seems promising, the parameter change can be decreased by dividing the first term of eq. 14 with double the previous amount. This means that in a first step it would be increased to 4, in a second step to 8, etc.

However, with this approach the resulting increased parameter could be out of the upper limit for that specific parameter. Therefore, in case the parameters exceeds the upper limit with the increase calculated with eq. 14, the following shall be adopted:

$$p_{new} = \frac{ul - p_{old}}{2} + p_{old} \quad (15)$$

where p_{new} and p_{old} represent the new and the old values of the parameter, and ul is the upper limit of the parameter in question.

Based on this procedure, the parameter variations displayed in Tab. 3-8 are performed.

Tab. 3-8 Summary of the calibration steps performed on the squeeze flow simulations for the rheological parameters showing the changed parameters, the old and new values, the lower limit (ll) for the calculation, the reference material card for the new adaptation, as well as the result.

Step		p_{old}	ll	Change	p_{new}	Reference	Result
1st cal	a	2.13E+01	1.00E-10	↓	1.06E+01	Basis	+
2nd cal	n_{visc}	4.32E-01	1.00E-03	↓	2.17E-01	1st cal	-
3rd cal	b	8.94E+03	1.00E-03	↓	4.47E+03	1st cal	-
4th cal	τ	2.90E+00	1.00E-10	↓	1.45E+00	1st cal	-
5th cal	a	1.06E+01	1.00E-10	↓	5.32E+00	1st cal	+
6th cal	τ	2.90E+00	1.00E-10	↑	4.35E+00	5th cal	+
7th cal	a	5.32E+00	1.00E-10	↓	2.66E+00	6th cal	+
8th cal	τ	4.35E+00	1.00E-10	↑	6.53E+00	7th cal	+
9th cal	a	2.66E+00	1.00E-10	↓	1.33E+00	8th cal	-
10th cal	τ	6.53E+00	1.00E-10	↑	9.79E+00	9th cal	-

As can be seen in Tab. 3-8, the changes obtained with the first step with the new parameter a improved the result of the simulation as desired. Therefore, for the subsequent calibration steps, this change was kept. However, for a decrease of $n_{viscosity}$, b and τ the result became worse than with the previous value, as can be seen in Fig. 3-23, summarizing all simulation results for the calibration.

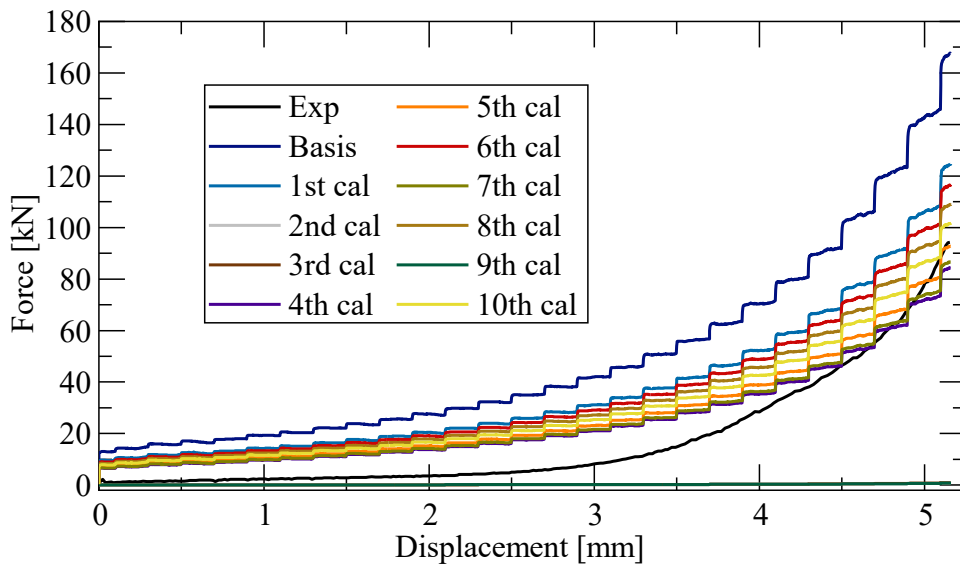


Fig. 3-23 Calibration steps performed on the squeeze flow simulations starting with the parameters from the fitting of the curing kinetics and the viscosity parameters.

As Fig. 3-23 shows, a decrease of the parameter a improves the simulation result. However, the following calibration steps of the 2nd and 3rd calibration result in the force remaining 0 kN during the displacement. In the 4th calibration, the decrease in τ improves the first part of the curve by lowering the increase in the linear portion. However, the second half becomes worse, as the maximum force is much lower. Therefore, the considered approach for the following steps is a further decrease for a , to improve the linear section of the experimental curve, followed by an increase in τ to improve the exponential force increase in the second half of the compression. This alternation between decreasing a and increasing τ is performed three times. Only until the second variation an improvement is visible, while for the 9th calibration step, the decrease in a completely flattens the curve. In the 10th calibration step the result improves compared to the previous step, but it is worse than after the 8th calibration step based on a qualitative comparison of the curves. Furthermore the deviation in the qualitative behavior of the curve is minimal. The quantitative difference is due to the clamping force leaving to a higher force signal from the start. Furthermore another calibration step is performed for the out-of-plane flow, where the parameters will be further varied. Based on the obtained results from the calibration, the chosen settings for the final material card to be used for the subsequent steps are those of the 8th calibration step and are summarized in Tab. 3-9. As can be seen in Tab. 3-9, only two parameters of the viscosity were reduced. All other parameters remain unchanged.

Tab. 3-9 Rheological parameters resulting from the in-plane calibration to be used as a basis for the subsequent steps in direct comparison with the original parameters from the fitting result.

Par	Fitting	Ip cal	Par	Fitting	Ip cal
m	7.30E-01	7.30E-01	n	4.32E-01	4.32E-01
n	1.90E+00	1.90E+00	τ	2.90E+00	6.53E+00
A1	1.00E+02	1.00E+02	a	2.13E+01	2.66E+00
A2	7.00E+06	7.00E+06	b	8.94E+03	8.94E+03
E1	5.00E+04	5.00E+04	D	1.20E+01	1.20E+01
E2	7.71E+03	7.71E+03	E	1.00E-01	1.00E-01

Based on these results and the requirements set at the beginning of this chapter, a procedure for the calibration of the in-plane flow could be identified, as drawn in Fig. 3-24.

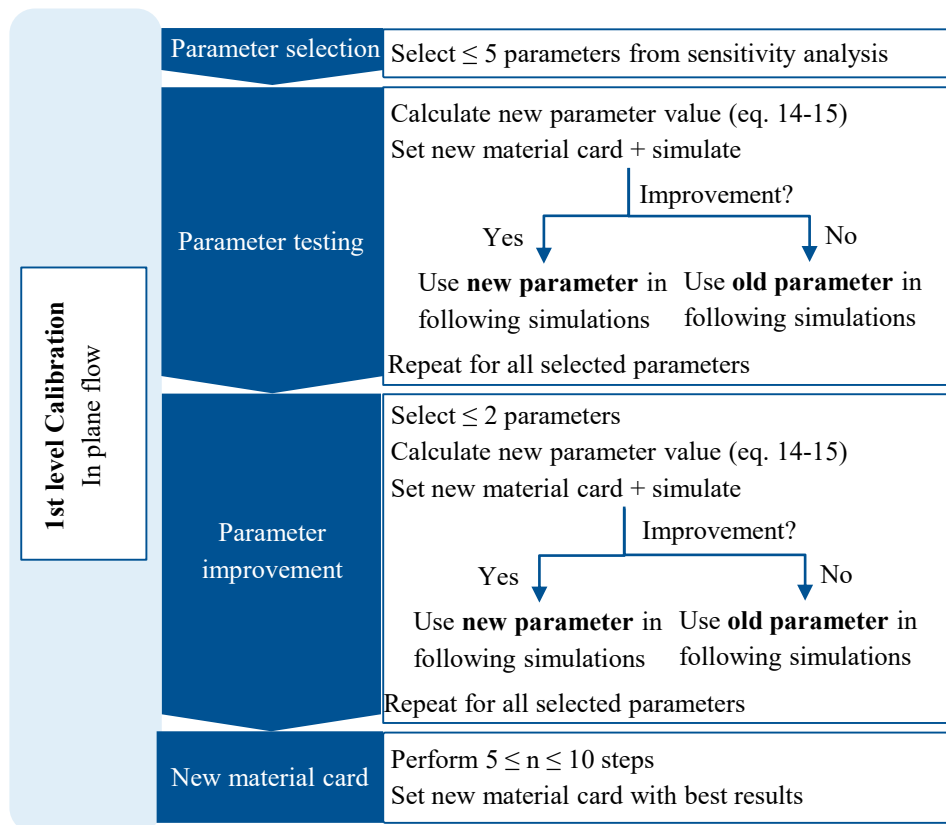


Fig. 3-24 Procedure for the calibration of the rheological parameters with squeeze flow tests for the in-plane flow.

In a first step up to five parameters are chosen with the sensitivity analysis that could improve the result. For each parameter the new parameter has to be calculated following eq. 14 and 15. With the adapted material card, simulations shall be run. If the new result is qualitatively closer to the experimental curve, the parameter shall be overtaken for all following simulations. If the result makes the qualitative overlap worse, the old parameter shall be kept. The sequence of the parameters does not matter. Once all parameters

have been tested, the most promising two parameters shall be further varied. To determine the new parameters the same procedure is followed as before with eq. 14 and 15. Once again, after each calibration a decision shall be made about whether the new parameter improves the result. If so, it shall be used for all following simulations. Once up to 10 calibration steps have been performed in total, the best result shall be selected for the subsequent out-of-plane calibration.

3.3.1.3 Summary and discussion

Within this subsection, flow simulations of previously performed squeeze flow tests are replicated in the software 3DTimon and compared to experimental results. The aim is the improvement of the simulation result, by adapting the parameters previously fitted with data obtained from squeeze flow tests. In order to understand the influence each parameter has on the calibration outcome, a sensitivity analysis was performed. The parameters of the simulation are adapted accordingly, and a suitable procedure is derived.

However, several challenging factors could be identified during the evaluation. First and foremost, the effect one specific parameter has on the result of the simulation compared to the runs with the previous parameter can be an improvement for one temperature setting of the molds, but lead to a worsening for another temperature setting. Fig. 3-25 shows an example of the temperature influence on the parameter suitability performed with random values for parameter a .²

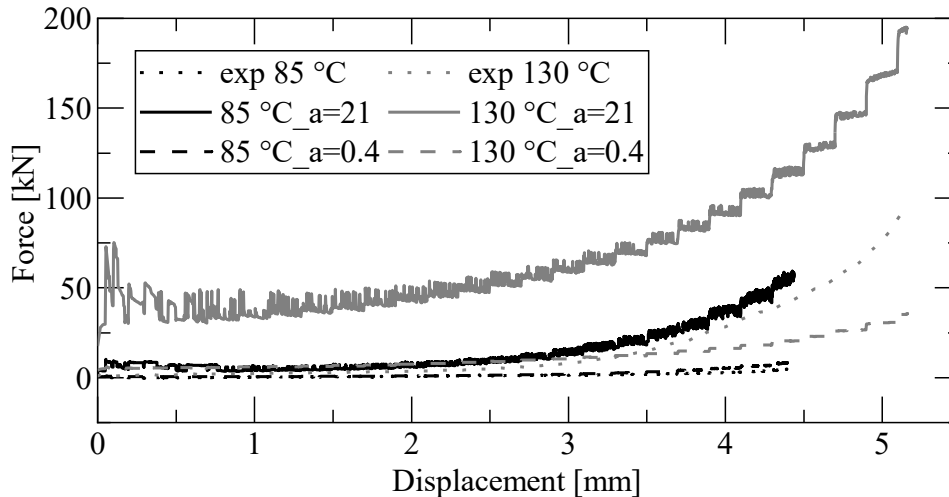


Fig. 3-25 Influence of the temperature on the suitability of a specific parameter value, exemplarily setting parameter a to 21 compared to 0.4.

² The simulations were performed with no waiting time before the compression and an initial temperature of the charge of 60 °C. Furthermore, the software version 3DTimon R4.0 was used. All other settings are identical with those applied throughout this research. The influence of the software version is highlighted in the following figure, and does not compromise the validity of the qualitative assessment of these numerical curves.

For example, in a direct comparison of the simulation settings considered above of 130 °C and 10 mm/min closing speed and the process settings of 85 °C and 1 mm/min closing speed, a change in the parameter a to 0.4 improves the simulation in comparison to the experiment for the lower temperature, but makes it worse for the higher temperature. Therefore, the suitability of specific parameters varies depending on the actual temperature. Due to 130 °C being a normal processing temperature for the SMC, this temperature has been considered as a basis. It is recommendable to use a temperature within the typical processing range for SMC for the calibration, which typically is between 130 °C and 160 °C. However, it has to be suspected that the result may change if an even higher temperature is considered. This temperature dependency within the processing range shall be investigated in the future. Furthermore, other influencing factors could be identified, such as the version of the software, as well as the subdivision in z-direction, as shown in Fig. 3-26.

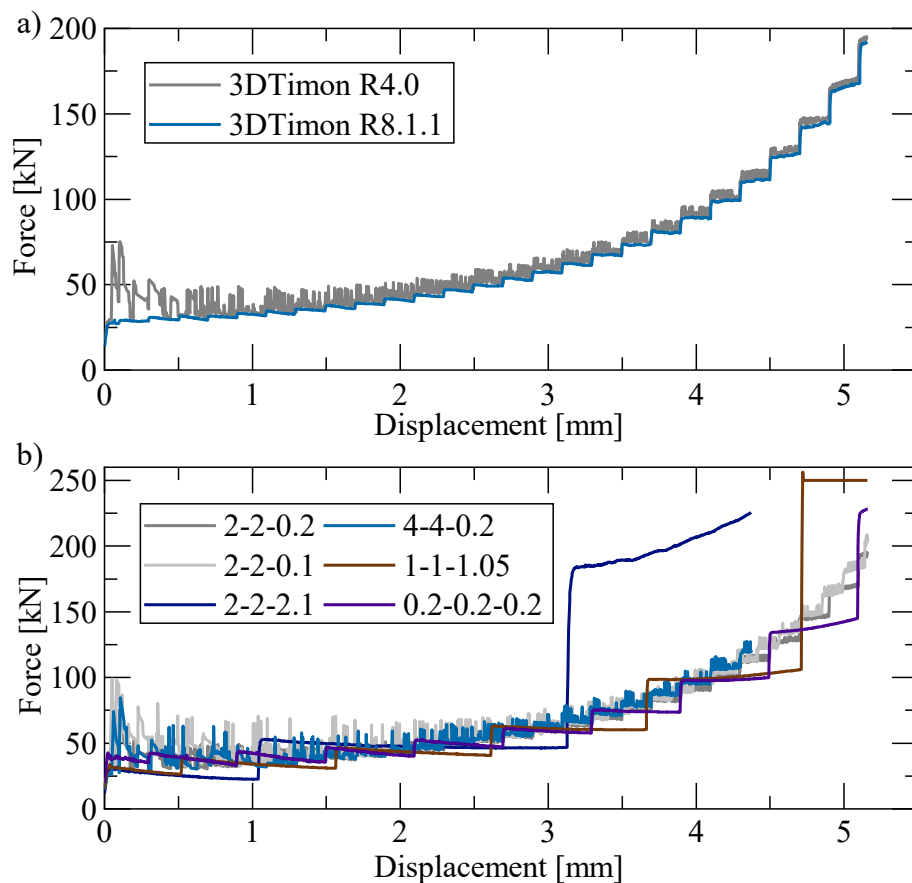


Fig. 3-26 Influence of simulation settings on the outcome of the simulation: a) comparison of the two adopted versions for this research being 3DTimon R4.0 from 2020 and 3DTimon R8.1.1 from 2023; b) comparison of different mesh sizes in x-, y-, and z-directions.

Fig. 3-26a shows that in the previous version of the software 3DTimon R4.0 adopted in 2020 for first trials of the squeeze flow tests, as well as for the sensitivity analysis, the oscillation in the obtained force signal is significant. However, the values for the force are very similar in the two versions, the more recent one being slightly lower throughout.

Despite the difference being low, it is still visible. Therefore, the version of the software is a critical fact in assessing the comparability of results. Whenever a comparison between simulation results is performed, it has to be stated whether there has been a change in version. To this purpose, the calibration for a specific material should ideally be repeated with every version or at least a simulation shall be run comparing directly the results for past squeeze flow simulations and new ones. Nevertheless, it is legit to use less recent versions of the software, as long as all simulations being compared have been run with the same version. This confirms the validity of the sensitivity analysis, which has entirely been performed in 3DTimon R4.0. Moreover, Fig. 3-26b shows the influence of the mesh subdivision in z-direction. The final chosen setting for the sensitivity analysis and the calibration is 0.2 mm, because as displayed in the diagram, a further reduction of the side length in z-direction to 0.1 mm does not change the overall quantitative result of the simulation except for the increase in the stepping. The overall relevant values, such as the maximum force and its development throughout the compression are not influenced. The bigger the element size, the shorter the computation time. However, for side lengths of 2.1 mm (blue) and 1.05 mm (brown) in z-direction the results deviated significantly from the previous settings. Therefore, the biggest side length was chosen that did not influence the relevant aspects for this evaluation in the result of the simulation. For a change in x- and y-direction it is visible that a smaller side length of 1 mm (brown) or even 0.2 mm (purple) leads to more significant stepping, making the discerning of the qualitative development and a direct comparison to the experimental result more difficult. On the other hand, bigger side lengths of 2 mm or even 4 mm mainly difference in the length of the resulting force signal. As the side length of 2 mm reaches a similar length to the empirical result, the comparison of this signal to the experimental curve is more convenient.

Not only the simulation settings can have an influence on the result, but also the experimental data utilized for the comparison. Due to the high variability of SMC, in the future it is necessary to assess the influence of small differences in the process settings, as they can happen in reality. To this purpose, at least three ideally five tests for each high temperature should be performed, the average of the force over displacement be calculated and this average and ideally also the overall distribution be compared to the result of the simulation.

Overall the calibration process is quite time consuming, and therefore, the suitability for the industrial context should be improved further. For example, it is evident when considering the calibration process that a manual adjustment of the parameters of the viscosity as is provided for the curing kinetics within the fitting tool would simplify the process of finding the right parameters. In order to allow a manual adjustment, the result of the fitting has to be displayed. To this purpose a new fitting tool shall be programmed, allowing for this manual adjustment in both the curing kinetics and the viscosity parameters.

3.3.2 Out of plane calibration

The second calibration step applied within this Thesis is the out of plane flow calibration, to determine the material parameters to describe the more complex out-of-plane flow. This flow is present in the majority of SMC applications. For this calibration, the process settings should be as close to the real process as possible. In the standard procedure, as explained in Section 2.3, an SMC part is produced, that presents similar features to the part that is meant to be simulated. This means that the calibration, and therefore, more accurate simulations can only be performed if similar parts, and the tools and processes to produce them already exist. Furthermore, the force data considered for the calibration usually stems from the recording of the press itself, which is inaccurate. Moreover, this approach impedes the use of simulations for new SMC parts that do not have geometrical features in common with previous parts. Nevertheless, flow simulations are important for several goals:

- being used for tool development in regards to part orientation inside the mold
- process development, in regards to temperatures and pressures
- charge shape and placement.

Therefore, a generally valid test tool shall be used for this calibration. This test tool has to display the following features:

- Have an accurate recording of the pressure
- Allow processing parameters similar to the real process, with regard to temperature and pressure profiles and closing speed.
- Show geometrical features that are typical for complex SMC parts.

The last point necessarily includes out-of-plane flow, as SMC parts can be rather complex. As presented in Section 2.3, several tools for flow characterization have been introduced over the past decades. Unfortunately, all previously existent flow testing tools have been found to be unsuitable to fulfill these requirements. An extensive evaluation of the preexistent solutions and their shortcomings is presented in Chapter 4, which focuses on the development of a new in-house test bench that fulfills all the above mentioned requirements. This test bench shall be used for the evaluation of the calibration with displacement control, presented in Subsection 3.3.2.1. As stated in the state of the art (Section 2.1), displacement control is the type of control with broader application among SMC part producers. However, exceptions exist, where an SMC part is produced with force control. As this setting option is available within 3DTimon, this type of control will also be considered within this study in Subsection 3.3.2.2. Depending on the intended control for the test setup the calibration procedure shall be chosen.

3.3.2.1 Displacement control

Materials and methods

As mentioned in the introduction to this chapter, for this evaluation a newly developed test bench was adopted. The in-depth presentation of the development of the test bench and its application in a RUCKS thermoforming machine is presented in Chapter 4. A simple schematic of the test setup and the specimens used for this evaluation are shown in Fig. 3-27.

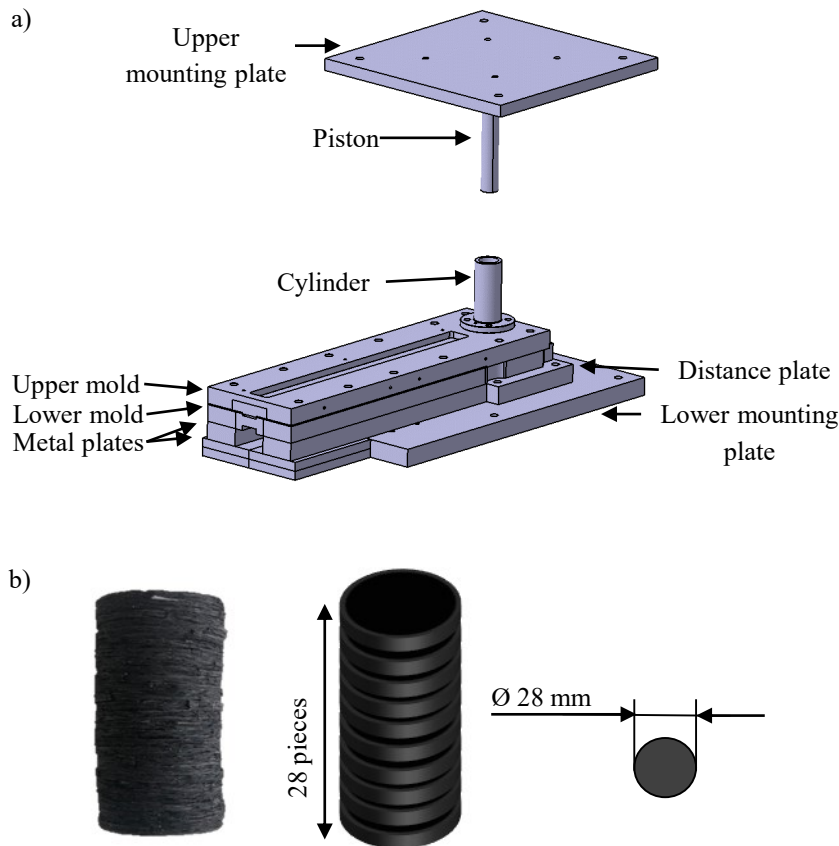


Fig. 3-27 Schematics of the test: a) the bar flow test setup developed in Chapter 4; b) disc pile specimens adopted for the flow characterization with displacement control.

The bar flow setup (Fig. 3-27a) consists in an upper and lower mold to be mounted to an industrial press. A piston attached to the upper half compresses the material placed in the cylindrical opening in the second half. Underneath the piston, a pressure sensor is integrated, tracking the compression pressure in the center of the opening. Furthermore, the lower side of the flow channel is equipped with eight temperature sensors to track the temperature, and the flow speed. Additional metal plates are placed around the channel tool to enhance the thermal management of the setup. The specimens (Fig. 3-27b) are cut from the material adopted throughout this Thesis CARBKID PGK5250 [44]. The specimens consists of 28 discs of 28 mm in diameter stacked to form a cylinder.

The test settings in the RUCKS thermoforming machine, as well as the simulation settings for the sensitivity analysis and the subsequent calibration are summarized in Tab. 3-10.

Tab. 3-10 Process settings and material data utilized for this evaluation, as well as the corresponding chosen simulation settings for the process settings and the material. Purely simulative settings are also summarized.

	Unit	Simu Sens Ana	Simu Cali	Reality
Compression settings				
Temp upper mold	°C	160	160	160 ± 5
Temp lower mold	°C	160	160	160 ± 5
Clamping force	ton	25	25	25
Closing speed	mm/s	2.72	2.72	2.72
Waiting time	s	40	40	~40
Charge				
Material		fitting	ip calib	CARBKID
Volume	mm ³	34965	34965	36860
Fiber orientation		2D random	2D random	2D random
Temperature	°C	25	25	~25
Simulation settings				
Mesh	x-y-z	1.25-1.25-1.25	1.25-1.25-1.25	-
Steps		Flow	Flow	-
Mesh method		Euler	Euler	-

As can be seen in Tab. 3-10, the process settings are overtaken from the tests for the temperatures of the upper and lower mold of 160 °C, the clamping force of 25 tons³, the closing speed of 2.72 mm/s and the waiting time before the compression of 40 s. These values were the intermediate values measured during the tests. Furthermore for the tests a total of five repetitions is set in order to capture the variability of the material. The temperature is set on the upper limit of typical processing temperatures for SMC, because the effects that are due to temperature are the most evident. The heating of the test tool is done over the heated plates of the press. The closing speed is set to 40 % of the compression speed of the press, which was determined to be 2.7 mm/s, which is in the typical range. The simulation is setup in 3DTimon and consists of a cavity replicating the bar flow cavity. The mesh is set to 1.25 mm cubic Euler elements, flow simulations were performed. For the charge the starting temperature is RT, which in simulation is set to 25 °C, the fiber orientation is 2D random. The material card chosen for the simulations is the one resulting from the fitting with the first set of parameters for the sensitivity analysis, and the one resulting from the in-plane calibration for the out-of-plane

³ The unit used in the software to input the clamping force is tons, since in most SMC applications the necessary input is the tonnage of the press. In the tests the press was set to 250 kN maximum compression force, which can be divided by the gravitational acceleration (rounded up to 10 mm/s²) to obtain the value in tons.

calibration. The volume considered in the tests resulted in an average of 36.9 cm³, which was reproduced in simulation with 35.0 cm³. The simulation with the initial charge geometry is visible in Fig. 3-28.

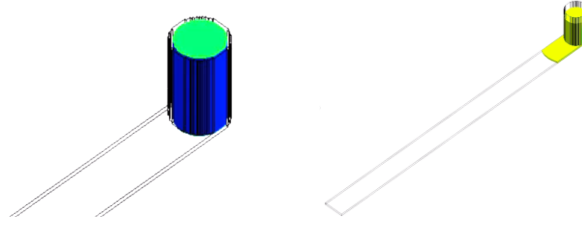


Fig. 3-28 Simulation of the bar flow test with the initial charge and the flow of the material in the bar during the compression.

As can be seen in Fig. 3-28, the initial charge is placed inside the cylindrical opening. During the compression the material flows into the bar.

For the comparison between the simulation results and the empirical results the resulting compression force is considered, since it can be calculated from the pressure sensor below the piston and it is a result given in the simulation software for each moment of the simulation. For the calculation of the force from the data obtained from the pressure sensor, it was considered that the area recording the pressure is a circle of 4 mm in diameter [142]. The compression force F_{sens} is calculated following the standard equation

$$F_{sens} = p_{sens} * A_{sens} \quad (16)$$

with p_{sens} being the compression pressure recorded by the sensor, and A_{sens} being the measuring surface of the sensor. This compression force is then related to the entire compression surface in the cylinder:

$$F_{comp} = \frac{F_{sens}}{A_{sens}} * A_{comp} \quad (17)$$

with F_{comp} being the compression force acting over the entire surface of the piston A_{comp} . F_{comp} corresponds to the compression force predicted in the simulation. This equation can be further simplified

$$F_{comp} = \frac{F_{sens}}{\left(\frac{\emptyset_{sens}}{2}\right)^2 * \pi} * \left(\frac{\emptyset_{comp}}{2}\right)^2 * \pi = \frac{F_{sens}}{\emptyset_{sens}^2} * \emptyset_{comp}^2 \quad (18)$$

where \emptyset_{sens} is the diameter of the sensor and \emptyset_{comp} the diameter of the cylinder.

In order to know which parameters to adapt for an improvement of the result, a sensitivity analysis is performed following the same method as in the previous Subsection 3.3.1.2, by changing only one parameter of the curing kinetics or viscosity model to its

upper or lower limit for each simulation. Afterwards, the calibration is carried out, also following the previously presented procedure in Subsection 3.3.1.2.

Sensitivity analysis for displacement control and calibration

The comparison between the experimental results and the numerical results with the parameters obtained from the in-plane calibration is shown in Fig. 3-29.

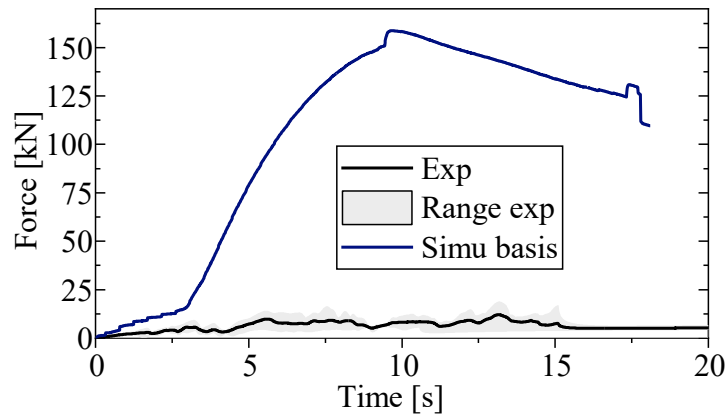


Fig. 3-29 Juxtaposition of the compression force in the simulation with the material card resulting from the in-plane calibration with compression force in the experimental result, including its range from the performed tests.

It is evident in Fig. 3-29 that the prediction of the compression force in the simulation is much higher than the compression force obtained during the experiments. For example the maximum value predicted in the simulation of 158.7 kN is 8.5 times higher than the 18.6 kN being the maximum measured in the range of the experiments. Furthermore, the qualitative development of the two curves is rather different, as the numerical curve does not display the unsteady behavior shown by the experimental curve. The reasons behind this result are explained in a very detailed manner in Chapter 5, but in summary the oscillations come from the configuration of the charge. However, in the numerical replica several simplifications are present in order to reduce the computation time. For example, the fibers are not considered as having any influence on the flow of the material. Neither are the subdivisions in z-direction of the sheets considered, despite the knowledge of the formation of lubricating layers in between. In the numerical result, during the first 2.5 s the charge is compressed to fill the entire circumference of the cylinder. Only then the force signal starts increasing significantly. The peak force is reached at around 10 s, after which it starts steadily decreasing. At first the pressure increases as the material is compressed in itself. However, a portion of the material can exit into the bar, releasing the pressure built up internally. Nevertheless, the opening towards the bar is smaller than the compression area underneath the piston, not allowing the material to move fast enough into the bar to avoid pressure build-up. Once the maximum compression is reached, the flow velocity at the exit into the bar increases to over 16 mm/s and the compression force can steadily reduce itself as the amount of material it has to push away is steadily decreasing. The simulation also displays two jumps in the force signal: once at half of the compression, and once right before the end. For the first

jump it is not clear what it is due to. However, for the second jump it could be concluded that it is linked to the smoothing of the mesh, an option activated in the settings of the simulation. With this option, the geometry is slightly modified to optimize the mesh in regions where the cross section changes. In a direct comparison of the resulting specimens, the compression seems to be completed for both the experiment and the simulation, as can be seen in Fig. 3-30.



Fig. 3-30 Specimens resulting in the bar flow experiment and the simulation.

In addition to the compression being completed in both, it is visible that the real specimen is shorter, although its volume is bigger than the material considered in simulation. This is due to material losses creating the burrs on the sides on the geometry, as the resin and fibers flow in between all contact surfaces. Furthermore, the material flows up along the piston in opposite direction to the compression direction.

Despite the good agreement in the resulting specimen, it is clear for the force signal that with the material card from the squeeze flow calibration the simulation result is not satisfactory.

For the sensitivity analysis a simulation was run with each parameter being set once to the upper and once to the lower limit. The reference simulation defined as “basis” is then compared to the two simulations with the upper and lower limits defined for the considered parameters. An exemplary result can be seen in Fig. 3-31, while all results are summarized in the appendix b.

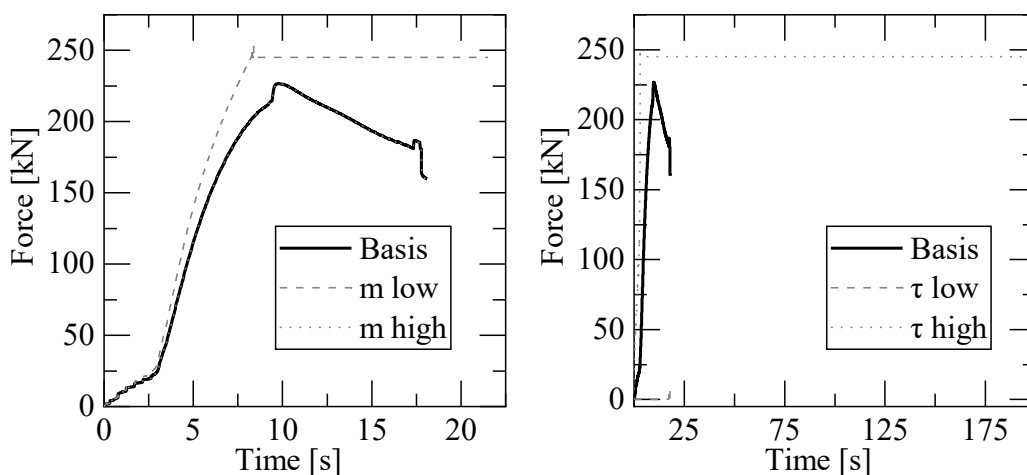


Fig. 3-31 Exemplary result for the sensitivity analysis for displacement control for the parameters m of the curing kinetics and τ of the viscosity model.

It is visible in Fig. 3-31 that a decrease in the kinetic exponent m leads to an increase in the compression force. However, the change is not significant. An increase of the kinetic exponent m on the other hand does not show any change compared to the original curve. For the parameter τ an increase leads to a significant increase in force, but also to an increase in the compression time. If the value of τ is decreased to the lower limit, the resulting force is 0 kN. The result of the sensitivity analysis is summarized in Tab. 3-11.

Tab. 3-11 Result of the sensitivity analysis for displacement control related to the force signal and the curing behavior.

	Parameter	Limit Low	F	Curing	Limit high	F	Curing
Curing kinetics	m	1.00E-01	↑↑	↑	2.00E+00	=	=
	n	1.00E-01	=	=	2.00E+00	=	=
	A1	1.00E-05	=	=	1.00E+10	=	=
	A2	3.00E+06	=	=	1.00E+08	↑↑	=
	E1	1.00E-05	SS	SS	1.00E+10	=	=
	E2	6.00E+03	↑↑	↑↑	9.00E+03	=	=
Viscosity	n	1.00E-03	0	-	9.99E-01	↑↑	-
	τ	1.00E-10	0	-	1.00E+10	↑↑	-
	a	1.00E-10	0	-	1.00E+10	↑↑	-
	b	1.00E-03	0	-	1.00E+05	↑↑	-
	D	1.20E-04	=	-	1.20E+04	↑↑	-
	E	1.00E-04	=	-	1.00E+04	=	-

SS = short shot

Based on Tab. 3-11, the curing parameters do not seem to improve the resulting curve. For the viscosity parameters $n_{viscosity}$, τ , a and b are identified as the parameters to be changed to optimize the simulation outcome. The procedure followed for the calibration is the same as presented in the previous Subsection 3.3.1.2. The main objective of the calibration is to obtain a good prediction of the maximum compression force to be expected. The secondary goal is an overall good agreement between the two signals of the compression force. The result of the calibration can be seen in Fig. 3-32.

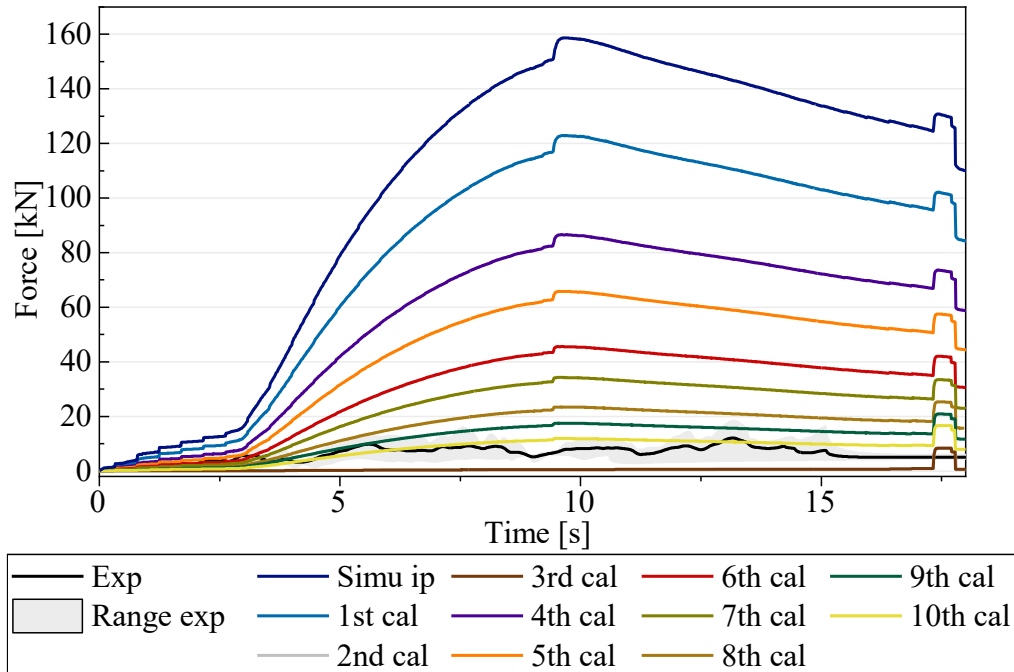


Fig. 3-32 Calibration of the curing kinetics and viscosity model in the bar flow simulation starting with the result from the in-plane result showing the ten applied calibration steps in direct comparison with the experimental average and the covered range of the experimental curves.

As can be seen in Fig. 3-32, the 10th calibration step is very close to the experimental result, with the maximum compression pressure of 16.7 kN being very close to the experimental maximum of 18.6 kN. However, in the initial 2.5 s the numerical compression pressure is much lower than the experimental one. Out of ten calibration steps, only two were not satisfactory, being the 2nd and 3rd steps, which resulted in the same curve of 0 kN throughout, except for the last second of the compression. The exact parameter changes and steps in the calibration are summarized in Tab. 3-12.

Tab. 3-12 Summary of the calibration steps performed on the bar flow simulations for displacement control for the rheological parameters showing the changed parameters, the old and new values, the lower limit (ll) for the calculation, the reference material card for the new adaptation, as well as an evaluation of the result.

Step		pold	ll	Change	pnew	Reference	Result
1st cal	a	2.66E+00	1.00E-10	↓	1.33E+00	Basis	+
2nd cal	b	8.94E+03	1.00E-03	↓	4.47E+03	1st cal	-
3rd cal	nvisc	4.32E-01	1.00E-03	↓	2.17E-01	1st cal	-
4th cal	τ	6.53E+00	1.00E-10	↓	3.26E+00	1st cal	+
5th cal	a	1.33E+00	1.00E-10	↓	6.64E-01	4th cal	+
6th cal	τ	3.26E+00	1.00E-10	↓	1.63E+00	5th cal	+
7th cal	a	6.64E-01	1.00E-10	↓	3.32E-01	6th cal	+
8th cal	τ	1.63E+00	1.00E-10	↓	8.16E-01	7th cal	+
9th cal	a	3.32E-01	1.00E-10	↓	1.66E-01	8th cal	+
10th cal	τ	8.16E-01	1.00E-10	↓	4.08E-01	9th cal	+

As visible in Tab. 3-12, in the first four simulations the most promising parameters are tested. From the 5th calibration on the focus relay solely on the two parameters τ and a . The final set of parameters obtained from the calibration is shown in Tab. 3-13.

Tab. 3-13 New set of parameters for the curing kinetics and viscosity model after the out-of-plan calibration in comparison to the parameters from the in-plane calibration. The changed parameters are highlighted by being bold.

Par	Ip cal	Oop cal	Par	Ip cal	Oop cal
m	7.30E-01	7.30E-01	n	4.32E-01	4.32E-01
n	1.90E+00	1.90E+00	τ	6.53E+00	4.08E-01
A1	1.00E+02	1.00E+02	a	2.66E+00	1.66E-01
A2	7.00E+06	7.00E+06	b	8.94E+03	8.94E+03
E1	5.00E+04	5.00E+04	D	1.20E+01	1.20E+01
E2	7.71E+03	7.71E+03	E	1.00E-01	1.00E-01

Tab. 3-13 shows that only the parameters τ and a are changed, decreasing them respectively from 6.53 to 0.408 and from 2.66 to 0.166.

Conclusion

Within this subsection, an improvement of the prediction of the compression force is obtained by calibrating the parameters of the curing kinetics and of the viscosity model for the out-of-plane flow. To this purpose, bar flow tests have been performed with a newly developed test bench presented in Chapter 4. In order to select the most suitable parameters for the calibration a sensitivity analysis is performed. In the subsequent calibration a total of ten steps is performed, displaying a clear improvement with the last parameter adaptation in reference to the maximum expected compression force. However, the overall development of the numerical and the empirical curve differ in many aspects. First and foremost the oscillation present in the real tests, due to the simplifications necessary in the simulation. However, it would be interesting to improve the simulation accuracy by utilizing one of the many descriptions of the lubricating layer formed between two sheets and between the outer layers and the tool. Although this approach could not be applied within the simulation software 3DTimon. Another interesting approach would be to model the SMC charge with a higher level of detail, maybe defining the roving strands and their orientation. Each batch of roving strands with the same orientation would have to be imported into the simulation as one piece of the charge, because each charge part can only have one fiber orientation degree in x-y-z. Another aspect to be considered is the effect of the element size, which has not been further investigated within this study. In Chapter 5 variations of the same charge as used within this chapter are compared to each other. Considerations and guidelines are drawn on how to utilize the information obtained from the comparison when setting up flow simulations and when defining the charge configuration for a specific geometry.

3.3.2.2 Force control

The content of this subsection has been previously published in similar form [P1].

Despite the most common SMC processing technique being displacement controlled compression, sometimes force control is applied. The choice depends on the available equipment. In order to provide the necessary data and allow an out-of-plane calibration for both processing cases of displacement and force control, another out-of-plane calibration is carried out, this time with force control.

Measurement method with pressing parameters and simulation approach

For this study on the parameter calibration with force control, a test bench and a procedure was adopted, that had been developed at Blackwave GmbH within a Bachelor's Thesis [131].

The general setup in CAD of the test bench can be seen in Fig. 3-33 [131].

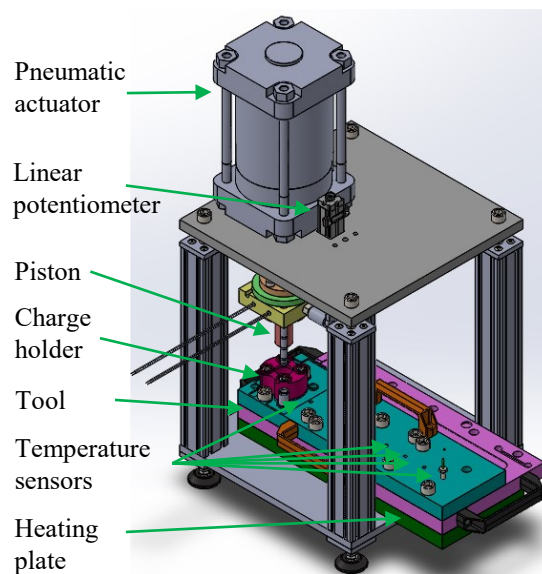


Fig. 3-33 Bar flow test setup in CAD [131] with highlight of crucial features.

The setup consists of a pneumatic actuator attached to a piston, which compresses the SMC placed inside the cylindrical charge holder underneath. The piston movement is tracked with a linear potentiometer, the flow is tracked with temperature sensors along the flow channel. Heating cartridges are placed inside the heating plate below the tool. Below the opening for the charge is the tool, which allows to switch between three channel thicknesses: 2 mm, 2.5 mm and 3 mm.

The overall measurements for the cavity are displayed in Fig. 3-34

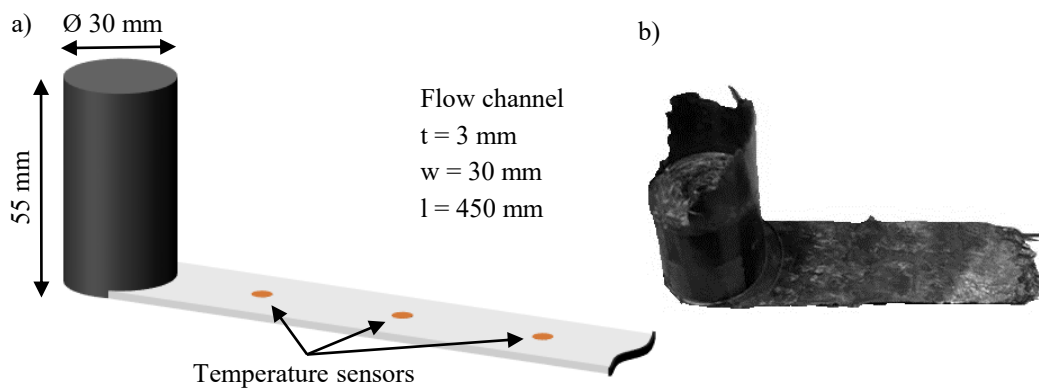


Fig. 3-34 Material placement, cavity and flow pattern: a) overall measurements of the cylindrical opening and charge placement, b) exemplary result after the compression, with material that has flown into the bar.

The cavity consists in a channel with a length of 450 mm, a width of 30 mm and a thickness of 3 mm, as shown in Fig. 3-34a. Due to the applied pressure, the material flows towards the open bar, leading to a geometry as shown in Fig. 3-34b. Given the volume for the charge in the cylindrical opening, a charge geometry was chosen, as shown in Fig. 3-35.

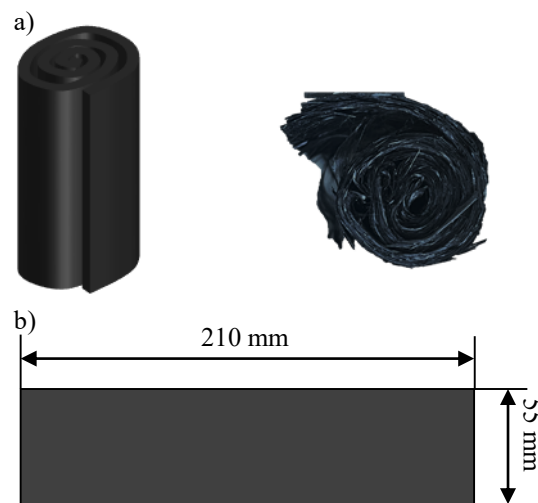


Fig. 3-35 Spiral charge of SMC: a) front and top view, with top view being an actual specimen, b) measurements of each rectangle rolled up to a spiral

The charge configuration tested in these bar flow tests consists of spirals made with SMC rectangles of 260 x 55 mm. The material used is Astar CARBKID PGK5250-R63 [44], the same material used throughout this research and presented more in detail in Section 1.3. The aim for the charge was to put as much material as possible into the charge holder, making a comparison with simulation more accurate. With a maximum diameter of the opening of 30 mm the length of several specimens had to be shortened by up to 50 mm as the thickness of SMC sheets varies.

The applied testing parameters and the settings for the simulation are summarized in Tab. 3-14.

Tab. 3-14 Process parameters applied for the bar flow tests, as well as process simulation settings within 3DTimon depicting the tests.

	Unit	Simulation	Reality
Compression settings			
Temp upper mold	°C	132	132 ± 2
		-	128 ± 2
Temp lower mold	°C	132	132 ± 2
		-	128 ± 2
Pressure	bar	-	9
Clamping force	ton	0.0636	-
Closing speed	mm/s	10.76	10.76
Waiting time	s	37	~37
Charge			
Material		CARBKID	CARBKID
Volume	mm ³	34402.5	~35000
Fiber orientation		3D random	complex
Temperature	°C	25	~25
Simulation settings			
Mesh	x-y-z	1.5-1.5-1.49	-
Steps		Flow	-
Mesh method		Euler	-

The pneumatic actuator was permanently set to the maximum compression pressure of 9 bar, much lower than the usual 150 bar or more in a typical SMC process. For this bar flow test bench the compression is force controlled, leading to variations in the closing speed. Based on the recommendations from Kröger [131], the tests were performed at 132 °C with a tolerance of ± 2 °C and at 128 °C with the same tolerance. To provide a basis for the comparison between the tests, the time between the start of the recording until the start of the compression was set to be 10 s. From the start of the recording until drawing the piston back up five minutes passed to ensure that the curing of the material had completed. The bar flow tests were once again implemented into 3DTimon. The temperatures of the upper and lower mold were set to 132 °C. The charge was placed in the cylinder with the average volume of the tested SMC of 35000 mm³. The simulation was performed with constant force, set at 636,173 N corresponding to the pressure of 9 bar applied on the surface of the specimen in the cylinder of 30 mm in diameter. For the meshing method Euler elements were selected, with an edge length of 1.5-1.5-1.49 mm in x-, y-, and z-directions respectively. The closing speed before the contact with the material is set to 10.76 mm/s, the same as measured in the experiments. The temperature of the material at the beginning of the process was set at 25 °C for RT. An average of 15 s pass once the specimen was placed in the opening before the start of the piston motion. Another 22 seconds pass before the piston touches the material starting

the actual compression. Therefore, a waiting time of 37 s is implemented in the simulation. Due to this delay, the material has time to already heat up on the outside of the charge. The model with the initial charge settings can be seen in Fig. 3-36.

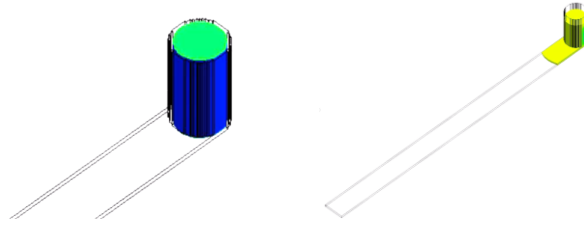


Fig. 3-36 Process simulation model of the bar flow test, with the initial cylindrical charge at the tip of the flow channel on the left and the full model with the material flowing into the channel on the right.

In order to compare the experimental results to the simulation, the piston position during the compression has to be derived with a linear dependency.

Results and discussion

The result of the piston displacement can be seen in Fig. 3-37.

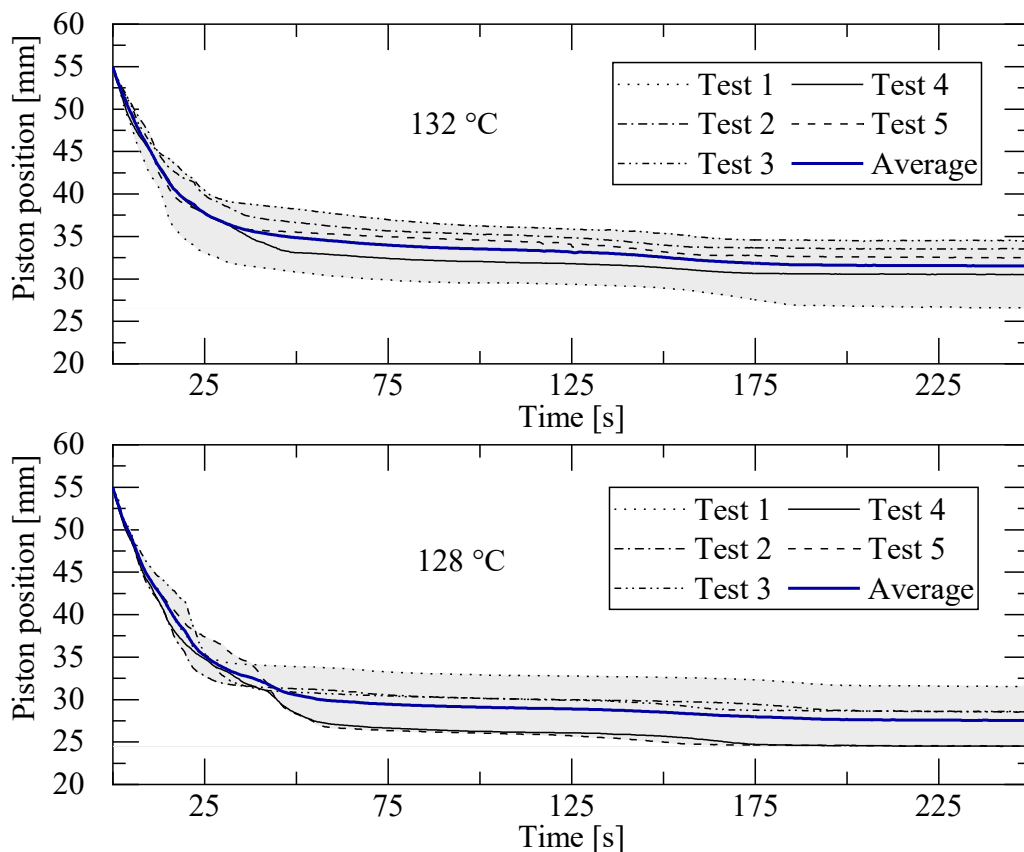


Fig. 3-37 Results of the piston position over time for all five performed tests and the respective average for 132 °C (top) and 128 °C (bottom).

As can be seen in Fig. 3-37, all specimens cured during the compression, as almost 1 min passed before the compression started, giving the material enough time to heat up.

With increased heat the viscosity decreases, which allows the material to flow faster. Therefore, the compression is rather fast at the beginning with around 0.8 mm/s. After a considerable decrease in the piston position the piston movement slowed down significantly after 50 s, with only a very small movement of 5 mm happening after that moment for the following 200 s. However, for 132 °C the curing happens a bit earlier, leading into the linear descent of the piston position already at 40 s. Moreover, the linear descent starts at 35 mm of piston position, whereas for 128 °C it is at 30 mm. This is due to the curing happening a little earlier for the tests with a higher temperature. The high variability of SMC is also visible here, as each curve displays a unique development.

The simulation result for the displacement differs from the experimental result, as the curing is complete earlier, as can be seen in Fig. 3-38.

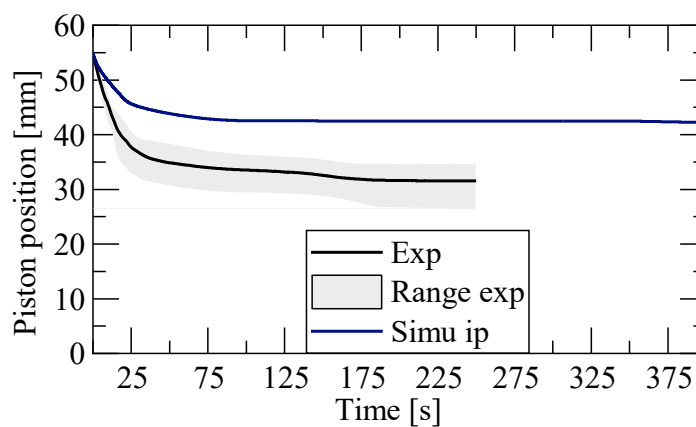


Fig. 3-38 Simulation result compared to experimental result considering the material card obtained after the in-plane fitting.

The piston movement in simulation is much slower than in the experiments, which is mainly due to the viscosity being lower in reality. Towards the end of the compression, the displacement still shows a difference of approximately 10 mm, which is significant considering an overall displacement of 23.5 mm in the experiment for the average curve. A decrease in the viscosity is necessary in order to improve the result. However, the start of the curing signaled by the end of the linear descent of the piston happens around 20 s for both curves. Furthermore, the curve resulting from the decreasing compression speed in the range of 20 to 50 s has a similar development for the simulation and the reality. The compression also seems to be concluded at the same time stamp around 50 s. Although, in the experiments at least some of the curves showed a second faster interval around 160 s. It is evident that the simulation result for the stroke signal needs to be improved by changing the material behavior related to the viscosity.

Sensitivity analysis for force control

The sensitivity analysis with regard to the displacement was performed in the same fashion as had been done for the previous sensitivity analysis. An exemplary diagram with the results for the upper and lower limits of the parameters m and τ of the rheological

model can be seen in Fig. 3-39, whereas the upper and lower limits used for the analysis are summarized in Tab. 3-15 underneath.

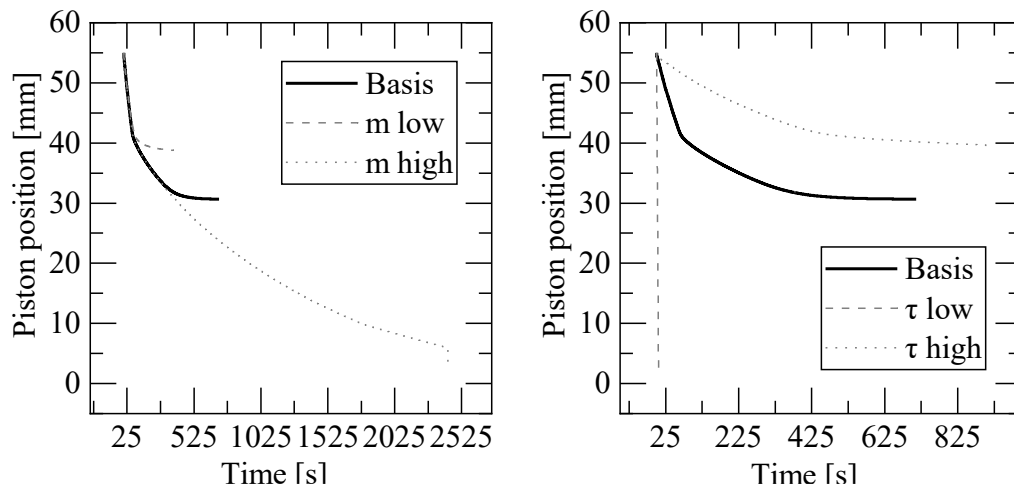


Fig. 3-39 Sensitivity analysis result with upper and lower limit compared to the numerical reference for the parameters m (left) and τ (right).

It is visible in Fig. 3-39 that a change in the kinetic exponent m to its lower limit leads to a shorter compression and therefore, faster curing. The higher limit, on the other hand, leads to a slower curing and a longer compression. However, the initial compression speed is not influenced by this parameter. This is different for τ , where both the higher and lower limit change the compression speed. For the upper limit the compression happens slower and is interrupted earlier, which suggests a faster curing. With the lower limit, on the other hand, the compression happens very fast, as if there was no material to counteract. Therefore, a high τ is connected to a low viscosity. All other diagrams can be seen in the appendix b. The result of the influences is summarized in Tab. 3-15.

Tab. 3-15 Sensitivity analysis of the curing kinetics and viscosity parameters, summarizing the influence on the curing and the compression speed.

	Parameter	Limit Low	Curing	Limit high	Curing
Curing kinetics	m	1.00E+02	earlier, steady	2.00E+03	=
	n	1.00E+02	=	2.00E+03	=
	A1	1.00E-02	=	1.00E+13	=
	A2	3.00E+09	=	1.00E+11	earlier, steady
	E1	1.00E-02	SS	1.00E+13	=
	E2	6.00E+06	faster	9.00E+06	longer
	Parameter	Limit Low	Compression speed	Limit high	Compression speed
Viscosity	n	1.00E+00	constant and slower	9.99E+02	≈ max
	tau	1.00E-07	constant and slower	1.00E+13	≈ max
	a	1.00E-07	constant and slower	1.00E+13	≈ max
	b	1.00E+00	≈ max	1.00E+13	SS
	D	1,20E-04	constant and slower	1,20E+04	max
	E	1,00E-04	min increase at end	1,00E+04	=

SS = short shot

Based on these findings, for this bar flow case the accuracy of the piston movement in simulation can be improved by decreasing τ , a , n or b .

Calibration for out-of-plane values with force control

Based on the sensitivity analysis, the simulation result was calibrated by following the same procedure as presented in Section 3.3.1, and by applying eq. 14 and 15. The main objective of the calibration is increasing the piston movement to the real displacement, because the overall goal of flow simulations is to see the filling of a part, and whether a part will be completely filled. Fig. 3-40 shows the result of the calibration.

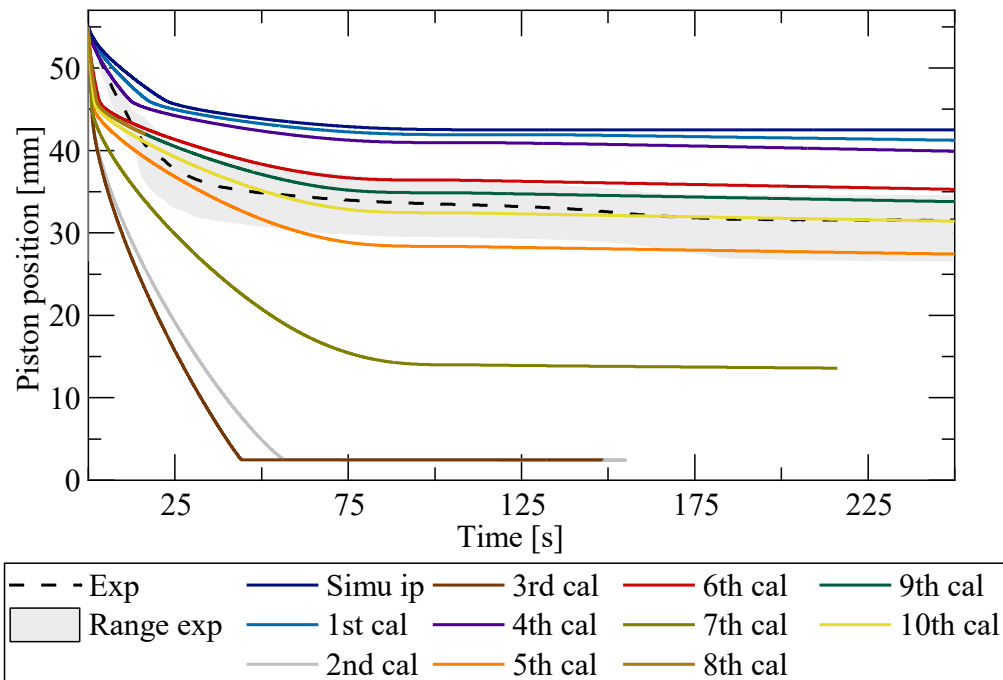


Fig. 3-40 Calibration steps performed on the bar flow simulations for force control, starting with the parameters from the calibration of the in-plane flow of the curing kinetics and the viscosity parameters.

As can be seen in Fig. 3-40, an improvement of the simulation result could be obtained, with the displacement being almost identical between the experimental result and the numerical result. However, the curve shows significant discrepancy in the piston movement until approximately 50 s.

The parameter variations performed in Fig. 3-40 are summarized in Tab. 3-16. When looking at the most plausible parameters to be varied, only a and τ improved the result with the first try. For $n_{viscosity}$ and b two further reductions are tested, but only b leads to an improvement after two steps. In the final two steps, another decrease of a and τ are attempted, both improving the result.

Tab. 3-16 Summary of the calibration steps performed on the bar flow simulations for force control for the rheological parameters showing the changed parameters, the old and new values, the lower limit (II) for the calculation, the reference material card for the new adaptation, as well as an evaluation of the result.

Step		p _{old}	II	Change	p _{new}	Reference	Result
1st cal	a	2.66E+00	1.00E-10	↓	1.33E+00	Basis	+
2nd cal	b	8.94E+03	1.00E-03	↓	4.47E+03	1st cal	-
3rd cal	n _{visc}	4.32E-01	1.00E-03	↓	2.17E-01	1st cal	-
4th cal	τ	6.53E+00	1.00E-10	↓	3.26E+00	1st cal	+
5th cal	b	8.94E+03	1.00E-03	↓	6.71E+03	4th cal	-
6th cal	b	8.94E+03	1.00E-03	↓	7.82E+03	4th cal	+
7th cal	n _{visc}	4.32E-01	1.00E-03	↓	3.24E-01	6th cal	-
8th cal	n _{visc}	4.32E-01	1.00E-03	↓	3.78E-01	6th cal	-
9th cal	a	1.33E+00	1.00E-10	↓	6.64E-01	6th cal	+
10th cal	τ	3.26E+00	1.00E-01	↓	1.63E+00	9th cal	+

With this result, the final set of parameters for the curing kinetics and the viscosity models is obtained as shown in Tab. 3-17.

Tab. 3-17 Parameters for the curing kinetics and the viscosity model resulting from the calibration of the bar flow with force control.

Par	Ip cal	Oop cal	Par	Ip cal	Oop cal
m	7.30E-01	7.30E-01	n	4.32E-01	4.32E-01
n	1.90E+00	1.90E+00	τ	6.53E+00	1.63E+00
A1	1.00E+02	1.00E+02	a	2.66E+00	6.64E-01
A2	7.00E+06	7.00E+06	b	8.94E+03	7.82E+03
E1	5.00E+04	5.00E+04	D	1.20E+01	1.20E+01
E2	7.71E+03	7.71E+03	E	1.00E-01	1.00E-01

As can be seen in Tab. 3-17, the curing parameters have not been changed, whereas for the viscosity parameters three out of six have been reduced.

Conclusion

Within this study an improvement of the material parameters of the curing kinetics and the viscosity model has been obtained by calibrating the numerical result to the empirical result for force controlled SMC compression. Following the procedure presented in Sub-section 3.3.1, new values have been set leading to a maximum displacement in the simulation that almost coincides with the real process. However, the displacement velocity leading to the final position deviates more significantly between the two signals. Therefore, predicted forces in the simulation during the first seconds will most likely be higher than in reality, since a faster compression is predicted. Furthermore, it has to be considered that the force applied within this study was low compared to typical SMC processing with only 9 bar as opposed to 100-150 bar. The influence of the compression pressure on the displacement needs to be further investigated in order to establish the scalability of this result to actual process settings. The second processing aspect making the quantification of these results challenging is the temperature control, as the signal of the temperature sensors was not optimal. Therefore, it is not exactly known what the

temperature of the material was at the start of the compression, nor what the exact temperature of the upper and lower mold were during the tests. As shown within this study, a change of only 4 °C leads to a visible difference in the experimental result. For the simulation results mainly two aspects can be critical in relation to the validity of the results. The first critical aspect is the simulation algorithm being setup for displacement controlled compression, the industrial standard. Therefore, the option of force control being selectable only after finishing all other settings of the compression steps could be less accurate than the standard setting of displacement control. A practical example of these settings is shown in Fig. 3-41.

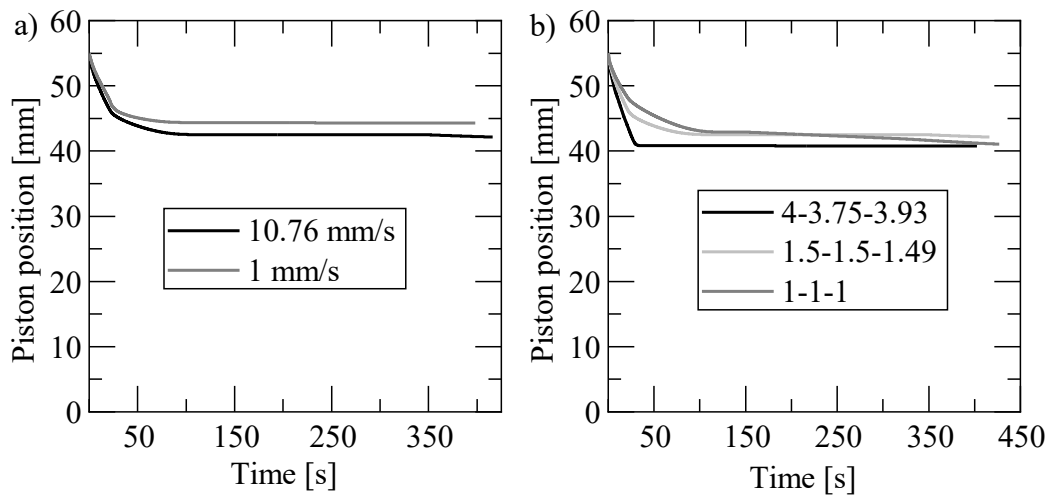


Fig. 3-41 Influence of simulation settings on the outcome of the displacement signal: a) comparison of the set closing speed and the closing speed of 1 mm/s; b) comparison of different mesh sizes in x-, y-, and z-direction.

As can be seen in Fig. 3-41a, the compression speed adopted throughout this study of 10.76 mm/s is compared to a lower compression speed of 1 mm/s. Since the process is force controlled, and the 1 mm/s is the actual compression speed once the piston is in contact with the material, this change in speed should not influence the result at all. However, it is evident that such a difference is visible. The second aspect to be careful with is the same as for the previous calibration evaluations and concerns the setting of the mesh. The result of the comparison for the considered variations can be seen in Fig. 3-41b. It is visible that a decrease in the mesh size from 4-3.75-3.93 mm to 1.5-1.5-1.49 mm leads to a decrease in the overall displacement. However, for a further reduction of the element size, the overall displacement is similar. The main difference is that the visible kink in the curve at the beginning of the compression is not so evident. Applying this change in element size to the simulation with the final material card obtained from this calibration would most likely improve the difference between the experiment and the simulation in the first part of the compression, where the deviation is quite significant. However, this conclusion needs to be confirmed. Nevertheless, a decrease from 1.5 to 1 mm side length of the cubic elements increases the simulation time by more than double, making it inconvenient. A compromise was chosen as basis for this study by

selecting the intermediate options, but it has to be kept in mind that the mesh size leads to differences in the result. These shall be quantified in future studies.

3.3.2.3 Summary and discussion

Within the two chapters for the out-of-plane calibration with displacement and force control, experimental and numerical results were compared. With a sensitivity analysis performed for both options, recommendations could be given for the calibration of the parameters. The applied procedure for the calibration is the same as applied in the previous in-plane calibration (see Fig. 3-42).

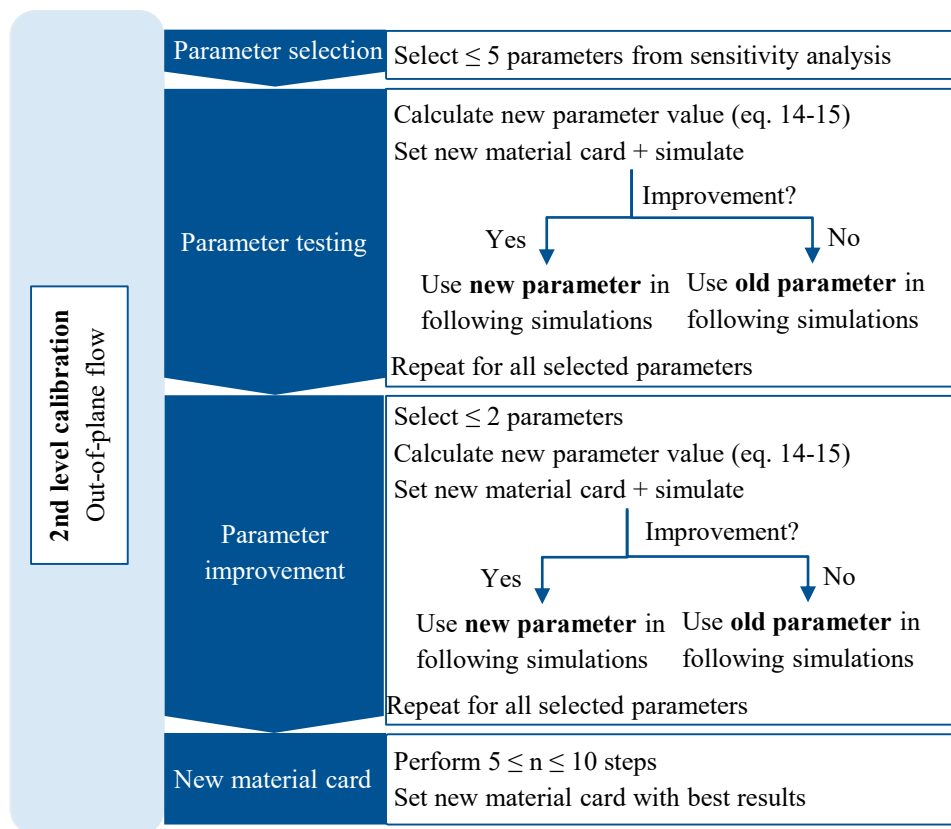


Fig. 3-42 Procedure for the calibration of the out-of-plane flow, applied for both the displacement control and the force control results.

As the procedure is the same, the calibrations performed for displacement control and force control led to two different step sequences and also different parameters at the end of the calibration. However, since the same material is calibrated, ideally the same steps can also be applied to the other setup. The result for applying all steps of the calibration for displacement control on the setup with force control, as well as the direct comparison of the resulting 10th calibration step for both procedures is shown in Fig. 3-43.

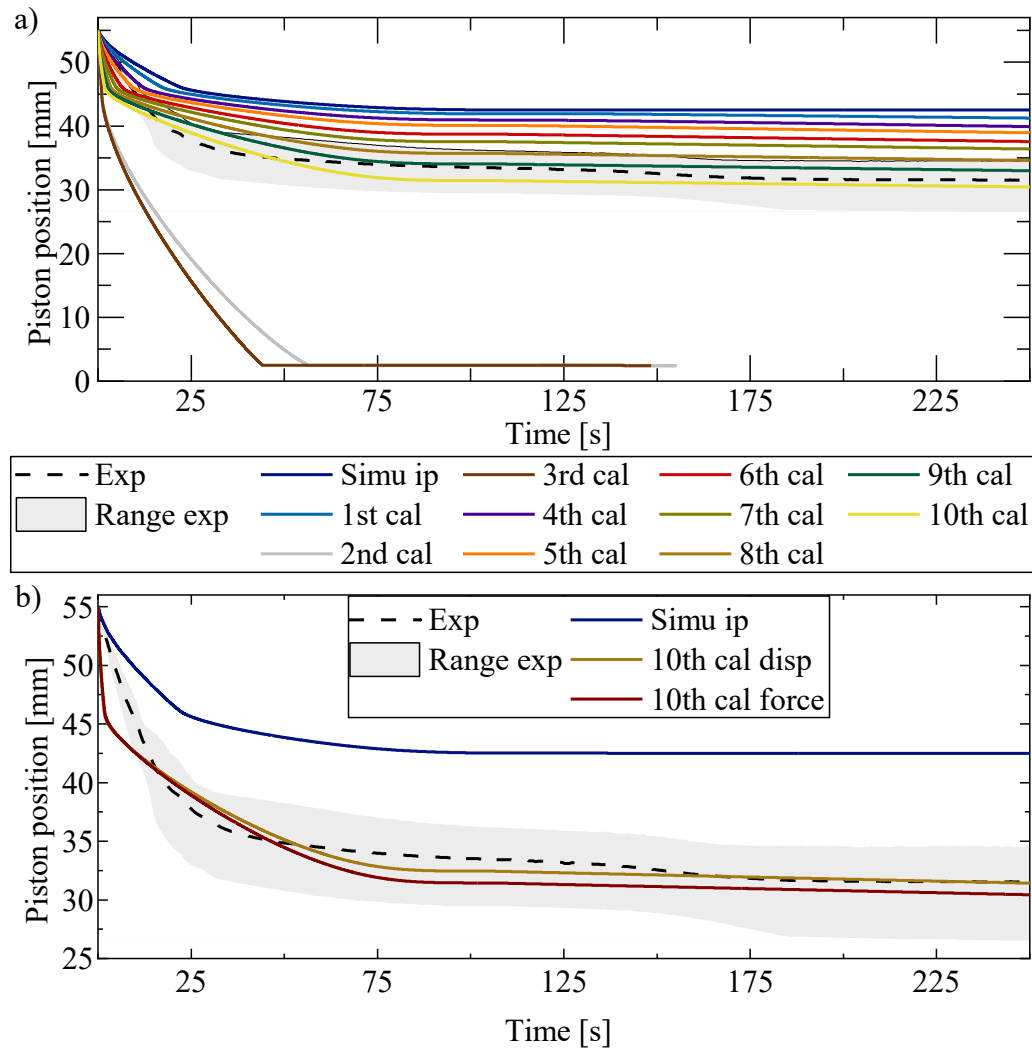


Fig. 3-43 Application of the calibration steps from the displacement control to the force control and comparison of the results for the two different procedures: a) result for all ten calibration steps; b) direct comparison of the resulting piston position for both procedures.

It is visible in Fig. 3-43a that the application of the calibration steps from the displacement control to the setup of the force control also leads to the best simulation result. Although, the result of the 9th calibration is also quite good. In a direct comparison between the results of the two calibration versions, as shown in Fig. 3-43b, the curves are very similar. However, the calibration steps applied for the first version seem to lead to a slightly better result. The corresponding parameters are summarized in Tab. 3-18.

Tab. 3-18 Parameters used in the two material cards, with the parameters that were changed in the calibration and therefore, differ in bold.

Par	Cal disp	Cal force	Par	Cal disp	Cal force
m	7.30E-01	7.30E-01	n	4.32E-01	4.32E-01
n	1.90E+00	1.90E+00	τ	1.63E+00	4.08E-01
A1	1.00E+02	1.00E+02	a	6.64E-01	1.66E-01
A2	7.00E+06	7.00E+06	b	7.82E+03	8.94E+03
E1	5.00E+04	5.00E+04	D	1.20E+01	1.20E+01
E2	7.71E+03	7.71E+03	E	1.00E-01	1.00E-01

Only three parameters differ between the two calibrations, and all of them have been reduced during the calibration, leading to a reduction of the viscosity. This proves that there is no one right calibration, but different options, all leading to the same objective. Overall, a and τ seem to be the most suitable parameters to begin the calibration with, as the change in the parameter value following the presented procedure leads to a suitable change for a steady improvement. The change in n and b on the other hand, is very small, and therefore, needs more than one iteration in the calibration. Therefore, although the result might be better when changing n and b , for improved efficiency it is better to focus on a and τ .

On a more general note, for the calibration the ideal settings are as close to the real SMC process as possible. This facilitates the replicability in simulation and improves the transferability of the results to real conditions. If the replicability is better, the reliability of the results is also improved. Therefore, as the standard setting of 3DTimon is displacement control, performing simulations with displacement control is recommendable. Nevertheless, for industrial applicability the sensitivity analysis for force control is included, as to provide suitable data for any available test equipment.

3.3.3 The new calibration procedure

Within this subsection, calibration for the ip flow and oop flow have been performed. It is evident, that the ip flow calibration is not sufficient to depict the material behavior in the more complex bar flow setup. The ip calibration seems to be necessary for a first improvement of the parameters, which are then optimized in a subsequent oop calibration. However, in order to fully assess the necessity for the ip calibration, a further study shall be performed. Within this study the first calibration shall be omitted, and the oop calibration shall start with the parameters from the fitting. Maybe it is sufficient to perform more oop calibration steps, and reach the same accuracy as can be reached with the ip calibration step. This has not been further investigated, but since the force signal depends on many factors it is likely that the material card obtained in the ip calibration is more accurate when simulating relatively simple geometries with simple flow patterns, while the material card from the oop calibration is better suited for complex ge-

ometries. However, this arises the question, what can be considered a simple flow pattern and geometry and what has to be considered complex. This differentiation and any related implications have to be further investigated.

Based on the findings presented for the three different calibrations and the three related sensitivity analysis, a recommended calibration procedure could be identified to cover both in-plane flow for simple 2D geometries, and our-of-plane flow for complex parts, consisting in two steps, as shown in Fig. 3-44.

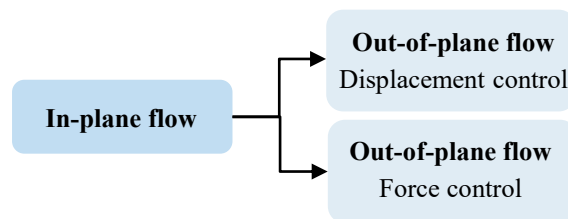


Fig. 3-44 Schematics of the calibration procedure with in-plane procedure as first step, followed by the out-of-plane calibration, where it can be chosen between displacement control and force control.

The recommended procedure for the calibration consists in performing both an in-plane and an out-of-plane calibration, in order to have a suitable material card for both categories. Since both calibration steps are recommended, the out-of-plane calibration shall be performed based on the in-plane calibration in order to start with an already improved result that may be already satisfactory. If the intention is to simulate only a one geometry type, one calibration step with the suitable flow pattern is sufficient. For the out-of-plane calibration it can be chosen whether a displacement control or force control setting shall be used, based on equipment availability. However, among the two options, displacement control is preferable as it is closer to the actual process.

3.4 The new procedure for flow characterization

On the basis of all findings reported in the previous subsection, a general procedure for the determination of the parameters for the curing kinetics and the rheological model has been identified (see Fig. 3-45). The existing process for each step of the procedure has been extended and detailed in order to optimize the procedure for industrial applications taking into account the high variability of the material. In the first step of determining the curing kinetics a new analysis procedure is developed to include the variability of the material in the final result of the fitting. In the second step of the fitting of the squeeze flow test results to the viscosity models for low and high temperature viscosity, several practical guidelines have been derived and a suitable procedure proposed. The final step of the calibration has been split into two steps, where the first step is an in-plane calibration with the comparison of the squeeze flow tests with squeeze flow simulations. In a second step, the out-of-plane flow is calibrated by comparing bar flow

tests to bar flow simulations. For this step both possible compression settings of displacement control and force control are evaluated. For each calibration a sensitivity analysis has been performed and the results summarized.

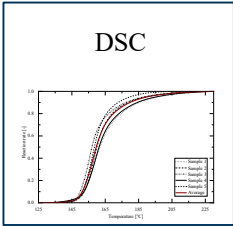
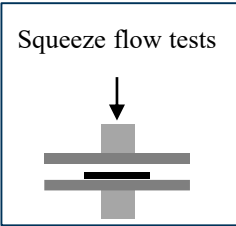
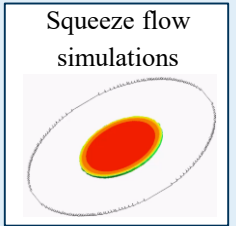
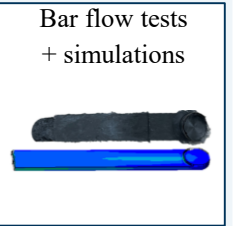
	Curing kinetics	Viscosity	Calibration	
Procedure	Kamal Equation Curing rate $\frac{d\alpha}{dt}$	Andrade Model $f(T)$ Castro-Makosco Model $f(\alpha)$ Cross Model $f(\dot{\gamma})$	Calibration In plane flow	Calibration Out-of-plane flow <ul style="list-style-type: none"> • Displacement control • Force control
Activity	DSC 	Squeeze flow tests 	Squeeze flow simulations 	Bar flow tests + simulations 

Fig. 3-45 Schematic overview of the modified characterization procedure for the establishment of a suitable material card for SMC.

The derived procedure for the evaluations, the calibrations, and guidelines have been summarized in the conclusions of each subsection. Furthermore, a summary of an overall procedure and of the tables with the result for each sensitivity analysis are given in the appendices d and b respectively in order to be used as a handbook for future calibrations.

3.5 Discussion

Within this chapter a new procedure has been developed, to determine the parameters for the curing kinetics and the rheological behavior. The new procedure has been developed from the state of art on the basis of several requirements set in the introduction of this chapter.

The first requirement was to include the variability of the material. This was met in most evaluations since five repetitions were performed for almost all tests. The only exception is the squeeze flow tests, where for the low temperature only three repetitions were done and for the high temperature only one. In future evaluations it is recommendable to increase the number of repetitions, even if that means having less settings overall, i.e. less different temperatures or compression speeds.

The requirement of simplicity is met by providing detailed step by step instructions for the analysis with the developed procedure. The fast application requirement however, is only partially met, since a fully automatic evaluation of the data is not set. In future

endeavors the whole analysis procedure shall be fully automatized in an in-house fitting tool, so that the user only has to select the files of the raw test data of DSC measurements and squeeze flow test and the start and end point of the baseline in the DSC measurements. Everything else necessary for the fitting is done automatically. The same shall be developed for the calibration procedure, with a tool importing and analyzing the raw data obtained in simulation in order to compare it to the tested results.

The industrial applicability of the procedure can also be deemed to be high, since only standard equipment is used for the tests and for the out-of-plane calibration potentially any kind of press and tool can be used. However, it is recommendable to apply settings that are as close to reality as possible.

Furthermore, the developed procedure presents full flexibility towards the mathematical description of the rheological model and curing kinetics, allowing for unhindered applicability for any fitting tool. However, the flexibility is limited to viscosity models with the same functional dependency of the viscosity from temperature, shear rate and curing rate.

The last requirement set for the new procedure of being valid for the production of any SMC part is also fulfilled, since the calibration is not linked to specific geometrical features for the calibration. Therefore, it is not necessary to repeat the calibration with a different geometry for every new part produced. This saves time and resources. However, it has to be understood more in detail what the influence of specific geometrical features is.

Despite the found procedure being satisfactory in many regards, several further investigation possibilities have been mentioned at the end of each section. Overall, it is clear that further understanding has to be gathered about the behavior of the material for specific process settings, such as temperatures, compression speeds and compression pressure. Also a different industrially produced SMC material shall be characterized with the procedure, in order to determine the applicability to all SMC materials. The SMC itself also needs to be better understood in relation to its variability within one batch and between different batches of the same material. A better understanding of the involvement of the fibers in the flow would also be beneficial. But a good quantification can only be done for glass fibers for now, since NDT methods to investigate the fibers in finished CSMC parts in a statistically relevant volume do not exist yet.

4 A new bar flow test bench for SMC flow characterization

The rheological characterization process of SMC to obtain the viscosity parameters requires a calibration step, typically performed by producing a part similar to the geometry that shall be simulated with that specific material card. The similarity regards mainly the overall size and geometrical features like ribs, inserts or wall thicknesses (characterization process described in detail in Section 2.3). This approach is rather inconvenient, as it implies that accurate simulations can only be performed if similar geometries already exist. Therefore, a generally valid calibration tool is necessary, catering to most desired complex flow patterns. The flow test bench has to be able to capture the spectrum of the variability of the rheological behavior in order for the simulation to numerically depict all possible variation.

The overall goal of the test bench is the rheological characterization of SMC to:

- Calibrate the material card for SMC flow simulation;
- Capture the variability in flow behavior of SMC.

As discussed in the state of the art, the flow behavior of SMC has many influences, among which the complexity of the shape, the flow length, the process settings, etc. Furthermore, due to the dependence of the flow behavior on the compression speed and the temperature of the molds (see Subsection 2.3.2.2), the process settings should be as close to the real process as possible. Based on those findings, the characterization tool has to display the following features:

- Investigate out-of-plane flow, as it is typical for SMC parts, and should complement the in-plane flow of the squeeze flow tests;
- Allow processing parameters similar to the real process, with regard to temperature and pressure profiles and closing speed, improving transferability to other SMC parts;
- Show geometrical features that are typical for SMC parts, such as ribs;
- Have an accurate recording of the pressure.

As presented in Section 2.3, several tools for flow characterization have been introduced over the past decades. These setups have been evaluated based on their suitability for this evaluation based on the criteria presented above. The evaluation is summarized in Tab. 4-1.

Tab. 4-1 Evaluation of flow test setups adopted in literature for the investigation of the flow behavior of SMC, with regard to the type of flow to be obtained, the application site of the setup, the complexity of the geometry, and the accuracy of the pressure data.

	Kia 1993	Bird 2003	Lee et al. 1981	Duhovic et al. 2018	Schommer et al. 2019	Kotsikos et al 1998	Barone et al. 1985	Le Corre et al. 2002	Dumont et al. 2003	Olsson et al. 2009	Guiraud et al. 2012	Oelgarth 1997	Abrams et al. 2004	Ritter 2003
Reference	[20]	[107]	[69]	[106]	[42]	[110]	[70]	[117]	[65]	[115]	[66]	[122]	[120]	[123]
Flow	Ip	Ip	Ip	Ip	Ip	Ip	Ip	Ip	Ip	Ip	Ip	Ip	Ip	Ip
Site	UTM	UTM	Press	Press	Press	UTM	Press	UTM	UTM	Press	UTM	UTM	-	Press
Geometry	plate	plate	plate	plate	plate	plate	plate	plate	plate	plate	plate	plate	plate	plate
Accuracy p	high	high	high	low	low	high	-	high	high	-	high	high	-	low
	Specker 1990	Hohberg et al. 2017	Vahlund et al. 1999	Rienesl et al. 2022	Gibson et al. 1999	Odenberger 2004	Castro et al. 1989	Kau et al. 1987	Silva-Nieto et al. 1981	Lin et al. 1997	Hohberg et al. 2022	Kim et al. 1997	Dumont et al. 2007	Kröger 2017
Reference	[125]	[67]	[112]	[111]	[109]	[61]	[36]	[124]	[116]	[119]	[40]	[130]	[128]	[131]
Flow	Ip	Ip	Ip	Ip	Ip	Ip	Ip	Ip	Ip	Ip	Oop	Oop	Oop	Oop
Site	Press	Press	Press	UTM	UTM	Press	Press	Press	UTM	UTM	Press	UTM	Press	Sep.*
Geometry	plate	plate	plate	plate	plate	plate	plate	plate	plate	plate	rib	rib	steps	rib
Accuracy p	low	high	low	high	high	low	high	high	high	high	low	high	high	low

*separate setup

Most test setups only test in-plane flow, which does not include the complexity of the SMC material, excluding most of the state of the art applications. The site indicates where the test setup is to be applied. This is typically in SMC press or a UTM, except for the test stand in [131], which can be operated on its own. "Geometry" refers to the configuration of the test setup featuring only a plate, with potential sensors or more complex features, such as ribs. As the test settings should be as close as possible to the real process settings, an application in a press is to be preferred. However, the pressure recordings of industrially available presses are not highly precise, as the recording is done over the compression cylinders, which behave differently depending on the local temperature and loads. Therefore, in order to have a higher accuracy than 1 % in the pressure signal when using a press, additional pressure sensors have to be placed inside the mold. In a UTM, on the other hand, the accuracy of the pressure signal is already sufficiently high. Based on this evaluation, none of the setups satisfies the set criteria.

Therefore, a new test bench was developed internally, depicting a more complex flow state and typical industrial processing parameters for SMC parts.

4.1 Methods

For the development of the test bench the process defined in by VDI 2221 was followed [143]. The layout of the control cycle underlying the guideline is shown in Fig. 4-1.

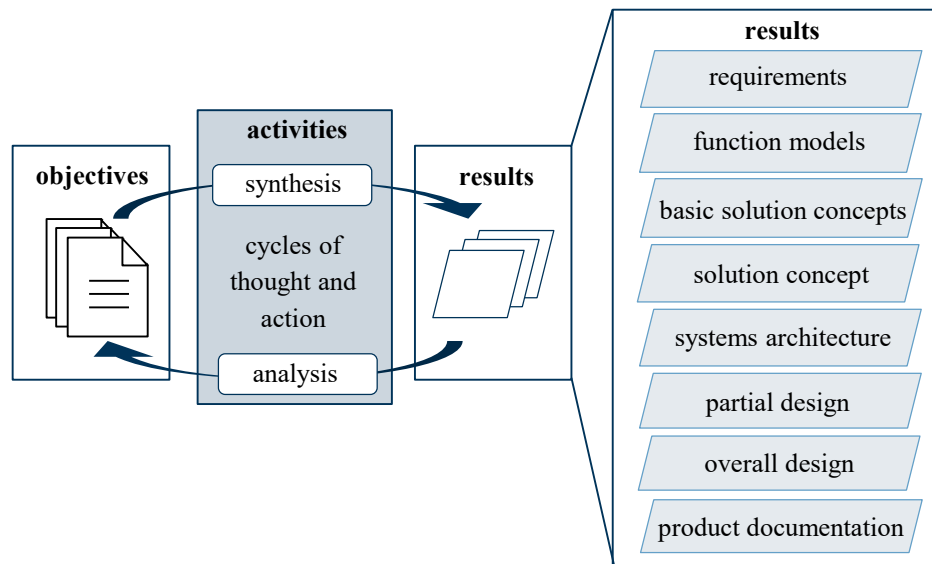


Fig. 4-1 Control cycle between objectives, activities and results, and detail of results, adapted from [143–147]

The control cycle to find a solution to any problem consists in four main steps: identifying the objectives, pursuing activities to find solutions, obtaining results, and analyzing the results, in order to define new objectives and start the cycle anew. The different obtainable results are listed in detail on the right. In this development task, in the concept phase, ideas were collected with brain storming in a workshop with four people with an engineering background. Afterwards, a morphological box was set up within the same constellation of participants. The implementation is concluded with a test phase and the documentation. Necessary improvements are implemented with a new loop of the phases.

4.2 Development process

The content of this section has been partially developed in two student thesis [S10, S14].

In a first step, requirements for the flow test bench were collected. Overall the main requirements were the goals pointed out in the introduction to this chapter:

- accurate recording of the pressure;
- geometrical features typical for SMC parts;

- the process parameters shall be close to a real process in terms of compression pressure, temperatures, heating behavior, mold characteristics, etc. as explained in Chapter 2 State of Art.

The morphological box setup for possible solutions is represented in Tab. 4-2.

Tab. 4-2 Morphological box for the flow test bench, with the chosen configuration marked with blue (1st version) and green (2nd version) dots. The main configurations are connected with a blue (1st version) and a green (2nd version) line.

Module	Parameter	Solution 1	Solution 2	Solution 3
Heating system	Principle	Oil	Water	Electric ●
	Heating Area	Local	Uniform ●	
Geometry	Shape	Spiral Flow	Squeeze	Channel ●
	Channel thickness	Constant Single ●	Constant Double	Changing
	Channel height	Constant Single ●	Constant Double	Changing
	Charge placement	Beginning of flow Channel ●	Middle of the flow Channel	
	Charge pattern	Roll ●	Cut stack ●	Uncut stack
	Flow Channel Kinematics	Unidirectional	Bidirectional	Multidirectional ●
	Functioning principle	Force actuation	Pneumatic	Hydraulic
Speed		Constant Single	Constant Multiple	Variable ●
Compression direction vs flow		Parallel	Perpendicular ●	Variable
Control System		Force Control ●	Displacement Control ●	
Signals and control	Pressure Sensor	Beginning of flow channel ●	End of flow channel	Middle of flow channel
	Temperature Sensor	In line over channel length ●	Randomly	
	Flow Tracking	Pressure Sensors	Temperature Sensors ●	Video Tracking ✕
Sensors	Body Material	Stainless Steel ●	Aluminium	
	Integration	In contact with material ●	Contact-free	
Overall Setup	Connections	Electric ●		
	Mobility	Palette	Separate stand	Tool for press ●
	Mold (Stainless steel)	No Glass ●	Glass on the upper side ●	Glass on the lower side
Heating system	Heat transfer	Air ●	Metal ●	
	Homogenization	Glass fiber mat ●	Aluminium box ●	Metal parts ●

● chosen configuration of first version ● adaptations in second version

The solutions are the result of a workshop with four engineering researchers and students (Y. Shinoura, R. Sharwalla, J. Hoffelner, and Chukwunonso H. Uzodinma). The chosen settings for the first version are marked with blue dots and linked by blue lines. In some cases the chosen possibilities are multiple, such as for the control system, as in the final setup both displacement and force control are possible. However, the main setting is linked by the blue line, the secondary option is only marked with a dot. The main requirement was for the test bench to be as close as possible to a typical SMC process. Therefore, comparable compressions speeds and pressures were required. Furthermore, the application of more than one constant compression speed had to be possible to replicate the typical displacement control. The temperature distribution had to be as uniform as possible and the temperature distribution had to be done with metal contact. The additions and changes performed during the second loop are marked in green. For this step, the last two points for the heating system were added to the evaluation. Therefore, the first solutions, marked with blue dots, are not linked with the blue line. As can be seen, the main changes were the elimination of the optional flow tracking via video as the glass plate on the upper mold was taken out. This step is explained in Section 4.3 in the section about the first version of the test bench. Furthermore, the heating system was significantly improved by implementing a heat transfer with metal plates and covering the setup with an aluminum box. The first and final versions of the test bench are described in detail in the following section.

4.3 The test bench

The content of this subsection has been published in similar form [J2].

The final test bench, as well as the intermediate iteration can be seen in Fig. 4-2.

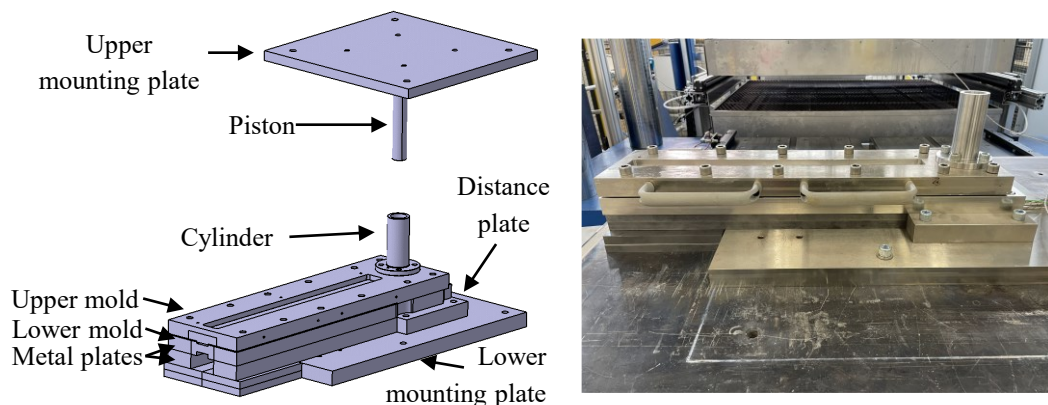


Fig. 4-2 Setup of the test bench and identification of the main components.

The final test bench consists of an upper half mounted to the top plate of a press with a mounting plate. The main feature of the upper half is the piston that will apply the pressure on the SMC during the test. The lower half consists of the main mold, which is completely closed. Furthermore, a cylinder is placed at the beginning of the mold to contain the raw material that is going to be compressed. At the front of the upper tool

handles are placed, which are also visible in Fig. 4-3, showing the detail of the metal plates and the handles, as well as a broader image of the setup inside the intended press.

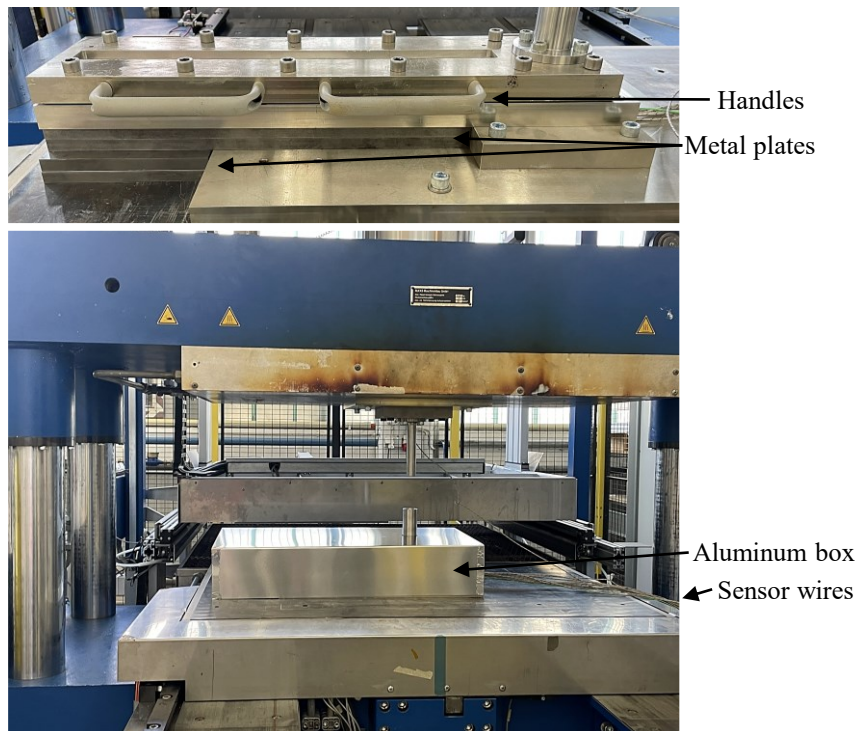


Fig. 4-3 Barflow test setup with detail of handles and metal plates and placement inside RUCKS thermoforming press covered with an aluminum box for improved thermal management.

In the broader perspective the aluminum box used to cover the setup for improved thermal management can be seen. Also the sensors wires can be identified on the right side exiting the cover. The test bench was developed to be adopted in a RUCKS Thermoforming KV 289.00 machine, which can apply the typical processing conditions present in SMC part manufacturing. Those include a heated upper and lower plate, constant closing speed during the compression and it can apply the required pressure. To improve stability and the thermal management of the setup, but also keep the setup flexible, several metal plates were introduced, to hold the mold and spread the temperature from the heated press more evenly. Moreover, an aluminum box was developed, to closely fit over the setup. As the mold is closed during the test, it has to be opened to extract the specimen. For more convenient handling of the heavy upper mold when opening the mold after each test, handles were attached (further details about the functioning principle below).

Along the lower mold several in-mold sensors track the temperature and pressure data, as shown in Fig. 4-4.

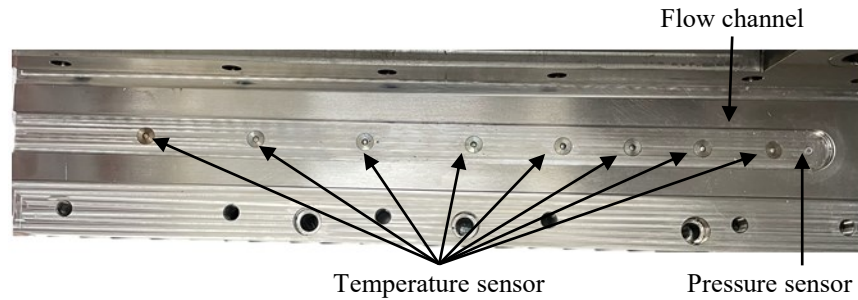


Fig. 4-4 Inside of the lower mold with a pressure sensor at the beginning of the flow channel and eight temperature sensors aligned along the low channel.

As can be seen in Fig. 4-4, right underneath the piston there is a cavity pressure sensor of the type 6163AC3,0 from Kistler Instrumente GmbH to record the compression pressure. A load amplifier from Kistler Instrumente GmbH, a measuring amplifier QuantumX MX410B and the software MX Assistant 4 are used for the data acquisition. The sensor can be calibrated to the pressure of 100 bar and 1000 bar. Along the flow channel additional eight temperature sensors are placed, to track the temperature of the channel. The first four temperature sensors are placed closer together, for a more precise flow front tracking in the first part, as most charges will only flow that far. Additionally, three temperature sensors were placed on top of the upper mold, one on the cylinder and one on the piston to track the overall temperature of the test setup.

4.3.1 Functioning principle

The general functioning principle of the test bench, with the closed mold and the moving piston is shown in Fig. 4-5.

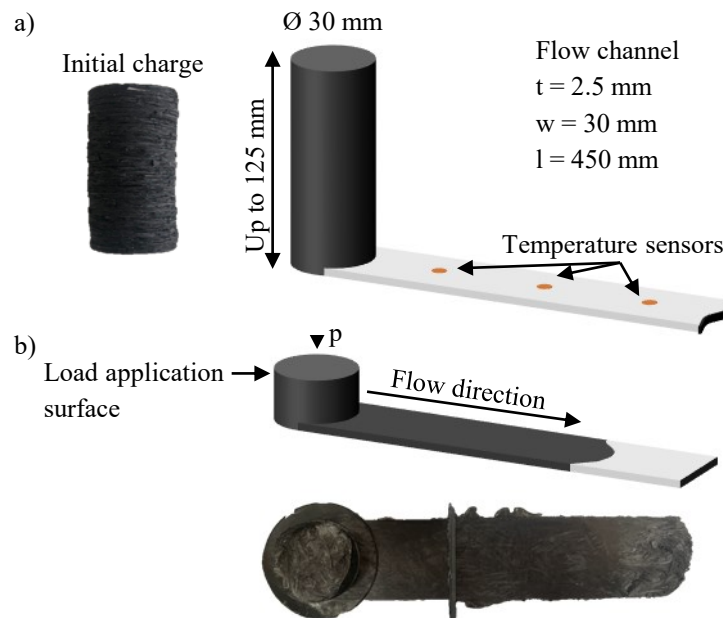


Fig. 4-5 Functioning principle: a) measurements of the cavity and the initial charge, with exemplary charge from the test series, b) load application surface and flow direction with exemplary specimen from the test series.

A cylindrical charge is placed inside the cylinder, and the piston presses it into the bar inside the closed mold. Once the compression is complete, the press stays closed for the necessary time to insure full curing of the material. After the opening of the press, the specimen can be taken out of the closed mold by unscrewing the upper mold half from the lower mold half. The opening of the mold reduces the overall temperature of the setup, which has to be reheated to the desired temperature before performing a subsequent test. The cavity consists of a 450 mm long 2.5 mm thick and 30 mm wide flow channel, as shown in Fig. 4-5a. The thickness of 2.5 mm corresponds to a typical wall and rib thickness adopted in SMC part design. The width was chosen to 30 mm in order to be as small as possible but still a little wider than the fiber length to facilitate the flow in the central area and have at least a small amount of fibers not redirected by the walls or cut for the charge preparation. The length of 450 mm is relatively long for SMC, in order to be able to cover cases that exceed the typical applications. In Fig. 4-5b the compression process is schematically represented. With the application of a compression force on the circular load application surface in the cylinder, the material is compressed and flows into the flow channel. An exemplary resulting specimen with the typical cylindrical shape on the left and the bar to the right is shown underneath.

4.3.2 First version of the test bench

After the first development loop, a first version of the test bench was setup. This first version of the test bench in direct comparison to all implemented improvements can be seen in Fig. 4-6.

As can be seen in Fig. 4-6 the first version of the test bench is very similar to the final design. The first adaptation consisted in substituting the glass plate in the upper mold with a metal plate, as it could not withstand the high in-mold pressure. The glass plate was fixed to the containing cavity with silicone glue. The metal plate fit perfectly into the hole and has not been fixed in its position by further means than positive locking. Unfortunately, with this adaptation the option to observe the flow via camera is not possible anymore. But as the flow observation and tracking via camera was only optional, it does not limit the test bench in its principle purpose. In confirmation of the in-mold pressures being too high, the glass broke only as far as the material would flow, as can be seen in the picture displaying the problem related to the feature. The second major aspect that had to be improved in terms of usability was the heat management. The floating concept of the mold and therefore, the very consistent air contact made the heating to a homogeneous temperature along the flow channel very difficult. Furthermore, in the first version the insulation of the tool was done with a glass fiber fleece. In the new version, as shown in the final test setup, this was substituted with an aluminum box, as the glass fiber mat melted and the insulation did not work satisfactorily. One test cycle would take about 3-4 h, and the initial waiting time before the first test was about 5 h. These times were reduced to 1-1.5 h on average between tests, and 2.5 h before the first test of each day.

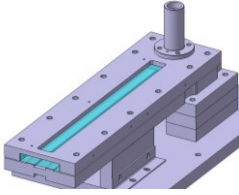


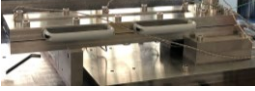
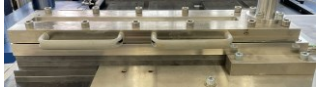


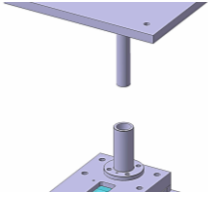

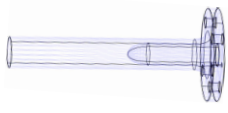

	First version	Problem	Solution
Glass plate			 Metal plate
Heat transfer to mold		Very slow heating of the entire channel	
Insulation of the setup		Glass fiber vlies melted Fast heat dissipation	
Centering			Smaller circumference for piston
Compression pressure with DMS		Pressures too high	 Piston without hole

Fig. 4-6 Configuration in the first version, related problems and their respective solutions for the new version. All options have been implemented, except for the last one, which shall be done before any future testing.

Another adaptation was the decrease in circumference of the piston from 30 mm to 28 mm. Originally, the cylinder and the piston were thought to also work as centering unit. However, this approach proved to be too optimistic. In the final version, no centering was applied. Furthermore, in the first version the piston was designed with an opening in the middle that would allow a tracking of the actual compression pressure by applying a DMS within the opening. However, this decreased the compression strength of the piston significantly, and lead to heavy deformations, which made the centering efforts mentioned above irrelevant. In the new design the piston was intended not to have the opening, but due to material scarcity, eventually the same piston was simply adapted for the smaller circumference. This led to new deformations during the last test performed with the test bench. However, the last test series was not intended for this thesis. The adaptation of the piston shall be pursued before any future test series.

In summary, three main adaptations have been pursued:

- the glass plate in the upper mold for optional flow tracking was replaced with a metal plate, as the glass could not withstand the high in-mold pressures;

- Metal plates were added below the mold for better support and especially for improved heat transfer from the heated lower press surface to the mold;
- The Aluminum box was added for improved thermal management.

For further evaluations, it was intended to add a displacement tracking option. However, due to delivery issues the parts did not arrive on time for all the performed tests. Nevertheless, this optimization is recorded for future utilization of the test bench.

4.3.3 Functional tests

In order to establish, whether the setup meets all requirements, and which improvements could be implemented, functional tests were run. The exact parameters and the setup of the tests can be found in Chapter 5 in the materials and methods. An exemplary result of the outcome data from the first version and from the new version can be seen in Fig. 4-7.

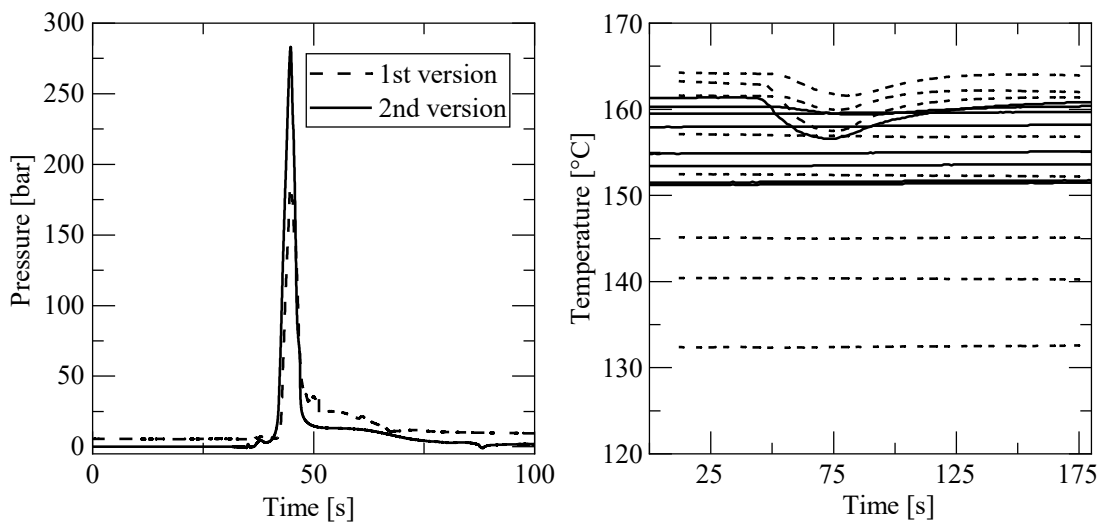


Fig. 4-7 Result of the pressure and temperature recording during the functional tests for the final version and the first version.

As can be seen in Fig. 4-7, in both versions the data tracking for the temperature and the pressure worked well. Therefore, in this regard the tests were successful. However, whenever the piston would scratch along the inner walls of the cylinder in the first test round, the resulting pressure signal on the bottom of the cylinder is influenced, as can be seen in the curve oscillation around 50 s. The implemented improvements helped reduce the influence of the setup on the resulting compression pressure significantly. Furthermore, it is evident, that the temperature difference between the eight temperature sensors over the whole flow channel was significantly reduced from over 30 °C to a little over 10 °C. Therefore, the test setup was significantly improved from the first to the second and final version.

4.4 Discussion

As already mentioned, the functional tests were successful, with a typical set of process parameters for SMC, and a satisfactory data collection for the temperature and pressure sensor signals. Therefore, the test bench complies with all three main requirements set at the beginning of the development:

- it has an accurate recording of the pressure;
- it allows processing parameters similar to the real process, with regard to temperature and pressure profiles and closing speed;
- it shows geometrical features that are typical for SMC.

Advantages

The developed bar flow test bench has several significant advantages, which are:

- allows complex flow;
- closed shape, comparable to real SMC parts with walls stopping the flow
- thickness of the bar mimics a typical thickness of ribs, in order for the results to be transferable to the filling of ribs
- use in a production press, allowing the use of industrially relevant pressures and closing speeds;
- constant compression speed applicable, as in the industrial process;
- good thermal management with a cycle time per test of 1-1.5 h on average;
- good tracking of the compression pressure;
- good transferability of the setup into simulation for the calibration of material parameters (more details in Chapter 3);
- flexibility of the setup, with modular sizing of the molds and additional plates;
- good maintainability, due to easy exchange of relevant parts, such as the contact surface area in the upper mold.

Further improvements

Despite the newly developed bar flow setup having several significant advantages, it also presents a few challenges. Among the challenges is the tracking of the exact position and closing speed. A feasible solution is the installation of a displacement sensor. The press tracks the displacement by default along the guiding cylinders. However a specific device on the test bench would increase the precision. Another aspect, that needs to be improved, is the piston, which was designed to have a DMS inside to track the compression of the material and therefore, the pressure applied from the piston. In theory, this would give a more precise value for the pressure applied on the material compared to the pressure sensor on the lower side of the mold. However, in reality the opening weakens the piston significantly and the tracking of the pressure with a DMS is quite challenging to realize. In order to improve the press capacity of the piston and prevent bending, a new piston shall be produced without the opening for the DMS.

Next to highly recommendable changes, there are a few other improvement options that could increase the application spectrum of the test bench. For instance, flow tests under vacuum could be interesting for another industrially relevant application. Although, in SMC processing the application of vacuum is present in only 50 % of applications, constituting an interesting adaptation or increase of its functions. Furthermore, different flow channel sizes could be of interest. Especially, successful flow tests with thicknesses that are smaller than the typical 2.5 mm would allow manufacturers to risk producing parts with thinner walls and ribs, reducing the amount of material used. Another significant improvement could be reached with a common control for all recorded data, as at the moment the compression starts, the tracking of the temperature and the pressure have to be started separately.

Further applications

A significant advantage of the test bench is the option to be adopted for further evaluations. For example the temperature data also allows a quantification of the flow speed, as the temperature signal is disturbed once the material reaches a sensor. Furthermore, the exothermal curing reaction can be identified, due to a noticeable temperature increase. The generated heat could be used for the data fitting of the curing behavior, as described in Chapter 3. Although, this application would be challenging, as the material only reaches the first sensor after several seconds, and therefore, with a high probability, the curing has already started. Another suitable application of the test bench is the adoption for incoming inspection for SMC part manufacturers and outgoing inspection for SMC prepreg producers, comparing new batches to old ones. The flow test would be performed in order to see whether the characteristics have changed and therefore, maybe the processing parameters have to be changed too. This comparison of batches is particularly important, as batches can vary significantly, despite officially being the same material, as can be seen in Chapter 5. Another important application is for SMC part manufacturers when using new SMC material. With the tests, the material can be compared to other SMCs previously tested with the setup, in order to find similar materials. Consequently, the range of processing parameters to be tested can be chosen accordingly, reducing the time and costs for the typical trial-and-error approach.

5 Investigation of charge variations influencing the flow behavior with numerical representation

Parts of the content of this chapter have been previously published in similar form [J2].

As presented in Subsection 2.3.2.2, many aspects influencing the flow behavior of SMC have been investigated closely, such as the temperature [46, 69, 110, 120], the void content [66], closing speed [61, 70, 115, 134], the application of vacuum [115], and the volume of the material [70]. Even the deformation of single layers has been investigated closely [70, 115], as well as the deformation of the outermost layer in contact with the press [65, 68]. Moreover, the charge placement in the press was also investigated [36]. However, none of the previous researchers have investigated the influence of charge variations on the material.

The charge is one of the main influencing factors of the flow of SMC material, as discussed in Subsection 2.3.1. The charge is the source of the flow and determines the flow front and directions. It also determines the fiber orientation resulting in the final part, as well as flow-induced defects, such as weld lines. Due to the production process of the sheets (Subsection 2.3.1), the assumption of isotropic material behavior in the plane of the sheet due to random fiber orientation does not apply, as proven by Nony-Davadie et al. [35] and internal mechanical investigations [S20]. Research shows that the fibers have a slight preferred orientation in the movement direction of the carrier foil. Furthermore, the material is highly variable in several characteristics, such as the thickness [S20]. Therefore, a charge made of stacked SMC sheets will have an uneven thickness overall.

Further variation in the charge is introduced in the production process. Here the sheets can be cut into a specific shape and stacked or a rectangle is cut and folded back and forth. SMC parts can be highly complex, as shown in Subsection 2.3.1, especially when parts like trunk lids are produced [31]. In order to ensure complete filling, the SMC is cut to a shape very similar to the part to be produced, with very short flow lengths. In case there are ribs, additional snippets of SMC are placed inside the ribs to ensure complete filling. Both the cutting of the sheet to a shape near the final part shape and the additional cutting and placing of SMC snippets are time consuming. Furthermore, one of the main advantages of almost no scrap during SMC production is lost, if the sheet is

cut to almost the final geometry. The complexity of the parts also leads to a high complexity in the flow patterns. Furthermore, the flow length influences the mechanical characteristics, as the fibers tend to orient along the flow direction [S19].

Especially in sight of a numerical representation, these aspects have to be investigated and an appropriate approach for their consideration in numerical representations has to be identified.

The goals of the study performed in this chapter are the following:

1. Understand the influence of the charge on the flow, by varying and separately evaluating several charge configurations.
2. Develop an approach to include the most relevant aspects into SMC process simulation
3. Derive guidelines from the tests for better processing and simulation.

In order to reach these goals, features of the charge influencing the flow of the material are identified and tested with the newly developed test bench presented in Chapter 4. Different charge configurations are tested with typical SMC process settings. The results are compared to one another and quantified, in order to determine the most relevant aspects. These aspects are integrated into the SMC process simulation approach. Furthermore, guidelines are derived for future charge configurations optimizing the process.

5.1 Test parameters

The material adopted in this study is CARBKID PGK5250-R63 [44], the same as throughout the Thesis. It is described in detail in Section 1.4. The material presents a fiber weight content of 52 %, 25 mm fiber length, 3k tows and is based on a vinyl ester resin. Furthermore, it is isotropic in the plane, the most common sheet configuration on the market.

5.1.1 Specimen configurations

Two charge configurations were considered as a basis in this study (as depicted in Fig. 5-1): a disc pile and a spiral charge.

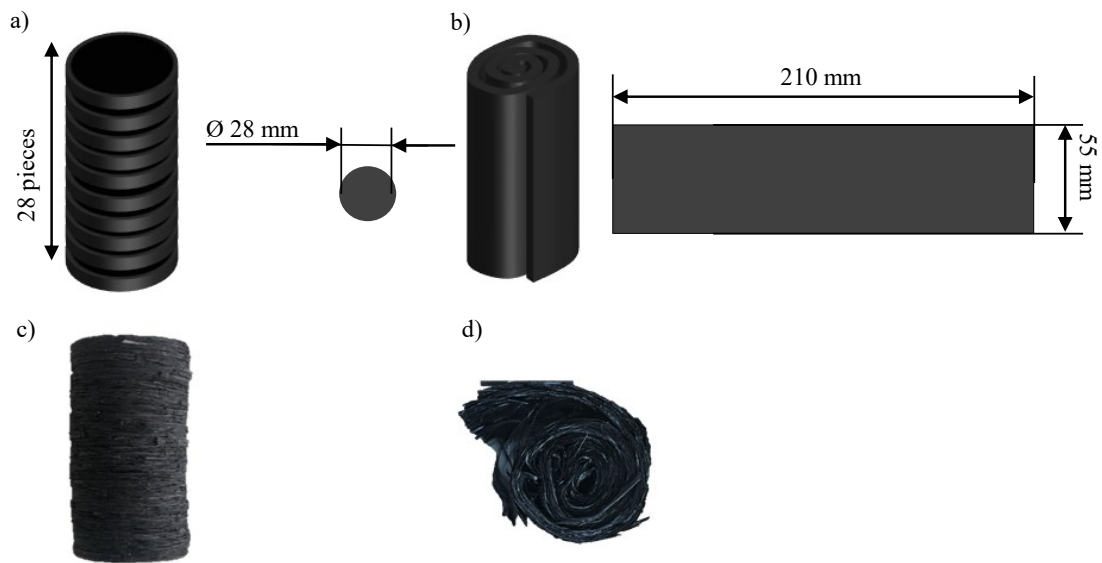








Fig. 5-1 The charge configurations considered in this study: a) configuration of a disc pile charge, b) configuration of a spiral charge, consisting of a rolled up rectangle, c) prepared disc pile charge, d) prepared spiral charge

As can be seen in Fig. 5-1a, 28 discs of a diameter of 28 mm comprised one disc pile charge. The spiral charge shown in Fig. 5-1b consists of a rectangular sheet of 210*55 mm that was rolled up to a cylinder of approximately 28 mm in diameter. In Fig. 5-1c a disc pile charge specimen and in Fig. 5-1d a spiral charge specimen can be seen before the test. As can be seen in the last picture, due to the aforementioned layering in the SMC production, when rolling up the spiral the layers tend to separate from each other, creating additional waviness inside the spiral.

These two base configurations were further varied to a total of six test series (Tab. 5-1).

Tab. 5-1 Performed charge variations

	Disc		Spiral	
Volume	single 	double 	single 	double 
Orientation	oriented 	non-oriented 	—	
Age	new		one year old	

Each configuration was repeated five times, in order to capture as much as possible of the spectrum of results due to the variability in the material, and be able to stipulate a statistically relevant conclusion. The considered variations are related to the amount, the orientation and the age of the material. The amount variation consisted in using double the amount of material, meaning 56 discs stacked for the disc charge and two spirals

stacked for the spiral charge. The definition “oriented” in this case is related to the production direction of the sheet. As mentioned in the introduction, the sheets are assumed to be isotropic in the plane. However, this is not true, as there is a slight preferred orientation of the fibers in the movement direction of the carrier foil [35]. Therefore, in the oriented charge all discs are stacked so that the production direction and consequently, the preferred orientation of the contained fibers is the same. In the “non-oriented” pile the discs were alternated in their orientation to replicate an orthogonal stacking. The third variation is the age. To this purpose, material obtained four months prior to the tests was defined as “within pot life”, as it was stored following the requirements from the producer and therefore, was compliant with all requirements for usually adopted SMC. A second batch defined as “after end of pot life” had been in refrigeration for 13 months. According to the recommendations of the producer, this period exceeds the acceptable storage time, and curing may have progressed too much to still be used for production. Both batches have been stored as recommended at -21°C from the time of delivery. The reference configuration is the non-oriented single amount disc pile charge with new material, as this replicates the most common charge configuration in SMC manufacturing. The variations are applied on this basis.

5.1.2 Process Conditions

The tests are performed with the test bench described in Chapter 4. Therefore, the pressure and the displacement control were set for the press designated for the flow test setup: the RUCKS thermoforming machine produced by Rucks Maschinenbau GmbH. To guarantee the applicability of the obtained results to a series production of SMC, the compression process is displacement controlled. The process profiles of the piston displacement, the force, and the closing speed are shown in Fig. 5-2.

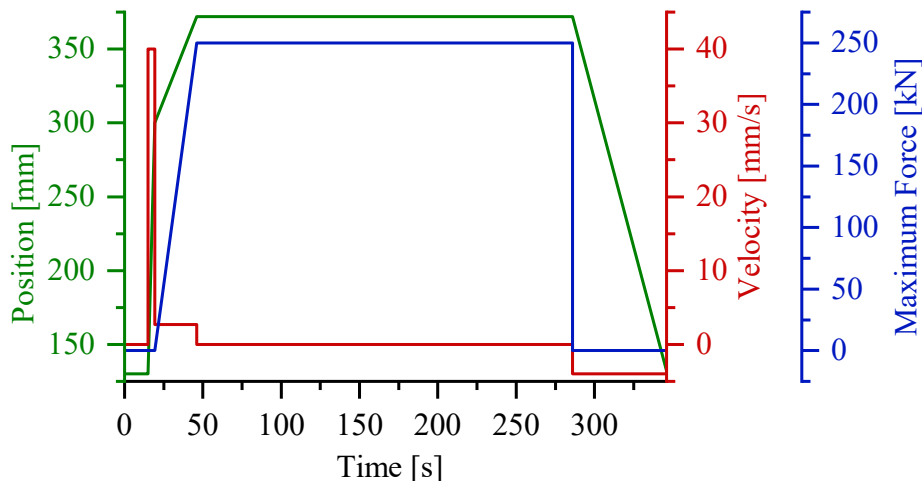


Fig. 5-2 Press profile showing the upper tool displacement position and speed, and the maximum force set for the compression step

After inserting the specimen, a timer of 15 s was started, after which the press program was started. The recording of both the pressure signal and the temperature signal were started at the same time. Before the contact with the material, the piston moved at a speed of 40 mm/s, before slowing down to 2.7 mm/s. The closing speed is set as a percentage of the possible compression speed. For the performed flow tests it was set to 40 % of the compression speed, which was recorded to be 2.7 mm/s. This aligns with an industrial SMC process, where the closing speed is set in a range between 1 and 3 mm/s. The maximum force to be held once the compression was completed was set to 250 kN. Once the press was closed, a timer of 4 min started to allow the material to completely cure before reopening the press. The temperature was set to 160 °C, with a tolerance of ± 5 °C for the sensors inside the flow channel. Once the press was open, the specimen was extracted from the mold and the setup was heated back up to 160 °C.

5.2 Results and discussion

The results of all five tests for each configuration and the related averages can be seen in Fig. 5-3. In order to calculate the averages, the moment the pressure recorded by the sensor underneath the piston was 5 bar was set to $t=0$. The reasons for this adjustment are of two natures: the charges had varying heights, which varied the time of the first contact, and the light barrier of the press was oversensitive and sometimes interrupted the compression. Due to these two factors, the first contact with the material could vary by 2 to 3 seconds. This adaptation allows for a better comparison of the pressure signals, which are the relevant result. From the test signals it is evident that for each configuration the results in the pressure signal are variate, as expected, due to the variability of the material. Furthermore, all disc charges show an oscillating signal with several pressure increases and drops, whereas the spiral specimens show an overall linear development. All configurations show an increase in the pressure signal until the peak. The increasing force necessary to press the material into the bar causes the peak. Two factors cause the increase of the compression force, first of which being the cross section normal to the movement direction becoming smaller from the cylinder to the bar, and therefore, increasing the amount of material to be moved. The second reason is that the material already starts curing during the movement, which increases the viscosity significantly. The compression end criteria where either a force maximum of 250 kN or the piston end position in the cylinder was reached, which corresponded to a final material thickness underneath the piston of 2 mm. In all tests the final position was reached, meaning that in all tests curing happened after the compression. This can also be seen in all the tested specimens. Once the compression stops, the pressure drops as the material relaxes for a very short time before slightly increasing again during the curing, where the material expands slightly. It is visible, that even for tests with the same parameters and charges, the pressure peaks differ in height and in occurrence time. Both aspects are due to the varying heights of the specimens. However, this is not the only cause for differences, as explained more in detail below.

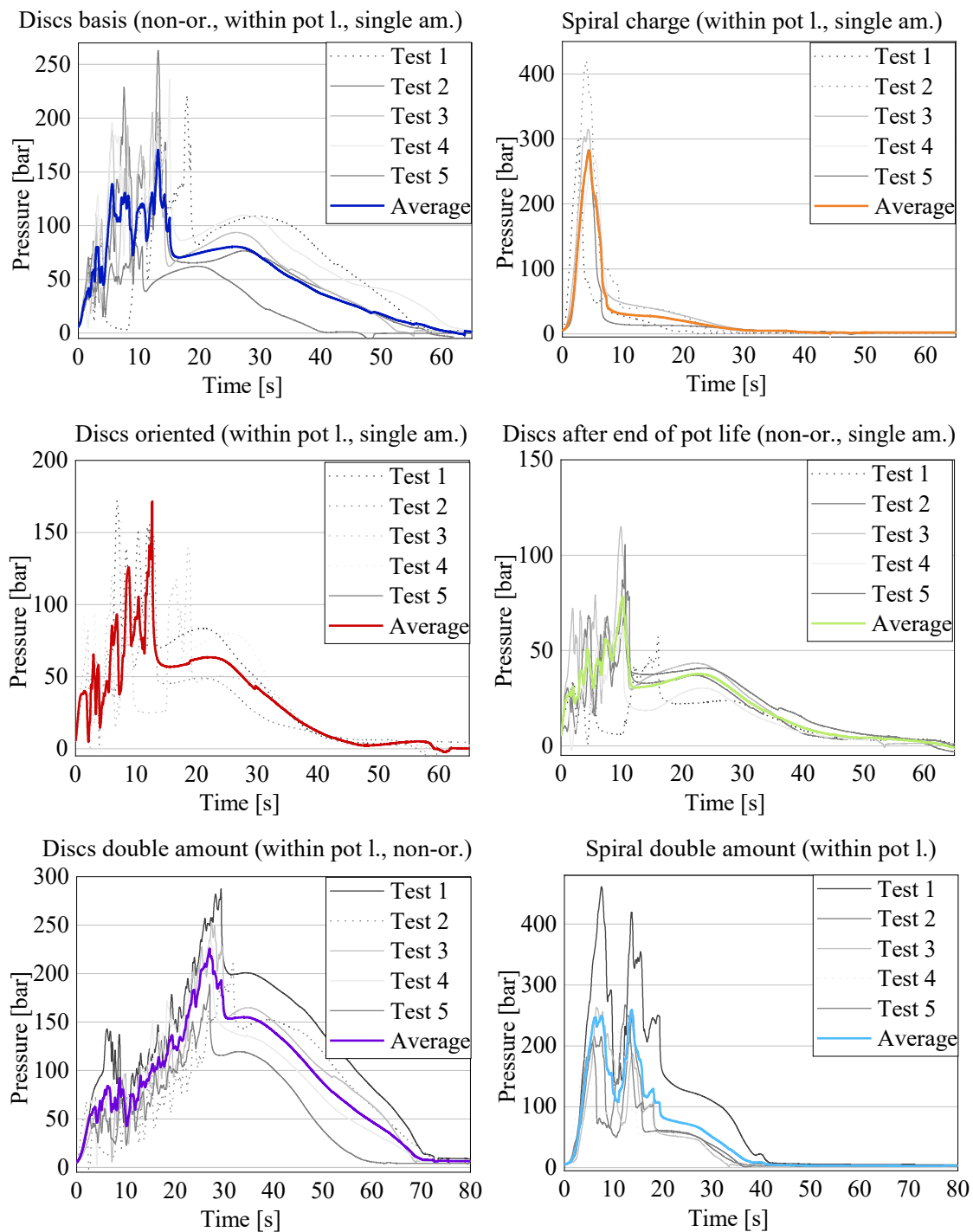


Fig. 5-3 Results for all performed tests and the averages calculated for each sequence

For the calculation of the averages only the continued lines were chosen. The dotted lines are the result of tests where the compression was interrupted due to the oversensitive photoelectric barrier of the press. The change in the signal due to such an interruption can be seen in Fig. 5-4.

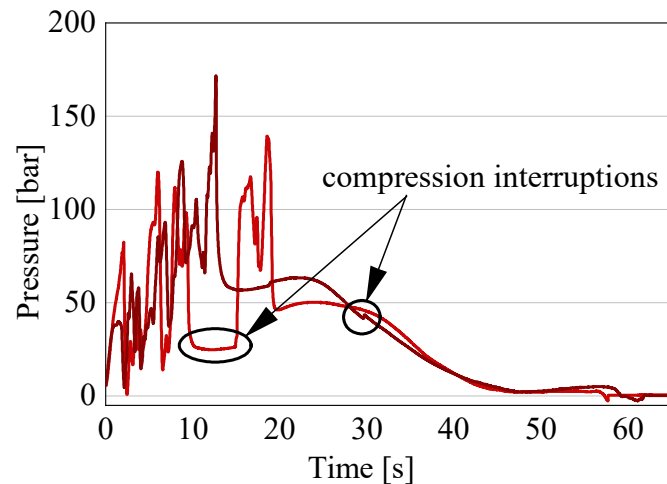


Fig. 5-4 Exemplary interruptions during the compression reflected in the recorded pressure signal

The interruption of the compression leads to a relaxation of the material, and consequently, a significant decrease in the pressure signal. The error was quit within seconds, as can be seen in Fig. 5-4, but the peak pressure is not valid for a comparison. For the test series with the oriented discs, unfortunately, every test except for one has interruptions during the compression. When the interruption happened after the peak, as exemplarily shown for the dark red line, the test was considered for the average, as the topic of interest is the compression step.

5.2.1 Comparison of basic configurations

In a direct comparison between the results for the disc pile charge and the spiral charge the pressure signals show clear differences (see Fig. 5-5).

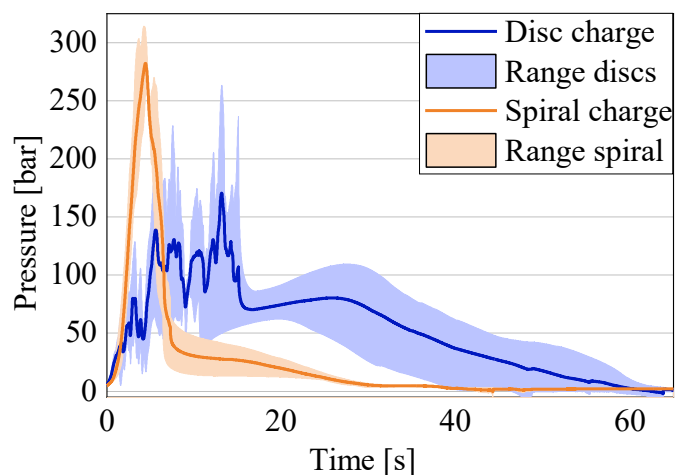


Fig. 5-5 Comparison between the single amount non-oriented disc pile charge and the spiral charge

The average for the basis (single amount disc pile charge, with non-oriented discs and new material), represented in blue, shows a clear oscillation, which is due to various

reasons. Firstly, the fibers are lying in the flow plane, and the cutting edges of the discs are open towards the channel, which makes it easier for the material to flow. Furthermore, between the sheets a small lubricated area is formed, leading to the discs being squeezed into the flow channel separately or in small batches. This leads to a linear pressure increase, while the material collects in the cylinder. When the pressure is high enough, there is a sudden release in the pressure as one or a few discs pour into the flow channel. The rise and drop of the pressure signal repeats itself until the compressions stops, because all the material is in the flow channel or the curing has already started and the viscosity has become too high for the material to continue flowing. This behavior can be seen in all the specimens with a disc pile charge, and is confirmed by all specimens, where at the tip of each specimen the disc shape is still clearly distinguishable, as can be seen in Fig. 5-6.

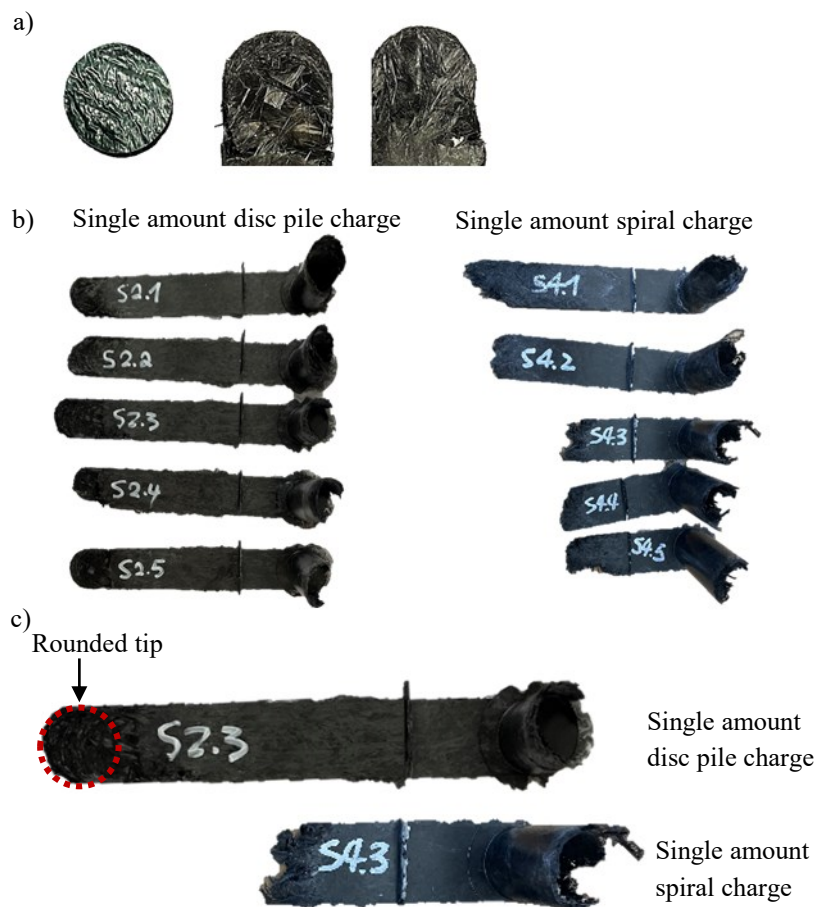


Fig. 5-6 All specimens of the basis (single amount disc pile, non-oriented, within pot life) and the single amount spiral charges: a) detail of the tips for disc charges after the test (right) compared to a disc of uncured SMC before the test (covered with carrier foil); b) all specimens in comparison; c) direct comparison of exemplary specimen for each test series

In Fig. 5-6a the rounded tip replicating the shape of the discs constituting the charge is represented in detail, with a direct comparison of a charge disc of uncured SMC on the left and the tips of two specimens in the center and on the right. This behavior is also

clearly distinguishable in Fig. 5-6b, where all specimens from the two series are displayed. It is also visible, that the material used in the spiral tests is less than for the disc pile charge, especially when considering the last three tests of the spiral charge. The exact difference in weight can be seen in Tab. 5-2 addressing the key values of the test series. In Fig. 5-6c the length difference can be seen again, as well as the very different tip shape, which does not seem to follow any specific pattern for the spiral charges. This is due to two reasons, first of which the orientation of the sheet in the charge, as the fibers are oriented in a plane perpendicular to the flow plane. This means that the fibers have to reorient, before being able to flow into the channel. The second reason is the complexity of the configuration of the uncured sheet resulting from the separation between sheet layers when rolling up the specimen. This phenomenon can be seen in Fig. 5-7.



Fig. 5-7 Spiral charge showing the recurring separation between inner and outer layers of fibers within the sheet

This complex material configuration hinders the flow significantly. Thus, the flow can only be achieved by applying a high pressure. Furthermore, the spiral charge is one piece, with no interruptions in flow direction, leading to the linear increase of the pressure signal.

An overview of the key parameters for the comparison can be seen in Tab. 5-2.

Tab. 5-2 Key results for the basis disc charge (single amount, quasi-isotropic, new material), and the single amount spiral charge

	No.	Peak pressure [bar]	Weight [g]	Compression start [s]
Disc charge	1	221.68	50.7	37.1
	2	263.20	51.4	36.2
	3	205.61	52.3	33.4
	4	236.29	50.4	32.8
	5	84.69	49.5	39.4
	average (2-5)	170.63	50.9	
Spiral charge	1	298.75	39.3	48.5
	2	420.05	44.5	36.8
	3	314.41	34.7	40.1
	4	271.32	33.9	46.0
	5	283.23	30.8	40.5
	average (3-5)	282.32	33.1	

The maximum pressure reached during the tests for the disc charge varies between 84.69 bar and 263.20 bar. The lowest pressure corresponds to the lowest charge weight of 49.5 g. However, the highest weight tested being 52.3 g in test 3 only reached 205.61 bar, the second lowest value. Therefore, against previous expectations, a higher amount of material, does not necessarily lead to an increase in the peak pressure. The spiral charge has an average peak pressure of 282.31 bar, higher than the highest peak pressure obtained for the disc pile charge. The high pressure is due to the complex configuration of the charge, as previously shown in Fig. 5-7, and the fiber orientation perpendicular to the flow direction. Therefore, the orientation and shape of the charge is of the utmost importance, as it can double the necessary compression pressure. When producing complex parts, the charge should be placed so that the cutting edges are facing the longest flow direction in order to guarantee complete filling and keep the compression pressure low. Structures like ribs perpendicular to the sheet are reflected in the test with the spiral charge, allowing to conclude that the necessary pressure for successful filling has to be considerably higher.

5.2.2 Variations of the single amount charges

A direct comparison between the basis (single amount disc pile charge with no preferred orientation) and the results for the variations of the single amount disc pile charge, as can be seen in Fig. 5-8. In all curves for the average, the aforementioned oscillation of the pressure signal can be seen. It is consistent for all tests performed with the disc pile charges. The first diagram shows the comparison between the reference with non-oriented discs and the pile charge with all discs oriented in the same direction as the flow channel. The range for the oriented charges includes all performed tests, whether or not they had an interruption during the compression. It is visible that the highest peak in the oriented charge is 171.53 bar, which is only 0.9 bar higher than the peak in the average curve for the basis (exact data in Tab. 5-3). However, the range of the non-oriented charge includes several peaks exceeding the average significantly. Thus, the general pattern confirms that the slight preferential orientation of the fibers in sheet production direction does have an influence on the necessary compression force when producing an SMC part. This means that the stacking orientation of a charge of SMC is very important in order to reduce production costs, as the compression pressure can be reduced significantly.

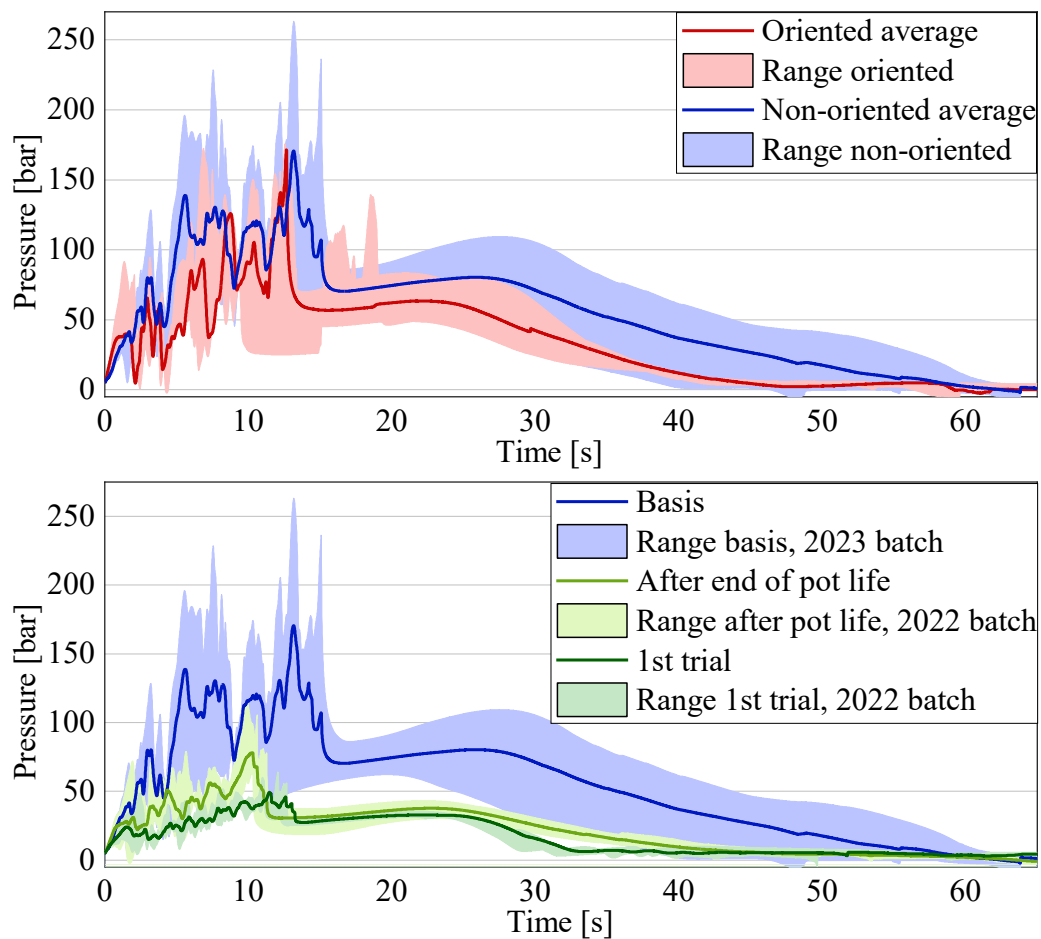


Fig. 5-8 Results for disc pile charges compared to reference (in blue): a) oriented (red) vs. non-oriented reference (blue), b) old material newly tested (light green) vs. old material tested one year earlier (dark green) vs. reference with new material (blue)

When the processing settings remain the same, but the charge orientation varies, as is the case in current SMC production, the flow of the charge will be different and therefore, the final parts will differ. In order to fully quantify the influence of the orientation, an additional evaluation with an oriented pile placing the sheet production direction perpendicular to the flow direction is planned for the future.

A summary of the key values for this first comparison and the following one can be seen in Tab. 5-3.

Tab. 5-3 Key results for the basis, the oriented charge, the tests with the old material, and for the old material in tests performed one year prior

	No.	Peak pressure [bar]	Weight [g]	Compression start [s]	
Discs	Basis*	1	221.68	50.7	37.1
		2	263.20	51.4	36.2
		3	205.61	52.3	33.4
		4	236.29	50.4	32.8
		5	84.69	49.5	39.4
		average (2-5)	170.63	50.9	
	Oriented	1	172.51	44.2	–
		2	147.97	45.9	39.7
		3	139.40	46.9	38.7
		4	175.79	46.7	33.2
		5	171.53	46.5	39.1
		average (5)	171.53	46.04	
	After pot life	1	57.31	43.5	38.1
		2	81.11	44.2	39.9
		3	115.06	43.1	35.5
		4	62.64	41.7	40.8
		5	105.46	41.7	35.8
average (2-5)		78.01	42.84		
1 year old tests	1	56.10	–	37.9	
	2	56.28	–	39.0	
	3	60.22	–	39.5	
	4	63.97	–	38.2	
	average (1-4)	49.40	–		

*quasi-isotropic, new material and tests

Another interesting result can be seen for the comparison between the tests with new and old material. The pressure signals for the tests performed with the old material despite being one year apart are very similar: the peak pressure for the new tests is 78.01 bar, and 49.40 bar for the tests performed one year prior. According to SMC producers, the material can be conserved at -21°C for about a year in order to still be processed without problems. Afterwards, the curing has already proceeded enough for the material to be partially or fully hardened. However, the results show that the conservation of the material in the freezer does not lead to a significantly different compression pressure even when stored over one year. Nevertheless, the results differ significantly from the reference with the peak of the new tests being 45.7 % of the reference peak. All specimens of the old material have a lower weight, which contributes partially to the difference in the pressure signal compared to the basis. However, the decrease should not be as significant, when comparing the signal variations within one batch. Further investigations are necessary to fully explain the difference between the two material batches, as they are labelled as the same material. The authors are currently not aware of changes in the resin formulation. As can be seen in Tab. 5-3, the weights of the

charges show a variation of up to ± 2 g, which is due to the difference in thickness of the industrially produced SMC sheets. This difference in thickness also leads to a difference in the specimen height and therefore, the compression start, which corresponds to the first contact of the piston with the material. Fig. 5-9 exemplifies this issue, showing two specimens before being tested consisting of 28 discs each with very different heights.



Fig. 5-9 Two disc pile charges with 28 discs with different heights due to varying sheet thickness

Therefore, in a future evaluation, it could be interesting to perform the tests with the same weight for the charge, independent from the amount of discs used. The same difference appeared in the tests performed for the double amount charges, as presented in the next subsection.

In the previous test series that included the tests with single amount disc pile charges, also spiral charges were tested. A comparison between the data from the tests of April 2022 and April 2023 can be seen in Fig. 5-10.

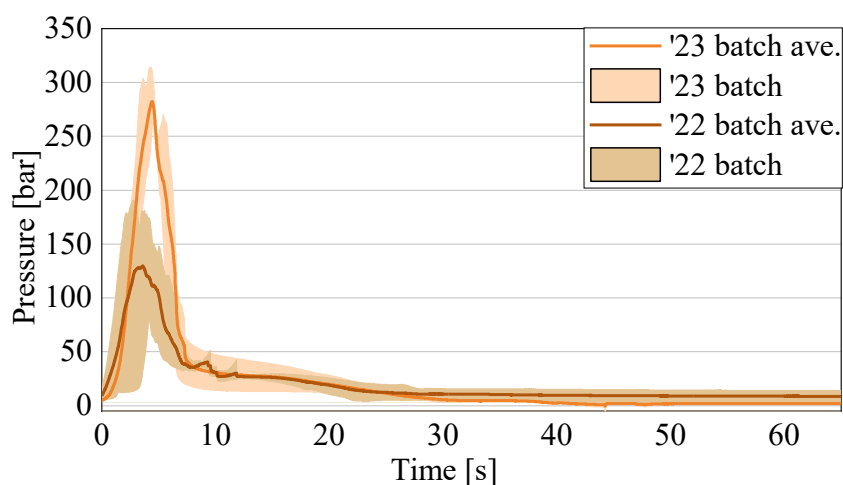


Fig. 5-10 Comparison of the averages and the covered range of the data for the results of the first and second trial of the spiral charges

As can be seen in Fig. 5-10, the range of the previous results is significantly wider than for the second trial, which is probably due to the piston slightly scratching on the surface of the cylinder. Furthermore, the curves resulting for the previous tests of April 2022 are lower than the more recent ones from April 2023, with pressure peaks related to the average of 282.32 bar versus 129.59 bar (see Tab. 5-4). Therefore, for both charge configurations the results obtained one year prior during the first trial are significantly lower, being 54 % and 71 % for the spiral charge and the disc pile charge respectively.

Tab. 5-4 Key parameters resulting for the single amount spiral charge in the first and second (and final) trial

	No.	Peak pressure [bar]	Weight [g]	Compression start [s]
Spiral charge	1	298.75	39.3	48.5
	2	420.05	44.5	36.8
	3	314.41	34.7	40.1
	4	271.32	33.9	46.0
	5	283.23	30.8	40.5
	average (3-5)	282.32	33.1	
1 year old tests	1	148.04	-	41.1
	2	181.21	-	41.1
	3	190.84	-	41.1
	4	169.86	-	41.1
	average (1-4)	129.59	-	

As can be seen in Tab. 5-4, the average peak pressure for the first trial is lower than any separate peak pressure. This is due to the average being based on the same time stamp, highlighted in the column “compression start” with being 41.1 s for all tests, as the pressure increase seems to start there. However, as presented in Subsection 4.3.2, the centering in the first version of the test bench caused some scratching between the piston and the cylinder, which influenced the measurement. Nevertheless, although the results cannot be evaluated strictly in a quantitative fashion, it is clear that the old material batch leads to lower pressure, and therefore, flows more easily given the results of the disc pile charges with material after pot life, the same batch of material tested during this first trial. The smaller range of the results for the second trial also confirms that the repeatability of the new version significantly improved.

5.2.3 Evaluation of the double amount charges

The detailed comparison of the double amount charges can be seen in Fig. 5-11.

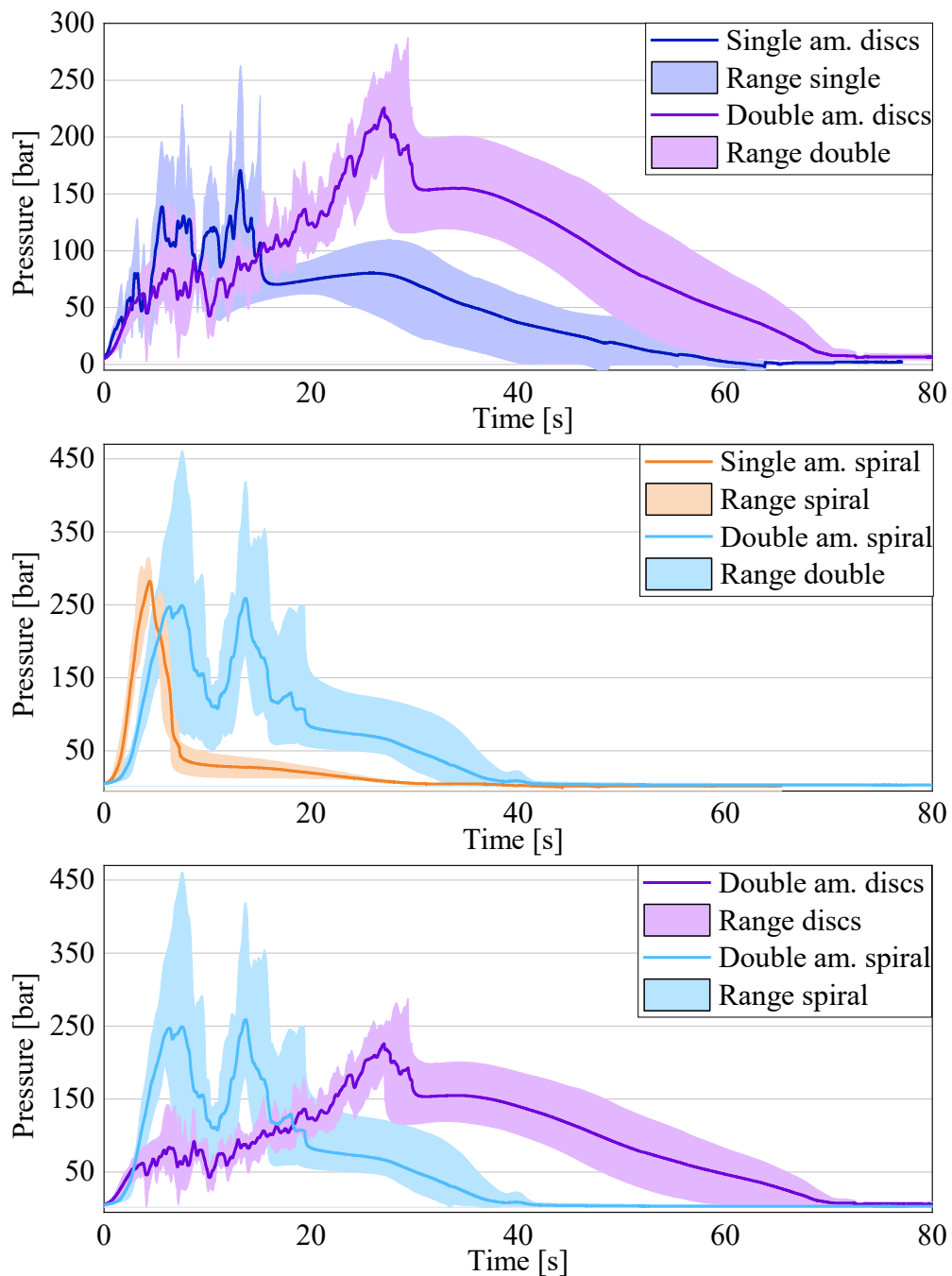


Fig. 5-11 Comparison of the averages of the results for double amount charges with single amounts

The upper left diagram shows that an increase in the material amount leads to an increase in the overall pressure, with the average for the double amount being 225.92 bar compared to the 170.63 bar of the single amount. Nevertheless, the oscillation of the pressure signal, observed in all previous disc pile charge results, is also visible in this configuration. The results for the double amount spiral charge are shown in the upper right diagram. The linear increase in the pressure signal is visible for both the single and the double amounts. However, all results for the double amount charge show a drop of the

pressure signal at half of the displacement, followed by a second steep increase, which corresponds to the separation of the two single amount charges constituting the double amount. The drop due to the separation of the two single amount spiral charges is so significant, that the second peak pressure of 258.67 bar is still lower than the peak for the single amount charge of 282.32 bar. Therefore, when transferring the results to industrially relevant applications, such as to the filling of a rib, it is evident, that a separation between sheets can help the flow significantly. This means that when a charge is placed perpendicular to a rib, a cut in the charge underneath or in close proximity to the rib decreases the necessary compression force significantly. In order to fully understand and quantify the influence of the separation, and the charge weight, additional tests shall be performed in the future, in order to allow for quantified production guidelines. A summary of the key results for the above shown diagrams for the single and double amount charges can be seen in Tab. 5-5.

Tab. 5-5 Key results for the single and double amount disc pile charges, and for the single and double amount spiral charges

		No.	Peak pressure [bar]	Weight [g]	Compression start [s]
Discs	Single amount	1	221.68	50.7	37.1
		2	263.20	51.4	36.2
		3	205.61	52.3	33.4
		4	236.29	50.4	32.8
		5	84.69	49.5	39.4
		average (2-5)	170.63	50.9	
	Double amount	1	287.54	94.9	17.2
		2	210.65	92.9	19.4
		3	252.08	94.2	17.4
		4	233.68	89.5	23.3
		5	188.69	87.8	19.9
average (1, 3-5)		225.92	91.6		
Spiral	Single amount	1	298.75	39.3	48.5
		2	420.05	44.5	36.8
		3	314.41	34.7	40.1
		4	271.32	33.9	46.0
		5	283.23	30.8	40.5
		average (3-5)	282.32	33.1	
	Double amount	1	461.38	74.6	27.7
		2	251.72	71	28.6
		3	262.81	67.6	32.6
		4	224.69	60	30.9
		5	266.65	61.4	28.2
average (1-3, 5)		258.67	68.65		

The oscillation of the charge weight observed previously for the disc pile charges is also visible for the double amount charges, and for the spiral charges. In the double amount disc charge the weight variation for 56 discs increases to ± 3.6 g. For the double amount

spiral charge the variation in the weight is even ± 6.6 g. Furthermore, the heaviest spiral charges for both single and double amount caused the highest peak pressures of 420.05 bar for the single amount and 461.38 bar for the double amount, confirming an overall weight dependence, already observed previously. This weight dependence needs to be further studied and quantified, as exceptions have been observed. It also needs to be specified, i.e. it needs to be defined what derives from the weight that leads to an increase in the pressure peak.

In the direct comparison of both double amount charges, the qualitative development of the curves is very similar to the single amount. However, the peak pressures of 258.67 bar for the spiral charge and 225.92 bar for the disc pile differ by merely 12.7 %, decidedly less than for the single amounts. This highlights again the importance of the separation within the charge. As Tab. 5-5 shows, the weights for the spiral charges compared to the disc charges are much lower. Fig. 5-12 displays a direct comparison between the resulting charges.

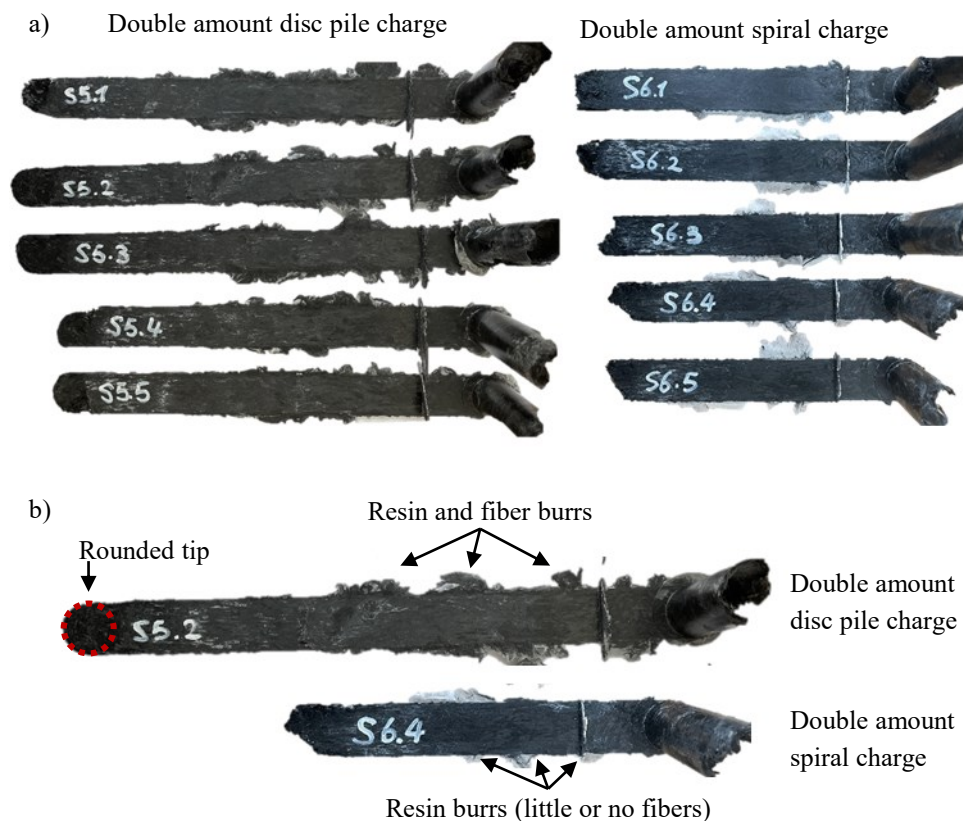


Fig. 5-12 Specimens resulting for the double amounts: a) all specimens for the double amount disc and spiral charges, b) comparison between a double amount spiral charge (top) and a double amount disc charge (bottom)

It is evident, that all disc pile charges (Fig. 5-12a on the left) are significantly longer than the spiral charges (Fig. 5-12a on the right). In the detailed comparison in Fig. 5-12b the rounded tip reproducing the contours of a disc is visible, confirming the repeatability of this behavior throughout all disc pile charges. Another visible difference between the

specimens are the burrs. In the disc pile charge the burrs contain a mixture of fibers and resin, whereas in the spiral charge they mainly consist of fibers. This is due to the fiber orientation within the charge, which in the spiral charge leads to close entanglement of the fibers. Therefore, they cannot easily separate from the bulk i.e. when forming a burr. In the disc pile charge, on the other hand, the open edges in the discs and the flow direction corresponding with the orientation of the fibers is favorable to the fibers moving freely within the resin. This further confirms the necessity of open edges in flow direction, as well as the avoidance of complex charge shapes, in order to achieve complete filling even in complex geometries.

5.3 Numerical representation

In order to improve the prediction of the flow in SMC process simulation, the charge variations tested above and their influence on the resulting pressure have to be included. To this purpose an approach is necessary that is:

- easily applicable in the industrial context,
- simple, meaning with no complicated or too many steps,
- fast, meaning that the evaluation only takes a few hours.

In the software tool 3DTimon described in Subsection 2.2.1, the charge settings that can be defined are:

- the geometrical shape and total volume, as one piece,
- the specific fiber orientation degree in each direction.

If the charge consists of stacked SMC sheets it can be specified that there is isotropy in the plane. It is also possible to input a preferential orientation or 3D-random for bulk molding compound (BMC). However, the subdivision into layers for the sheets is not possible. The same applies for the spiral shape of the sheet for the spiral charge. Within this study, an approach is defined to integrate the results from the testing to the simulation approach.

5.3.1 Simulation settings

The geometry for the test is the same as shown in Subsection 3.3.2.1. The material card is the one resulting from the calibration in Chapter 3. All other simulation settings are the same as in the previous evaluation, and can be seen in Tab. 5-6.

Tab. 5-6 General simulation settings for the charge variations.

	Unit	Simu	Reality
Compression settings			
Temp upper mold	°C	160	160 ± 5
Temp lower mold	°C	160	160 ± 5
Clamping force	ton	25	25
Closing speed	mm/s	2.72	2.72
Waiting time	s	40	~40
Charge			
Material		oop calib	CARBKID
Temperature	°C	25	~25
Simulation settings			
Mesh	x-y-z	1.25-1.25-1.25	-
Steps		Flow	-
Mesh method		Euler	-

The only difference is in the modelling of the charge. In a first comparison, the charge was defined as 3D random and 2D random in the x-y plane. There was no difference in the result, since the fibers are only considered as a result of the flow and not as a cause [97]. Afterwards, the charges are varied further by juxtaposing their overall characteristics, as summarized in Tab. 5-7.

Tab. 5-7 Characteristics of the disc pile charge and the spiral charge in comparison, and related replica in simulation. Experimental values refer to the average values obtained during the tests.

Overall	Disc pile		Spiral		
	Test	Simu	Test	Simu 1	Simu 2
Material	CARBKID	Oop cal	CARBKID	Oop cal	Oop cal
Fiber orientation	isotropic	2D random	isotropic	3D random	3D random
Shape	cylinder	cylinder	spiral	cylinder	spiral
Metrics					
weight	g	50.86	-	36.64	-
vol	mm ³	36860	36283.8	26552	26125
Diameter	mm	28	-	~30	-
Height	mm	~55	55	55	55

The two charges are made of the same material using a different geometry. Therefore, the resulting fiber orientation is different, being 2D random for the disc pile charge and a complex 3D configuration for the spiral charge. Furthermore, the weight and therefore, the initial charge volume of the two specimens differ. Since the fibers do not influence the flow of the material, the aspects investigated for a possible influence are the volume of the charge and the shape. As summarized in Tab. 5-7, simulations are run with the two charge volumes represented as a cylinder, and then a third variation is run, with the charge defined as a spiral, as can be seen in Fig. 5-13.

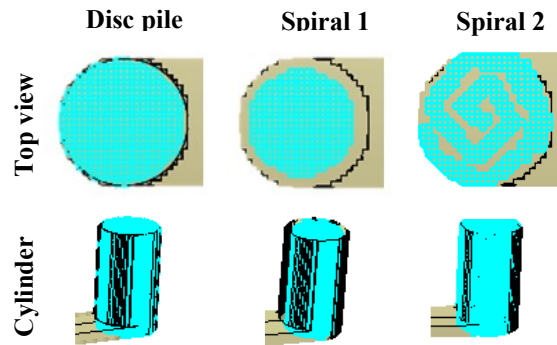


Fig. 5-13 Charge configurations used in flow simulation for the disc pile charge and for the two versions of the spiral charge.

From the charge pictures in Fig. 5-13 it is visible that all charges cover the entire height of the cylinder for 55 mm. However, in order to obtain the correct volume of material for each configuration in the disc pile and in the first version of the spiral charge a cylindrical charge with different diameter is selected. The diameter was chosen with the goal of having the desired volume. It has to be kept in mind in the charge definition, that the material is assumed as incompressible, and therefore, should represent the material after the first compression where the high amount of trapped air is pressed out of the specimen [97]. Since the volume of the tested charges is calculated with the density given in the data sheet, which considers the value without air, the two measures are directly comparable. The spiral was set by using the line selection option for the charge. However, the automatically selected thickness of the material is quite considerable. Therefore, a thinner spiral cannot be set within the software. Fig. 5-14 shows the comparison of the force signals recorded for the three settings in comparison to the simulation used for the bar flow calibration and to the experimental curves for the basic configuration (discs, non-oriented, single amount, within pot life, charge of 2023).

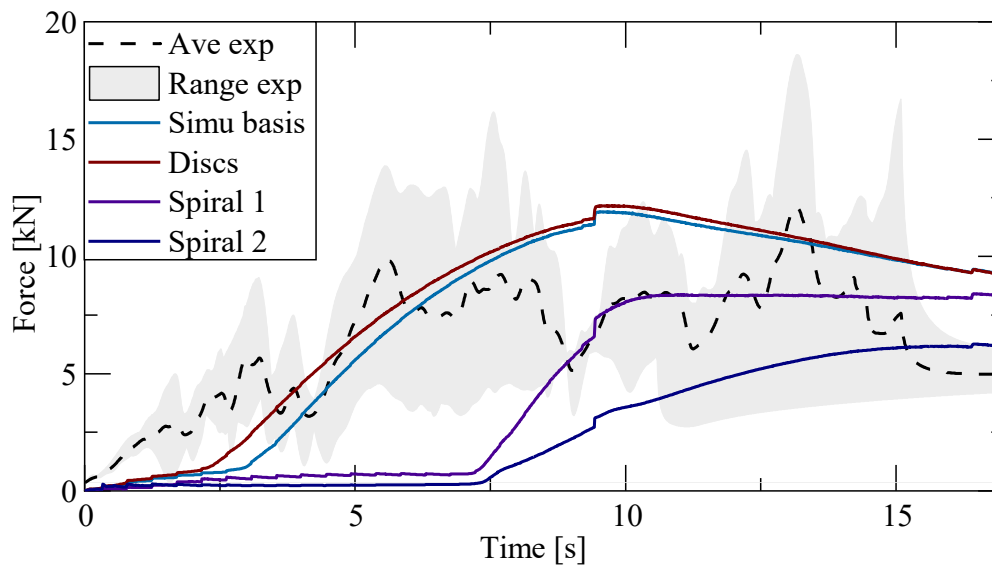


Fig. 5-14 Comparison of the simulation results for different charge settings replicating the disc pile charge and the spiral charge.

Since the charge volume of the discs is a bit bigger than for the simulation basis utilized in the evaluations in Chapter 3, the overall resulting force is slightly higher. For the spiral charges a smaller volume is considered, and also for these cases the same dependency is visible, with the force signals being lower than the basis. Furthermore, the initial section of the force signal with very low value is the shortest for the biggest volume of the disc pile charge, and the longest for the smallest volume. This is due to the initial charge covering only a fraction of the available space in the cylinder. The signal only increases when the charge has been compressed enough to completely fill the cylinder. Interestingly, the difference in volume between the spiral configuration (spiral 2) and the cylindrical configuration (spiral 1) for the spiral charge, display quite a significant difference in the force signal. This is probably due to the spiral shape displaying more air pockets and therefore, a bigger surface of the charge, where flow can originate from. Consequently, the force remains on an overall lower level. Based on these results, it is possible to influence the flow with the charge shape and volume. Therefore, it is necessary to capture the experimental variability in the simulation.

5.3.2 Calibration to the experimental variability

In order to come closer to reality with the simulation, it is necessary to cover the range of possibilities of the experiments. This is achieved by having three material cards in total, with one being the average value, and therefore, the most likely case. Additionally, two material cards are established predicting the highest and the lowest force signals. For the calibration, the procedure presented in Subsection 3.3.2.1 is applied. The result of the calibration can be seen in Fig. 5-15.

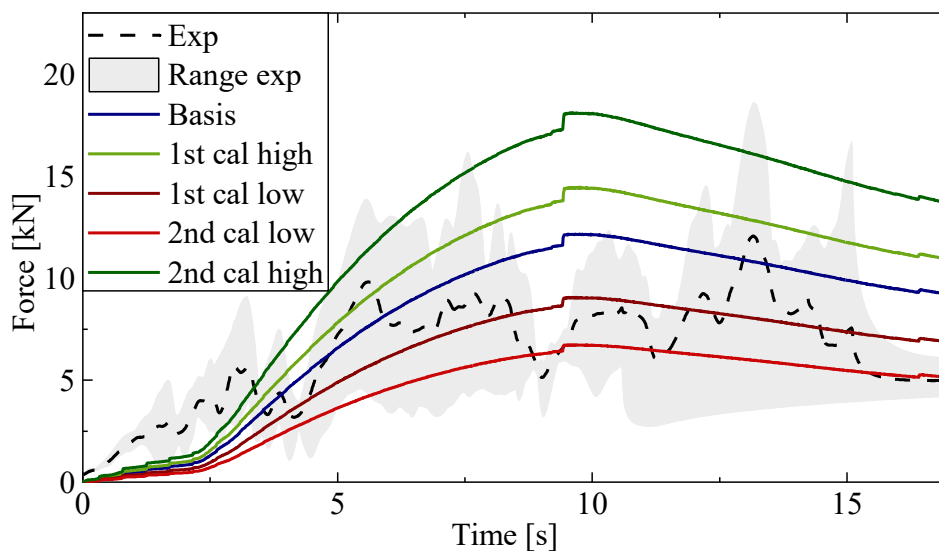


Fig. 5-15 Process of calibration of the material card to the upper and lower limits of the experimental range.

As can be seen in Fig. 5-15, the first goal is obtaining a curve with a maximum in the force signal with a maximum difference of 1 % of the maximum compression force set

for the test. In this case 250 kN were set as the maximum, leading to a maximum difference in the force of 2.5 kN. For the upper limit of the experimental range two steps were necessary for a satisfactory result. For the lower limit also two steps were necessary. The calibration steps performed, as well as the resulting material cards in direct comparison can be seen in Tab. 5-8.

Tab. 5-8 Calibration steps performed for the lower and upper limit of the experimental range and final viscosity parameters for the three material cards (changes in bold).

	Step		p_{old}	l_l	Change	p_{new}	Reference	Result
Low	1st cal	a	1.66E-01	1.00E-10	↓	8.30E-02	10th cal bar	+
	2nd cal	a	8.30E-02	1.00E-10	↓	4.15E-02	1st cal	+
High	1st cal	a	1.66E-01	1.00E-10	↑	2.49E-01	10th cal bar	+
	2nd cal	τ	4.08E-01	1.00E-10	↑	6.12E-01	2nd cal	+

Par	Oop cal	Discs low	Discs high
n	4.32E-01	4.32E-01	4.32E-01
τ	4.08E-01	4.08E-01	6.12E-01
a	1.66E-01	4.15E-02	2.49E-01
b	8.94E+03	8.94E+03	8.94E+03
D	1.20E+01	1.20E+01	1.20E+01
E	1.00E-01	1.00E-01	1.00E-01

For the calibration, the previously performed calibration of the out-of-plane flow in Chapter 3 was considered as a basis for the variations and constitutes the parameters for the most likely case. In order to obtain the most suitable parameters for the upper and lower limit, once again the parameters a and τ are considered.

Depending on the configuration of the charge intended for the SMC part to be simulated, the range considered for the upper and lower limit could also include other tested configurations. From the results obtained for different variations of the disc pile charge, the range resulting for the oriented charge could also be considered. However, in order to obtain a balanced distribution, it would be necessary to have the data also for the opposite orientation option, which has not been tested. Furthermore, also the moment within the pot life of the charge used is relevant, especially since it is never exactly known how far the curing has already progressed due to transport, intermediate handling steps, storage temperature, etc. Therefore, an inclusion could be interesting. However, for this material, the tests were performed a significant amount of time after the recommended storing time. Therefore, this material would not be used for the production of industrial parts. In order to include these values, it is necessary to perform tests for two charges or even two different batches within a reasonable range of SMC usage.

The data and variation of the spiral charge, on the other hand, cannot be included in the same calibration, as the configuration especially with regard to the fiber arrangement is significantly different. Therefore, for the spiral charge a separate calibration is performed, since the result of the simulation with the spiral charge shape and the material

card obtained from the bar flow calibration is very different from the configuration adopted for the disc pile charge. The result of the calibration is visible in Fig. 5-16.

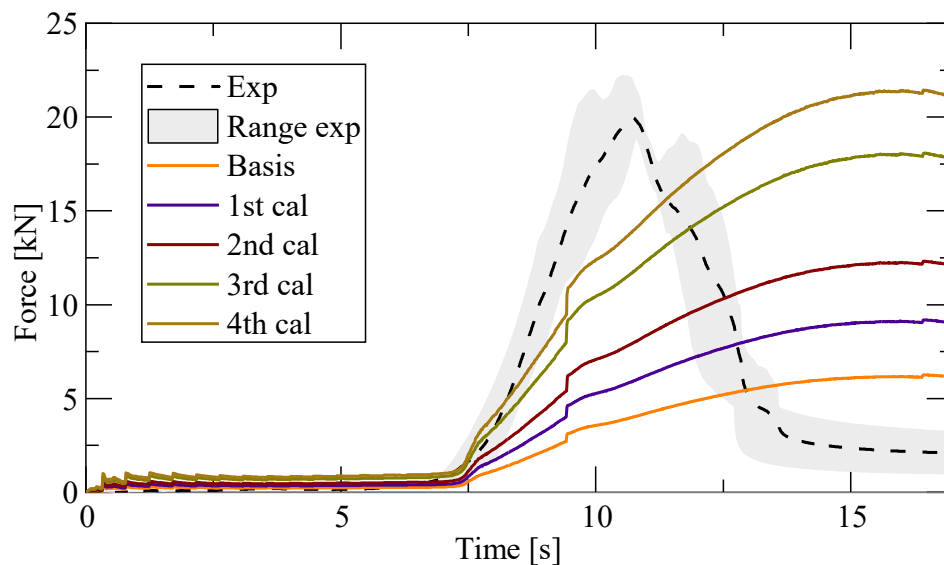


Fig. 5-16 Calibration of the material card for the spiral charge showing the experimental average and the variation in the force signal in comparison to the result with the material card from the out-of-plane calibration and the results for the calibration steps.

As can be seen in Fig. 5-16, the experimental range is of 3.3 kN related to the highest obtained force. With an objective aim in the calibration for the upper and lower limit of 1 % of the maximum compression force (here 250 kN) the three curves would be extremely close. Therefore, for the spiral charge only one curve as close as possible to the experimental average is determined. It is visible that a total of four parameter changes were necessary to obtain the best result. The calibration steps are summarized in Tab. 5-9.

Tab. 5-9 Calibration steps performed for the spiral charge and resulting viscosity parameters. The changes induced by the calibration are highlighted in bold.

Step	pold	ll	Change	pnew	Reference	Result	
1st cal	-	-	↑	-	9th cal bar	+	
2nd cal	-	-	↑	-	8th cal bar	+	
3rd cal	-	-	↑	-	7th cal bar	+	
4th cal	a	3.32E-01	1.00E-10	↑	4.98E-01	7th cal bar	+

Par	Oop cal	Spiral
n	4.32E-01	4.32E-01
τ	4.08E-01	1.63E+00
a	1.66E-01	4.98E-01
b	8.94E+03	8.94E+03
D	1.20E+01	1.20E+01
E	1.00E-01	1.00E-01

As can be seen in Tab. 5-9, the parameters that were increased are α and τ . In the first three calibration steps, the used material cards were directly taken from the previously performed out-of-plane calibration. Only for the last step a smaller change in the parameters following the procedure presented in Chapter 3 was applied. The best result is obtained after the fourth calibration step, with the experimental result and the simulation result differing only by 1.48 kN in the maximum force.

In order to evaluate the validity of the determined objective range in the force of 1 % of the set compression force, the variability in the simulation has also been assessed. The simulation has been repeated for the same settings only changing the charge placement within the cylinder. For the settings of the discs and the spiral charge the values presented in Tab. 5-7 and Fig. 5-13 are used. For the spiral charge specifically the settings from “spiral 2” are applied. The results of the simulations are shown in Fig. 5-17.

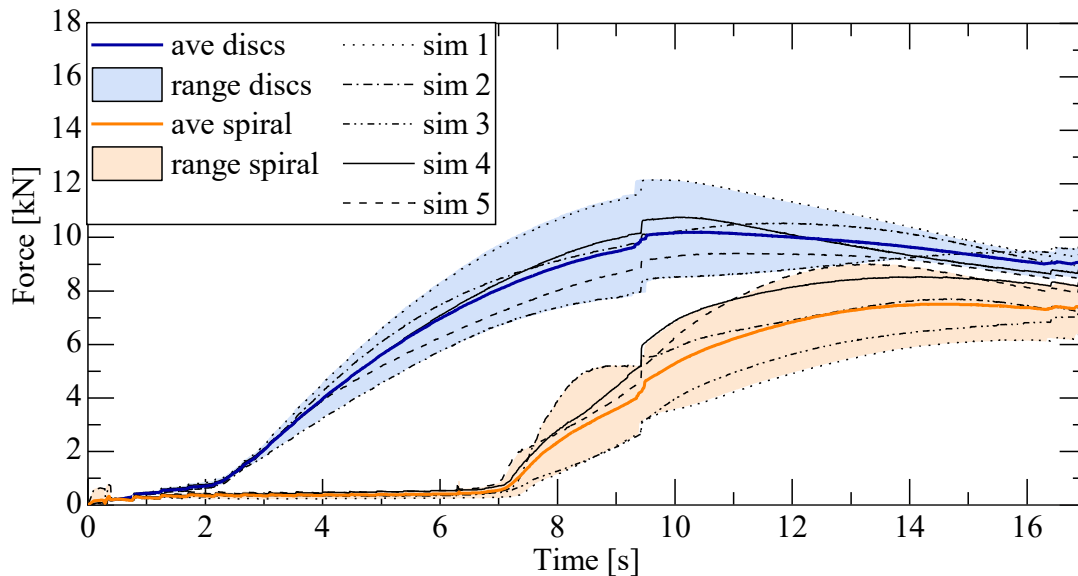


Fig. 5-17 Assessment of the variability for the simulation with disc pile charges and spiral charges, displaying the result for the five tests, the average and the covered range.

The variance present in the two simulation setups is very similar with a difference in the maximum force between the upper and lower limit of the range of 1.15 kN for the disc pile charge and 1.91 kN for the spiral charge. The charge volumes and the exact configurations of the spiral charges varied slightly and are shown in Fig. 5-18.

a)		Discs	Spiral
Sim 1	mm ³	36297.4	25906.2
Sim 2	mm ³	36283.8	26096.1
Sim 3	mm ³	36718.7	26312.1
Sim 4	mm ³	36345	26546.6
Sim 5	mm ³	36422.8	26778.7


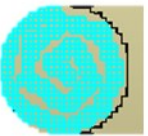
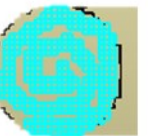
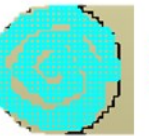

b)		Sim 1	Sim 2	Sim 3	Sim 4	Sim 5
						

Fig. 5-18 Charge variations simulated in the evaluation of the variability of the simulation: a) weights of each charge; b) top view of the simulated spiral charges.

As can be seen in Fig. 5-18a, despite high accuracy in selecting the charge, slight variations of the volume are inevitable if the shape is generated within the software of 3DTimon and not an extensive amount of time is spent perfecting the selection. Interestingly, the two disc pile charges with the highest volume resulted in the lowest force signal. For the spiral charge the variation is much more significant, which is also due to the variation in the spiral, as can be seen in Fig. 5-18. It is evident, that the exact configuration of complex charges in the simulation does have an influence on the result, despite the charge volume remaining almost unchanged. In future research the variation in the simulation result based on the complexity of the charge shall be quantified, in order to be able to give exact guidelines.

5.4 Guidelines

Within this study, six different charge configurations were tested and compared to each other. The study has shown many influences on the resulting specimens, and especially on the resulting pressure signal. Especially in processing regards, being able to keep the compression pressure low decreases the production costs significantly. Therefore, the possibility to choose the charge accordingly represents a considerable benefit. A summary of the influence of the charge configuration on the peak pressure is shown in Tab. 5-10.

Tab. 5-10 Summary of the influence of each charge configuration on the peak pressure comparing the left to the right

		Oriented	After pot life	1 year old tests	Double amount	Single amount	Double amount
		Discs				Spiral	
Discs	Basis*	↑↓	↑↑	↑↑	↓↓	↓↓	—
	After pot life			↑	—	—	—
	Double amount					—	↓
Spiral	Single amount						↑

* single, non-oriented, new material

Peak pressure	
↑/↓	higher/lower
↑↑/↓↓	much higher/lower
↑↓	indifferent

It is visible, that the basis configuration of the disc pile charge has the highest peak in comparison with all other tests with single amounts. The orientation of the charges in the direction of the longest flow path could lead to a slight decrease in pressure. However, for the difference in the pressure resulting for the different material batches, it is not possible to draw any conclusion at the point of this study. In comparison with the spiral charges, the pressure for the disc pile charge is decisively lower. Furthermore, all disc pile charges showed the same stepping behavior in the pressure signal. Meanwhile, the spiral charges all show a very steep linear increase. Although, the charge separation is clearly visible in the double amount spiral charge.

Overall it could be shown that all configurations of the disc pile have an oscillating pressure signal, due to the layering in the charge, and the formation of lubricating layers between the discs. It could be confirmed, that the sheet production direction does contribute to the resulting pressure, as with all discs oriented in the flow direction the pressure signal was lower than in a charge that also included discs perpendicular to the flow. Furthermore, each material batch seems to be different and therefore, has to be tested to know the required compression force. However, this has to be further investigated, in order to better understand the exact origin of the difference. Nevertheless, it could be concluded, that storing the material at -21 °C for over one year does maintain the flow characteristics, leading to an almost unchanged pressure signal. The spiral charge proved to be the least convenient in terms of necessary pressure, as the resulting pressure is much higher than for the disc pile charge. This can be compared to the filling of a rib or

a complex structure that is placed perpendicular to the flow direction, showing that the pressure necessary to fill such an area is much higher than if the part were less complex. When performing the tests with the double amounts, an overall direct proportionality between the amount of material and the pressure increase could be observed in the disc pile, although exceptions have been pointed out. For the double amount spiral charge consisting of two single amount spiral charges, a significant pressure drop can be seen when the separation between the two spirals reaches the channel entrance. Therefore, when producing complex structures like ribs, that are perpendicular to the sheet surface, cutting the charge on the surface in proximity of the rib can greatly reduce the necessary pressure to fill the whole geometry. It also increases the chances of a complete filling, reduces the probability for the occurrence of weld lines on top of the ribs, and reduces the turbulences in the flow, minimizing fiber entanglement. These findings and the derived guidelines shall improve the definition of a charge in order to reduce production costs and improve the repeatability, and the probability of a quality part as outcome. Nevertheless, several aspects have to be further investigated and quantified more precisely, such as the influence the disc orientation has, the applicability to other bar thicknesses and a wider channel, the influence of the charge weight, as well as other configurations like a continuous double amount spiral charge.

On the basis of the performed tests the following guidelines could be derived:

1. perform five repetitions to capture the variability of the material
2. A charge should be placed with the open edges towards the longest flow path
3. The compression pressure can be decreased by increasing the amount of separations in the charge perpendicular to the compression direction. The separation of the charge in flow direction can also decrease the influence of flow variability, and therefore, improve its prediction.
4. In close proximity to ribs the sheet shall be cut on the surface perpendicular to the shape. This leads to a higher likelihood of completely filled ribs, favors an even filling, avoiding weld lines at rib tips. Currently SMC part producers places pieces of sheet inside the ribs before the compression in order to make sure that the part is completely filled. However, this is time consuming both for the preparation of the charge and for the placement.
5. For complex shapes the same applies as for ribs in point 4.
6. The same batch of SMC can be stored well for over a year at very low degrees around $-21\text{ }^{\circ}\text{C}$, without significant changes in the flow behavior.
7. Different SMC batches can lead to very different pressure peaks. Therefore, a delivery control of each batch consisting in a flow test is crucial.
8. Lower height of the specimen and therefore, shorter compression time leads to a lower pressure signal.

5.5 Summary of the numerical approach and discussion

Within this study, the single amount disc pile charge and the spiral charge were replicated in simulation. The disc pile charge was modeled as a cylinder with 2D random fiber orientation in the plane. The spiral charge was also modelled as a cylinder in a first trial with the same height, but lower circumference in order to match the weight difference between the two configurations. In a second trial, the spiral charge was modelled as a spiral. The disc pile charge showed a good correlation with the numerical curve obtained, as expected, since only the weight of the charge changed slightly between the two simulations. The first trial of the spiral charge showed a significant decrease in the compression force due to the lower amount of material. The most different result was obtained with the spiral charge, confirming the influence of the charge shape on the outcome of the compression force. However, the force was lower than for the previous settings, while in the real tests it was the opposite. This difference is due to the neglect of the fibers in the simulation as a cause for the flow [97]. In this regards, whenever small geometries or intricate geometries are considered, it could be better, to adopt a mechanistic model able to predict fiber agglomerations with higher accuracy [91, 96].

In order to capture the variability of the material, the simulation was calibrated to the lower and upper limits of the range covered for the single amount disc pile charge. Another calibration was performed for the spiral charge, since the force prediction in simulation differed significantly from the tested compression force. In the first calibration, the same procedure as developed in Chapter 3 was applied. For the calibration with the spiral charge, however, in the first steps the previous calibration material cards from Chapter 3 were tried out, since the direction of the change of the signal seemed promising. Both calibrations were performed with the aim of obtaining a maximum compression force differing no more than 1 % of the maximum set compression force being 2.5 kN. The variability of the simulation was also established by varying the positioning of the cylindrical charge of the disc pile and the spiral charge five times, without changing the weight significantly. Related to the maximum force a difference of 1.15 kN for the disc pile and 1.91 kN for the spirals was obtained. This confirms that for the spiral charge with a small difference in the overall experimental range, the intermediate value is sufficient, to obtain the best result. Within this evaluation it could also be established that the linear dependency of the compression force from the charge volume does not apply when the differences are very small. In future evaluations it could be interesting to widen the considered experimental range by including all possible and plausible variations. This could include tests done at different moments of the pot life or different storage options, different batches, etc. Any aspect can and should be varied that can also vary when producing parts with SMC in order to cover the entire possible range of the flow behavior.

Based on these findings, as an overall guideline it can be stated that the configuration of the charge tested and consequently simulated for the bar flow tests, should be as similar as possible in geometry. The disc pile charge shall be adopted for predominantly flat and thin shapes and almost all flow in direction of the sheet. However, if geometries are small and intricate, the spiral charge shall be adopted.

Nevertheless, several aspects need further understanding in their influence on the flow and their integration in simulation. First and foremost, as previously stated, the influence of the fibers needs to be considered in the simulation in order to forecast the correct compression force. The solution with calibrating the simulation of the complex geometry can help in the forecasting of the compression force, but all other predictions, like the flow front, flow velocity, etc. are not reliable. Furthermore, the influence of the lubricating layer between sheets and between the SMC and the tool is a crucial factor not considered in 3DTimon or in any other commercially available tool. From the test results it is evident that the compression force is significantly influenced from charge separation in the direction of the flow. The implications derived from the assumed incompressibility of the material in the simulation are another aspect that needs deeper understanding. If the charge is modelled considering the volume and geometry it has once the air is gone, the accuracy is high enough. However, this shape is not automatically known, especially in relation to the variability of the material.

The last aspect needing better understanding is the influence of the weight. It could be established within this study that an overall linear dependency seems to exist between the compression force and the weight, but the exact link is not known. Furthermore, it became clear that for small variations this dependency is not valid anymore.

6 Validation of the developed approach for SMC filling simulation

Within this research, the flow behavior of SMC has been investigated thoroughly by improving the existent procedure for the flow characterization (Chapter 3), developing a new flow test bench for optimized out-of-plane characterization (Chapter 4), and investigating the influence of charge variations on the compression pressure and the flow (Chapter 5). From Chapter 3 a material card has been obtained for the SMC used throughout this research CARBKID PGK5250. The material card contains only one set of specific parameters, no range of possibilities. However, with the study conducted on the charge variations in Chapter 5, it is clear that several aspects of seemingly identical charges can lead to differences in the resulting compression pressure. Within this chapter, the outcomes of each previous chapter are brought together and validated by producing SMC parts and comparing the empirical results to the numerical results.

6.1 Approach

In order to evaluate the validity of the material card determined within Chapter 3 under consideration of charge variations determined in Chapter 5, the reality and simulation of the production of an SMC part are compared. Suitable geometries are chosen that satisfy a set of requirements:

- a simple geometry, at least for one of the parts, the second can be more complex
- a common geometry among SMC part manufacturers, in case it is desired to replicate the setup
- typical charge geometry for SMC part production to ensure industrial relevance
- charge configuration (shape and fiber orientation) that can be easily reproduced in simulation.

Once the geometries are defined, appropriate process settings are chosen. Once again the vicinity to industrial applications is sought out, but also the possibility to replicate the settings in simulation relatively easily. The variation in the simulation results due to simulation settings shall be kept as low as possible. As seen in previous chapters this endeavor is challenging. For the simulation the only requirement is to be as close to reality as possible.

The goal of the validation is the determination of the validity of the forecasted flow within the simulation. Therefore, the flow fronts from reality and simulation shall be compared for incomplete filling of the chosen geometries. The production of the parts

and the process parameters, as well as the simulation setup are explained in detail in the next sections.

6.1.1 SMC part production

The chosen geometries for the validation are a simple plate, and a more complex variation with a rib placed one third off-center parallel to two edges of the plate. The schematics of the two plates with the intended charge and its placement is shown in Fig. 6-1.

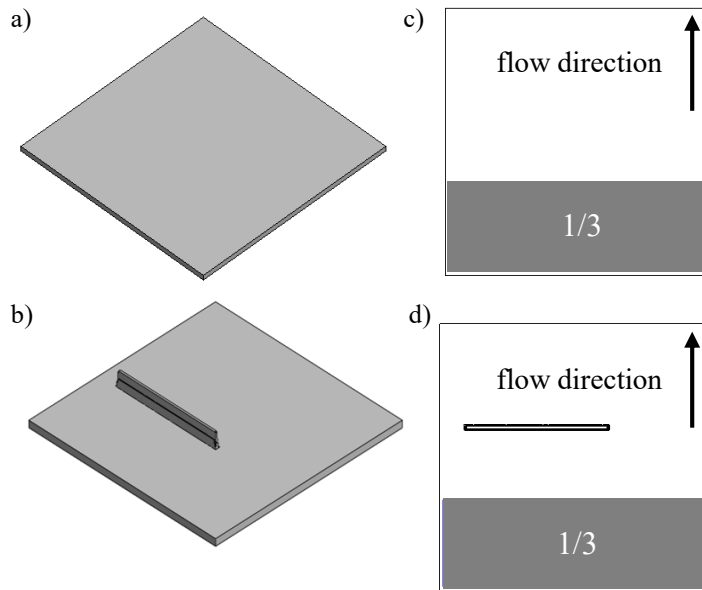


Fig. 6-1 SMC parts produced within this study, with charge configuration and main flow direction: a) geometry of simple plate; b) geometry of plate with rib; c) charge configuration with 1/3 coverage for the simple plate; d) charge configuration with 1/3 coverage for the plate with rib.

As can be seen in Fig. 6-1, the overall size of the plate is the same for the version with rib and the one without rib and is 400 x 400 mm. Furthermore, the charge placement is also identical. For the plate with rib the notable aspect is the placement of the charge so that the longest flow path is perpendicular to the rib. The rib consists of a 210 mm long (at the base), 20 mm deep and at the tip 2.5 mm wide cut out. The inclination of the rib walls is 0.39° , a standard for SMC parts, necessary for easy demolding. Both geometries satisfy all above listed requirements by being simple and typical geometries. The plate geometry is also common for all SMC part manufacturers. Furthermore, as can be seen in Fig. 6-1c and d, the charge geometry is a common rectangular charge of stacked sheets of 397 x 132 mm. This geometry can be easily reproduced in simulation. This satisfies both requirements previously set for the charge.

The production of the plates is done in a WKP 3000 S press from Wickert Maschinenbau GmbH [148] at the facilities of Toray AMCEU, as shown in Fig. 6-2.

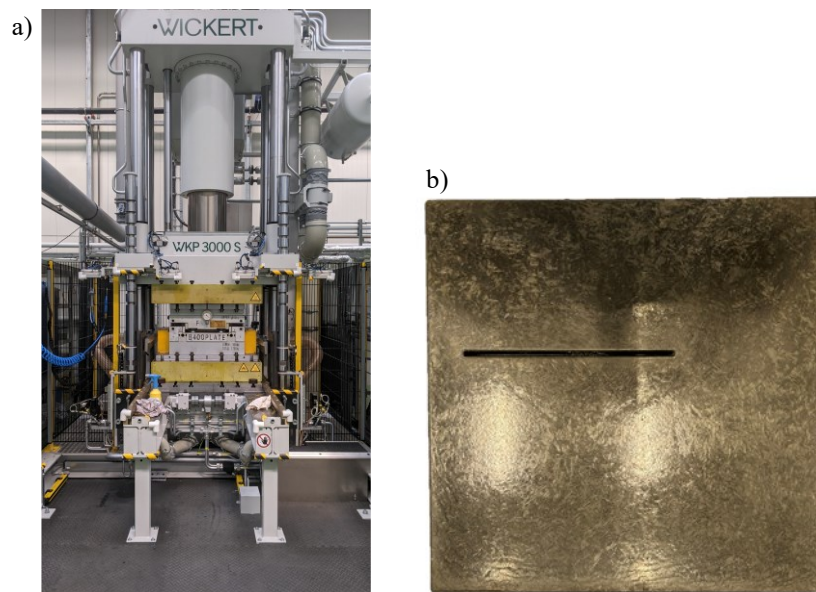


Fig. 6-2 Plate production: a) Wickert WKP 3000 S press at Toray AMCEU used for the plate production; b) lower mold made of SMC for the plate geometry with rib.

The overall capabilities of the press include a possible press force of up to 3000 kN, as well as temperatures within RT and 350 °C [148]. For this study, the temperature is set to 140 °C. The compression speed undergoes several changes starting at 75 mm/s from 405 to 220 mm, 20 mm/s to 45 mm, 10 mm/s up to 30 mm, where the first contact with the material happens. Then it is reduced to 1 mm/s for the compression. The maximum compression force is set to 1000 kN. Typically SMC parts are compressed until a desired pressure is reached. This pressure is then kept for a predefined amount of time. However, as in this case the goal is to obtain unfilled plates to see the flow front, distancing plates are placed around the centering bolts in order to stop the compression at the desired position. This workaround is necessary, because the settings of the press do not have the option of interrupting the compression at a specific position. The compression can only be stopped by reaching the pressure set at the beginning. Furthermore, the lower tool half consists of a plate made of SMC placed inside the actual steel tool used to produce SMC plates. The lower tool half for the rib geometry is shown in Fig. 6-2. This was chosen in order to allow a financially and timely convenient switch between the simpler configuration of the plate and the more complex one with the rib. However, due to the thermal conductivity difference in SMC, the temperature of the surface of the lower mold was always significantly lower than the upper mold half, reaching only ~ 100 °C.

The material used for the production of the parts is the same as has been adopted for all other contents of this thesis and described in detail in Section 1.3 CARBKID PGK 5250 [44]. The weight for all charges was set at 770 g for the simple plate and the plate with rib. The defined weight is obtained by stacking approximately five layers of SMC. Due to the variability in thickness and consequently also of the local weight of the charges, for all charges except one at least some material had to be cut off from one layer, in six

cases even about half of one layer. The shorter layer was placed in the center of the charge, both in thickness direction and in length direction, as can be seen in Fig. 6-3.

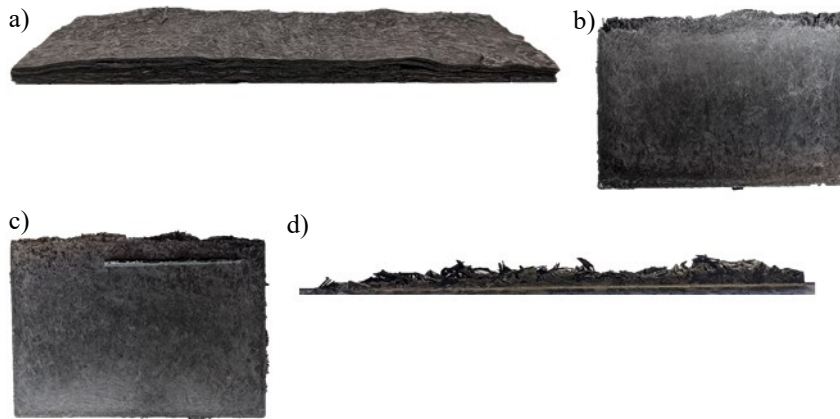


Fig. 6-3 Plate production: a) typical charge with five entire layers and a sixth partial layer placed between the third and fourth layer; b) exemplary incompletely filled plate; c) exemplary incompletely filled plate with rib; d) detail of incompletely filled rib.

Fig. 6-3a shows a typical charge with five layers of 397*132 mm and one additional layer to complete the 770 g of SMC of smaller size placed in the center of the SMC stack. Due to the variability in thickness of each sheet and the additional thickness difference due to the smaller SMC piece makes the specimen very uneven. The charge is placed at ~ 1 cm from the edge of the mold. The resulting plates without (Fig. 6-3b) and with rib (Fig. 6-3c) are exemplarily shown for one plate out of five repetitions. A detail of an incompletely filled rib is exemplarily shown in Fig. 6-3d. These experimental settings are replicated in simulation.

6.1.2 Simulation settings

The process applied for the production of the plates in reality is transferred into a numerical version within 3DTimon R8.1.1. Tab. 6-1 summarizes the settings adopted in simulation in direct relation to the settings used for the production of the empirical plates.

Tab. 6-1 Settings for the compression, the charge and the simulation in comparison to the values in the real production of the plates and the plates with rib.

	Unit	Plate	Simu plate	Plate with rib	Simu with rib
Compression settings					
Temp upper mold	°C	140	140	140	140
Temp lower mold	°C	98.4 ± 1.6	100	98.7 ± 2.3	100
Clamping force	ton	100	100	100	100
Comp speed	mm/s	1	1	1	1
Waiting time	s	13 (+~5, +2-3)	13	13 (+~5, +2-3)	13
Comp time	s	-	4.2	-	6.54
Charge					
Material		CARBKID	oop calib	CARBKID	oop calib
Weight	g	769.64 ± 0.9	-	769.83 ± 0.9	-
Void content [137]	%	23	-	23	-
Volume	mm ³	557971	557577	557971	549381
Charge layers		5 ± 0.5	5	5 ± 0.5	6
Thickness layer	mm	~2.46	2.46	~2.46	2.46
Fiber orientation		2D random	2D random	2D random	2D random
Temperature	°C	~25	25	~25	25
Simulation settings					
Mesh	x-y-z	-	1.5-1.5-0.73	-	1-1-0.50
Steps		-	Flow	-	Flow
Mesh method		-	Euler	-	Euler

The compression settings are based on the experimental values with a compression force of 1000 kN, equal to 100 tons, and a compression speed of 1 mm/s. The upper mold is set to 140 °C as in the production, the lower plate to 100 °C, since that was the goal temperature for each compression. However, in the experiments a small variation was present, due to the mold cooling down quickly once open due to the carbon fibers. For the waiting time all steps from the open position of 405 mm of the press down to the contact with the material are considered, leading to 13 s. However, the time from the placement of the charge until the start of the compression is not considered, and it is marked with ~5 s in the production data. Another interruption of 2-3 s happens sometimes during the production when a mechanism to keep the mold halves parallel is activated. Since this interruption sometimes does not happen, it was also not considered in the general evaluation of the results. However, the influence of a changing waiting time within these reasonable variations experienced in the production shall be evaluated in Section 6.3.

The charge was determined based on the known weight of each charge and the amount of layers used within the production. The layer thickness of 2.46 mm was obtained as an average from the evaluation of the variability of the thickness of CARBKID PGK5250 performed in [S20]. Since the simulation assumes the material to be incompressible, the thickness has to be reduced by the void content, which was assumed as 23 % based on

Ferré Sentis et al. [139]. The geometry of the charge was set as close to reality as possible, referring to the average thickness resulting for five or six layers of SMC for the plate and the plate with ribs respectively. The overall volume is in a similar range, and was calculated from the material density of 1.38 g/cm^3 and the weight of the real charges.

For the simulation, the mesh was defined with Euler elements with side lengths of 2-2-1.58 mm and 2-2-1.54 mm in x-y-z for the plate and the plate with ribs respectively. The focus relies on the flow behavior.

In Fig. 6-4 the simulation setup is exemplarily shown for both geometries.

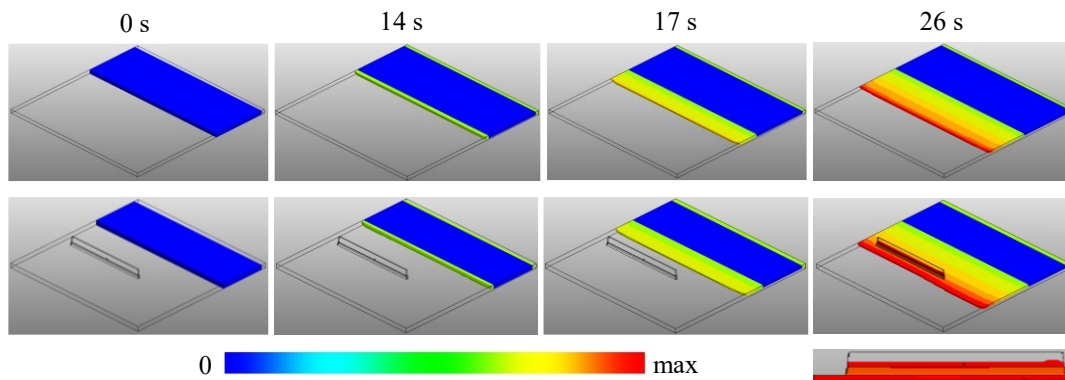


Fig. 6-4 Simulations of the filling time of the plate and the plate with rib at the beginning and end of the compression, as well as at two intermediate steps; a detail of the partially filled rib is also displayed on the bottom right.

At the beginning of the simulation the charge is very similar for both settings, with the main difference being the charge thickness, since for the plate with rib in the production in all repetitions more than five layers were necessary. In the first flow stage the material flows in all available directions, filling the small space left on one side of the charge with the intended distance from the edge of the mold of 1 cm. Afterwards, the material only flows in the main flow direction until the compression is interrupted. The rib is also only partially filled once the compression stops, as can be seen on the bottom right of Fig. 6-4.

6.2 Comparison of empirical and numerical results

For the overarching goal of comparing the empirical and the numerical results of the plate production, both results have to be thoroughly understood separately before determining an appropriate comparison. Therefore, within the next subsections, first the empirical results are addressed (Subsection 6.2.1), then the numerical results (Subsection 6.2.2), and finally follows the actual comparison (Subsection 6.2.3).

6.2.1 Empirical results

All five plates obtained from producing with exactly the same settings show a very inhomogeneous flow front in both the simple plate, and in the plate with rib, as can be seen Fig. 6-5.

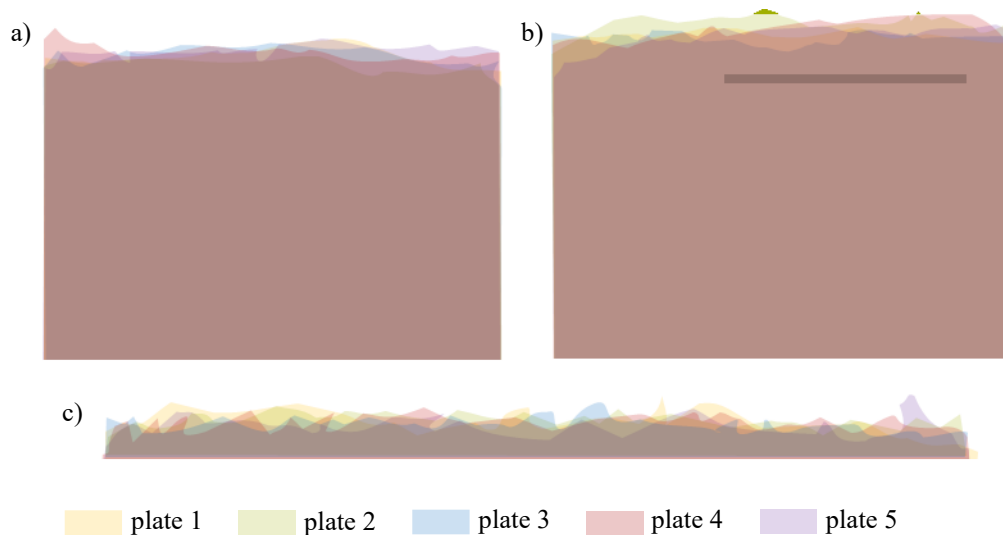


Fig. 6-5 Flow front results for all produced plates in direct comparison for: a) the simple plate; b) the plate with rib; c) the rib.

It is visible in Fig. 6-5a that in plates 1, 2, and 5 for the simple configuration the material flow faster in the center, showing a shorter flow on the sides. However, plates 3 and 4 have protruding edges. Overall the flow front is very irregular. The same inhomogeneous behavior can be seen in Fig. 6-5b for the plates with rib. However, the flow length is overall shorter on the side of the plate without the rib. The filling of the rib, shown in Fig. 6-5c, does not seem to follow any pattern. The filling was overall very little, with only some protruding fibers but no complete filling through thickness over a few millimeters. The flow length was determined for five different positions on the plate by measuring it at 2 cm from the left and right edges of the plates, in the middle, at the longest and at the shortest flow. At the flow front the material does not fill out the thickness of the plate, as can be seen in Fig. 6-6. Therefore, both the overall flow length and the fully filled flow length were determined. For the fully filled flow length, measurements were taken on both sides of the plate and included in the average. The exact flow length values and their variability referred to the fully filled thickness and the overall flow length are summarized in Tab. 6-2.

Tab. 6-2 Results for the flow length of each plate listed as maximum and minimum overall, maximum and minimum referred to the furthest flow front with complete through thickness filling and the average calculated from the five taken data points (max, min, 2 cm from left and right edge, and middle), as well as the flow length in each rib.

		overall		filled		average	
		max	min	max	min	overall	filled
plate 1		288	261	263	246	271.4	252
plate 2		273	252	261	243	265	252.6
plate 3	mm	281	262	268	245	270.4	255.4
plate 4		294	266	270	253	279.4	260.5
plate 5		286	258	280	248	275	261.7
ave	mm	284.4	259.8	268.4	247		
with rib 1		297	276	288	261	285.2	276.8
with rib 2		309	272	290	261	290.8	273.8
with rib 3	mm	297	280	285	266	287.8	279
with rib 4		300	280	282	265	291.6	274.4
with rib 5		296	266	290	262	283.6	270.8
ave	mm	299.8	274.8	287	263		

		max	min	ave
rib 1		14	3	8.4
rib 2		12	5	8.8
rib 3	mm	10	4	7.4
rib 4		12	6	9
rib 5		12	4	7.4
ave		12	4.4	

The variability of the flow length within one plate is very high, with the difference between the longest and the shortest flow length being between 19 and 28 mm for the simple plate and between 17 and 37 mm for the plates with ribs. This also confirms that the plates with variability show an even higher mobility related to the increased complexity of the geometry. The overall averages show that the flow in the plates with rib is longer than in the simple plates due to the experimental setup stopping the compression based on distancing plates, since the press cannot be stopped based on a goal position only based on a goal pressure. In a direct comparison between the average values calculated from the five performed measurements, the difference between the overall flow length and the flow length for the completely filled region is between 12.4 and 19.4 mm for the simple plate and between 8.4 and 17.2 mm for the plate with ribs. Therefore, the difference is significantly lower for the plate with rib. The filling of the ribs appears to be relatively similar for all produced plates with a minimum height of 3 mm and a maximum of 14 mm. However, in the filling of the ribs only very few millimeters are fully filled. Most of the filling is only partial with some fiber strands protruding from the material, as can be exemplarily seen for plate 3 in Fig. 6-6 together with other details of the produced plates.

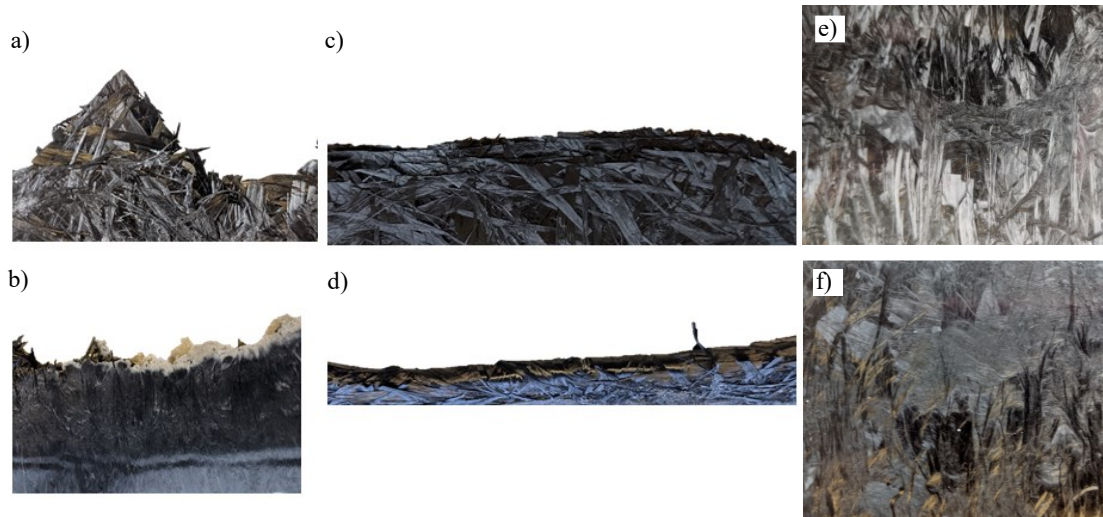




Fig. 6-6 Details of the flow front: a) protruding edge with visible sheet angle; b) Surface deformation along the flow front and pure resin and release agent front; c) layered structure of the flow front; d) closed flow front with bent layer slowing down the flow; e) detail of fibers oriented in flow direction on the surface of the plate; f) detail of chaotic fiber orientation for one strand within mostly fibers oriented in flow direction.

The complexity of the flow is evident with a closer look at the details of the flow front and the plates in general, as shown in Fig. 6-6. In Fig. 6-6a the protruding corner of an SMC sheet at the edge of the plate is visible. The material does not fill the entire thickness, leading to the fiber strands being clearly visible and the surface being very uneven. In Fig. 6-6b, on the other hand, the surface is shining, hinting at a complete filling over the thickness up to the front. However, a region of pure resin and release agent accumulated at the front of the material. Furthermore, a wave is visible on the surface of the plate due to an uneven surface. In Fig. 6-6c and d the two possible options for the behavior of the fibers at the open flow front is visible, displaying either the layering of the sheets as all fibers remained oriented in the plane, or the fibers at the front bent over the thickness. The latter option happens when the outermost layer protrudes faster and comes in contact with the opposite mold half, where the fibers get stuck. Therefore, once the material surpasses the region where the fibers were stuck, a flow front as shown appears. This flow front moves slower than the other option and leads to a smaller difference between the filled and overall flow length. Fig. 6-6e and f show exemplary fiber arrangements on the surface of the finished plates. It is evident that most fibers are oriented in flow direction. However, some strands only display a chaotic appearance.

The reason for the inhomogeneous flow front is the inhomogeneous thickness of the sheets, as well as the fiber and sheet arrangement and placement, and the process settings. However, this does not translate into a very big variability on the final thickness of the plates, as can be seen in Tab. 6-3 summarizing the results for the thickness of all produced plates.

Tab. 6-3 Results for the thickness of each produced plate based on six measurements taken at 2 cm from the edges on each side of the plate and in the middle, as well as at 20 cm from the flow start with a micrometer gauge.

		max	min	ave	
plate 1		5.366	5.314	5.3372	
plate 2		5.389	5.296	5.3343	
plate 3	mm	5.361	5.283	5.3242	
plate 4		5.394	5.274	5.3212	
plate 5		5.392	5.241	5.3093	
ave	mm	5.3804	5.2816		
with rib 1		4.891	4.688	4.8283	
with rib 2		4.908	4.69	4.8252	
with rib 3	mm	4.923	4.709	4.8357	
with rib 4		4.945	4.715	4.8457	
with rib 5		4.927	4.734	4.843	
ave	mm	4.9188	4.7072		

For each value of maximum, minimum and average shown in Tab. 6-3 six measurements were taken with a micrometer gauge for each plate in the positions shown on the schematic representation on the right. All measurement points were placed 2 cm from the edge. The measurements taken close to the flow front on the left and right were taken at 20 cm from the flow start. The thickness difference in the plates is due to a slight tilting of the tool, due to the uneven pressure distribution with the charge only being placed on one side of the mold. However, the difference between the maximum and minimum is only 0.1 mm for the simple plate and 0.2 mm for the plate with rib. Once again, the higher variation is present in the more complex variant, showing the challenge related to the replicability in the parts increasing with increasing part complexity.

6.2.2 Numerical results

The results of the simulations performed with the settings presented in Subsection 6.1.2 are shown in Fig. 6-7.

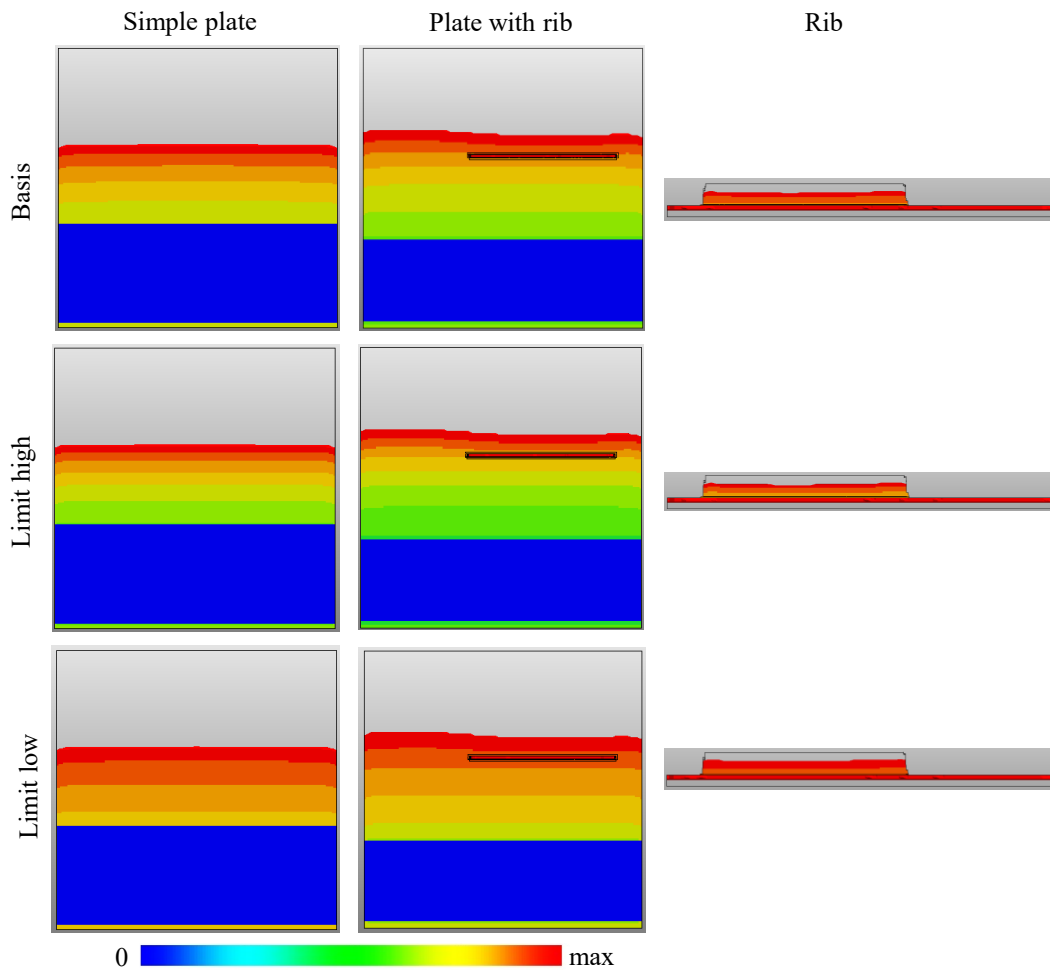


Fig. 6-7 Result of the filling time simulation for both the simple plate and the plate with rib for the three defined material cards of the basis, the higher and lower limits identified for the standard stacked SMC charge.

In a direct comparison of the two basis simulations, it is evident that the rib influences the flow front. For the simple plate, the flow length is almost the same over the width, with a slightly faster portion in the middle and a slower portion at the edges. For the plate with rib, on the other hand, the flow length is shorter where the material also has to fill the rib. However, the use of three different material cards, does not influence the flow length in the plane in neither configuration. Only the rib filling shows a more significant difference. The detail and all simulation results overlapped can be seen in Fig. 6-8.

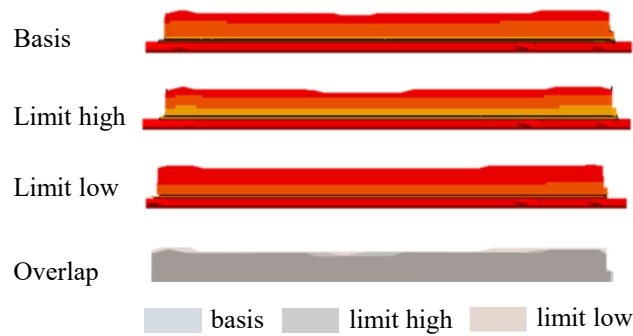


Fig. 6-8 Detail of the filling of each rib for the basis simulation settings and the limits with a representation of all results overlapped.

It is evident in Fig. 6-8 that the ribs are differently filled. The overlap shows that the plate with the lower limit displays the highest filling degree, while the higher limit has the lowest filling degree. The main difference to be seen between the results is the overall filling speed and therefore, the filling time. For the higher limit, the filling happens much slower, since the viscosity is higher and therefore, a higher force is necessary. For the lower limit, the contrary happens. The filling time for each configuration, and the flow lengths are summarized in Tab. 6-4.

Tab. 6-4 Results for the compression time, the final thickness, and the maximum and minimum flow length in simulation for all three configurations run for each geometry, as well as longest and shortest flow length of the material inside the rib.

	Comp time	Thickness	Flow l max	Flow l min
	s	mm	mm	mm
Plate				
Basis	22.55	5.27	262.76	257.35
limit high	26.48	5.27	262.76	257.35
limit low	19.12	5.27	262.76	257.35
Plate with rib				
Basis	27.79	5.01	283.23	275.78
limit high	33.52	5.01	283.23	275.78
limit low	23.02	5.01	283.23	275.78
	unit	mid	sides	
Rib				
Basis	mm	12.52	15.02	
limit high	mm	12.52	15.02	
limit low	mm	13.77	15.02	

As can be seen in Tab. 6-4, the thickness and the overall maximum and minimum flow lengths do not change despite the difference in the material card. However, the filling time differs by up to 3.93 s for the simple plate and up to 5.73 s for the plate with rib. Only for the flow length measured in the middle of the rib a difference can be seen between the lower limit and the basis simulation of 1.25 mm. The overall difference in

the flow length between the maximum and minimum value recorded for each setting is of only 4.41 mm for the simple plate and 7.45 mm for the plate with ribs. The difference in the filling of the ribs is mainly due to the default time step of the software.

When comparing the same moments in the simulation for the higher and lower limits of the simple plate (see Tab. 6-5), the flow length differs by 20.55 mm between the basis and the limit high, and by 22.71 mm between the basis and limit low.

Tab. 6-5 Comparison of the flow length for the same moments for the basis simulation and the simulations with the limit high and low.

	Comp time s	Flow l mm
basis	22.55	262.76
limit high	22.63	242.21
basis	19.29	240.05
limit low	19.12	262.76

Furthermore, in a direct comparison of the stroke signals, as shown in Fig. 6-9, it is visible that the overall displacement is the same for all simulations for the two configurations.

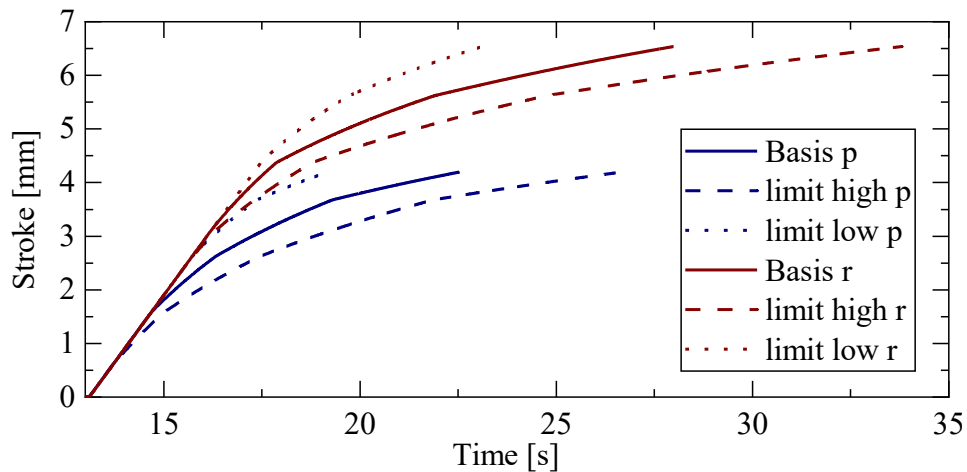


Fig. 6-9 Comparison of the stroke data for the three variations with the basis, the limit high and low for both configurations of the simple plate (p) and the plate with rib (r).

Despite the overall displacement being the same, each curve displays a different compression speed. The set velocity of 1 mm/s is kept for a different amount of time for each configuration, with the limit high version of the plate reducing the velocity already before 1 s. Therefore, the main difference for the different material cards is to be found in the overall compression time and force, but the final thickness will be as defined in the simulation settings.

6.2.3 Comparison

In a direct comparison between the empirical results and the numerical result (see Fig. 6-10), the average flow length is very similar.

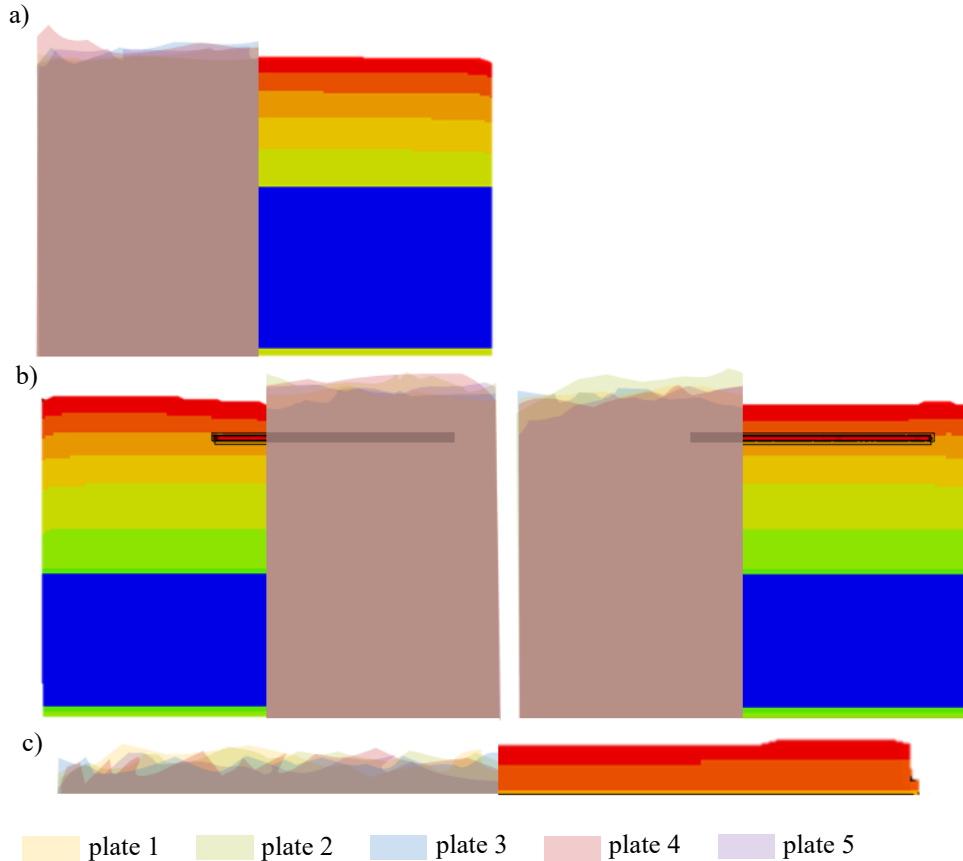


Fig. 6-10 Direct comparison between the results for the produced plates and the simulations with the “basis” material card: a) results for the simple plate; b) results for the plate with rib; c) detail of the rib.

As can be seen in Fig. 6-10a, for the flat plate the result of the flow length is extremely similar based on the average value for the real plates being 272.24 mm overall and 256.44 mm for the filled plate and for the simulation being 262.76 mm for the longest flow path. Therefore, the result of the simulation is within the range obtained in the tests, showing good agreement. However, as seen in Subsection 6.2.2, the use of other material cards does not change much the prediction of the flow length. Only the filling time and the compression force are influenced. Therefore, the limits do not represent the entire possible range of outcomes. Furthermore, the flow pattern in simulation with the edges moving slower, does not reflect the real behavior of the material, where the edges moved further in some plates. This behavior is influenced by the arrangement of the fibers and also by the lubricating layer forming between the mold and the SMC charge, where the viscosity decreases due to the increasing temperature in the charge. The missing description of the lubricating layer is one of the main drawbacks of the software 3DTimon [91,

96]. For the plate with rib, as shown in Fig. 6-10b, the qualitative behavior difference in the flow front with the edges protruding in reality in some plates can also be seen with this configuration. Moreover, the slower flow in proximity to the rib seen in the simulation is not visible in the real plates. In general the flow length in simulation of 283.23 mm is shorter than the overall flow length in the real plates of 287.8 mm, but longer than the average flow length for the filled real plate of 274.96 mm. However, the rib is overall filled further in simulation with an average filling of 13.77 mm compared to an average of 8.2 mm for the real plates and an overall maximum of all the plates of 14 mm. This overestimation of the rib filling compared to the flat areas has been pointed out in Qian et al. [89] and is a known issue for the software developers. To counteract it is possible to change the default setting of the flowability of single elements to replicate the real condition better. In this case, the flowability within the rib elements would have to be reduced. This approach shall be investigated closer in the future.

From the direct comparison it is evident, that the final thickness can be reached with high precision in the simulation. With the established material card from Chapter 3 a reliable numerical prediction of the flow length could be made. However, further assessment of parameters like the compression pressure could provide a more complete picture. To this purpose the data from the press shall be collected. Furthermore, a comparison of the pressure signals between fully filled plates would allow a suitable assessment of the suitability of the material cards. This procedure would provide an additional validation. Nevertheless, the drawbacks of 3DTimon also pointed out in previous research could be confirmed here with a qualitatively different behavior of the flow front and in the rib filling between simulation and reality. These differences can be even more enhanced considering the variations that can be present in the simulations and in the processing. In order to understand the influence of the main variable aspects identified in the simulation and in the processing, a study was performed on these aspects, as presented in the next section.

6.3 Influence of the process and simulation settings

During the production process for SMC part manufacturing, the process settings can underlie some variation, such as slight differences in temperature and slight changes in the charge configuration. These changes are seemingly small, but it is visible that the empirical plates show rather different flow fronts. The differences in the local thickness of the sheets surely is relevant to this variation, but also variations in temperature could be significant. To this purpose, these changes in settings are studied more in detail numerically.

The variations seen during the production are summarized in Tab. 6-6, as well as their consequence on the simulation settings. For the remainder, the simulation settings are the same as presented in Tab. 6-1.

Tab. 6-6 Overview of the identified variations found in reality and their translation into simulation settings, and the different mesh sizes compared to each other.

Variation	Unit	Reality	Sim	Volume	Mesh
Plate				mm ³	x-y-z
		100	100		
Temp. lower mold	°C	96	96	561267	
		98	98		
Charge configuration	layers	5	5	561267	2-2-1.58
		4+	5+	549119	
Time before comp.	s	13	13		
		13 + delay centering	15	561267	
		3 + delay centering + placement	20		
Mesh size	mm	-	2-2-1.58	561267	-
		-	1.5-1.5-0.73	557577	-
		-	1-1-0.50	550185	-
Plate with rib					
		100	100		
Temp. lower mold	°C	97	97	577726	
		98	98		2-2-1.54
		101	101		
Charge configuration	layers	6	6	577726	
		5+	5+	555256	
Mesh size	mm	-	2-2-1.54	577726	-
		-	1-1-0.75	550121	-
		-	1-1-0.50	549381	-

As can be seen in Tab. 6-6, 3 different temperatures for the lower mold could be recorded. This is due to the very high thermal conductivity of the SMC constituting the lower mold. Once the mold is opened to demold a part and place the new charge, the SMC mold half cools down much quicker than the steel half. The steel tool of the upper mold half was recorded at 140 °C before placing each charge. Therefore, it is assumed that the steel tool holding the SMC mold half has the same temperature. The temperature of the lower mold in the closed tool was not recorded. In the simulative replica the assumed temperatures of the lower mold were set at the same value as measured before the charge placement. Although it would be possible to record the temperature development of the lower tool and implement a temperature profile for the molds in the simulation [97], this was not done within this study. Since the objective comparable characteristic of the charges was the weight of 770 g, the amount of sheets varied between 4.5 and 5 for the simple plate and 5 and 5.5 for the plate with rib. In the real process this leads to a very complex charge, as shown in Fig. 6-3. In the simulation this charge configuration was recreated by placing a smaller block of charge on the main charge stripe. For the time before the compression in the main simulation it is set to 13 s based on the different closing speed steps used in the process. However, within this study two more variants are considered, starting with the consideration of the delay caused at the start of

the mechanism to ensure the parallelism of the two mold halves. This can be up to 3 s. Another delay not considered in the main simulations is the time between when the charge is placed in the mold and the compression process is started. This takes a few seconds, but since it was not recorded and an exact value is not known, it was set at 5 s, which is in a realistic range. This variation is only performed for the simple plate. The last variation to be performed is a change in the mesh size. With a new mesh, also the charge has to be newly selected, leading to a slight change in the material volume.

For the simulations performed for the changes in the temperature of the lower mold, the filling time remains exactly the same, being 24.77 s for the simple plate and 26.46 s for the plate with rib, as does the maximum temperature of the charge not exceeding 27.07 °C for the simple plate and 27.81 °C for the plate with rib. Moreover, no difference can be seen in the resulting force and pressure signals. The same unchanged result can be seen for the variation in the waiting time before the compression, no changes in temperature or filling time can be seen despite the material having a few seconds more time to heat up in contact with the press. Therefore, these variations in the waiting time due to the user and the press can be neglected if they are in a very small range of a few seconds.

The charges consisted in several sheets of SMC stacked upon each other, with the intent of having the same weight. This leads to a variation in the amount of sheets, were for several charges the fifth sheet had to be reduced sometimes even by half. As can be seen in Fig. 6-11, this smaller piece was placed in the middle of the sheets and in the middle of the plane.

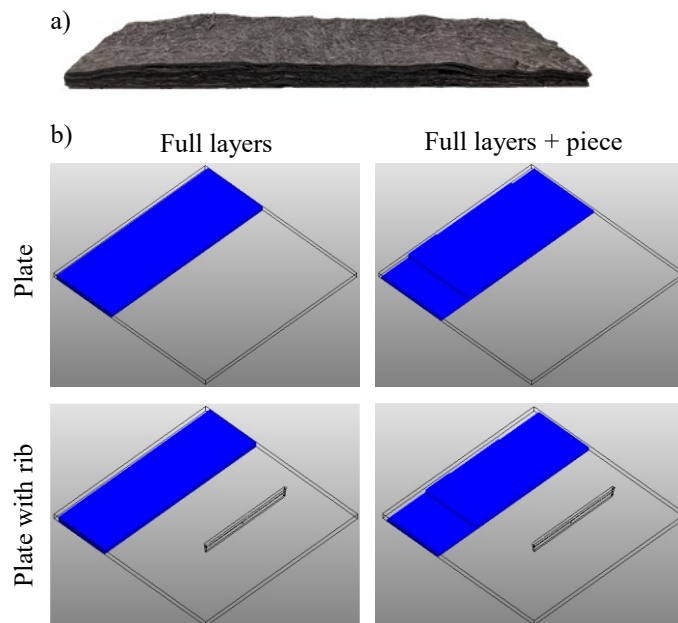


Fig. 6-11 Charge variation during the production: a) charge as tested, with a significant variation in the thickness; b) translation into simulation for both geometries with the representation of full layers compared to the more complex charge with full layers and an additional piece placed on top.

Despite the difference in the charge configuration, the volumes considered for the charge are very similar (as summarized in Tab. 6-6). This charge configuration increases the difference in thickness over the charge. In the simulative replica the charge is represented as having the smaller piece on top of the stack. This charge configuration does not comply with reality, because in reality there is no open edge on the top surface of the charge. The result of the filling in simulation can be seen in Fig. 6-12.

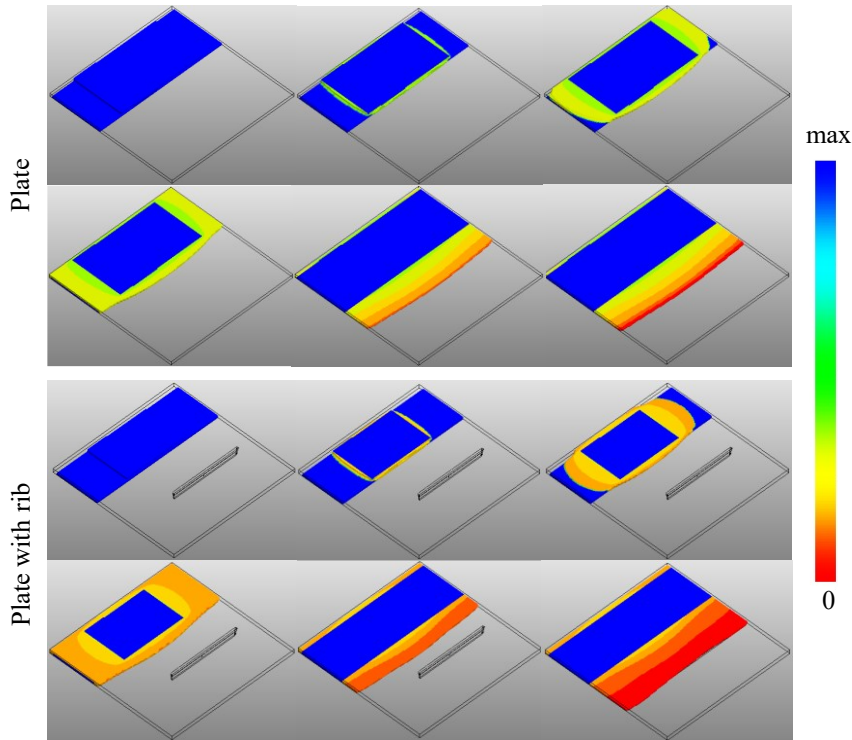


Fig. 6-12 Flow of SMC in the plate and the plate with rib for the charge variation with full layers and an additional smaller piece on top.

The first part of the charge to flow is the additional piece placed on top of the full-sized SMC layers. However, the material does not compress the underlying material, as would happen in reality due to the high void content, but it flows in all open directions. Only once the geometry has reached the thickness of the full-size layers, those begin to deform. Since more material is present in the middle of the geometry, the flow in the center progresses further than the edges. However, for the plate with rib, this progression of the flow is then compensated by the rib filling. In comparison to the basic variations with a simple charge, however, the flow front is more uneven, as can be seen in Fig. 6-13.

Charge variation	thickness	flow max l	rib max h	vol
	mm	mm	mm	mm ³
Basis plate	5.27	264.42	-	561267
Block var	4.74	262.05	-	549119
Basis with rib	5.5	278	14.2	577726
Rib with block var	5.5	270	9.6	555256

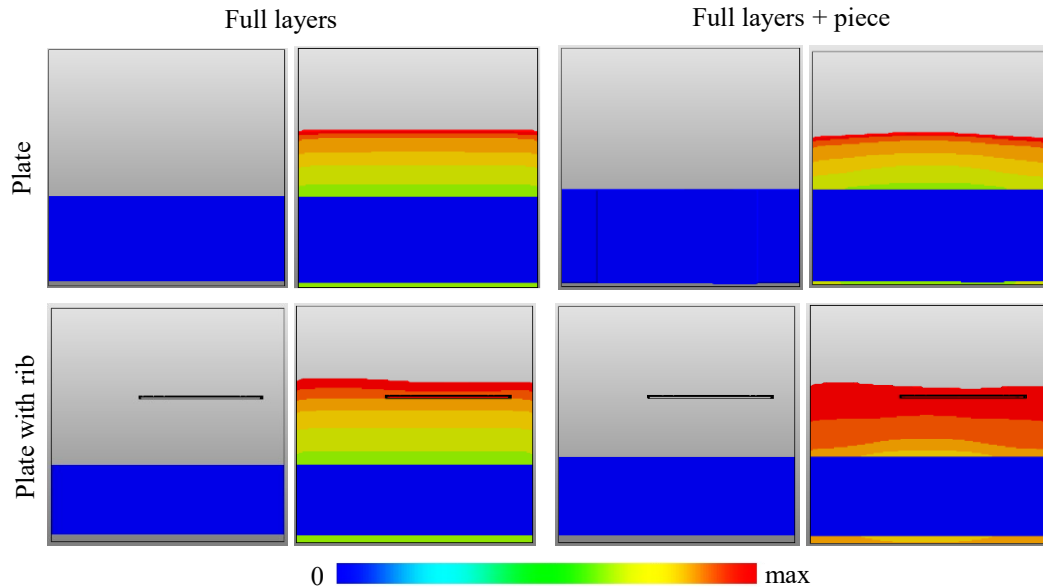


Fig. 6-13 Results for the simulations with the charge variation with a juxtaposition of the filling result and the summary of the final thickness of the geometries, and the maximum flow length and rib filling.

It is visible in Fig. 6-13 that due to the increased amount of material in the middle of the charge, the flow front in the center is longer than for the even charge. The same behavior can be seen in the real part produced with a charge made with a similar configuration in reality. Moreover, the pressure signal is much higher at the beginning of the compression for the uneven charge, although the applied force is the same due to the significant surface difference. Therefore, it is important to make the thickness variation as little as possible in order to keep the compression pressure in a reasonable range. Once the compression has progressed to have a charge of the same thickness overall, the pressure decreases instantly, as the surface of application of the force increases noticeably. In reality, as the charge does not have the step on the top of the stack, but has a more steady increase in thickness, this pressure change is certainly less evident, but it still has to be considered when producing parts with different charges, that the pressure can be significantly influenced by its configuration. For the simple plate it is also evident that the thickness and the maximum flow length are smaller for the more complex charge variation, which in this case seems to be due to the volume difference. Unfortunately, defining a charge with the right volume with the more complex shape was challenging, since the plate is rather thin. As can be seen for the charges before the compression, the overall length of the complex charge was already noticeably longer than for the standard charge.

Ideally this shape should have been kept of the same length. This could be obtained by increasing the plate thickness before the simulation and considering the added block as an additional layer. The same behavior of the charge being longer for the complex shape can also be seen in the plate with rib. The volume difference is also very similar. However, for the simple plate both thickness and flow length resulted lower for the complex charge, while for the plate with rib the thickness remained the same at 5.5 mm. The difference was in the rib filling and flow length.

The last performed variation was the element size of the mesh. To this purpose, three different mesh sizes were chosen. To remain in a reasonable range for the computation time (smallest mesh) and the division in z-direction (biggest mesh), the selected mesh sizes for the comparison were not set to be multiples. The results for the filling time, the temperature and the pressure for the simple plate can be seen in Fig. 6-14. The simulated volumes are also listed.

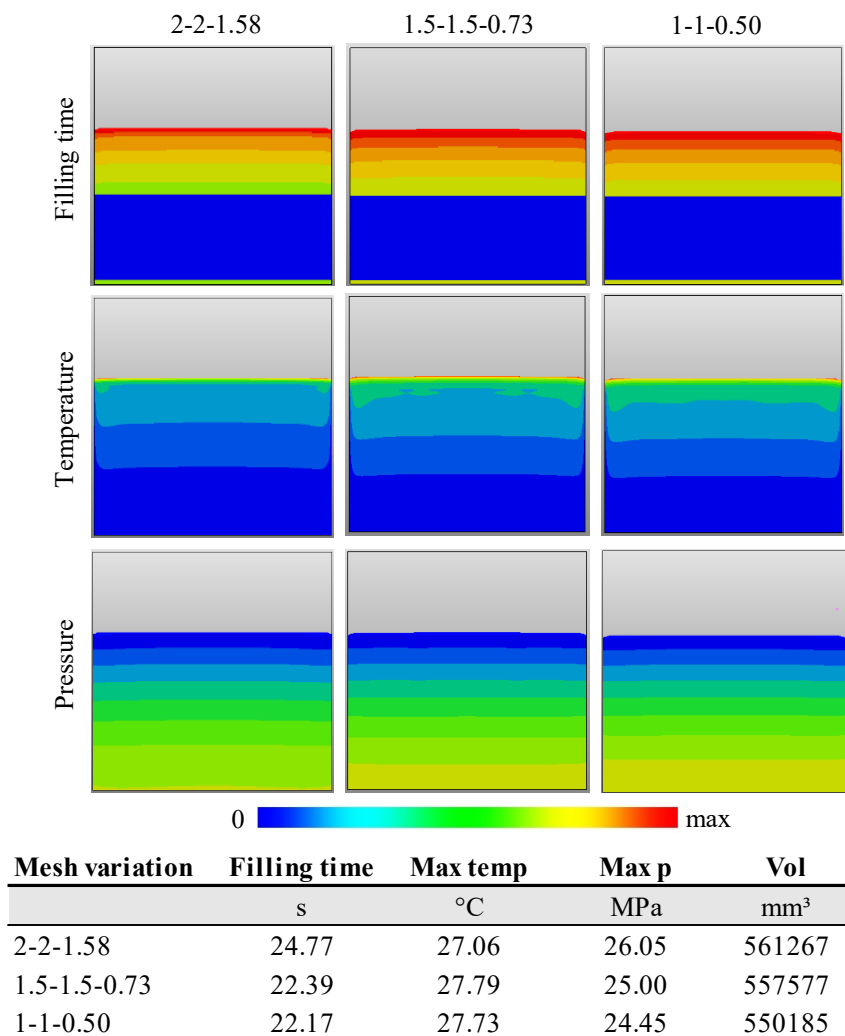


Fig. 6-14 Results for the filling time, the temperature distribution and the pressure distribution at the end of the compression for the mesh variations performed for the simple plates.

As can be seen in Fig. 6-14, the results obtained for the two smaller element sizes are very similar in every value. However, for the biggest mesh size of 2-2-1.58 mm in x-y-z respectively the values differ more significantly. Nevertheless, the mesh size is not the only reason behind the difference, since the charge volume considered for this configuration is bigger than for the others. The increased filling time and pressure are influenced by this mass difference. The temperature on the other hand, cannot be explained with the charge volume difference. The causality between the mesh size and the temperature shall be investigated further in future research.

In Fig. 6-15 the results for the plate with rib can be seen.

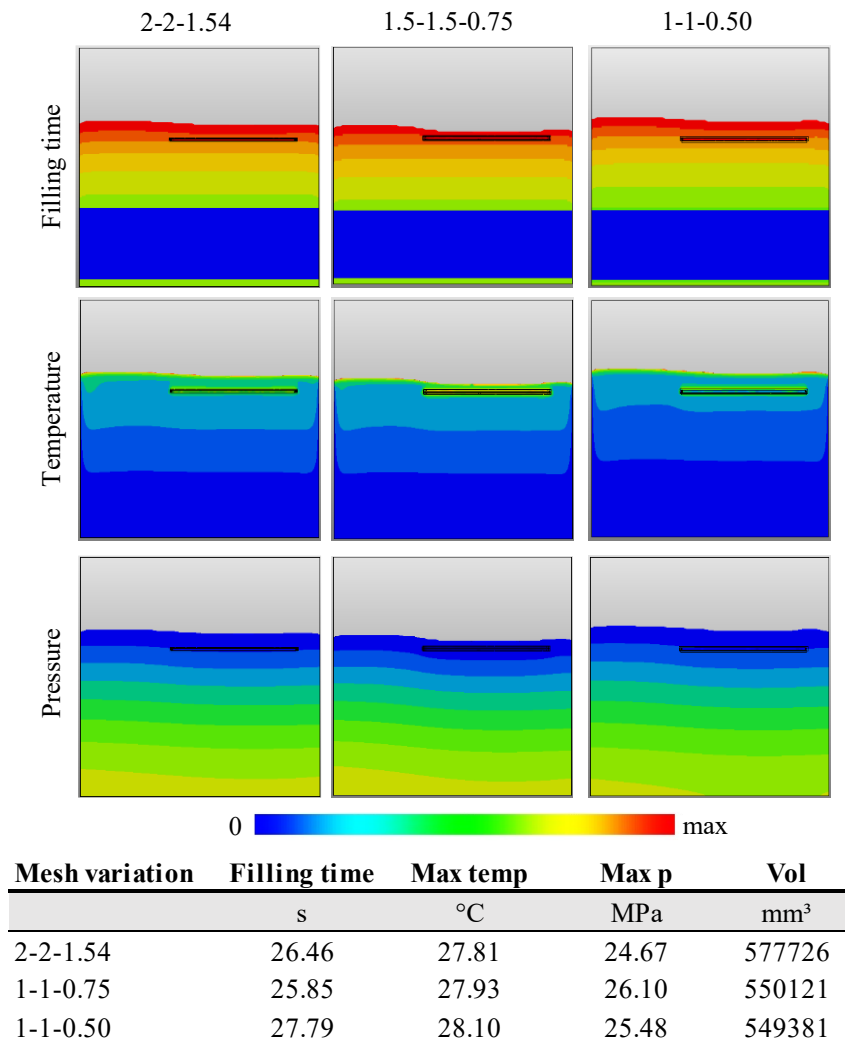


Fig. 6-15 Results for the filling time, the temperature distribution and the pressure distribution at the end of the compression for the mesh variations performed for the plates with rib.

For the results for the plate with rib, the temperature values are very similar for all settings. The pressure and the filling time however, have a more significant variation. A pattern in the values can also not be distinguished, since the variation does not follow the variation in mesh size or the volume of the material. Nevertheless, it can be seen that

the flow front is more variate for the smaller element sizes, leading the smallest element size of 1-1-0.5 mm in x-, y-, and z-directions to have the longest flow path of 283.23 mm despite having the smallest volume, as can be seen in the summary of the key values of the flow length, rib filling and geometry thickness in Tab. 6-7

Tab. 6-7 Resulting geometry thickness, longest flow length, maximum rib filling height and simulated volumes for the performed mesh variations.

	Mesh variation	thickness	flow max l	rib max h	vol
		mm	mm	mm	mm ³
	2-2-1.58	5.27	264.42	-	561267
Plate	1.5-1.5-0.73	5.27	262.735	-	557577
	1-1-0.50	5.27	259.12	-	550185
Plate	2-2-1.54	5.5	278	14.48	577726
with rib	1-1-0.75	5.08	268.39	13.09	550121
	1-1-0.50	5.01	283.23	15.02	549381

It is evident that the volume of the charge does induce the longest flow path for the simple plate, however, this does not apply for the plates with ribs, since the plate with the smallest volume not only reached the longest flow path, but also reached the highest rib filling. Furthermore, in the simple plate the final thickness was identical for all simulations, while for the plate with rib there seems to be a correlation with the simulated volume. However, this shall be investigated further in the future. Another issue is the use of different volumes for the charges. Since the meshes are not multiples of each other, the charge volume had to be chosen again. For industrial viability, the charge selection was done within the capabilities of the software. This process consists in selecting an area on the mold surface manually without receiving a feedback on the currently covered size until it is selected. Only afterwards single elements can be taken out, but the process is extremely time consuming and not industrially applicable. The charge can be created externally, but this approach will have to be evaluated in the future. In conclusion, it is evident that the mesh does have an influence on the result, although it is relatively small and the exact correlation is not clearly assessable, since other variables are also involved, such as the charge volume, the charge shape and placement. These aspects need to be further investigated.

6.4 Discussion and conclusion

Within this section, all the results previously obtained within this research work come together for an overarching validation. To this purpose, two similar geometries are produced with SMC by interrupting the compression when the parts are only half filled. The variability of the resulting plates is assessed in order to establish the transferability from small testing specimens to realistic SMC parts. The main comparison was done for the flow length in the plane of the plate and for the rib filling. It is evident that the flow progresses unevenly over the thickness of the plate, leading to some fibers and layers protruding. Also every plate showed a different flow front with a significant variation,

sometimes with protruding edges, sometimes with protruding center areas. For the fiber configuration in the flow, two main behaviors could be observed: either the layering remained persistent and clearly visible in the flow front, or the fibers from an outermost layer embraced the material through thickness, showing a slower flow with a more complex fiber architecture. This behavior confirms the importance of the fibers in the assessment of the flow of the material. The experimental flow length and thickness of the plates is then compared to numerical results obtained with the material cards previously determined. One of the material cards describing the most likely case for the outcome, is the material card obtained in the material characterization process presented in Chapter 3. The second and third material card were obtained in Chapter 5 by calibrating the simulation to the maximum compression force of the maximum and minimum curves obtained for the tests with the same settings. The prediction of the flow length and the thickness of the plate is very accurate. This is due to the simulation software performing the compression up to the desired stroke, even if the compression takes longer because the maximum force is reached and therefore, the compression speed has to be reduced. Therefore, in future production endeavors the velocity data shall be collected for a further comparison. The result for the simulations with the two material cards for the two limiting cases showed very little difference in the flow length and pattern of the material and the thickness remained unchanged. Therefore, the approach with the limiting cases needs to be perfected, since the goal was to predict the entire range of possibilities to be expected in the real production. To this purpose it could be helpful to evaluate the pressure and displacement data from the press obtained during the production and compare the data to the numerical results. For the more complex variant of the plate with rib the results were similar, with the average flow length from the production being predicted quite accurately in the simulation. However, a known issue of commercially available software solutions also appeared: the filling of the ribs happens much faster than in reality [89].

In a further study of the varying process settings, it was numerically established that a small variation in temperature for the lower mold or in the waiting time does not influence the resulting flow behavior or the pressure signal. However, the configuration of the charge especially in thickness direction does influence the shape of the flow front, with the center with more initial charge material protruding further. Furthermore, the result of the pressure signal is significantly influenced by the area upon which the compression force acts. Therefore, for a more even pressure distribution and consequently, better processing conditions in the real application it is important to distribute the smaller SMC pieces over the surface of the charge. The last variation in the settings performed was purely numerical and consisted in varying the charge. In both configurations the differences between the settings are small, but there does not seem to be a direct link between the mesh size and the filling time, temperature distribution and pressure distribution. Probably other aspects, such as the charge placement, shape and volume influence the result as well and need to be further investigated for a suitable understanding. In general a smaller mesh is preferable, but using a bigger mesh will also provide reliable

results. It simply has to be kept in mind that slight changes in the results can be seen and may be included in safety factors for the development.

Overall the validation allowed to obtain a better understanding of the flow behavior of the material both in reality and in simulation. However, it also showed the intricacy of the flow of the material, as well as the importance of the fibers for the flow behavior. Especially, in relation to the complexity of the geometry to be produced. Furthermore, the limitations of the software, such as the missing representation of the lubricating layer and of the fibers influencing the flow, could be clearly distinguished. Moreover, the variation of the charge, such as shape, placement and volume need to be further understood.

7 Conclusion and Outlook

SMC is a widespread material due to low cycle times, very little amounts of scrap, the suitability to produce complex parts, as well as a high potential for the usage of recycled fibers. The flow of the material is crucial in the reorientation of the fibers during the compression process and in the formation of flow-induced defects. However, the high variability of the material induces a high complexity in the flow behavior. This leads to the establishment of very general guidelines with high safety factors for the development of parts with SMC. Therefore, the material is not currently suitable for structural parts and the potential to save material is not used. In order to improve the development of lightweight structural parts with SMC accurate and reliable simulations of the filling process are necessary. However, the usage of simulations in the development process is not established, since a simulation describing the material in detail would result in almost endless computation times. In order to make simulation tools feasible, the complexity is reduced by simplifying the mathematical description of the material. In current industrially available simulation software only few inputs can be set that can have an influence on the outcome: the material card, the charge configuration and placement in the mold, the part geometry and the simulation settings. The goal of this thesis is the improvement of the inputs coming from the material card and the charge configuration with the derivation of guidelines. In the following Section 7.1 a summary of each main chapter is given and conclusions are drawn. The identified further research endeavors are presented in Section 7.2.

7.1 Summary and conclusion

For each of the four main contributions a summary and a conclusion are given separately.

Material characterization for flow simulation

In the first main chapter of this thesis (Chapter 3), the existing procedure for the characterization of SMC for flow simulations is adapted and specified to include the variability and enhance the industrial applicability. DSC measurements and squeeze flow tests are performed and for both measurement methods a procedure is developed involving five repetitions of each test setting. The existent analysis approach of the preparation of the data for the fitting to the curing kinetics and the viscosity model was adapted to include all repetitions. Once the fitting is done, the data is calibrated using a procedure that has also been enhanced. The first change in the new calibration is the splitting into in-plane and out-of-plane calibration. The in-plane calibration was performed by simulating the

already performed squeeze flow tests at high temperatures. For the out-of-plane calibration, bar flow tests were performed in both possible variants for SMC processing of displacement and force control. For each calibration procedure, a sensitivity analysis was performed in order to understand the influence each parameter change has on the resulting displacement or force signal. It is evident that to include the variability at least five repetitions of each test are necessary. Furthermore, it is recommendable to perform tests with settings as close as possible to typical SMC processing settings referring to the temperature, pressure and closing speeds. Overall the procedure is very time consuming. Therefore, it is recommendable to develop a fitting tool with integrated sensitivity analysis able to perform the analysis semi-automatically.

Development of a bar flow test bench

A flow test bench with a bar shaped opening was developed with the objective of being adopted in a standard press allowing process settings close to real SMC processing. The cavity is relatively complex, forcing the flow to change direction to flow into a geometrical feature similar to a rib. The intent of the test bench is to be used for the calibration of the out-of-plane flow of the material as a standard instead of using similar geometries to the intended geometry, which is the currently applied procedure. Therefore, the presence of typical geometrical features like ribs was compulsory. The developed test bench was adopted for both other main chapters of the material characterization and the investigation of charge configurations. The data recorded by the test bench is the pressure underneath the compression piston as well as the temperature along the flow channel recorded with eight temperature sensors. For an improved data tracking, since the displacement of the press and its recording are not highly accurate, a displacement sensor shall be added for reliable displacement tracking. Furthermore, it is necessary to assess the difference of the actual compression force from the force obtained with the pressure sensor placed on the mold half that is not moving.

Investigation of charge configurations

The second input of the simulation considered more closely is the charge configuration. To this purpose several charge configurations were tested to understand their influence on the flow behavior. Two basic configurations with the same cylindrical volume were defined, consisting of a disc stack and a rectangular sheet rolled up to a spiral. A significant difference could be observed between for the two basic configurations with the discs displaying oscillations and an overall much lower pressure signal compared to the spiral variant. This difference could be linked to the arrangement of the fibers hindering the flow of the spiral and therefore, leading to a high pressure signal. Additionally, the layering and the lubrication present between the SMC sheets in the disc stack leads to the oscillating signal. Further variations were tested for the disc stack charge such as the influence of the slight preferred orientation of the fibers in production direction in the sheets. However, despite seemingly influencing the pressure signal, a clear conclusion was not possible for this configuration without further tests. Other variations included

the moment of the pot life of the material, as well as different batches. It could be established, that the difference in pot life does not have such a significant impact as the use of different batches. This leads to the conclusion that a calibration is necessary for each new batch of material. Both basic configurations were also tested with the double amount. In the disc stack an almost linear dependency could be seen between the increasing height of the stack and the resulting maximum pressure signal. The oscillation in the signal was present in every single test sequence performed with the disc stack. For the double amount spiral charge, consisting of two separate spirals, a significant drop in the pressure signal was denoted in proximity to the separation between the two charges. Therefore, to decrease the necessary compression pressure a separation in the charge is required. For improved filling of structures like ribs with the charge placed perpendicular to it, cutting the charge on the surface should help the filling and reduce the necessary pressure. Both configurations for the basic charges were setup within the capabilities of the simulation software. A clear difference is visible between the simulations referring to the predicted compression pressure, although with opposite effect than seen in reality: for the spiral charge a lower compression force is necessary, while for the disc pile charge the compression force needs to be higher. This difference is mainly due to neglecting the fibers as an influencing factor on the flow in the numerical solution. To compensate for the difference in the prediction, a new calibration was performed for the compression force of the spiral charge. The newly obtained material card shall be adopted when simulating SMC manufacturing for small parts and complex charge configurations. Moreover, for the more traditional stacked SMC charge two new material cards were calibrated replicating the maximum compression force for the minimum and maximum force curves from the five repetitions performed with the same settings.

Validation

The results of the previous chapters are brought together by producing and simulating two SMC geometries: A simple plate and a plate with a rib. During the production the compression is interrupted in order to see the flow front as it progresses during the filling and be able to directly compare the flow length and the flow front pattern between the tests and the simulations. Both geometries show very variate flow lengths in the produced geometries, with the material protruding faster in some sections than others of the flow front. This behavior is probably due to differences in the thickness of the charge, but also to the fiber arrangement. The same behavior can be observed for the ribs. The simulation result for the flow length and final plate thickness is very similar to the experimental result, although the flow front pattern is very different. In the simulation the edges move slower than the rest of the material, while in reality in most plates the edges were the element protruding furthest. However, the flow length prediction in the simulation for the plate with rib is a little bit worse than for the simple plate, since the filling of the rib is overestimated in the simulation. This behavior of the software is known and probably due to the capillary effect of the material in small cross sections [89].

The simulations of the two geometries were also run with the material cards set for the limiting cases determined for the compression force obtained for the bar flow tests. However, no significant difference could be seen in the flow length and in the plate thickness for both geometries, although the difference was a bit bigger for the plate with rib. In future evaluations the compression pressure and compression velocity shall be recorded during the production and compared to the results predicted in simulation. During the production process it could be recorded that the temperature of the lower mold, the waiting time between the charge placement and the first contact of the upper mold with the material, and the charge shape and thickness varied slightly. These characteristics were replicated in simulation. Both the temperature and waiting time do not show any change in the results. The charge variation, however, does influence the result, since the central part of the charge has more material at the beginning and therefore, protrudes further than in the more even charge. This could also be observed in the real plates, but much less pronounced due to the overall variation being significantly more evident. It is clear that a more even thickness distribution in the charge is better for a more uniform flow front and pressure distribution at the beginning of the compression process. In addition to the variations seen in the real process, also the mesh was varied to assess its influence. The influence for the applied change of up to 100 % for x and y and of 150 % for z lead to a small change in the results of the filling time, the temperature distribution and the pressure distribution. However, a clear pattern for the changes could not be identified, since for some changes the values increased, for others they decreased. The issue is that several aspects influence the outcome of the simulation, such as the placement, volume and shape of the charge. Since for each mesh the charge selection needs to be done anew, each time these aspects vary slightly. In future evaluations it shall be tried to keep the charge constant by importing it. However, for this evaluation the assessment was done within the capabilities of one software tool.

7.2 Future research

With the contributions of this research work to the performance of simulations with SMC, the inputs of the material card and of the charge configuration could be improved. However, several aspects need further investigation and improvement. The main improvement and further development potentials are listed below.

Improvement of the inclusion of the variability in the characterization procedure: For the characterization procedure, the suggested approach shall be applied throughout with five repetitions for each test setting for a different commercially available SMC. Furthermore, since for the new tests performed with a different batch of the same material the results differ compared to the previous results, the influence of the batch and factors such as the pot life shall be investigated and understood further and assessed as part of the variability.

Automation of the material card setup: A significant improvement of the characterization procedure can be obtained by automating the data analysis, the fitting and the sensitivity analysis. To this purpose, the process can be implemented as presented in a program like python, where with appropriate GUIs for the test settings, the definition of baselines and the choice of the relevant data sections the data obtained from the measurement can be directly translated into a fitting result. Furthermore, manual adjustment shall be provided, as is available in the current version of the fitting tool provided with the software 3DTimon. The main advantages would be significant time saving, the inclusion of the variability and the reduction of human influence or error on the results.

Improvement of the test bench: In order to increase the functionality of the test bench and the potential aspects to be compared, the inclusion of a displacement sensor could be beneficial. The process was set to displacement control with a constant compression speed, but when the maximum force is reached, the speed is reduced. Since this behavior can be seen in the simulation, it would be favorable to be able to track the actual displacement of the press. Furthermore, a centering option shall be included, reducing the risk of uneven closure of the tool and therefore, ensuring the longevity of the compression piston. Another possible adaptation could be the inclusion of a flexible definition of the bar thickness, in order to reflect the varying rib thicknesses to be expected in SMC parts. Lastly, an overarching control unit allowing to start the recording of all sensors at the same time could be beneficial to reduce the impact of human factors on the result.

Systematic assessment of charge variability: Based on the variations performed within this study, further variations shall be tested that can be found within the same overall charge setting. A charge is usually solely defined by the width, length and weight, the thickness and all other settings are disregarded. Therefore, a wide variety of options is typical in SMC processing, spanning from the fiber orientation, to the batch-specific characteristics over the pot life moment. Within this study these aspects have been partially investigated with one variable setting. However, for the orientation of the sheets in the charge in relation to the production direction only one orientation was tested. Also for the moment of the pot life only two moments were inspected, one being well past the pot life. Tests with materials at four different moments of the pot life are recommendable, and shall be performed in the future. The influence of the SMC batch resulted very significant in the study. In order to confirm this finding and attempt to understand it in depth, further batch variations shall be performed. Furthermore, the flow shall be investigated deeper, by performing standard testing with the bars resulting from the bar flow tests. The results shall be compared to the results obtained in [S19]. The inspection of the fibers inside the bar and at the contact area between the cylinder and the bar, where the material changes direction would also allow conclusions on possible void inclusions and fiber entanglements.

Transfer of the variability of the charge to simulation: Similar to the approach done in this research, two material cards shall be established to forecast the range in which the maximum force signal is. However, all possible variations and their variability shall be

included in the calibration. For example the variation performed regarding the orientation of the SMC layers towards the flow direction shall include both options of the SMC production direction being parallel and perpendicular to the flow direction. Furthermore, different moments of the pot life shall be included that can be descriptive of the SMC to be used for the manufacturing of the part to be simulated.

Investigation of the influence of the fibers on the flow: Since the fibers do influence the flow of SMC significantly, as seen several times throughout this research, especially in small and intricate geometries, where fiber agglomerations and entanglements play a significant role the influence of the fibers needs to be assessed and quantified. The proposed standard testing of the specimens resulting from the bar flow tests can give a first indication of the influence of very long flow paths and the reorientation of the fibers due to different charge configurations. Furthermore, in the plate with ribs the filling of the rib in relation to the fiber arrangement with the sheets perpendicular to the flow direction compared to the sheet cut on the surface along the rib should be compared. The main hindrance for a closer look into the fibers for SMC has been finding an appropriate testing method to see the fibers that ideally leaves the specimen intact for further testing. However, improvements are being made in the non-destructive investigation of carbon fibers in SMC parts, paving the way for new approaches with X-rays [149–151]. Along with the testing of the fibers, also new simulation approaches are being developed including the fibers in the flow that are recommended to be used when simulating small and intricate geometries [91].

Optimized validation of the contents of this thesis: The validation performed for the pursued investigations into the material card and the charge, was satisfactory for the material card obtained from the material characterization. However, for a better understanding of the suitability of the two material cards calibrated to the limiting cases set in the charge variability, the force and closing speed applied during the production of the geometries should also be recorded and compared to the simulation outcomes. Furthermore, the results should be applied to more complex geometries, to assess whether the results are transferrable. The spiral charge has also not been validated within this study, despite a material card has been setup. To this purpose, the same geometries of the validation could also be produced by using a more complex charge configuration, possibly rolled up. However, a comparison of the results does only make sense for the compression force and speed, since the influence of the fibers is neglected in the simulation.

Within the current research project Deepflow (funding code KK5135814KL1) some of the appointed further improvements are being implemented, such as the automated fitting tool [S3], the testing [S1, S2, S7, S11, S22], the setup of a new material card [S4], and improving the flow simulation [S1, S23].

References

- [1] COP28UAE, Ed., "The UAE Consensus: We united. Acted. Delivered.," United Nations Framework Convention on Climate Change, Dubai, 2023. Accessed: Jan. 11, 2024. [Online]. Available: file:///C:/Users/ga54gor/Downloads/COP28_The%20UAE%20Consensus_Brochure_19122023.pdf
- [2] European Commission, Ed., "Communication and roadmap on the European Green Deal," Jan. 2020.
- [3] European Commission. "Providing efficient, safe and environmentally friendly transport." Accessed: Jan. 9, 2024. [Online]. Available: https://commission.europa.eu/strategy-and-policy/priorities-2019-2024/european-green-deal/transport-and-green-deal_en
- [4] European Commission, Ed., "Proposal for a regulation of the European Parliament and of the Council: amending Regulation (EU) 2019/1242 as regards strengthening the CO₂ emission performance standards for new heavy-duty vehicles and integrating reporting obligations, and repealing Regulation (EU) 2018/956," Rep. 2023/0042, Feb. 2023.
- [5] European Commission, Ed., "Sustainable and smart mobility strategy: The transport and mobility sector," 2020.
- [6] United Nations, Ed., "Paris Agreement," United Nations Framework Convention on Climate Change, 2015. Accessed: Jan. 9, 2024. [Online]. Available: https://heinenonline.org/hol-cgi-bin/get_pdf.cgi?handle=hein.journals/intlm55§ion=46
- [7] D. Jasinski, J. Meredith, and K. Kirwan, "A comprehensive review of full cost accounting methods and their applicability to the automotive industry," *0959-6526*, vol. 108, pp. 1123–1139, 2015. doi: 10.1016/j.jclepro.2015.06.040. [Online]. Available: <https://www.sciencedirect.com/science/article/pii/S0959652615007696>
- [8] M. Chiaberge, *New Trends and Developments in Automotive Industry*. Rijeka: IntechOpen, 2011.
- [9] L. W. Cheah, "Cars on a diet : the material and energy impacts of passenger vehicle weight reduction in the U.S: Cars on a diet : the material and energy impacts of passenger vehicle weight reduction in the U.S," Massachusetts Institute of Technology. [Online]. Available: <https://dspace.mit.edu/handle/1721.1/62760>
- [10] T. Bein *et al.*, "Enhanced Lightweight Design – First Results of the FP7 Project ENLIGHT," *2352-1465*, vol. 14, pp. 1031–1040, 2016. doi: 10.1016/j.trpro.2016.05.173. [Online]. Available: <https://www.sciencedirect.com/science/article/pii/S2352146516301740>

- [11] J. C. Kelly, J. L. Sullivan, A. Burnham, and A. Elgowainy, "Impacts of Vehicle Weight Reduction via Material Substitution on Life-Cycle Greenhouse Gas Emissions," *Environmental science & technology*, early access. doi: 10.1021/acs.est.5b03192.
- [12] M. Holmes, "Carbon composites continue to find new markets," *Reinforced Plastics(UK)*, vol. 61, no. 1, pp. 36–40, 2017, doi: 10.1016/j.repl.2016.12.060.
- [13] H. Singh, G. Singh Brar, H. Kumar, and V. Aggarwal, "A review on metal matrix composite for automobile applications," *2214-7853*, vol. 43, pp. 320–325, 2021. doi: 10.1016/j.matpr.2020.11.670. [Online]. Available: <https://www.sciencedirect.com/science/article/pii/S2214785320393457>
- [14] P. Weißhaupt. "Faserverbundwerkstoffe: Zukunftsmaterial mit offener Entsorgung." Accessed: Nov. 25, 2021. [Online]. Available: <https://www.umweltbundesamt.de/faserverbundwerkstoffe-zukunftsmaterial-offener#faserverbundwerkstoffe-und-ihr-potenzial-fur-klima-und-ressourcenschonung>
- [15] S. Kazilbash, "Embracing Circularity in Manufacturing with Carbon Fiber Recycling," *engineering.com*, 13 Jan., 2022.
- [16] M. Sauer, *Composites market report 2019: The global CF- und CC-Market 2019*, 2019. [Online]. Available: https://composites-united.com/media/3988/eng_ccev_market-report_2019_short-version.pdf
- [17] Composites United. "MAI CF-Pyro." Accessed: Nov. 25, 2021. [Online]. Available: <https://composites-united.com/projects/mai-cf-pyro/>
- [18] C. D. Han, *Rheology and Processing of Polymeric Materials, 1: Polymer Rheology*. Oxford: Oxford University Press USA, 2007.
- [19] E. J. Barbero, *Introduction to composite materials design*, 2nd ed. (Composite Materials). Boca Raton, FL: CRC Press, an imprint of Taylor and Francis, 2011. [Online]. Available: <https://www.taylorfrancis.com/books/mono/10.1201/9781439894132/introduction-composite-materials-design-ever-barbero>
- [20] H. G. Kia, *Sheet molding compounds: Science and technology*. Hanser Verlag, 1993.
- [21] S. B. Visweswaraiyah, M. Selezneva, L. Lessard, and P. Hubert, "Mechanical characterisation and modelling of randomly oriented strand architecture and their hybrids – A general review," *Journal of Reinforced Plastics and Composites*, vol. 37, no. 8, pp. 548–580, 2018, doi: 10.1177/0731684418754360.
- [22] M. Selezneva and L. Lessard, "Characterization of mechanical properties of randomly oriented strand thermoplastic composites," *Journal of Composite Materials*, vol. 50, no. 20, pp. 2833–2851, 2016, doi: 10.1177/0021998315613129.

- [23] R. L. Smith, "High-Volume SMC Exterior Body Panels - An Evolution in Productivity," in *Electronic control module network and data link development and validation using hardware in the loop systems*, 400 Commonwealth Drive, Warrendale, PA, United States, D. Williams, J. Allen, and R. Hukkeri, Eds., 2009, doi: 10.4271/880360.
- [24] E. Witten and V. Mathes, *The European Market for Fibre Reinforced Plastics/Composites in 2021*, 2023. [Online]. Available: https://www.avk-tv.de/files/20230425_2023_avk_market_report_final.pdf
- [25] P. J. Blanchard, D. H. Bank, J. S. Dahl, and J. R. Reese, *CF-SMC technology for high volume manufacturing*, 2018. [Online]. Available: https://speautomotive.com/wp-content/uploads/2021/01/blanchard_cf-smc-technology-for-high-volume-mfg_special-cc.pdf
- [26] J. Palmer, L. Savage, O. R. Ghita, and K. E. Evans, "Sheet moulding compound (SMC) from carbon fibre recyclate," *Composites Part A: Applied Science and Manufacturing*, vol. 41, no. 9, pp. 1232–1237, 2010. doi: 10.1016/j.compositesa.2010.05.005. [Online]. Available: <https://www.sciencedirect.com/science/article/pii/S1359835X1000134X>
- [27] H. J. Wolf, "Kunststoffe im Automobilbau - Eine neue Chance und Herausforderung," *Materialwissenschaft Werkst*, vol. 23, no. 8, pp. 305–308, 1992, doi: 10.1002/mawe.19920230809.
- [28] T. Rademacker, M. Fette, and G. Jüptner, "Nachhaltiger Einsatz von Carbonfasern dank CFK-Recycling," *Lightweight Des*, vol. 11, no. 5, pp. 12–19, 2018. doi: 10.1007/s35725-018-0046-7. [Online]. Available: <https://link.springer.com/article/10.1007/s35725-018-0046-7>
- [29] M. Revellino, L. Saggese, and E. Gaiero, "Compression Molding of SMCs," in *Comprehensive Composite Materials: Polymer Matrix Composites*, A. Kelly and C. Zweben, Eds., Amsterdam: Elsevier, 2000, pp. 763–806.
- [30] M. Fette, Ed., *High efficient material and process combination for future aircraft applications based on advanced sheet molding compound technologies*. Oklahoma State University, USA: Dr. Jim Smay, 2016.
- [31] Green Car Congress. "Toyota using Mitsubishi Rayon's carbon fiber SMC for hatch door frame of new Prius PHV." Accessed: Jul. 10, 2023.
- [32] C. D. Shirrell, "Variability in static strengths of sheet molding compounds (SMC)," *Polymer Composites*, vol. 4, no. 3, pp. 172–179, 1983, doi: 10.1002/pc.750040307.
- [33] D. W. Wilson, *High Modulus Fiber Composites in Ground Transportation and High Volume Applications: A Symposium*. ASTM International, 1985.

- [34] M. Cabrera-Ríos and J. M. Castro, "An economical way of using carbon fibers in sheet molding compound compression molding for automotive applications," *Polymer Composites*, vol. 27, no. 6, pp. 718–722, 2006, doi: 10.1002/pc.20257.
- [35] C. Nony-Davadie, L. Peltier, Y. Chemisky, B. Surowiec, and F. Meraghni, "Mechanical characterization of anisotropy on a carbon fiber sheet molding compound composite under quasi-static and fatigue loading," *Journal of Composite Materials*, vol. 53, no. 11, pp. 1437–1457, 2019, doi: 10.1177/0021998318804612.
- [36] J. M. Castro and R. M. Griffith, "Sheet molding compound compression-molding flow," *Polymer Engineering & Science*, vol. 29, no. 10, pp. 632–638, 1989.
- [37] L. M. Martulli, L. Muyschondt, M. Kerschbaum, S. Pimenta, S. V. Lomov, and Y. Swolfs, "Carbon fibre sheet moulding compounds with high in-mould flow: Linking morphology to tensile and compressive properties," *Composites Part A: Applied Science and Manufacturing*, vol. 126, p. 105600, 2019, doi: 10.1016/j.compositesa.2019.105600.
- [38] N. Meyer, L. Schöttl, L. Bretz, A. N. Hrymak, and L. Kärger, "Direct Bundle Simulation approach for the compression molding process of Sheet Molding Compound," *Composites Part A: Applied Science and Manufacturing*, vol. 132, p. 105809, 2020, doi: 10.1016/j.compositesa.2020.105809.
- [39] G. Alnersson, M. W. Tahir, A.-L. Ljung, and T. S. Lundström, "Review of the Numerical Modeling of Compression Molding of Sheet Molding Compound," *Processes*, vol. 8, no. 2, p. 179, 2020, doi: 10.3390/pr8020179.
- [40] M. Hohberg, *Experimental investigation and process simulation of the compression molding process of Sheet Molding Compound (SMC) with local reinforcements*. KIT Scientific Publishing, 2022. [Online]. Available: <https://library.oapen.org/handle/20.500.12657/53949>
- [41] M. Hohberg, L. Kärger, A. Hrymak, and F. Henning, "Prozesssimulation von Sheet Molding Compound (SMC) als Schlüssel zur integrierten Simulationskette," *NAFEMS Online-Magazin*, no. 42, pp. 49–56, 2017.
- [42] Dominic Schommer *et al.*, "Material Characterization and Compression Molding Simulation of CF-SMC Materials in a Press Rheometry Test," *Key Engineering Materials*, vol. 809, pp. 467–472, 2019. doi: 10.4028/www.scientific.net/KEM.809.467. [Online]. Available: <https://www.scientific.net/kem.809.467>
- [43] V. Romanenko, M. Duhovic, D. Schommer, J. Hausmann, and J. Eschl, "Advanced process simulation of compression molded carbon fiber sheet molding compound (C-SMC) parts in automotive series applications," *Composites Part A: Applied Science and Manufacturing*, vol. 157, p. 106924, 2022. doi: 10.1016/j.compositesa.2022.106924. [Online]. Available: <https://www.sciencedirect.com/science/article/pii/S1359835X22001178>

- [44] Astar S.A., "Technical Datasheet: CARBKID PGK5250-R63," 2019.
- [45] Quantum Composites. "AMC: Products."
- [46] M. M. Shokrieh and R. Mosalmani, "Modeling of sheet molding compound compression molding under non-isothermal conditions," *Journal of Reinforced Plastics and Composites*, vol. 33, no. 13, pp. 1183–1198, 2014, doi: 10.1177/0731684414526289.
- [47] T. Whelan and J. Goff, "Sheet Molding Compound," in *Molding of thermosetting plastics* (Pocket guides to plastics), T. Whelan and J. Goff, Eds., New York: Van Nostrand Reinhold, 1990, pp. 75–85.
- [48] W. Assmann and E. Witten, *Handbuch Faserverbundkunststoffe/Composites: Grundlagen, Verarbeitung, Anwendungen*, 4th ed. (Springer eBook Collection Computer Science and Engineering). Wiesbaden: Springer Vieweg, 2013.
- [49] G. W. Ehrenstein, *Faserverbund-Kunststoffe: Werkstoffe - Verarbeitung - Eigenschaften*, 2nd ed. (Hanser eLibrary). München: Hanser, 2006.
- [50] F. Henning and E. Moeller, *Handbuch Leichtbau: Methoden, Werkstoffe, Fertigung*, 2nd ed. (Hanser eLibrary). München: Hanser, 2020.
- [51] M. Neitzel, P. Mitschang, and U. Breuer, *Handbuch Verbundwerkstoffe: Werkstoffe, Verarbeitung, Anwendung*, 1st ed. s.l.: Carl Hanser Fachbuchverlag, 2014.
- [52] P. Eyerer, T. Hirth, and P. Elsner, *Polymer Engineering: Technologien und Praxis ; mit 155 Tabellen* (VDI). Berlin, Heidelberg: Springer, 2008.
- [53] ECPS Group. "LAMBORGHINI HURACAN LP580 LP610 FORGED CARBON AIR INTAKE FRAMES COVERS." Accessed: Jul. 10, 2023. [Online]. Available: <https://ecpsgroup.com/produkt/lamborghini-huracan-lp580-lp610-forged-carbon-air-intake-frames-covers/>
- [54] Astar S.A., "ASTAR Carbon Fibre SMC for Multifunctional Spare Wheel Pan of Mercedes-AMG E-Class," *Linkedin*, 01 Feb., 2018. Accessed: Nov. 28, 2019. [Online]. Available: <https://www.linkedin.com/pulse/astar-carbon-fibre-smc-multifunctional-spare-wheel-pan-astar-s-a->
- [55] Blackwave GmbH. "Formula Student RIM." Accessed: Nov. 25, 2021. [Online]. Available: <https://blackwave.de/en/portfolio-item/formula-student-rim/>
- [56] D. Bücheler, "Locally Continuous-fiber Reinforced Sheet Molding Compound," Dissertation, Fraunhofer ICT, KIT, Karlsruhe, 2018.
- [57] A. D. Evans, C. C. Qian, T. A. Turner, L. T. Harper, and N. A. Warrior, "Flow characteristics of carbon fibre moulding compounds," *Composites Part A: Applied Science and Manufacturing*, vol. 90, pp. 1–12, 2016. doi: 10.1016/j.compositesa.2016.06.020. [Online]. Available: <https://www.sciencedirect.com/science/article/pii/S1359835X16301993>

- [58] G. Nicoletto, E. Riva, and A. Stocchi, "Mechanical Characterization of Advanced Random Discontinuous Carbon/Epoxy Composites," *2214-7853*, vol. 3, no. 4, pp. 1079–1084, 2016. doi: 10.1016/j.matpr.2016.03.052. [Online]. Available: <https://www.sciencedirect.com/science/article/pii/S2214785316002571>
- [59] K. Johanson, L. T. Harper, M. S. Johnson, and N. A. Warrior, "Heterogeneity of discontinuous carbon fibre composites: Damage initiation captured by Digital Image Correlation," *Composites Part A: Applied Science and Manufacturing*, vol. 68, pp. 304–312, 2015. doi: 10.1016/j.compositesa.2014.10.014. [Online]. Available: <https://www.sciencedirect.com/science/article/pii/S1359835X14003261>
- [60] M. Piry and W. Michaeli, "Stiffness and failure analysis of SMC components considering the anisotropic material properties," *Macromol. Mater. Eng.*, vol. 284–285, no. 1, pp. 40–45, 2000, doi: 10.1002/1439-2054(20001201)284:1<40::AID-MAME40>3.0.CO;2-3.
- [61] P. Odenberger, H. Andersson, and T. Lundström, "Experimental flow-front visualisation in compression moulding of SMC," *Composites Part A: Applied Science and Manufacturing*, vol. 35, no. 10, pp. 1125–1134, 2004, doi: 10.1016/j.compositesa.2004.03.019.
- [62] L. M. Martulli, M. Kerschbaum, S. V. Lomov, and Y. Swolfs, "Weld lines in tow-based sheet moulding compounds tensile properties: Morphological detrimental factors," *Composites Part A: Applied Science and Manufacturing*, vol. 139, p. 106109, 2020, doi: 10.1016/j.compositesa.2020.106109.
- [63] F. Folgar and C. L. Tucker, "Orientation Behavior of Fibers in Concentrated Suspensions," *Journal of Reinforced Plastics and Composites*, vol. 3, no. 2, pp. 98–119, 1984, doi: 10.1177/073168448400300201.
- [64] P. Feraboli, E. Peitso, F. Deleo, T. Cleveland, and P. B. Stickler, "Characterization of Prepreg-Based Discontinuous Carbon Fiber/Epoxy Systems," *Journal of Reinforced Plastics and Composites*, vol. 28, no. 10, pp. 1191–1214, 2009, doi: 10.1177/0731684408088883.
- [65] P. Dumont, L. Orgéas, S. Le Corre, and D. Favier, "Anisotropic viscous behavior of sheet molding compounds (SMC) during compression molding," *International Journal of Plasticity*, vol. 19, no. 5, pp. 625–646, 2003.
- [66] O. Guiraud, P. Dumont, L. Orgéas, and D. Favier, "Rheometry of compression moulded fibre-reinforced polymer composites: Rheology, compressibility, and friction forces with mould surfaces," *Composites Part A: Applied Science and Manufacturing*, vol. 43, no. 11, pp. 2107–2119, 2012, doi: 10.1016/j.compositesa.2012.06.006.
- [67] M. Hohberg, L. Kärger, F. Henning, and A. Hrymak, "Rheological measurements and rheological shell model Considering the compressible behavior of long fiber reinforced sheet molding compound (SMC)," *Composites Part A: Applied Science*

- and Manufacturing*, vol. 95, pp. 110–117, 2017, doi: 10.1016/j.compositesa.2017.01.006.
- [68] S. Le Corre, P. Dumont, L. Orgéas, and D. Favier, "Rheology of highly concentrated planar fiber suspensions," *Journal of Rheology*, vol. 49, no. 5, pp. 1029–1058, 2005, doi: 10.1122/1.1993594.
- [69] L. J. Lee, L. F. Marker, and R. M. Griffith, "The rheology and mold flow of polyester sheet molding compound," *Polymer Composites*, vol. 2, no. 4, pp. 209–218, 1981, doi: 10.1002/pc.750020412.
- [70] M. R. Barone and D. A. Caulk, "Kinematics of flow in sheet molding compounds," *Polymer Composites*, vol. 6, no. 2, pp. 105–109, 1985, doi: 10.1002/pc.750060208.
- [71] R. Bertóti and T. Böhlke, "Flow-induced anisotropic viscosity in short FRPs," *Mech Adv Mater Mod Process*, vol. 3, no. 1, pp. 1–12, 2017. doi: 10.1186/s40759-016-0016-7. [Online]. Available: <https://link.springer.com/track/pdf/10.1186/s40759-016-0016-7>
- [72] C. F. Schmid, L. H. Switzer, and D. J. Klingenberg, "Simulations of fiber flocculation: Effects of fiber properties and interfiber friction," *Journal of Rheology*, vol. 44, no. 4, pp. 781–809, 2000, doi: 10.1122/1.551116.
- [73] D. E. Sommer, A. J. Favaloro, and R. B. Pipes, "Coupling anisotropic viscosity and fiber orientation in applications to squeeze flow," *Journal of Rheology*, vol. 62, no. 3, pp. 669–679, 2018.
- [74] I. Taketa, T. Okabe, H. Matsutani, and A. Kitano, "Flowability of unidirectionally arrayed chopped strands in compression molding," *Composites Part B: Engineering*, vol. 42, no. 6, pp. 1764–1769, 2011, doi: 10.1016/j.compositesb.2011.01.021.
- [75] Barone and D. A. Caulk, "A model for the flow of a chopped fiber reinforced polymer compound in compression molding," *Journal of applied mechanics*, vol. 53, no. 2, pp. 361–371, 1986.
- [76] M. R. Kamal, "Thermoset characterization for moldability analysis," *Polym. Eng. Sci.*, vol. 14, no. 3, pp. 231–239, 1974, doi: 10.1002/pen.760140312.
- [77] M. R. Kamal and M. E. Ryan, "The behavior of thermosetting compounds in injection molding cavities," *Polym. Eng. Sci.*, vol. 20, no. 13, pp. 859–867, 1980, doi: 10.1002/pen.760201305.
- [78] M. R. Kamal and M. E. Ryan, "Reactive polymer processing: Techniques and trends," *Adv. Polym. Technol.*, vol. 4, no. 34, pp. 323–348, 1984, doi: 10.1002/adv.1984.060040312.
- [79] M. R. Kamal and A. I. Isayev, *Injection molding: Technology and fundamentals*. Carl Hanser Verlag GmbH Co KG, 2012.

- [80] A. Yousefi, P. G. Lafleur, and R. Gauvin, "Kinetic studies of thermoset cure reactions: A review," *Polymer Composites*, vol. 18, no. 2, pp. 157–168, 1997, doi: 10.1002/pc.10270.
- [81] J. M. Castro and C. W. Macosko, "Kinetics and Rheology of Typical Polyurethane Reaction Injection Molding Systems," in *Soc Plast Eng Tech Pap Annu Tech Conf, 38th, Plast Prog Through Process*, New York, NY, USA, Society of Plastics Engineers, Ed., 1980, pp. 434–438.
- [82] J. M. Castro and C. W. Macosko, "Studies of mold filling and curing in the reaction injection molding process," *AIChE J.*, vol. 28, no. 2, pp. 250–260, 1982, doi: 10.1002/aic.690280213.
- [83] H. Kubota, "Curing of highly reactive polyester resin under pressure: Kinetic studies by differential scanning calorimetry," *Journal of Applied Polymer Science*, vol. 19, no. 8, pp. 2279–2297, 1975, doi: 10.1002/app.1975.070190819.
- [84] S. V. Muzumdar and L. J. Lee, "Mechanistic Modeling of Gel Time in the Reactive Processing of Unsaturated Polyester Resins," *ANTEC 92--Shaping the Future*, vol. 1, pp. 1582–1587, 1992.
- [85] R. Mohan and T. H. Grentzer, "Process Simulation in Thermoset Composites for Cure Response and Stress Prediction," *Journal of Reinforced Plastics and Composites*, vol. 14, no. 1, pp. 72–84, 1995, doi: 10.1177/073168449501400105.
- [86] M. R. Kamal and S. Sourour, "Kinetics and thermal characterization of thermoset cure," *Polym. Eng. Sci.*, vol. 13, no. 1, pp. 59–64, 1973, doi: 10.1002/pen.760130110.
- [87] W. W. Focke, M. S. Smit, A. T. Tolmay, L. S. van der Walt, and W. L. van Wyk, "Differential scanning calorimetry analysis of thermoset cure kinetics: Phenolic resole resin," *Polym. Eng. Sci.*, vol. 31, no. 23, pp. 1665–1669, 1991, doi: 10.1002/pen.760312306.
- [88] Toray Engineering Co. Ltd., Ed. *3DTimon Manual*.
- [89] C. Qian, A. Deshpande, M. Jesri, R. Groves, N. Reynolds, and K. Kendall, "A Comprehensive Assessment of Commercial Process Simulation Software for Compression Moulding of Sheet Moulding Compound," in *24th International Conference on Material Forming*, Liège, ESAFORM 2021, Ed., 2021.
- [90] F. Rothenhäusler *et al.*, "Experimental and Numerical Analysis of SMC Compression Molding in Confined Regions—A Comparison of Simulation Approaches," *Journal of Composites Science*, vol. 6, no. 3, p. 68, 2022. doi: 10.3390/jcs6030068. [Online]. Available: <https://www.mdpi.com/2504-477x/6/3/68>

- [91] C. Kuhn, E. Koerner, and O. Taeger, "A simulative overview on fiber predictions models for discontinuous long fiber composites," *Polymer Composites*, vol. 41, no. 1, pp. 73–81, 2020, doi: 10.1002/pc.25346.
- [92] M. Hohberg, "New simulation approaches for Sheet Molding Compound process simulation,"
- [93] R. Nakano and K. Sakaba, "Development of CAE software for injection and BMC/SMC molding including short/long fibers reinforcement," in *Proceedings of the International SAMPE Technical Conference*, Paris, France, 2014.
- [94] H.-S. Kim and S.-H. Chang, "Simulation of compression moulding process for long-fibre reinforced thermoset composites considering fibre bending," *Composite Structures*, vol. 230, p. 111514, 2019. doi: 10.1016/j.compstruct.2019.111514. [Online]. Available: <https://www.sciencedirect.com/science/article/pii/S0263822319327485>
- [95] R. Nakano and K. Sakaba, "Development of CAE software for injection and BMC/SMC molding including short/long fibers reinforcement," in *Proceedings of the SAMPE Technical Conference 2014*.
- [96] J. Teuwsen, S. K. Hohn, and T. A. Osswald, "Direct Fiber Simulation of a Compression Molded Ribbed Structure Made of a Sheet Molding Compound with Randomly Oriented Carbon/Epoxy Prepreg Strands—A Comparison of Predicted Fiber Orientations with Computed Tomography Analyses," *Journal of Composites Science*, vol. 4, no. 4, p. 164, 2020, doi: 10.3390/jcs4040164.
- [97] Toray Engineering Co. Ltd., "CompositePRESS," in *3DTimon Manual*, Toray Engineering Co. Ltd., Ed.
- [98] E. D. C. Andrade, "The Viscosity of Liquids," *Nature*, vol. 125, no. 3148, pp. 309–310, 1930. doi: 10.1038/125309b0. [Online]. Available: <https://www.nature.com/articles/125309b0>
- [99] M. M. Cross, "Rheology of non-Newtonian fluids: A new flow equation for pseudoplastic systems," *Journal of Colloid Science*, vol. 20, no. 5, pp. 417–437, 1965. doi: 10.1016/0095-8522(65)90022-X. [Online]. Available: <https://www.sciencedirect.com/science/article/pii/009585226590022x>
- [100] TA Instruments. "The case for a generic definition of Differential Scanning Calorimetry." TA. [Online]. Available: <http://www.tainstruments.com/>
- [101] Mettler Toledo. "Choosing the right baseline." UserCom.
- [102] Mettler Toledo. "Interpreting DSC curves." UserCom.
- [103] TA Instruments. "Interpreting Unexpected Events and Transitions in DSC Results." TA. [Online]. Available: <http://www.tainstruments.com/>

- [104] TA Instruments. "DSC Baseline Improvements Obtained by a New Heat Flow Measurement Technique." TA. [Online]. Available: <http://www.tainstruments.com/>
- [105] Laurent Orgéas and Pierre J. J. Dumont, "Sheet Molding Compounds," in *Wiley Encyclopedia of Composites*, John Wiley & Sons, Ltd, 2012, pp. 1–36.
- [106] M. Duhovic, V. Romanenko, D. Schommer, and J. Hausmann, "Material characterization of high fiber volume content long fiber reinforced SMC materials," in *The 14th International Conference on Flow Processing in Composite Materials*, Aconf, Ed., 2018.
- [107] R. B. Bird, "Transport phenomena," *Appl. Mech. Rev.*, vol. 55, no. 1, R1-R4, 2002.
- [108] A. G. Gibson, G. Kotsikos, J. H. Bland, and S. Toll, "Squeeze flow," in *Rheological measurement*, A. A. Collyer and D. W. Clegg, Eds. Dordrecht: Springer-Science+Business Media B.V, 1998, pp. 550–592.
- [109] A. Gibson and S. Toll, "Mechanics of the squeeze flow of planar fibre suspensions," *Journal of Non-Newtonian Fluid Mechanics*, vol. 82, no. 1, pp. 1–24, 1999. doi: 10.1016/S0377-0257(98)00127-X. [Online]. Available: <https://www.sciencedirect.com/science/article/pii/S037702579800127x>
- [110] G. Kotsikos and A. Gibson, "Investigation of the squeeze flow behaviour of Sheet Moulding Compounds (SMC)," *Composites Part A: Applied Science and Manufacturing*, vol. 29, no. 12, pp. 1569–1577, 1998. doi: 10.1016/S1359-835X(98)00094-3. [Online]. Available: <https://www.sciencedirect.com/science/article/pii/S1359835X98000943>
- [111] K. Rienesl, P. S. Stelzer, and Z. Major, "Squeeze flow rheometry and data analysis of carbon fiber sheet molding compounds," *Materials Today: Proceedings*, vol. 62, pp. 2433–2435, 2022. doi: 10.1016/j.matpr.2022.02.583. [Online]. Available: <https://www.sciencedirect.com/science/article/pii/S2214785322012445>
- [112] C. F. Vahlund and B. R. Gebart, "Squeeze flow rheology in large tools," in *Proceedings of the 5th International Conference on Flow Processes in Composite Materials*, Plymouth, UK, 1999, pp. 365–372.
- [113] J. Stefan, "Versuche über die scheinbare Adhäsion," *Annalen der Physik*, vol. 230, no. 2, pp. 316–318, 1875, doi: 10.1002/andp.18752300213.
- [114] L. F. Marker and B. Ford, "Flow and curing behavior exhibited by SMC during molding," *Modern Plastics*, no. 5, pp. 64–71, 1977.
- [115] N. E. J. Olsson, T. S. Lundström, and K. Olofsson, "Design of experiment study of compression moulding of SMC," *Plastics, Rubber and Composites*, vol. 38, 9-10, pp. 426–431, 2009, doi: 10.1179/146580109X12540995045886.

- [116] R. J. Silva-Nieto, B. C. Fisher, and A. W. Birley, "Rheological characterization of unsaturated polyester resin sheet molding compound," *Polym. Eng. Sci.*, vol. 21, no. 8, pp. 499–506, 1981, doi: 10.1002/pen.760210810.
- [117] S. Le Corre, L. Orgéas, D. Favier, A. Tourabi, A. Maazouz, and C. Venet, "Shear and compression behaviour of sheet moulding compounds," *Composites Science and Technology*, vol. 62, no. 4, pp. 571–577, 2002. doi: 10.1016/S0266-3538(01)00151-8. [Online]. Available: <https://www.sciencedirect.com/science/article/pii/S0266353801001518/pdffft?md5=c44cd8797e55c6fc876be849dff22c9f&pid=1-s2.0-S0266353801001518-main.pdf>
- [118] W. Michaeli, M. Mahlke, T. Osswald, and M. Nölke, "Analyse und Messung des Fliessens von SMC mit einem Pressrheometer," *Kunststoffe*, 1990, 1990.
- [119] C.-M. Lin, C.-I. Weng, and C.-T. Ho, "Anisotropy in sheet molding compounds during compression molding," *Polymer Composites*, vol. 18, no. 5, pp. 613–622, 1997, doi: 10.1002/pc.10312.
- [120] L. M. Abrams and J. M. Castro, "Predicting molding forces during sheet molding compound (SMC) compression molding. I: Model development," *Polymer Composites*, vol. 24, no. 3, pp. 291–303, 2004.
- [121] S. Boylan, L. M. Abrams, and J. M. Castro, "Predicting molding forces during sheet molding compounds (SMC) compression molding. II: Effect of SMC composition," *Polymer Composites*, vol. 24, no. 6, pp. 731–747, 2003.
- [122] A. Oelgarth, "Analyse und Charakterisierung des Fließverhaltens langfaserverstärkter Pressmassen," Dissertation, Fakultät für Maschinenwesen, RWTH, Aachen, 1997.
- [123] M. Ritter, "Materialcharakterisierung von langfaserverstärkten Pressmassen und Beschreibung des Pressprozesses durch Simulation und Messung des ...," Dissertation, Institut für Kunststoffverarbeitung, RWTH, Aachen, 2003.
- [124] H. Kau and E. M. Hagerman, "Experimental and analytical procedures for flow dynamics of sheet molding compound (SMC) in compression molding," *Polymer Composites*, vol. 8, no. 3, pp. 176–187, 1987, doi: 10.1002/pc.750080306.
- [125] O. Specker, "Pressen von SMC: Computersimulationen zur rechnerunterstützten Auslegung des Prozesses und zur Ermittlung der Bauteileigenschaften.," Dissertation, Institut für Kunststoffverarbeitung für Industrie und Handwerk, RWTH, Aachen, 1990.
- [126] M. Rabinovich, K. L. Olsavsky, B. Leach, M. Cabrera-Ríos, and J. M. Castro, "Sheet molding compound characterization using spiral flow," *Journal of Applied Polymer Science*, vol. 109, no. 4, pp. 2465–2471, 2008, doi: 10.1002/app.25160.
- [127] J. Engmann, C. Servais, and A. S. Burbidge, "Squeeze flow theory and applications to rheometry: A review," *Journal of Non-Newtonian Fluid Mechanics*, vol.

- 132, 1-3, pp. 1–27, 2005. doi: 10.1016/j.jnnfm.2005.08.007. [Online]. Available: <https://www.sciencedirect.com/science/article/pii/S0377025705001977>
- [128] P. Dumont, L. Orgéas, D. Favier, P. Pizette, and C. Venet, "Compression moulding of SMC: In situ experiments, modelling and simulation," *Composites Part A: Applied Science and Manufacturing*, vol. 38, no. 2, pp. 353–368, 2007, doi: 10.1016/j.compositesa.2006.03.010.
- [129] J.-H. Jeong, K.-T. Kim, and Y.-T. Im, "Plane-strain compression molding analysis of sheet molding compounds in flat and cross-sectional T-shape molds," *Journal of materials processing technology*, vol. 57, 3-4, pp. 320–331, 1996. doi: 10.1016/0924-0136(95)02077-2. [Online]. Available: <https://www.sciencedirect.com/science/article/pii/0924013695020772>
- [130] K.-T. Kim, J.-H. Jeong, and Y.-T. Im, "Effect of molding parameters on compression molded sheet molding compounds parts," *Journal of materials processing technology*, vol. 67, 1-3, pp. 105–111, 1997. doi: 10.1016/S0924-0136(96)02827-0. [Online]. Available: <https://www.sciencedirect.com/science/article/pii/S0924013696028270>
- [131] S. Kröger, "Entwicklung eines Prüfstands zur Beurteilung der Fließfähigkeit von Carbon-SMC Materialien," Bachelor Thesis, Chair of Carbon Composites, Technical University Munich, Garching bei München, 2017.
- [132] E. Comte, D. Merhi, V. Michaud, and J. Manson, "Void formation and transport during SMC manufacturing: Effect of the glass fiber sizing," *Polymer Composites*, vol. 27, no. 3, pp. 289–298, 2006, doi: 10.1002/pc.20193.
- [133] T.-H. Le, P. Dumont, L. Orgéas, D. Favier, L. Salvo, and E. Boller, "X-ray phase contrast microtomography for the analysis of the fibrous microstructure of SMC composites," *Composites Part A: Applied Science and Manufacturing*, vol. 39, no. 1, pp. 91–103, 2008. doi: 10.1016/j.compositesa.2007.08.027. [Online]. Available: <https://www.sciencedirect.com/science/article/pii/S1359835X07001741>
- [134] E. Schmachtenberg, D. Lippe, and K. Skrodolies, "Faser/Matrix-entmischung während des Fließpressens von SMC," *Journal of plastics technology*, 2005. [Online]. Available: <https://scholar.google.com/citations?user=k0ptcz0aaaaj&hl=en&oi=sra>
- [135] L. W. Crane, P. J. Dynes, and D. H. Kaelble, "Analysis of curing kinetics in polymer composites," *J. Polym. Sci. B Polym. Lett. Ed.*, vol. 11, no. 8, pp. 533–540, 1973, doi: 10.1002/pol.1973.130110808.
- [136] S. Sourour and M. R. Kamal, "Differential scanning calorimetry of epoxy cure: isothermal cure kinetics," *Thermochimica Acta*, vol. 14, 1-2, pp. 41–59, 1976, doi: 10.1016/0040-6031(76)80056-1.

- [137] W. Kouidhi, L. Thannimalay, C. S. Soon, and M. Ali Mohd, "Occupational exposure to bisphenol A (BPA) in a plastic injection molding factory in Malaysia," *Int J Occup Med Environ Health*, early access. doi: 10.13075/ijomeh.1896.00917.
- [138] M. Kardos, E. Körner, D. Penumadu, and N. Modler, "The influence of fiber volume fraction and fiber length on the evolution of pore content and the paintability of sheet molding compounds," *Composites Part B: Engineering*, vol. 185, p. 107760, 2020. doi: 10.1016/j.compositesb.2020.107760. [Online]. Available: <https://www.sciencedirect.com/science/article/pii/S1359836819316348>
- [139] D. Ferré Sentis, L. Orgéas, P. Dumont, S. Rolland du Roscoat, M. Sager, and P. Latil, "3D in situ observations of the compressibility and pore transport in Sheet Moulding Compounds during the early stages of compression moulding," *Composites Part A: Applied Science and Manufacturing*, vol. 92, pp. 51–61, 2017, doi: 10.1016/j.compositesa.2016.10.031.
- [140] T. S. Lundström and A. Holmgren, "Dissolution of Voids during Compression Molding of SMC," *Journal of Reinforced Plastics and Composites*, vol. 29, no. 12, pp. 1826–1837, 2010, doi: 10.1177/0731684409336369.
- [141] A. J. Imbsweiler, Y. Shinoura, D. Colin, S. Zaremba, and K. Drechsler, "Validation of an efficient viscosity characterization in Sheet Molding Compound filling simulation," in *SAMPE Europe Conference 2021*, Baden/ Zürich, Society for the Advancement of Material and Process Engineering, Ed., 2021.
- [142] Kistler Gruppe, "Cavity pressure sensor type 6163A...: for low-viscosity thermosetting materials and rubbers with ø6 mm front," 2017. Accessed: Feb. 17, 2024. [Online]. Available: https://kistler.cdn.celum.cloud/SAPCommerce_Download_original/000-889e.pdf
- [143] VDI-Verlag, Ed., "2221: Methodik zum Entwickeln und Konstruieren technischer Systeme und Produkte," VDI, Düsseldorf, 1993.
- [144] U. Lindemann, *Methodische Entwicklung technischer Produkte: Methoden flexibel und situationsgerecht anwenden*. Berlin, Heidelberg, New York: Springer, 2008. [Online]. Available: <https://link.springer.com/content/pdf/10.1007/b137764.pdf>
- [145] K. Ehrlenspiel and H. Meerkamm, *Integrierte Produktentwicklung: Denkläufe, Methodeneinsatz, Zusammenarbeit*, 5th ed. (Hanser eLibrary). München: Hanser Verlag, 2013.
- [146] T. Weilkiens, *Systems engineering with SysML/UML: Modeling, analysis, design* (The MK/OMG Press). Amsterdam: Morgan Kaufmann Publishers an imprint of Elsevier, 2007.

- [147] R. Sell and R. Schimweg, *Probleme lösen: In komplexen Zusammenhängen denken*. Berlin, Heidelberg: Springer, 2002. [Online]. Available: <https://link.springer.com/content/pdf/10.1007/978-3-642-56185-6.pdf>
- [148] Wickert hydraulic presses. "Plastic presses and press systems." [Online]. Available: <https://www.wickert-presstech.de/de/produkte/kunststoffe/>
- [149] E. A. Zwanenburg, D. G. Norman, C. Qian, K. N. Kendall, M. A. Williams, and J. M. Warnett, "Effective X-ray micro computed tomography imaging of carbon fibre composites," *1359-8368*, vol. 258, p. 110707, 2023. doi: 10.1016/j.compositesb.2023.110707. [Online]. Available: <https://www.sciencedirect.com/science/article/pii/S135983682300210x>
- [150] N. Morimoto *et al.*, "Talbot-Lau interferometry-based x-ray imaging system with retractable and rotatable gratings for nondestructive testing," *The Review of scientific instruments*, vol. 91, no. 2, p. 23706, 2020, doi: 10.1063/1.5131306.
- [151] T. Doki *et al.*, "Development of the X-Ray Phase Imaging Device for Industrial Applications," *Shimadzu Review*, no. 75, 2018, Art. no. 4.

A Appendix

a DSC measurements and analysis

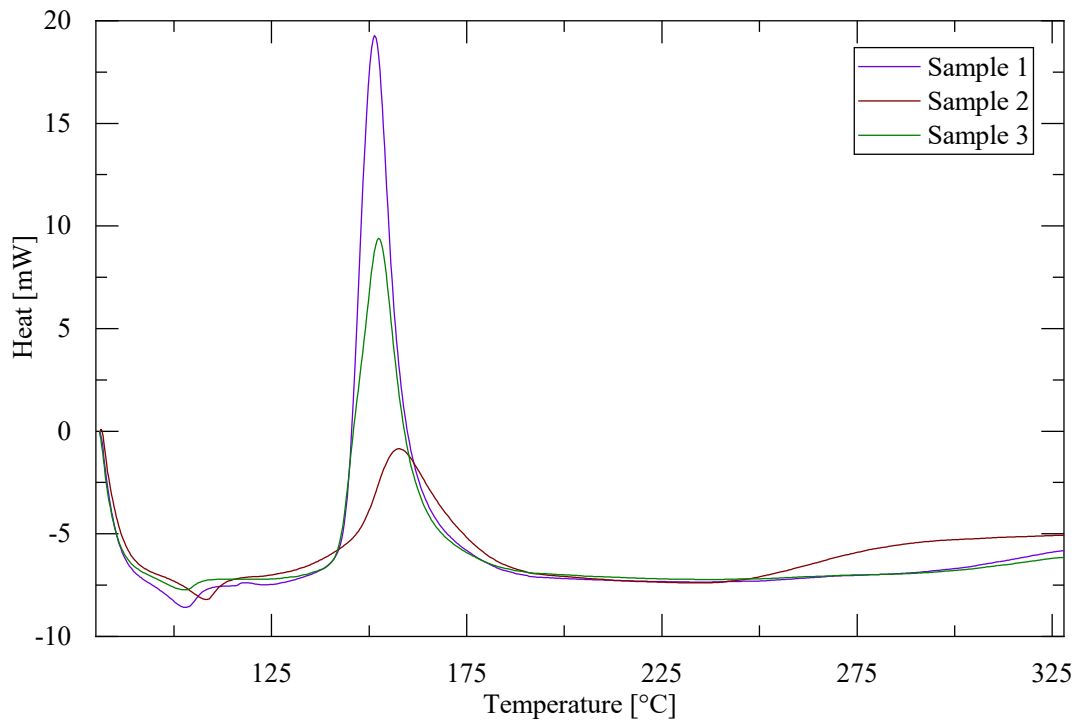


Fig. A-1 All tests at 20 K/min

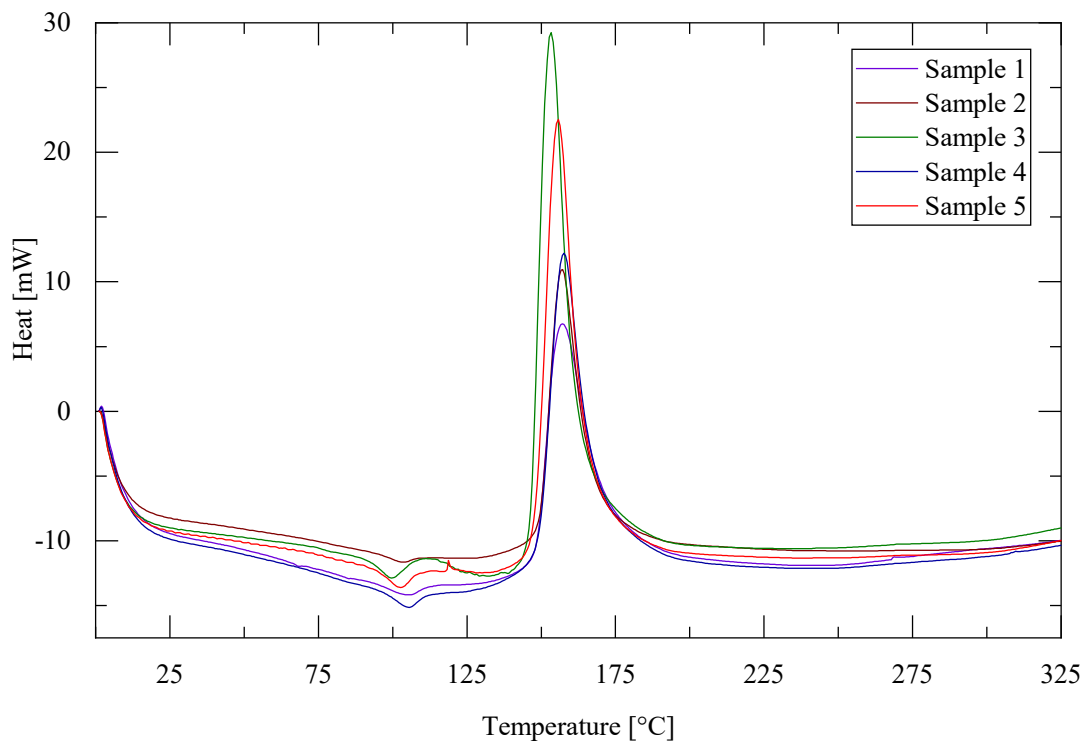


Fig. A-2 All tests at 30 K/min

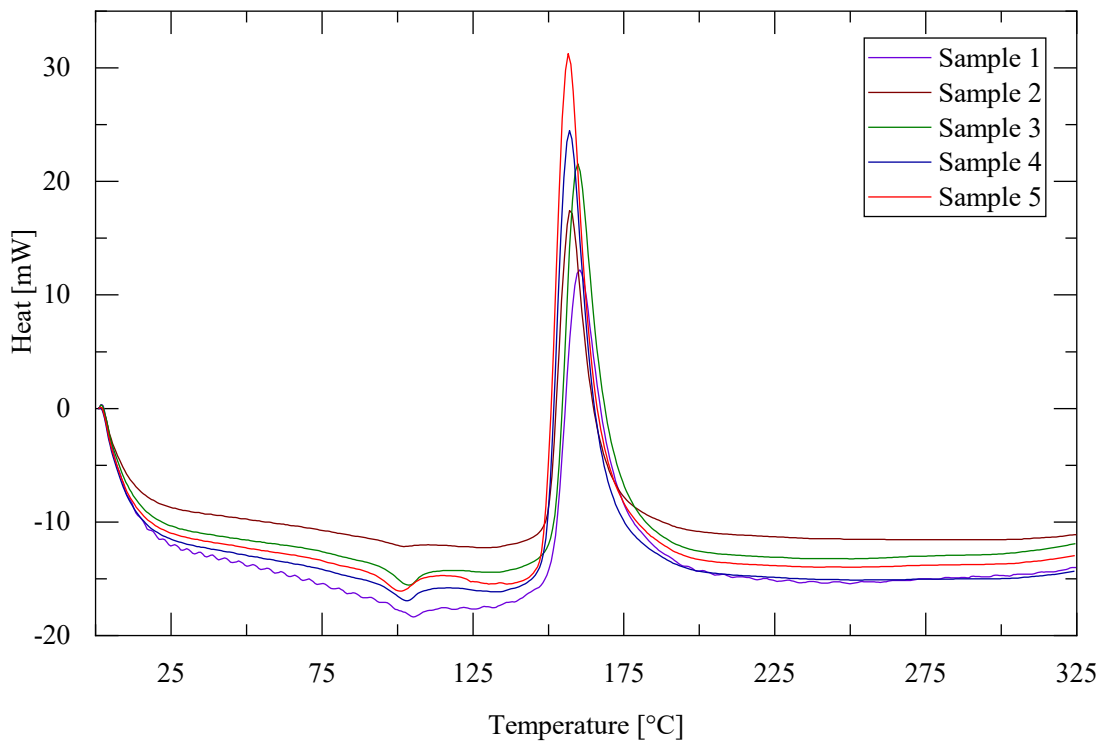


Fig. A-3 All tests at 40 K/min

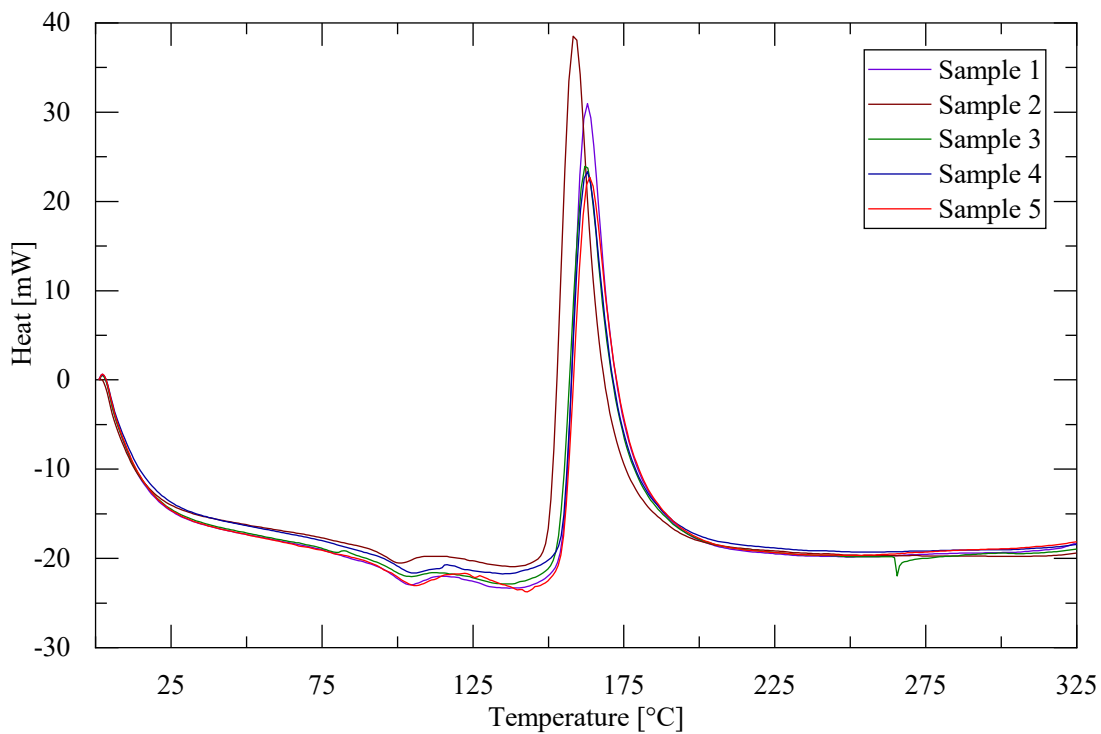


Fig. A-4 All tests at 50 K/min

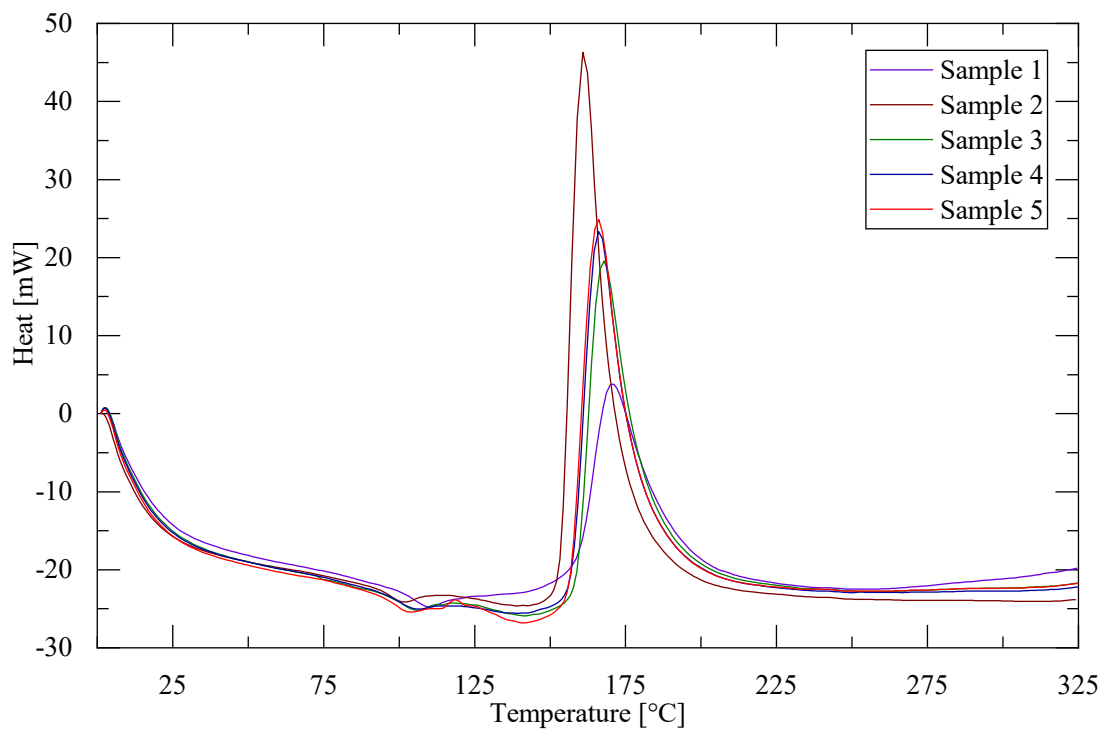


Fig. A-5 All tests at 60 K/min

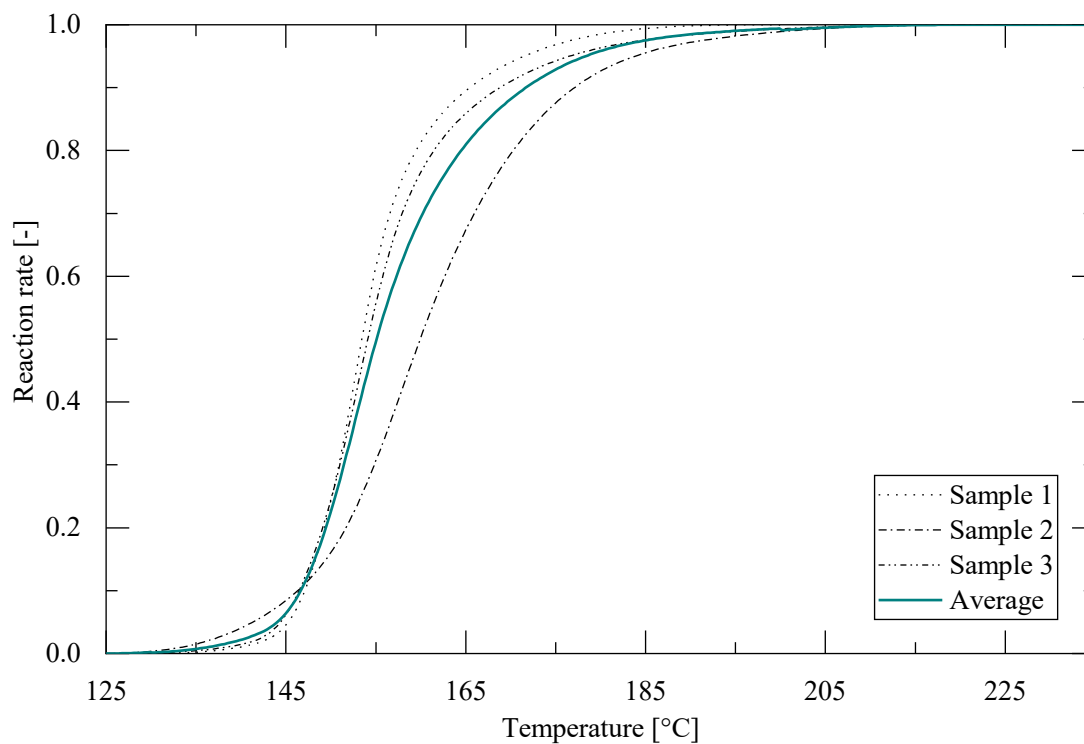


Fig. A-6 All reaction rates and resulting average at 20 K/min

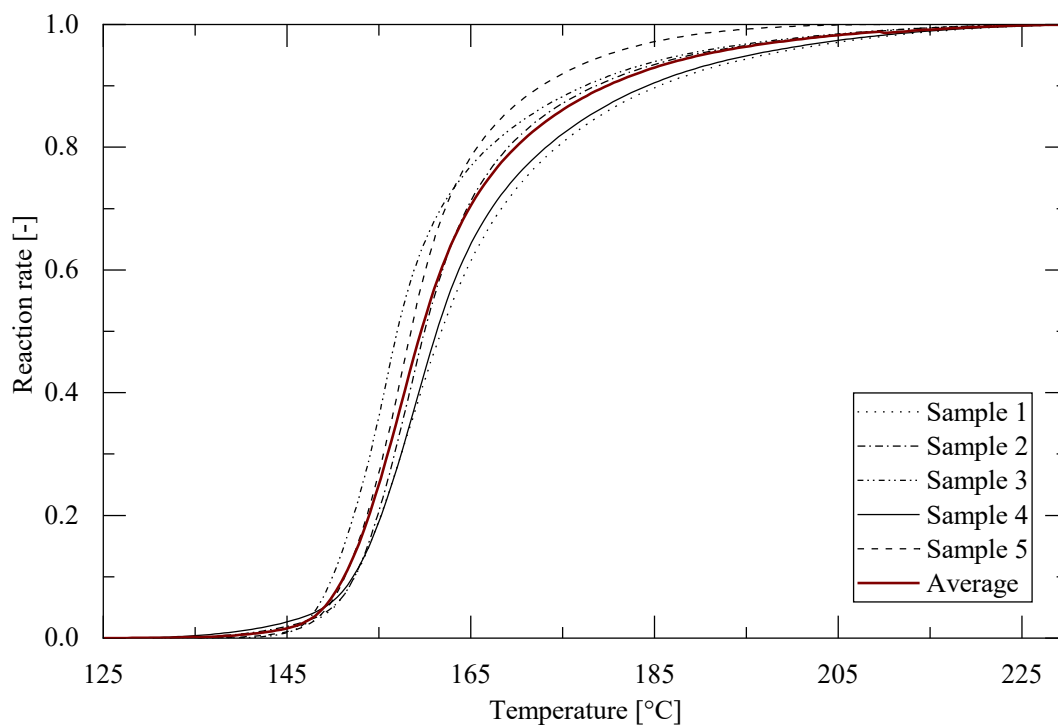


Fig. A-7 All reaction rates and resulting average at 30 K/min

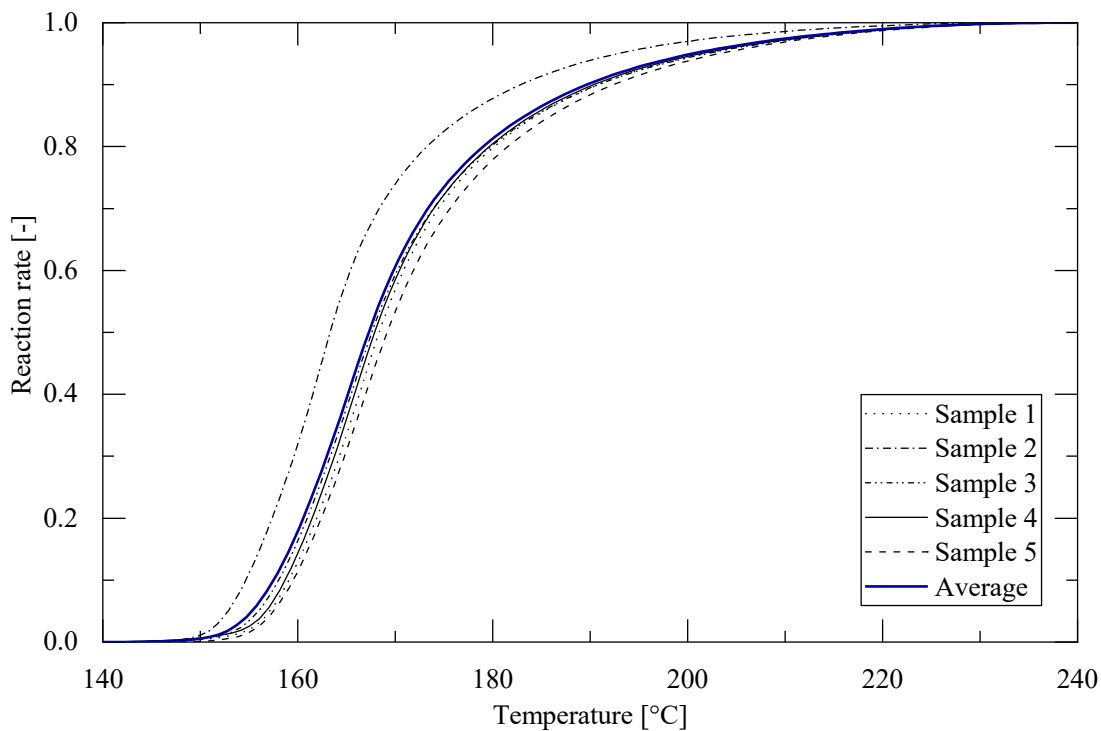


Fig. A-8 All reaction rates and resulting average at 50 K/min

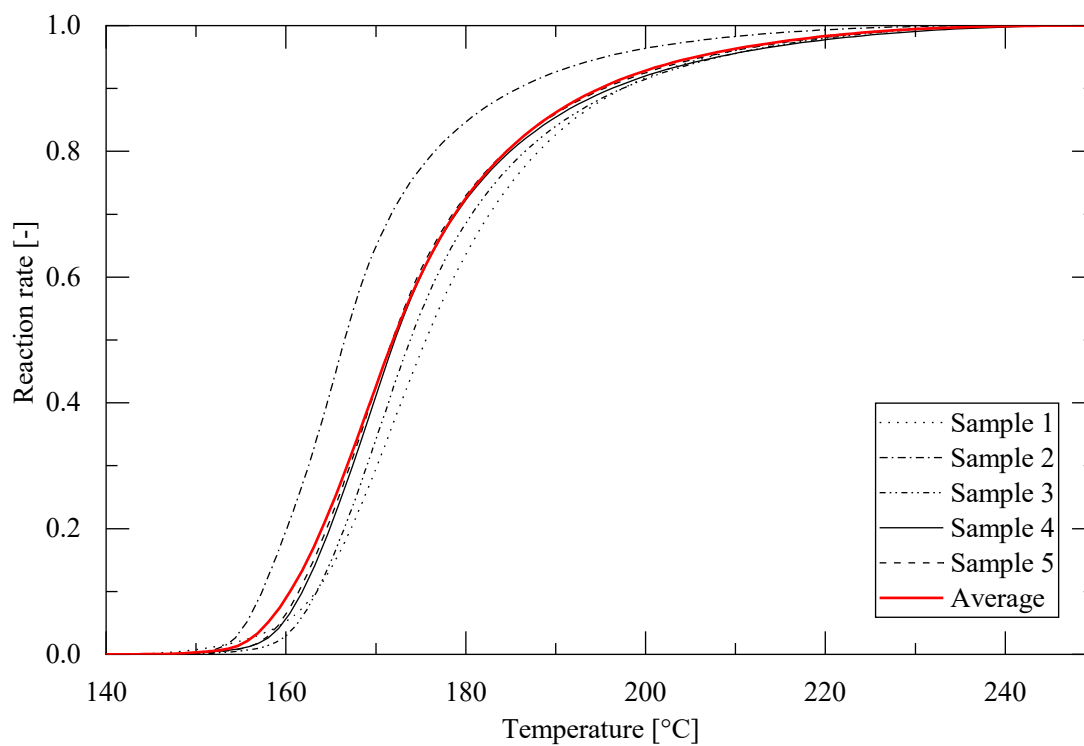


Fig. A-9 All reaction rates and resulting average at 60 K/min

b Sensitivity analysis results

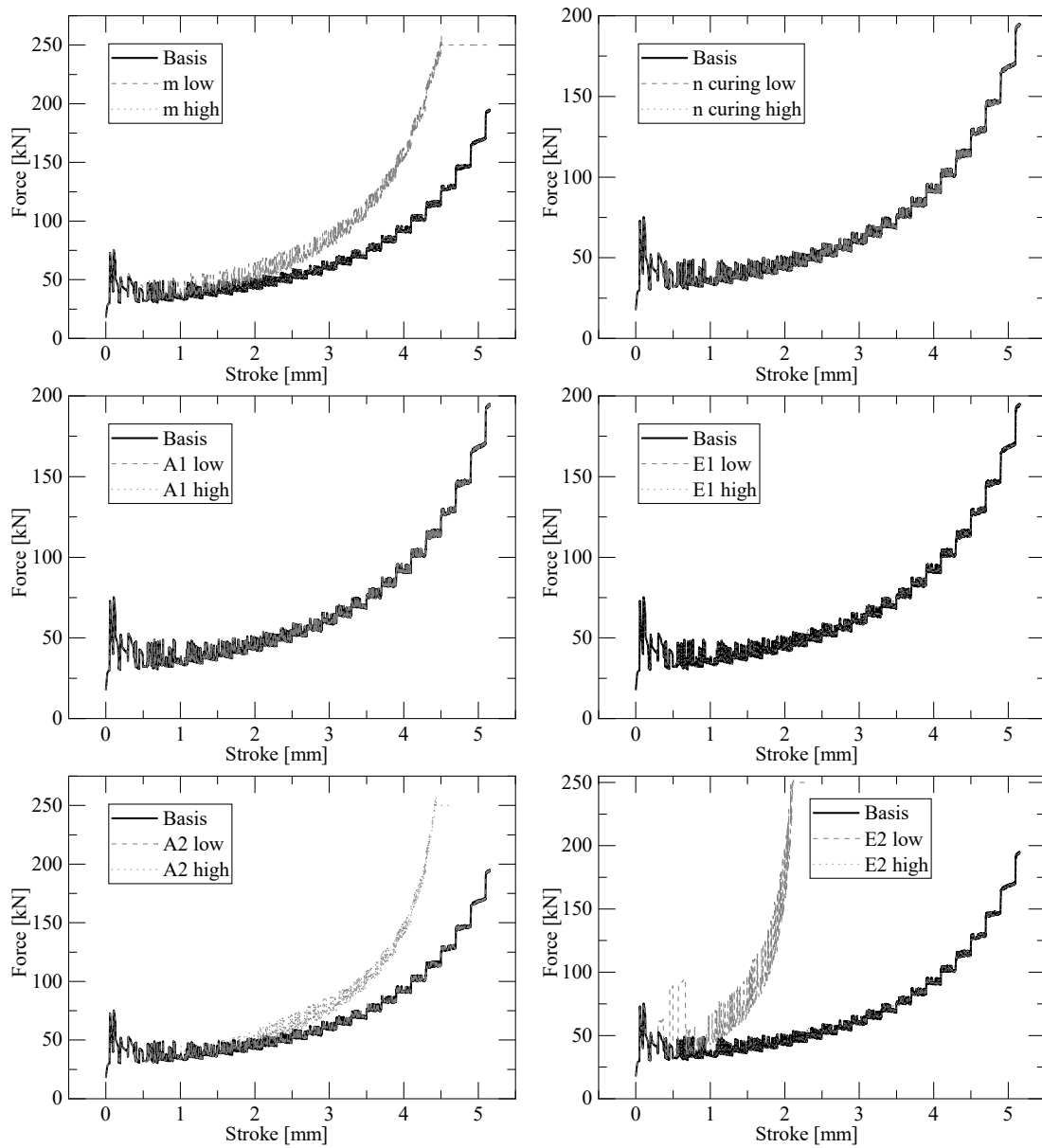


Fig. A-10 Sensitivity analysis of the curing parameters for squeeze flow tests

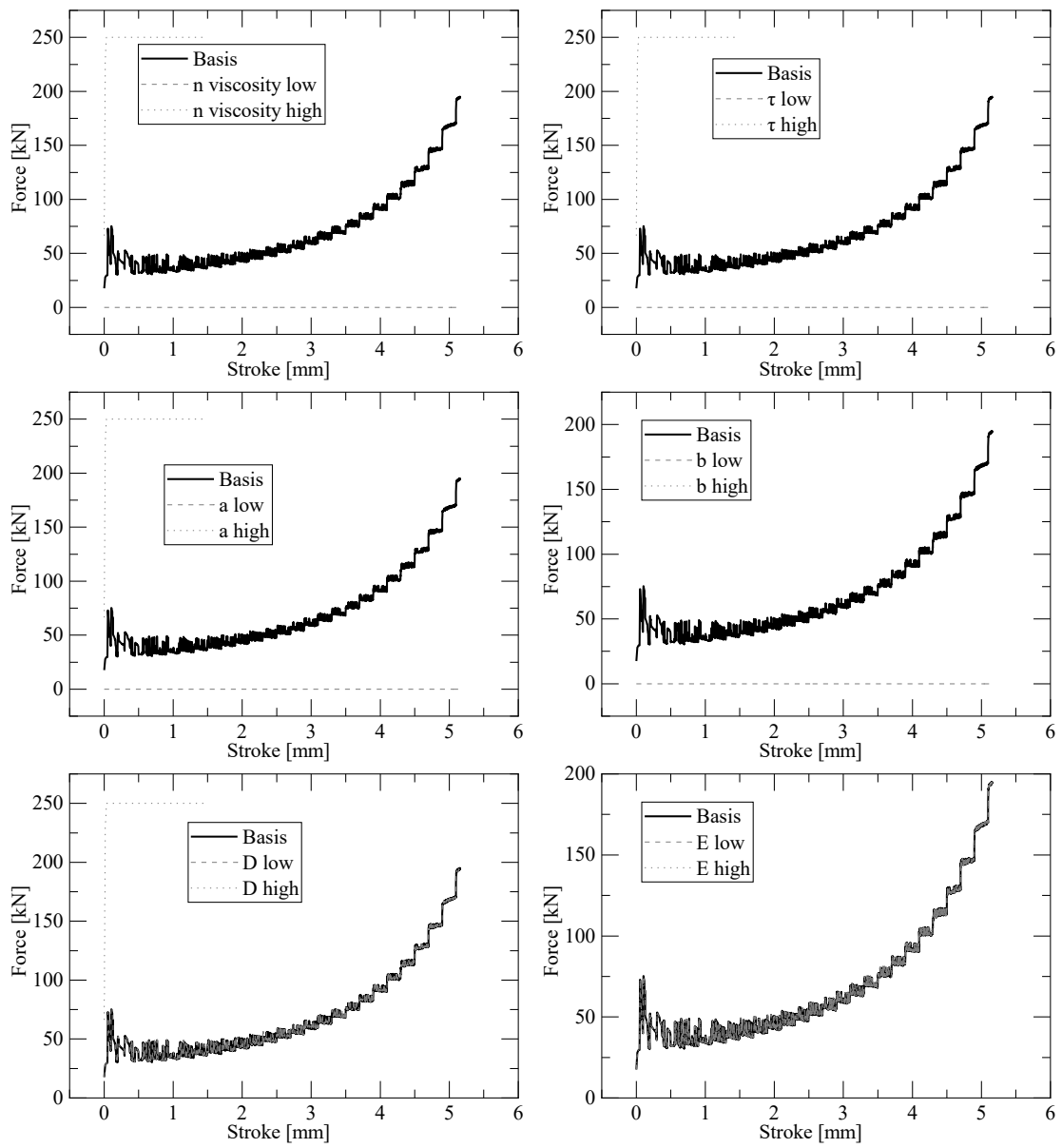


Fig. A-11 Sensitivity analysis of the viscosity parameters for squeeze flow tests

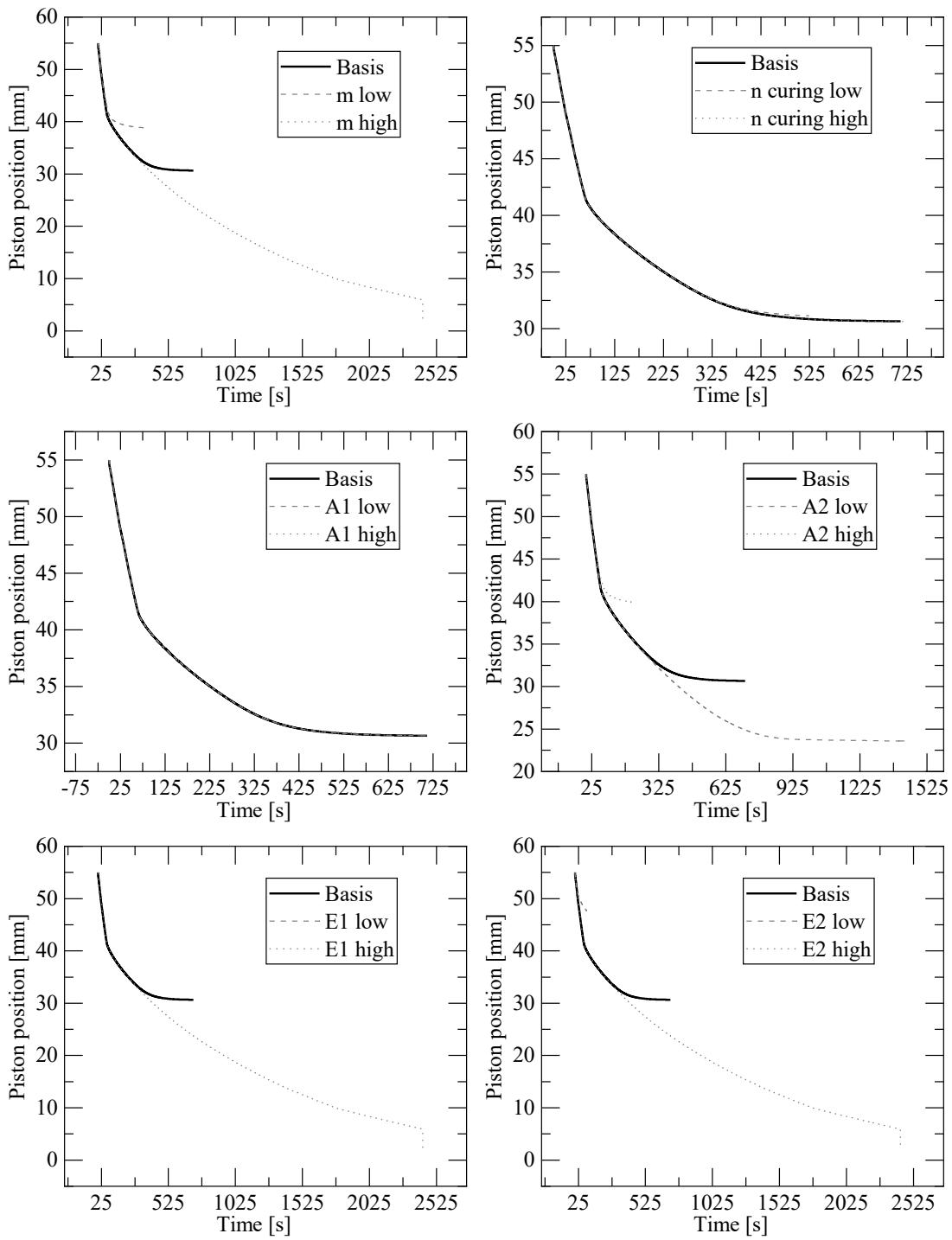


Fig. A-12 Sensitivity analysis of the curing parameters for bar flow tests with force control

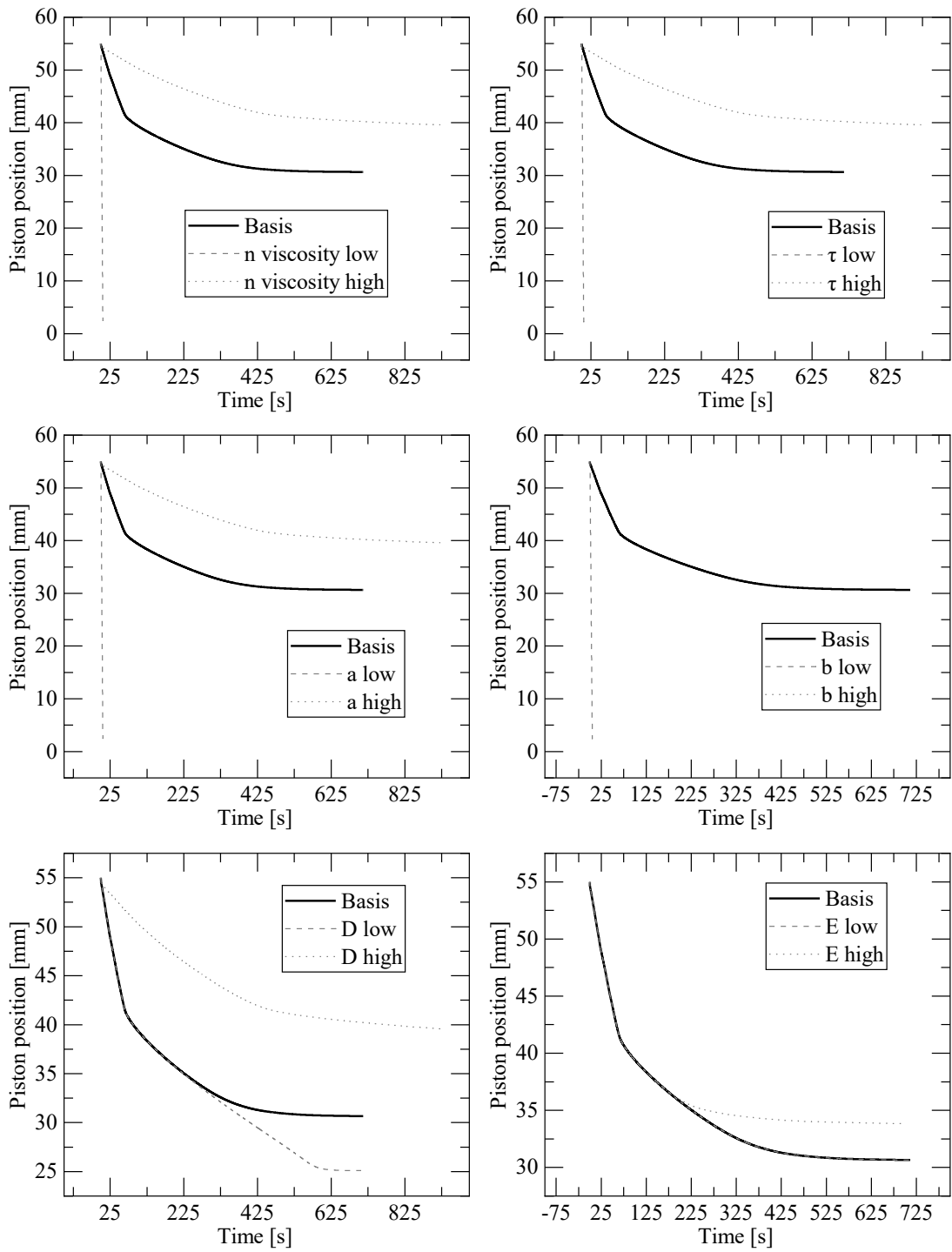


Fig. A-13 Sensitivity analysis of the viscosity parameters for bar flow tests with force control

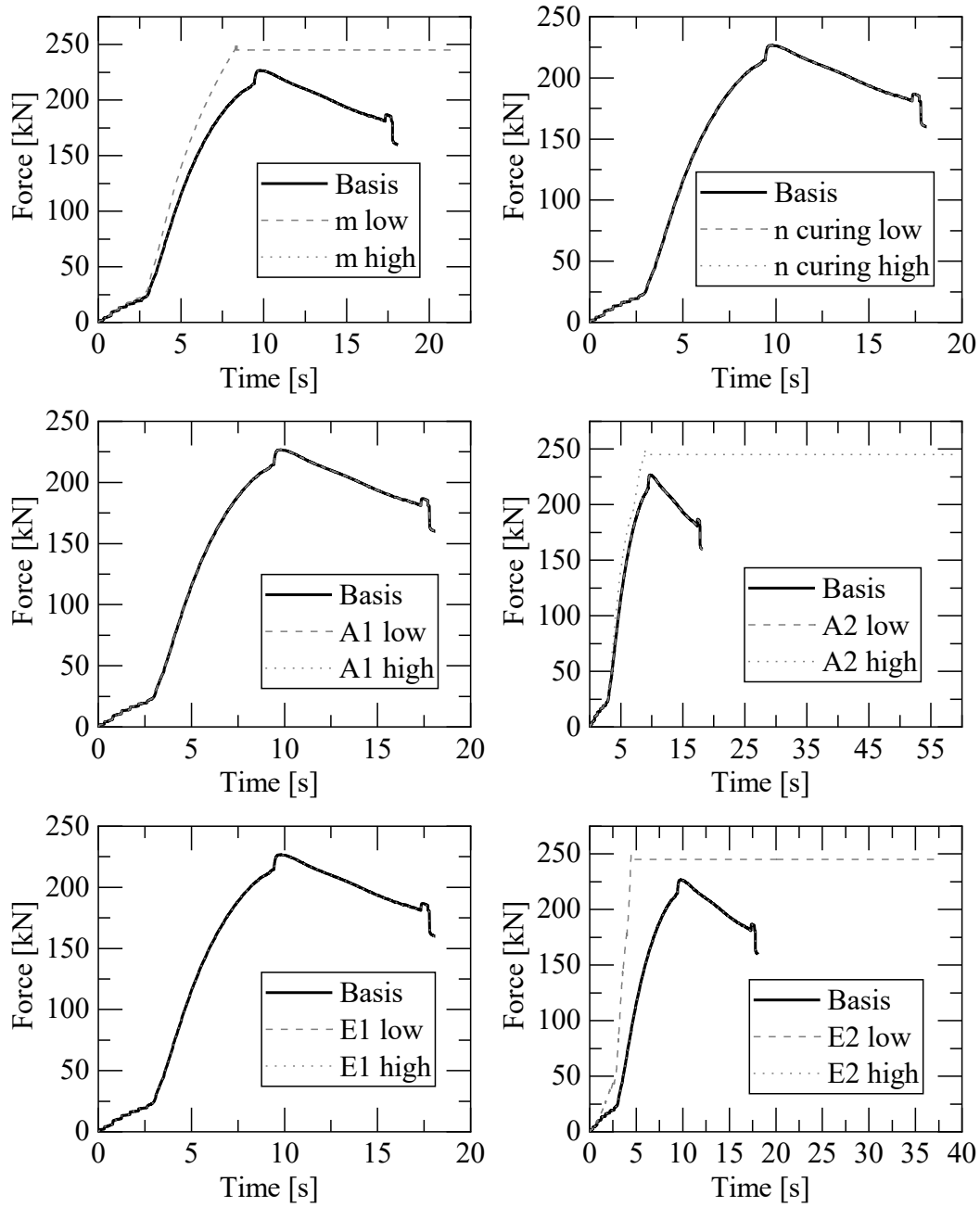


Fig. A-14 Sensitivity analysis of the curing parameters for bar flow tests with displacement control

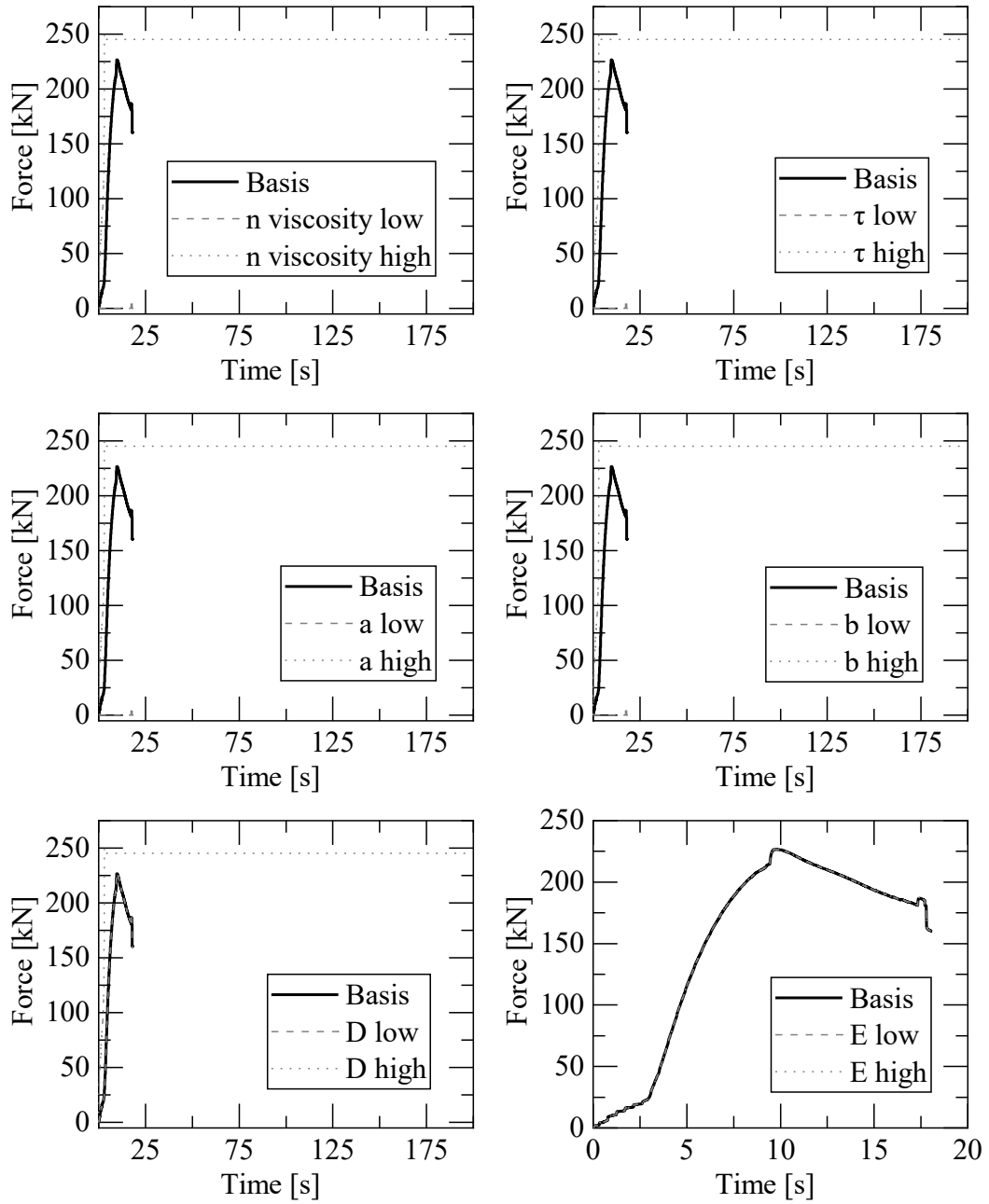


Fig. A-15 Sensitivity analysis of the viscosity parameters for bar flow tests with displacement control

c Data sheets



ASTAR S.A.
Sangroniz 30 • E-48150
Sondika • Vizcaya • Spain
Tel: +34 944 531 598
astar@astar.es • www.astar.es

TECHNISCHES DATENBLATT

Kunde Blackwave GmbH
Materialbezeichnung CARBKID PGK5250-R63
Farbe Black
Beschreibung @

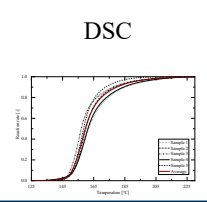
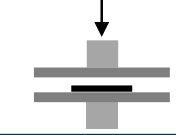
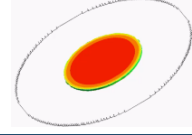

EIGENSCHAFT	NORM / METHODE	WERT	TOLERANZ	EINHEIT
Flächengewicht	IT.CA-11	2.5	± 0.2	kg/m ²
Kohlenstofffasergehalt	ISO 1172	52	± 2	%
Kohlenstofffaserlänge	ISO 1172	25		mm
Reaktivität:	ISO 12114			
- Härteszeit	-	35	± 5	s
- Formtemperatur	-	150		°C
- Wanddicke	-	3.4		mm
Dichte	EN ISO 1183-1	1.38	± 0.05	g/cm ³
Schwindung	ISO 2577	-0.05	± 0.05	%
Wasseraufnahme	ISO 62	< 0.3		%
Glasübergangstemperatur, T _g	EN 6032-A	170		°C
Biegefestigkeit	ISO 14125	≥ 330		MPa
Biege-E-Modul	ISO 14125	≥ 27000		MPa
Zugfestigkeit	ISO 527-4	≥ 240		MPa
Zug-E-Modul	ISO 527-4	≥ 30000		MPa
Dauerwärmeformbeständigkeit	ISO 75-2-A	> 250		°C
Termisches Ausdehnungskoeffizient	ISO 11359-2	10·10 ⁻⁶		m/m.K

ANMERKUNGEN

Vorstehende Angaben sind die Ergebnisse unserer Qualitätsprüfung. Sie entbinden den Käufer nicht von einer Eingangskontrolle und haben nicht die Bedeutung, die Eignung des Produktes für einen konkreten Einsatzzweck zuzusichern.

d Handbook for the rheological characterization

A summary of the intended process is below.

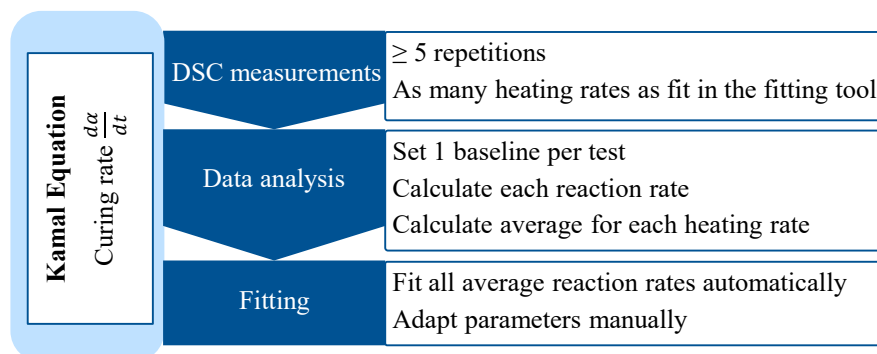
	Curing kinetics	Viscosity	Calibration	
Procedure	Kamal Equation Curing rate $\frac{d\alpha}{dt}$	Andrade Model $f(T)$ Castro-Makosco Model $f(\alpha)$ Cross Model $f(\dot{\gamma})$	Calibration In plane flow	Calibration Out-of-plane flow <ul style="list-style-type: none"> • Displacement control • Force control
Activity	DSC 	Squeeze flow tests 	Squeeze flow simulations 	Bar flow tests + simulations 

Process for the characterization of SMC materials for flow simulation together with the necessary testing and simulation activities

The steps in the process consist in

1. Determine the parameters for the curing kinetics by performing DSC measurements and fitting the results to the Kamal equation;
2. Determine the parameters for the viscosity by performing squeeze flow tests and fitting the results to the Castro-Macosko and Cross-Andrade models;
3. Calibrate the parameters for in-plane flow with squeeze flow simulations;
4. Calibrate the parameters for the out-of-plane flow with bar flow tests and simulation.

d.1 Curing kinetics



DSC measurements

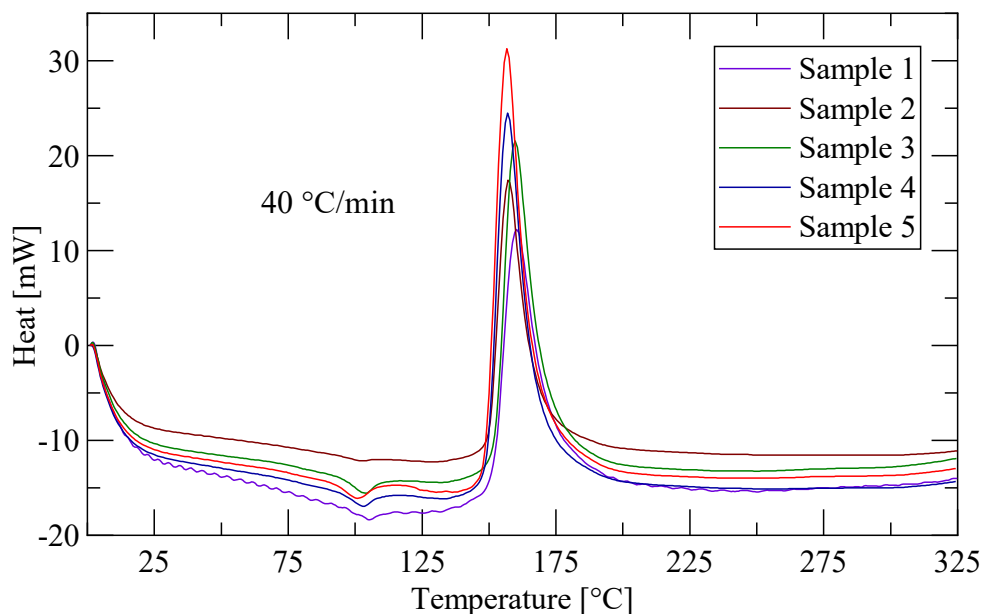
Do the measurements following the instruction of the adopted equipment.

Requirements for the DSC measurements:

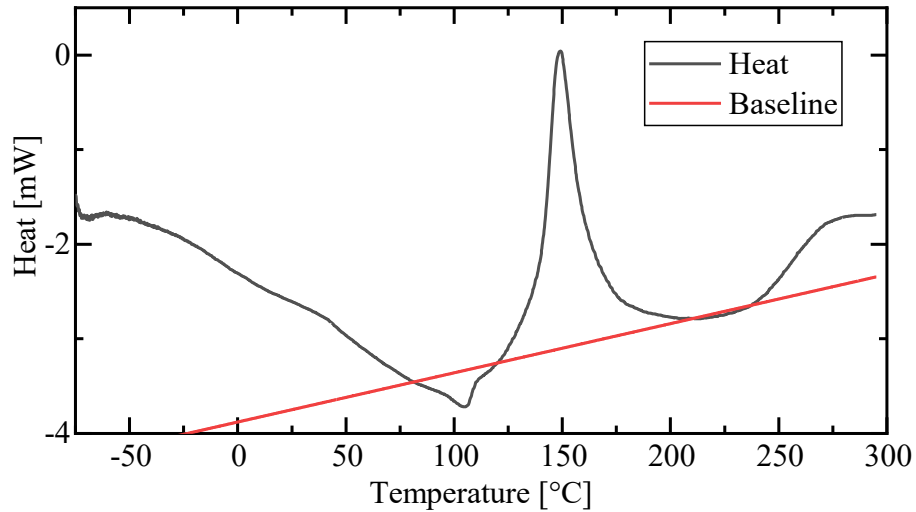
- At least 5 repetitions for each setting
- At least 3 different heating rates, but more are better
- The heating rates shall start at 10 °C/min and go up to the maximum possible for the used machine.

Data analysis

Select the right section of the tested data with the peak of the heat produced during the curing and at least ~50 °C before the start of the reaction and ~50 °C after the end of the reaction.



Determine a baseline for each curve by selecting two points, one before and one after the peak of the curing heat. The points shall be chosen, so that the line passing through them is tangential to the reaction curve before and after the peak.

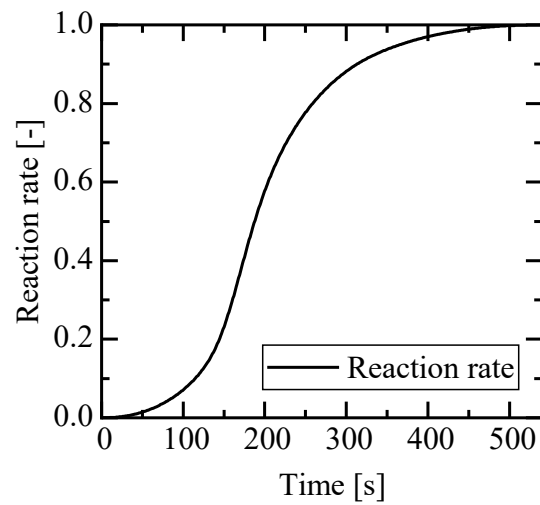
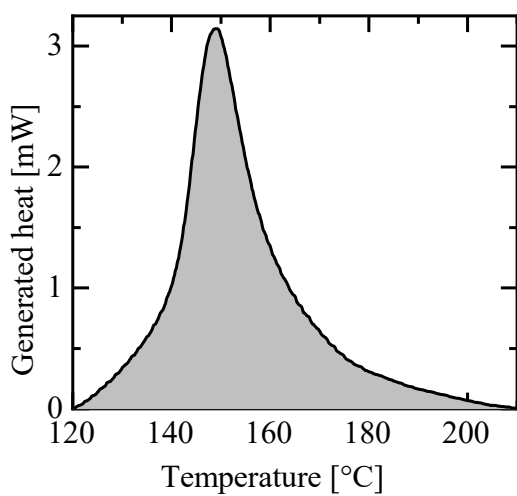


Calculate the generated heat

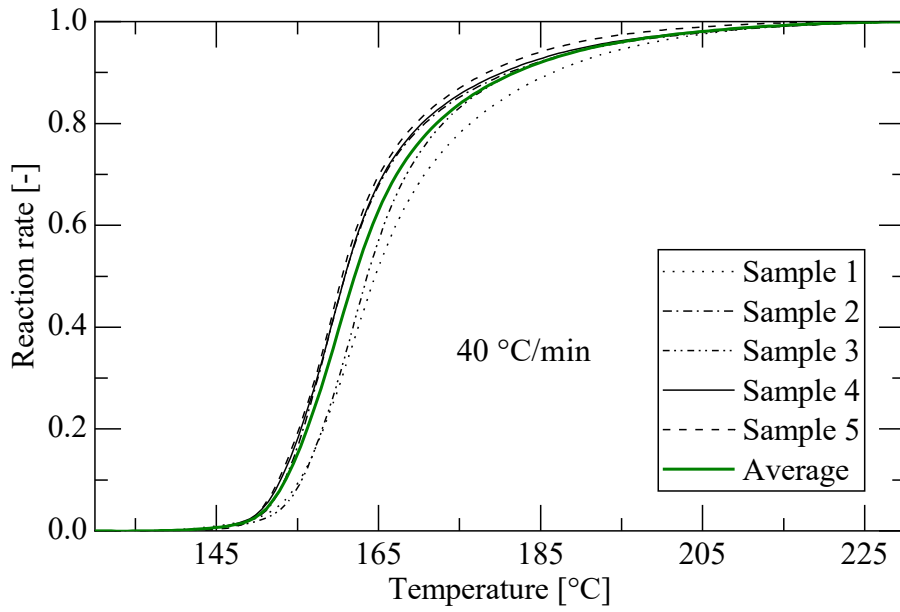
$$\dot{q} = Q(T)\Delta T$$

and the reaction rate

$$\alpha = \frac{Q(T)[T_0; T]}{Q(T)[T_0; T_{tot}]}$$



Calculate the average reaction rate resulting from the separately tested curves.



Fitting

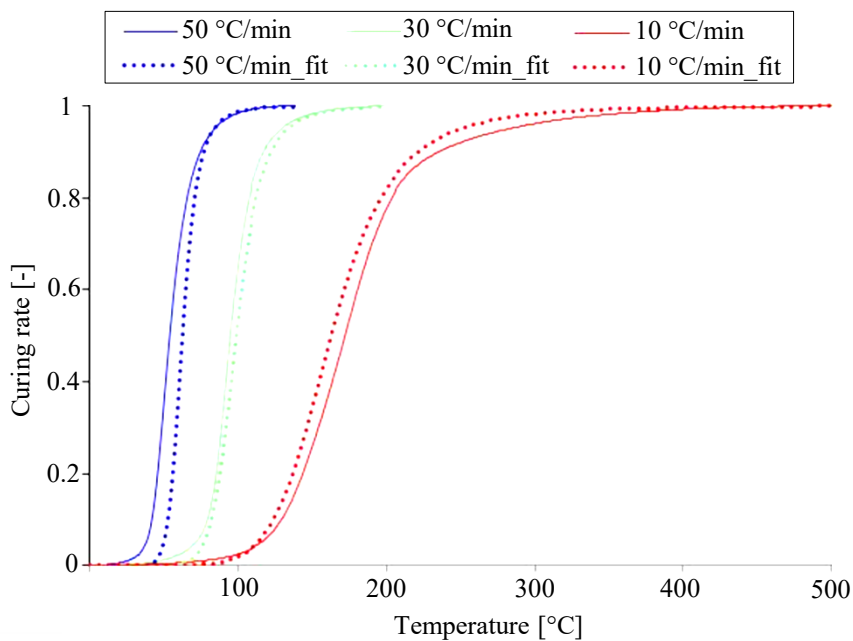
Perform the fitting to the chosen curing equation with the obtained average reaction rates.

The process is shown exemplarily for the Kamal equation, as adopted in the simulation software 3DTimon.

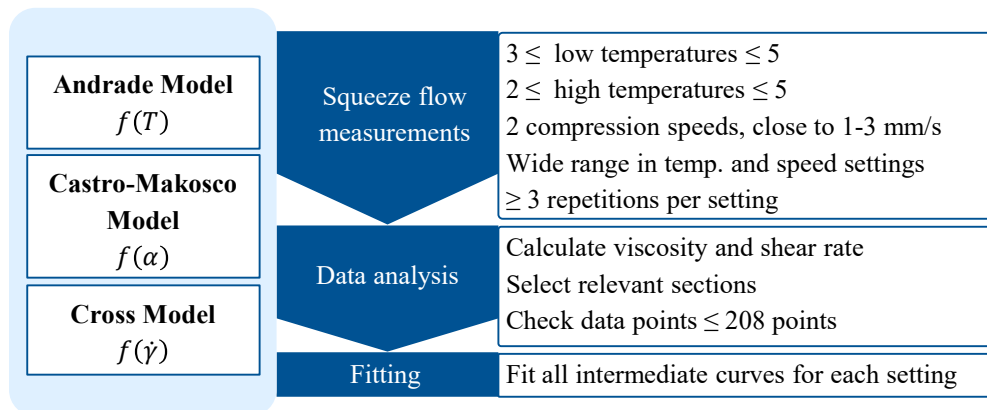
Kamal equation

$$\frac{d\alpha}{dt} = (A_1 e^{-E_1/T} + A_2 e^{-E_2/T} \alpha^m) * (1 - \alpha)^n$$

Exemplary fitting result



d.2 Viscosity



Squeeze flow measurements

Perform squeeze flow measurements for low (below the curing temperatures of the considered material) and high temperatures (range where the material cures). The tests can be performed in an industrial press or in a universal testing machine.

Low temperatures:

- from RT to 40 °C below the curing temperature from the data sheet,
- between 3 and 5 different temperatures.

High temperature:

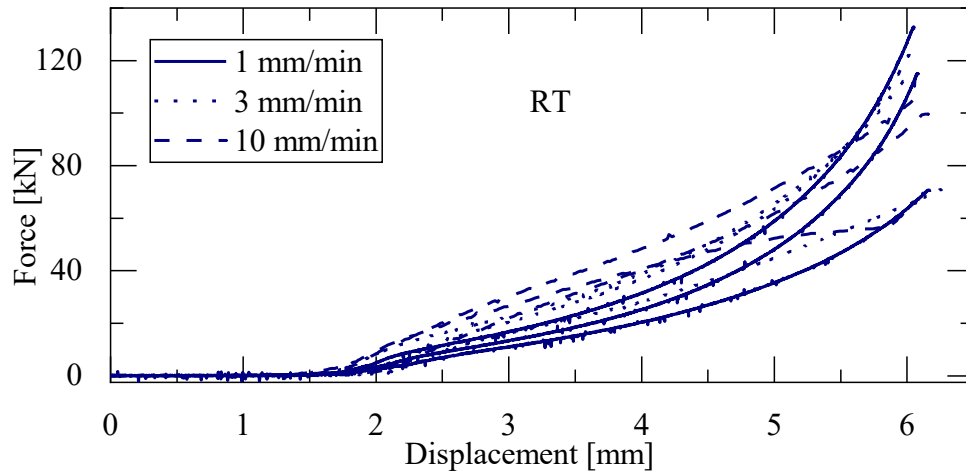
- from 30 ° below the appointed curing temperature on the data sheet and up to 20 °C above,
- between 2 and 5 different temperatures.

Overarching requirements:

- 2 compression speeds, within the range of 1-3 mm/s or as close as possible (depending on the equipment limitations)
- At least 3 repetitions
- Recording of force over displacement.

Data analysis

Select the range of the force over displacement where the compression starts (from the increase of the force signal until it reaches the maximum).



Calculate

- the viscosity over shear rate for the low temperature tests and
- the viscosity over time for the high temperature viscosity

from force over displacement.

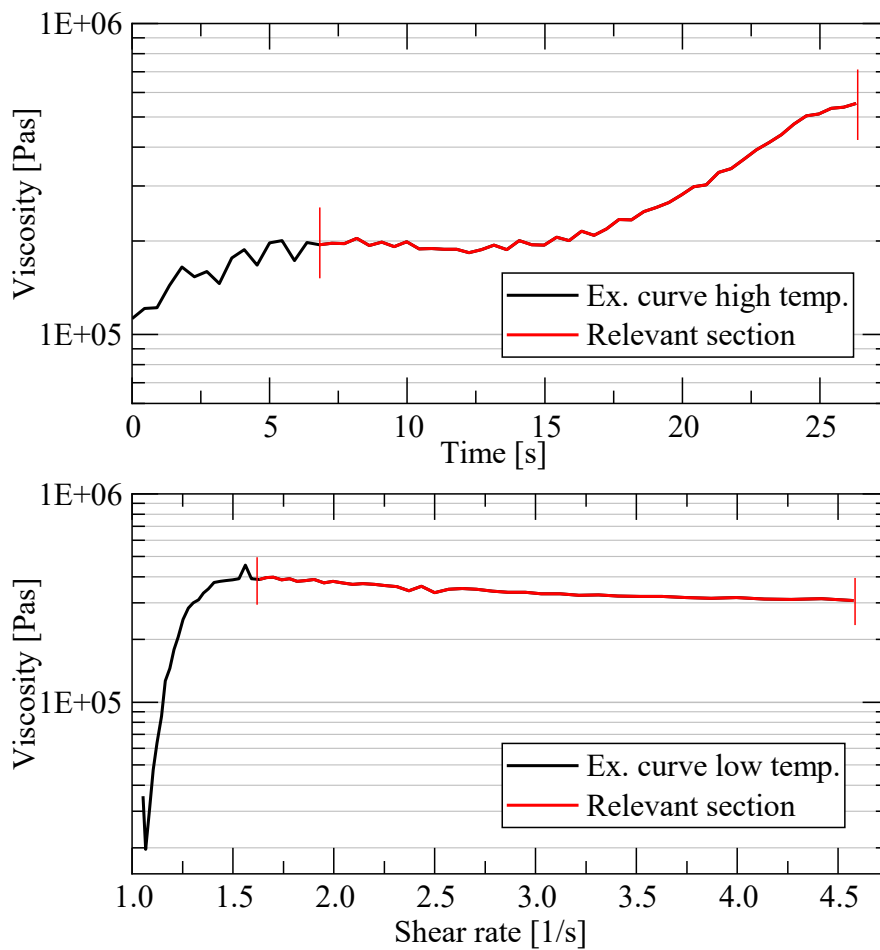
Viscosity

$$\mu = \frac{2[h(t)]^3 F(t)}{3\pi v_0 R^4}$$

Shear rate (Stefan equation)

$$\dot{\gamma} = \frac{3 * v(t)r(t)}{2 * h^2}$$

Select the relevant sections for both temperature ranges.



Fitting

Perform the fitting to the chosen viscosity model with the curve sections to be fitted.

The process is shown exemplarily for the viscosity model adopted in the simulation software 3DTimon.

Temperature-dependent Andrade model

$$\eta_0 = a * e^{-b/T} * T$$

Curing reaction rate-dependent Castro-Macosko model

$$\eta_1 = \eta_0 * \left(\frac{\alpha_{gel}}{\alpha_{gel} - \alpha} \right)^{D+E\alpha}$$

shear rate-dependent Cross model

$$\eta = \frac{\eta_1}{1 + \left(\frac{\eta_1 \dot{\gamma}}{\tau^*} \right)^{1-n}}$$

Depending on the adopted fitting tool, the data amount may have to be reduced.

d.4 Calibration

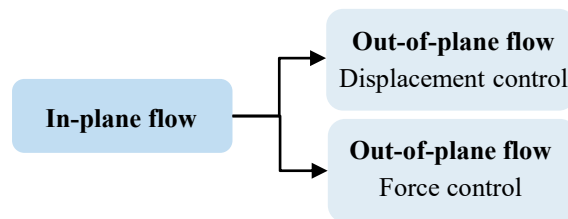
The calibration is subdivided into

- In-plane calibration and
- Out-of-plane calibration.

For the latter it can also be subdivided into

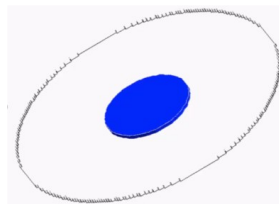
- Displacement control and
- Force control

depending on the available machines. However, displacement control shall be preferred.

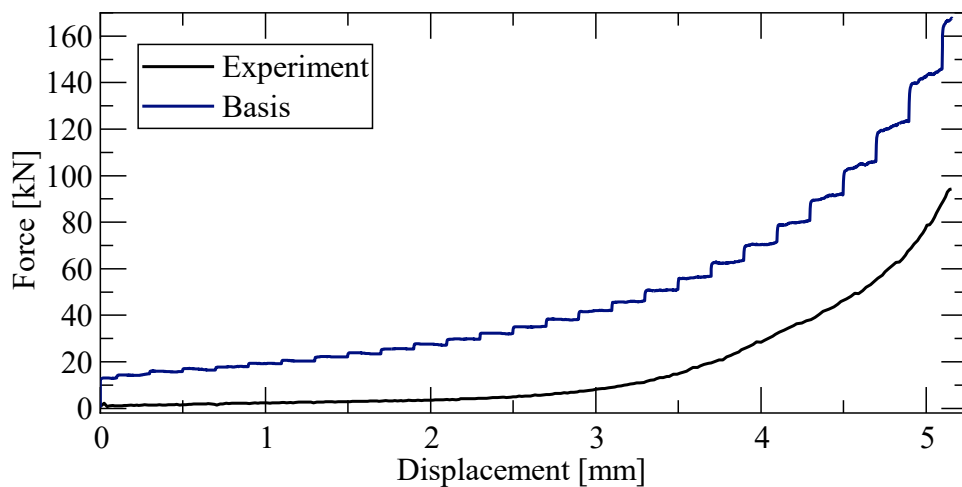


In-plane calibration

Set up a simulation for one configuration at high temperature for the performed squeeze flow tests



Export the force data from the simulation and compare it to the results from the tests.



Improve the result by performing the calibration as described in the section “Calibration process”.

Once the ip calibration is done, the oop calibration can be performed.

Out-of-plane calibration

Select a low test bench or a SMC tool with a complex flow including oop flow. The test should ideally be performed with settings as close to actual molding conditions as possible. Therefore, a test performed in a press shall be preferred. However, a separate test bench or a UTM are acceptable. Displacement control should also be preferred, since it reflects the typical SMC processing.

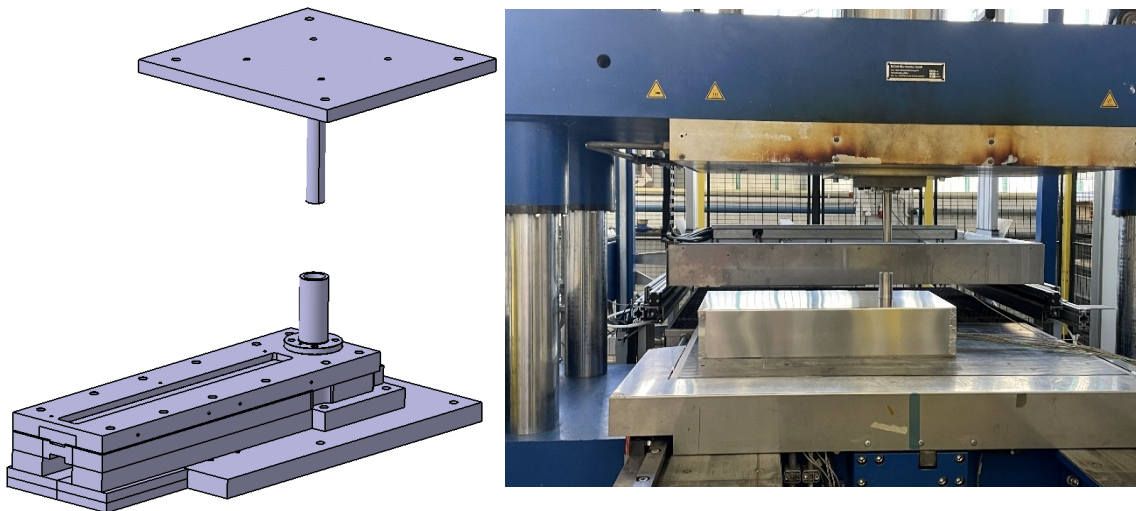
The general process for the oop calibration is very similar for both methods of constant force or constant displacement. Therefore, it is described together.

Perform tests for:

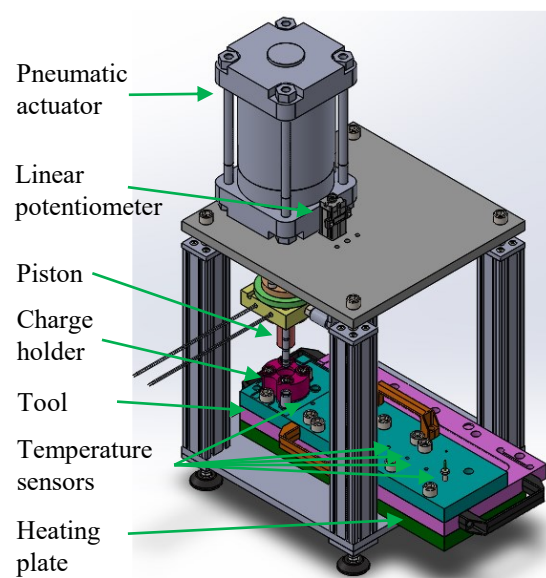
- At least one configuration of process settings
- Temperature in the range of the high temperature (between 30 °C below the indicated curing temperature and 20 °C over it)
- Closing speed or applied force in typical range (1-3 mm/s and 100-150 bar to be converted into kN based on the compression surface)
- At least 5 repetitions
- Force/pressure recording for displacement control and displacement recording for force control are present.

Exemplary test benches for either testing option are shown below.

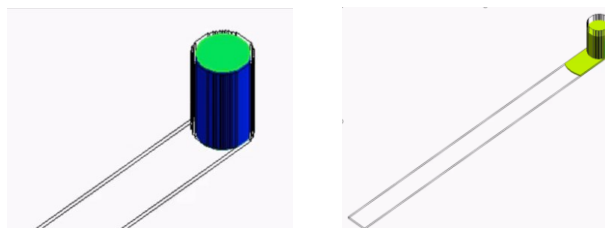
Displacement control with bar flow test bench in SMC press.



Force control with separate test setup for bar flow tests (developed within BA-2017-0014).

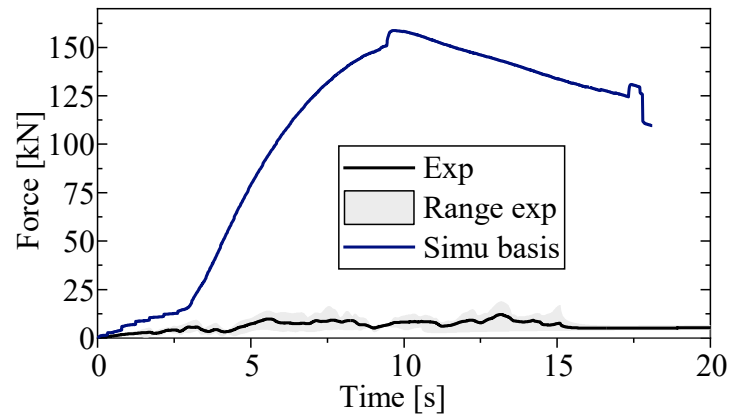


Replicate the setups in simulation.

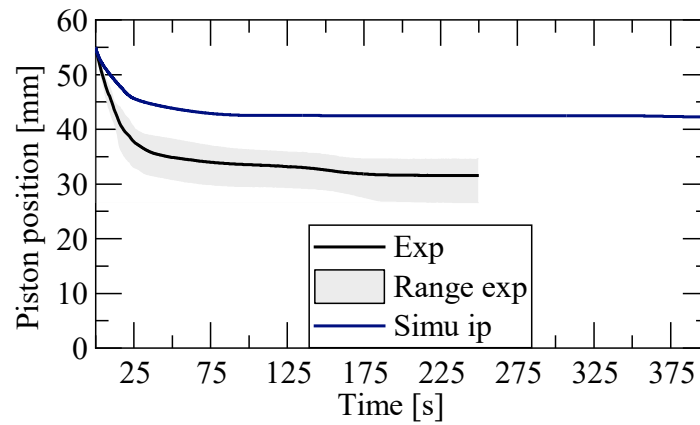


Compare the resulting values with the values obtained from the real tests:

- Displacement control: pressure or force over time



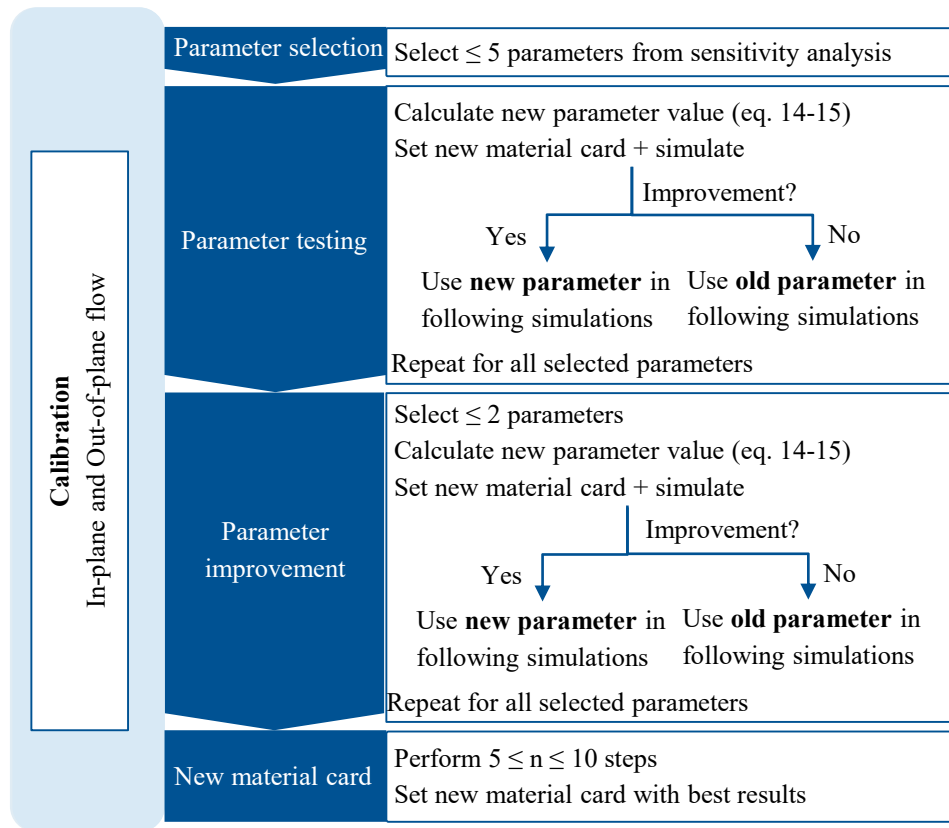
- Force control: displacement over time.



Calibration process

In order to reduce the difference between the simulation result and the tested result, the parameters for the curing kinetics and the viscosity model shall be calibrated.

The process for the calibration is summarized below.



Parameter selection

From the table below summarizing the results of the sensitivity analysis performed for all parameters of the curing kinetics and the viscosity model up to 5 parameters shall be chosen.

In-plane sensitivity analysis

	Parameter	Limit Low	Force	Limit high	Force	
Curing kinetics	m	1.00E+02	$\uparrow\uparrow$	2.00E+03	\downarrow	$\uparrow\uparrow$ increase
	n	1.00E+02	=	2.00E+03	=	\downarrow minimal decrease
	A1	1.00E-02	=	1.00E+13	=	= equal
	A2	3.00E+09	=	1.00E+11	$\uparrow\uparrow$	$\downarrow\downarrow$ decrease
	E1	1.00E-02	SS	1.00E+13	=	SS short shot
	E2	6.00E+06	$\uparrow\uparrow$	9.00E+06	\downarrow	e error
Viscosity	n	1.00E+00	$\downarrow\downarrow$	9.99E+02	$\uparrow\uparrow$	
	τ	1.00E-07	$\downarrow\downarrow$	1.00E+13	$\uparrow\uparrow$	
	a	1.00E-07	$\downarrow\downarrow$	1.00E+13	$\uparrow\uparrow$	
	b	1.00E+00	$\downarrow\downarrow$	1.00E+13	e	
	D	1,20E-04	=	1,20E+04	=	
	E	1,00E-04	=	1,00E+04	=	

Out-of-plane sensitivity analysis (top: displacement control; bottom: force control)

	Parameter	Limit Low	Ip	Oop vconst	Oop Fconst	
			F	Curing	F	Curing
Curing kinetics	m	1.00E+02	↑↑	earlier, steady	↑↑	↑
	n	1.00E+02	=	=	=	=
	A1	1.00E-02	=	=	=	=
	A2	3.00E+09	=	=	=	=
	E1	1.00E-02	SS	SS	SS	SS
	E2	6.00E+06	↑↑	faster	↑↑	↑↑
			F	Vcomp		
Viscosity	n	1.00E+00	=	constant and slower	0	-
	tau	1.00E-07	0	constant and slower	0	-
	a	1.00E-07	0	constant and slower	0	-
	b	1.00E+00	0	≈ max	0	-
	D	1,20E-04	=	constant and slower	=	-
	E	1,00E-04	=	min increase at end	=	-

	Parameter	Limit high	Ip	Oop vconst	Oop Fconst	
			F	Curing	F	Curing
Curing kinetics	m	2.00E+03	↓	=	=	=
	n	2.00E+03	=	=	=	=
	A1	1.00E+13	=	=	=	=
	A2	1.00E+11	↑↑	earlier, steady	↑↑	=
	E1	1.00E+13	=	=	=	=
	E2	9.00E+06	↓	longer	=	=
			F	Vcomp	F	Curing
Viscosity	n	9.99E+02	max	≈ max	↑↑	-
	tau	1.00E+13	max	≈ max	↑↑	-
	a	1.00E+13	max	≈ max	↑↑	-
	b	1.00E+13	e	SS	↑↑	-
	D	1,20E+04	=	max	↑↑	-
	E	1,00E+04	=	=	=	-

SS = short shot

Parameter variation

Calculate the new parameter value:

$$p_{new} = \frac{p_{old} - ll}{2} \pm p_{old} \quad (1)$$

where p_{new} and p_{old} represent the new and the old values of the parameter, and ll is the lower limit of the parameter in question.

- For a decrease use the subtraction of the two factors,

- for an increase the sum.

If the result for the increase $\geq ul$, adopt:

$$p_{new} = \frac{ul - p_{old}}{2} + p_{old} \quad (2)$$

where p_{new} and p_{old} represent the new and the old values of the parameter, ul is the upper limit.

Compare simulation and reality: discard the parameters that lead to changes that are too big, keep at least two parameters to vary further.

Parameter improvement

Select the two most promising parameters.

Improve the selected parameters further by following eq. 1 and 2. If the increase of a parameter with eq. 1 lead to a too significant change, decrease the difference between the old and new parameter by dividing the first term of eq. 1 with double the previous amount (i.e. after trying 2, try 4, then 8, etc.).

New material card

Repeat the process for 5 to 10 parameter adaptations (5-10 simulations).

Two sets of parameters will be set:

- Set for in-plane flow for simple flat geometries with open edges;
- Set for out-of-plane flow for complex geometries.

Write the parameters for the best results in the material card.

B Publications

Scientific journal papers

- [P1] A. J. Imbsweiler, Y. Shinoura, D. Colin, S. Zaremba, and K. Drechsler, "Towards a Holistic Approach for an Efficient Determination of the Rheological Behavior of Sheet Molding Compounds for Process Simulation," *KEM*, vol. 926, pp. 1864–1873, 2022, <https://doi.org/10.4028/p-3xkfn9>
- [P2] A. J. Imbsweiler, J. Wang, R. Sharwalla, J. Hoffelner, D. Colin, S. Zaremba, K. Drechsler, "Quantification of the Influence of Charge Variations on the Flow Behavior of Sheet Molding Compounds," *Polymers*, vol. 16, no. 16, 2024, Art. no. 2351, . doi: 10.3390/polym16162351.
- [P3] J. Schnell, H. Knörzer, A. J. Imbsweiler, and G. Reinhart, "Solid versus Liquid- A Bottom-Up Calculation Model to Analyze the Manufacturing Cost of Future High-Energy Batteries," *Energy Tech*, vol. 8, no. 3, 2020, Art. no. 1901237, doi: 10.1002/ente.201901237.

Conferences

- [K1] A. J. Imbsweiler, Y. Shinoura, D. Colin, S. Zaremba, and K. Drechsler, "Optimization of the determination of Kamal's parameters in SMC process simulation," in *SAMPE Europe Conference 2020*, Amsterdam, Society for the Advancement of Material and Process Engineering, Ed., 2020.
- [K2] A. J. Imbsweiler, Y. Shinoura, D. Colin, S. Zaremba, and K. Drechsler, "Validation of an efficient viscosity characterization in Sheet Molding Compound filling simulation," in *SAMPE Europe Conference 2021*, Baden/ Zürich, Society for the Advancement of Material and Process Engineering, Ed., 2021.
- [K3] A. J. Imbsweiler, Y. Shinoura, D. Colin, S. Zaremba, and K. Drechsler, "Towards a Holistic Approach for an Efficient Determination of the Rheological Behavior of Sheet Molding Compounds for Process Simulation" in *ESAFORM Conference 2022*, Braga, Transtech Publications, Ed., 2022.

C Supervised student theses

During my employment at the Chair of Carbon Composites of the Technical University of Munich (TUM-LCC) I supervised the following student theses:

- [S1] F. Matrinez Quiles, „Experimental investigation and simulation of flow-induced defects in a leisure product made of Sheet Molding Compound (SMC)”, Master Thesis, Lehrstuhl für Carbon Composites, TUM, 2025.
- [S2] C. Cholvi Mifsud, „Characterization of Sheet Molding Compound (SMC) materials for automotive applications“, Bachelor Thesis, Lehrstuhl für Carbon Composites, TUM, 2024.
- [S3] P. Yuan, „Further Development and Validation of a Fitting Tool for Sheet Molding Compound (SMC) Rheological Data to obtain Material Parameters for Process Simulation“, Master Thesis, Lehrstuhl für Carbon Composites, TUM, 2024
- [S4] J. Wang, „Test setup for LSA and Tensile Testings for Bulk Molding Compound Materials, and 3DTimon simulation“, Master Thesis, Lehrstuhl für Carbon Composites, TUM, 2024.
- [S5] Y. Sun, „Numerical investigation of the flow behavior of recycling Bulk Molding Compound with varying obstacles in automotive parts“, Semester Thesis, Lehrstuhl für Carbon Composites, TUM, 2024.
- [S6] Y. Yan, „Validation of a simulation platform for the prediction of Sheet Molding Compound flow behavior in automotive parts“, Master Thesis, Lehrstuhl für Carbon Composites, TUM, 2024.
- [S7] F. Poller, „Bestimmung und Vergleich der Viskosität von Sheet und Bulk Molding Compound Materialien durch Squeeze Flow Tests“, Bachelor Thesis, Lehrstuhl für Carbon Composites, TUM, 2023.
- [S8] B.K. Reddy Guggulla, „Development of a fiber orientation investigation software for Sheet Molding Compound materials“, Master Thesis, Lehrstuhl für Carbon Composites, TUM, 2023.
- [S9] K.J. Suckfüll, „CFK-Bauteile im automobilen Rohbau“, Master Thesis in cooperation with Toray Industries Europe GmbH, Lehrstuhl für Carbon Composites, TUM, 2023.
- [S10] J. Wang, „Advancement and Evaluation of a Test Setup for the Viscosity Assessment of Sheet Molding Compound Materials“, Semester Thesis, Lehrstuhl für Carbon Composites, TUM, 2023.
- [S11] E. Shi, „Characterization of Sheet Molding Compound (SMC) materials for automotive applications“, Bachelor Thesis, Lehrstuhl für Carbon Composites, TUM, 2023.

- [S12] A. Alabras, „Investigation of pressing processes of resin and structured layers in microelectronics”, Semester Thesis, Lehrstuhl für Carbon Composites, TUM, 2023.
- [S13] K.J. Suckfüll, „Pressen von SMC und Prepreg am Beispiel von Carbonfasern”, Semester Thesis in cooperation with Toray Industries Europe GmbH, Lehrstuhl für Carbon Composites, TUM, 2022.
- [S14] R. Sharwalla, „Aufbau und Validierung eines Flussprüfstands zur Bestimmung der Viskosität in Sheet Molding Compound Materialien”, Bachelor Thesis, Lehrstuhl für Carbon Composites, TUM, 2022.
- [S15] J. Li, „Investigation of defects and fiber orientation in Sheet Molding Compound parts”, Master Thesis, Lehrstuhl für Carbon Composites, TUM, 2022.
- [S16] E.M. Sandoval Perez, „Identification of discrepancies between glass fiber and carbon fiber Sheet Molding Compound materials”, Bachelor Thesis, Lehrstuhl für Carbon Composites, TUM, 2022.
- [S17] F.J Martinez Quiles, „Identification of Variability, Defects and Fractural Differences in Glass Fibre and Carbon Fibre Sheet Moulding Compounds”, Bachelor Thesis, Lehrstuhl für Carbon Composites, TUM, 2022.
- [S18] M. Adil, „Comparison of different process simulation tools for Sheet Molding Compound Materials”, Master Thesis, Lehrstuhl für Carbon Composites, TUM, 2021.
- [S19] S. Singhara Na Ayuthaya, „Simulation and Mechanical testing of Sheet Molding Compound (SMC) products with varying fiber orientations“, Master Thesis, Lehrstuhl für Carbon Composites, TUM, 2020.
- [S20] M. Li, „Characterization of variability in Sheet Molding Compound (SMC) materials for automotive applications”, Bachelor Thesis, Lehrstuhl für Carbon Composites, TUM, 2020.
- [S21] C. Tang, „Characterization of fiber orientation in Sheet Molding Compound (SMC) materials for automotive applications”, Bachelor Thesis, Lehrstuhl für Carbon Composites, TUM, 2020.
- [S22] T. Akinpelu, „Characterizing the in-plane flow of Sheet Molding Compound (SMC) materials for automotive applications“, Semester Thesis, Lehrstuhl für Carbon Composites, TUM, 2024.
- [S23] P. Parameshwaranaik, „Numerical investigation of the flow behavior of recycling Bulk Molding Compound with the integration of UD reinforcement “, Semester Thesis, Lehrstuhl für Carbon Composites, TUM, 2024.

Parts of the above listed theses contributed to the underlying doctoral dissertation, as indicated in the text.